Title
Development of Small Molecule Ligands for Voltage-gated Potassium Channels and Functional Characterization of Voltage-gated Phosphatases

Author
Bell, Sarah C.

Publication Date
2010

Peer reviewed|Thesis/dissertation

Development of Small Molecule Ligands for Voltage-gated Potassium Channels and Functional Characterization of Voltage-gated Phosphatases

by

Sarah C. Bell

A dissertation submitted in partial satisfaction of the

requirements for the degree of

Doctor of Philosophy

in

Chemistry

in the

Graduate Division

of the

University of California, Berkeley

Committee in charge:

Professor Ehud Y. Isacoff, co-chair

Professor Carolyn R. Bertozzi, co-chair

Professor Christopher J. Chang

Professor Richard H. Kramer

Spring 2010

Development of Small Molecule Ligands for Voltage-gated Potassium Channels and Functional Characterization of Voltage-gated Phosphatases

by Sarah C. Bell

Abstract

Development of Small Molecule Ligands for Voltage-gated Potassium Channels and Functional Characterization of Voltage-gated Phosphatases

by

Sarah C. Bell

Doctor of Philosophy in Chemistry

University of California, Berkeley

Professor Ehud Y. Isacoff, co-chair
Professor Carolyn R. Bertozzi, co-chair

Membrane proteins respond to both chemical and electrical stimuli. This work explores the molecular mechanisms by which membrane voltage controls voltage-gated proteins and describes the development of tools to modulate voltage-gated protein function.

Voltage-gated potassium (K_v) channels are tetrameric transmembrane proteins that translate changes in the membrane electric field into the controlled permeation of potassium across the plasma membrane. K_v channels mediate the initiation and regulation of action potentials, muscle contraction, hormone secretion, and information processing, rendering them important drug targets. We employed organic synthesis, molecular dynamics and electrophysiology techniques to demonstrate that calix[4]arenes with free phenolic OH groups at the lower rim and positively-charged groups at the upper rim constitute a versatile class of reversible ligands for homotetrameric K_v1.x channels. Synthesis of a panel of calix[4]arenes with variable upper and lower rim substituents enabled the systematic development of K_v1.x channel-compatible ligands. We used molecular modeling to predict calix[4]arene binding to the pore domain, and through electrophysiology experiments, we demonstrated that the calix[4]arene ligands function as reversible blockers of K_v1.x channels. We probed the mechanism of calix[4]arene-channel interactions using voltage clamp fluorometry and found these ligands modify the voltage-dependent motions of the Shaker K_v channel in addition to inhibiting ion current. These calix[4]arene ligands provide a new set of tools to control cell excitability by specifically targeting K_v channels.

Until recently, ion channels were the only proteins known to sense changes in membrane potential. This changed with the discovery of *Ciona intestinalis* voltage-sensor containing phosphatase (Ci-VSP) which has a voltage sensing domain like voltage-gated ion channels and a cytosolic phosphatase domain resembling the phosphoinositide phosphatase PTEN. Ci-VSP is the first member of the voltage dependent family of proteins that is not an ion channel. Instead, Ci-VSP takes an electrical signal in the form of membrane voltage and converts it to a chemical signal through its phosphatase activity. To study the mechanism of voltage-sensing in Ci-VSP, we combined electrophysiology and fluorescence methods in living cells to determine the oligomerization state of Ci-VSP and monitor the functional transitions that result in Ci-VSP

mediated changes in phosphoinositide pools. We find that Ci-VSP is a functional monomer which undergoes complex voltage-dependent conformational changes to control a cytosolic phosphoinositide phosphatase domain. As Ci-VSP catalyzes several reactions, we also developed fluorescent-based methods to study Ci-VSP substrate specificity and monitor Ci-VSP-mediated changes in multiple phosphoinositide pools in a single cell. Finally, we find that basic residues in the interdomain linker connecting the voltage sensing domain and phosphatase domains in Ci-VSP are essential for coupling the two domains. Our results indicate that a single voltage sensing domain can function in the membrane on its own and suggests that voltage sensing domains are modular units that can impart voltage sensitivity to a variety of effector domains.

Dedication

To my family and friends:
Thank you for your constant motivation and support.

Table of Contents

Chapter 3

Chapter 4

Appendix 1

Acknowledgements

I came to graduate school with a background in synthetic chemistry and a desire to do biological research, and the chemical biology graduate program at UC Berkeley allowed me to explore both areas of research freely and develop my own course of study. Thank you to the UC Berkeley professors and administrators for developing the Chemical Biology Graduate Program and providing a well-supported infrastructure for students interested in chemical biology. I was very lucky to have many talented and supportive classmates in both the chemical biology graduate program and the synthetic division of the chemistry department. Thanks to everyone for all their help and support in everything from working on physical organic problem sets and preparing for our qualifying exams to covering lab sections and office hours and offering career advice.

I worked in four amazing labs as a chemical biology rotation student during my first year of graduate school. Each experience was crucial to my development as a scientist and I am very grateful to the members of the Bertozzi, Chang, and Marletta, and Isacoff labs for their help and guidance during my rotations. For my final rotation, Professor Ehud (Udi) Isacoff enthusiastically accepted me (a chemist) into the Isacoff lab even though I had little knowledge of ion channels or any neurobiology. The Isacoff lab became my home for the next four years of graduate school, and I want to thank Udi for his help and support throughout my time in the lab. During my rotation in the Isacoff lab, I was very fortunate to have three mentors: Dr. Max Ulbrich, Dr. Francesco Tombola, and Medha Pathak. These three scientists were extremely patient, always took the time to help me, and thoroughly trained me in all the techniques I needed to become an independent researcher in the lab.

Once I officially joined the Isacoff lab, Max and Francesco continued to serve as mentors. I am eternally grateful for their help with experimental design, data analysis, and the art of crafting a good scientific paper. Thanks to Max for sharing a bench with me for most of my graduate career and always pushing me to do better. Thanks to Francesco for always taking the time to help and for his wealth of good advice both research and career wise. I would also like to thank my other Isacoff lab mates for all their help and support throughout the years. For the majority of my graduate career, I have worked closely with Dr. Susy Kohout, a postdoctoral fellow in the Isacoff lab, on the functional characterization of Ci-VSP. I am grateful for her dedication and perseverance as we worked together to devise new methods to characterize a protein whose function became ever-more complex with each experiment we conducted. Sandra Wiese is the glue that holds the Isacoff lab together and I am very thankful for all her help in making sure our lab runs smoothly. I would like thank all other members of the Isacoff lab, past and present for their hard work and support during my time in the lab. Thanks to Tracey, Whitney, and Shayan, three fantastic technicians in the lab whose hard work has helped me immensely in conducting my research. Thanks to all the undergraduate frog surgeons for

regularly providing oocytes for my experiments. My fellow graduate students in the Isacoff lab served as a constant support system on all matters both scientific and person, so many thanks to Medha, Robin, Hanson, Gautam, Steph, Orapim, Grant, Erica, and Ryan. The postdoctoral fellows in the Isacoff lab were also extremely helpful teaching me how to properly analyze my data, how to tell a good story about my research, and how to succeed in the job market. Thanks to Harald, Jordan, and Claire for all your help and advice! Finally, thank you to Dr. Guillaume Sandoz, Dr. Jordan Patti, Dr. Max Ulbrich and Orapim Tulyatham for taking the time to edit chapters of this thesis.

One of the best parts of working in the Isacoff lab was the opportunity to collaborate with scientists from different areas of expertise and even different parts of the world. I was fortunate to work on an ion channel pharmacology project with Vera Martos, a very talented synthetic organic chemist from Spain. Vera's enthusiasm and dedication to the project was instrumental in this successful collaboration. I would also like to thank Professor Javier de Mendoza, Professor Dirk Trauner and Udi for their help in developing this collaboration and overseeing its progress over the years. During the last year of graduate school, I have had the pleasure of working closely with Dr. Guillaume Sandoz, a visiting scholar from France. Guillaume's optimism and enthusiasm came at exactly the right time as I was pushing to complete experiments for this thesis, and I am very thankful for his help. Finally, I would like to thank Professor Terry Machen and the members of his laboratory for "housing" me in their student office and providing a very welcoming place to do most of my writing.

None of the above research would have been possible without the constant support and motivation from my family and friends. My parents have always been supportive of my academic endeavors, even when that meant I would have to move 3000 miles away from home to start my Ph.D. at UC Berkeley. I can not thank them enough for their emotional as well as financial support throughout my 22 years of schooling. Living far from home brought along many challenges, and I am grateful to my friends for serving as a surrogate family throughout the years. Also, thanks to both friends and family members for coming out to visit and providing great excuses for me to leave the lab and explore the Bay Area.

Finally, I would like to thank my fiancé, Scott P. West for his never-ending love and support throughout my graduate career. In addition to earning his own Ph.D. at UC Berkeley, he has also weathered every storm that graduate school has thrown my way and made sure that I'm still standing at the end. I look forward to the next chapter of our lives when we tackle the chemical industry together.

Chapter 1

The role of electrical and chemical signals in regulating cell excitability

Ion channels control electrical excitability

The conversion of electrical signals into chemical signals controls many cellular processes including neural excitability. The neuronal plasma membrane separates the interior and exterior of the cell to ensure electrochemical homeostasis with greater concentrations of sodium (Na^+) and calcium (Ca^{2+}) in the extracellular fluid and greater concentrations of potassium (K^+) in the cytosol. Electrical signaling is mediated by the flux of Na^+ K^+ and Ca^{2+} through ion channels, transmembrane proteins which provide a pathway for ions to move down their concentration gradients through the plasma membrane.[1] At rest, the plasma membrane has a negative membrane potential with the cytoplasm holding more negative charge than the extracellular media. The flux of Na^+ and Ca^{2+} through cation channels increases the positive charge in the cytosol and depolarizes membrane voltage. This depolarization enhances the cell's excitability and activates intracellular signaling cascades. To decrease electrical excitability, K^+ selective channels conduct K^+ out of the cytosol and thus repolarize the neuron to its resting membrane potential. Ion channels can be controlled by a variety of stimuli including changes in transmembrane voltage, neurotransmitter binding, and phosphoinositide binding and their function underlies electrical signaling in excitable cells. Figure 1.1 shows the synapse formed between a neuron and a target cell which allows for the transmission of both chemical and electrical signals between these two cells.

For example, membrane depolarization in the neuron will activate voltage-gated Ca^{2+} channels which mediate the flow of Ca^{2+} into the cell. This flux of Ca^{2+} will trigger the exocytotic release of neurotransmitters, chemical signals that mediate signaling between neurons and their targets. Neurotransmitters will diffuse through the synapse and activate ligand-gated-ion channels causing a flux of ions into the post-synaptic cell. Cytosolic proteins can also regulate ion channel function. For example, lipid kinases and phosphatases regulate the pools of plasma membrane phosphoinositides. These minor lipid components of the plasma membrane can serve as direct chemical regulators of ion channels or serve as indirect regulators through their mediation of cellular signaling pathways. Through this chain of events which mediates cell-cell communication, electrical and chemical signals are interconverted.

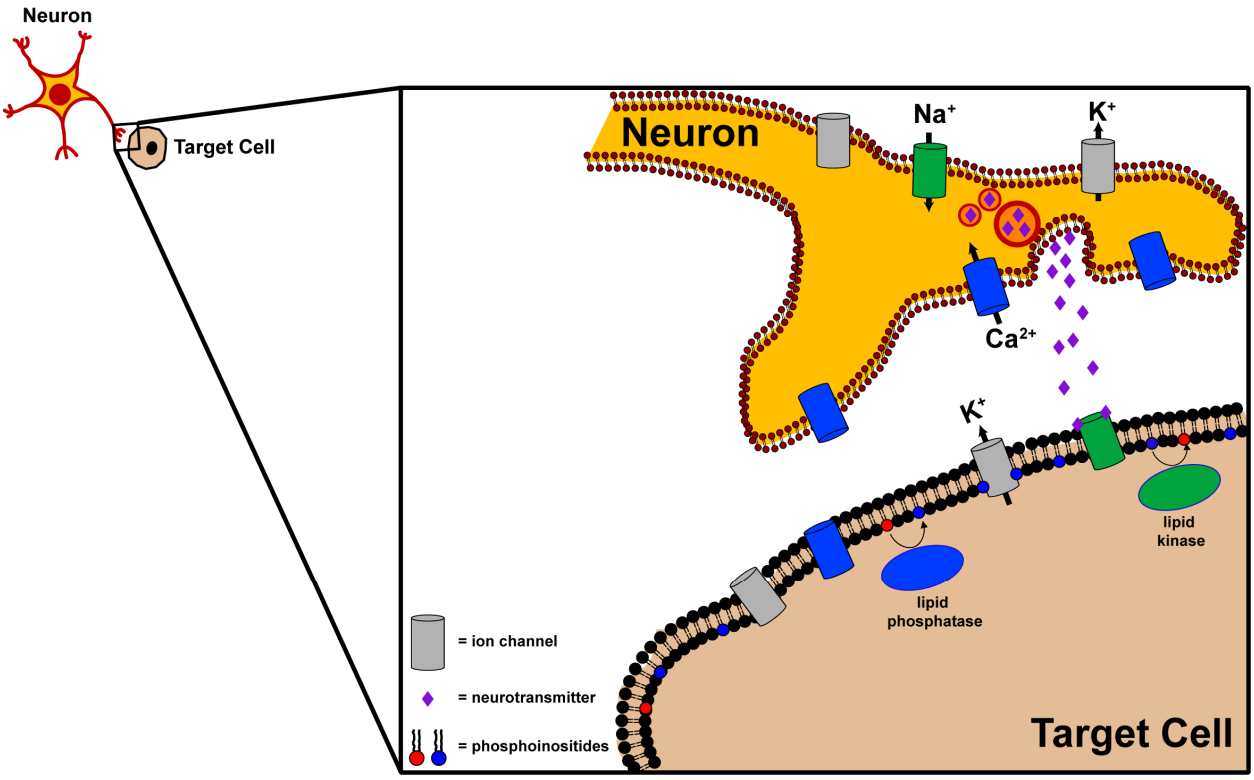

Figure 1.1. Cells communicate via electrical and chemical signals. A neuron can communicate with neighboring cells using both electrical and chemical signals. The flux of ions through ion channels controls the electrical excitability of both the neuron and its target cell. The exocytotic release of neurotransmitters or the lipid kinase and phosphatase mediated creation and depletion of phosphoinositide pools provide chemical regulators of ion channels.

Voltage-gated potassium (K_v) channels respond to electrical signals

Potassium (K^+) channels are responsible for stabilizing the resting potential of a cell and serve as "off" switches for many electrical signaling processes. K^+ channels are essential membrane proteins in all cell types. In the human body, these proteins regulate neuronal excitability, heart beat, hormone secretion, and epithelial transport of electrolytes.[2]

Voltage-gated K^+ (K_v) channels represent the largest family of the K^+ channels and the human genome contains 40 genes encoding these tetrameric channels.[3] Each alpha subunit comprised of six transmembrane helices (S1-S6) (Figure 1.2A). The N-terminus of an alpha subunit contains a cytosolic tetramerization domain which mediates association with other K_v alpha subunits to form homotetramers or heterotetramers.[4] The first four transmembrane helices of an alpha subunit (S1-S4) form the voltage sensing domain (VSD). The S5 and S6 helices along with a short pore helix form the pore domain of the channel. K_v channels translate changes in the membrane electric field into the controlled permeation of K^+ ions. The S4 helix contains a series of positively-charged residues separated by two hydrophobic residues that move in response to changes in the membrane electric field. These movements are directly coupled to the

opening and closing of the channel (Figure 1.2B). The Shaker channel, a member of the $K_v1.1x$ channel family from Drosophila melanogaster, was the first cloned K_v channel and has been studied extensively.[5] Decades of functional studies of the Shaker channel using a variety of experimental methods has resulted models for the channel opening and closing and has served as the foundation for voltage-gated ion channel research [reviewed in [5]]. In chapter 2 of this dissertation, we use these models as a frame work in our study of the binding mechanism of small molecule K_v channel ligands. In chapter 4 and appendix 1 of this dissertation we extend the models of voltage-sensing to study the mechanism of voltage sensing in voltage-gated enzymes.

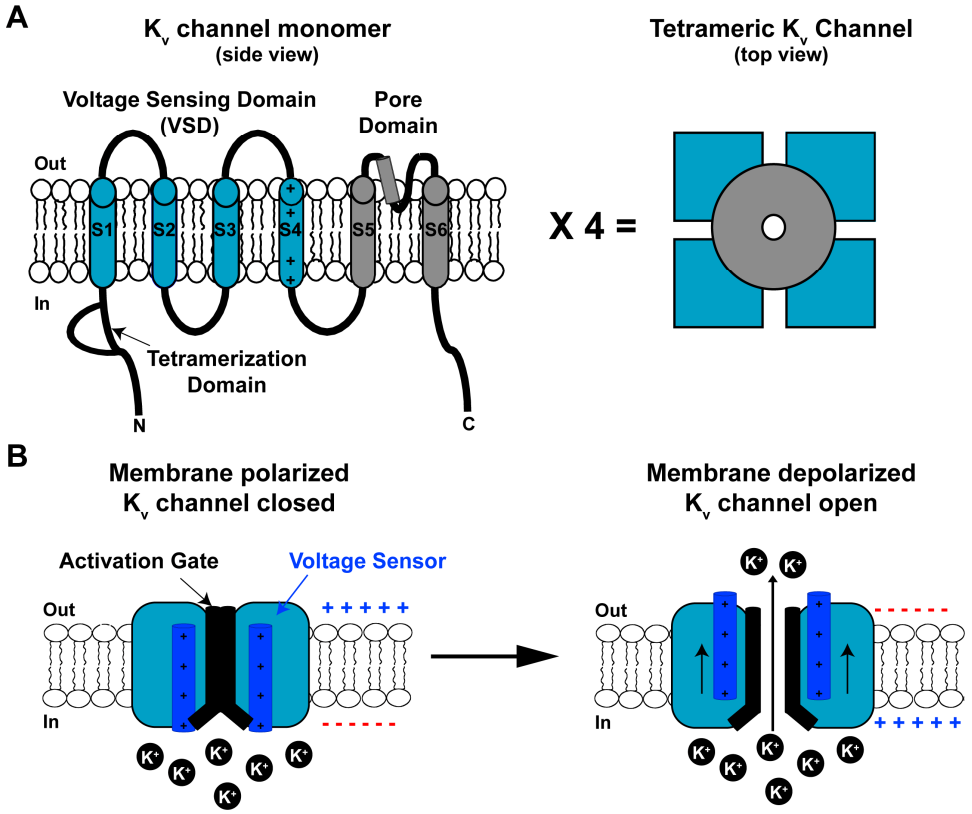

Figure 1.2. K_v channel topology and function. (A) Architecture of a K_v channel alpha subunit and tetrameric K_v channel. Helices are represented by cylinders with voltage sensing domains shaded in blue and pore domains shaded in gray. **(B)** Schematic of K_v channel function. At rest, the channel is closed. Membrane depolarization elicits movement of the voltage sensor which is translated into channel opening and allows for the flux on K^+ ions through the channel.

X-ray crystal structures of the K_v channel $K_v1.2$ from rat [6, 7] and other related K_v channels[8] show that the alpha subunits assemble as tetramers to form a pore comprising the turret loop, the P-helix and the K^+ selectivity filter (Figure 1.3).[9] This structural information has enabled the development of rationally designed ligands to modulate K_v channel function.[10, 11]

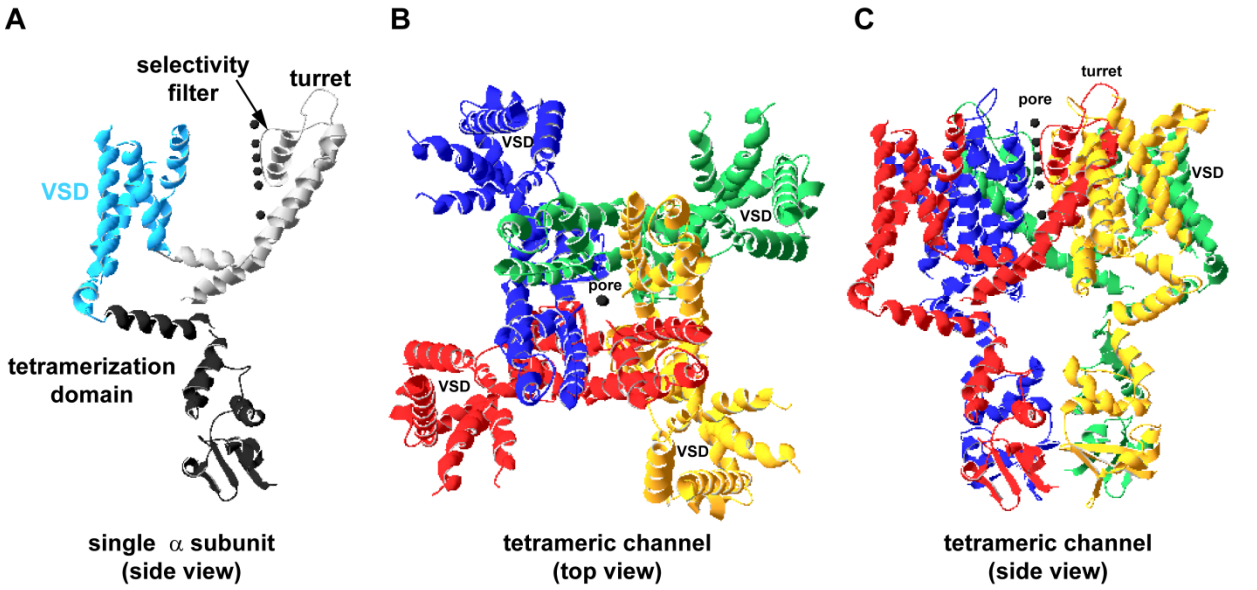

Figure 1.3. Crystal structure of rK$_v$1.2. (A) Side view of single rK$_v$1.2 subunit. Tetramerization domain (black), voltage sensing domain (blue) (VSD), and pore domain (gray) are highlighted. **(B)** Top view (extracellular side) of tetrameric rK$_v$1.2 channel. Each alpha subunit is shown in a different color. **(C)** Side view of tetrameric rK$_v$1.2 channel. Each alpha subunit shown in a different color. Potassium ions are shown as black spheres in all panels. Coordinates obtained from PDB file 2A79. All images created using Swiss PDB Viewer (http://spdbv.vital-it.ch/).

Development of small molecule modulators for K$_v$ channels

Chapter two of this dissertation describes the development of a new class of calix[4]arene-based small molecule ligands to modulate K$_v$ channel function. Calix[4]arenes have been used as platforms for multivalent ligands to efficiently bind proteins and nucleotides.[12] This building block of supramolecular chemistry is a series of four phenol macrocyclic oligomers linked through methylene bridges which form basket-like structures with wider upper rims and narrower lower rims (Figure 1.4A).[13]

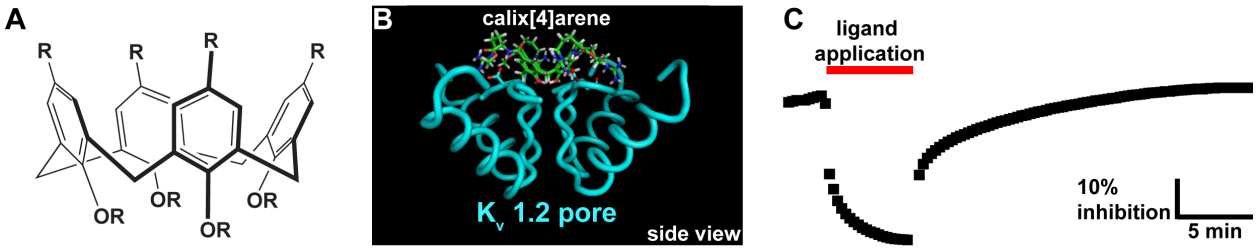

Figure 1.4. Calix[4]arene ligands for K$_v$ channels. (A) Calix[4]arene scaffold **(B)** Calix[4]arene ligand docked in pore domain of K$_v$ 1.2 channel (PDB ID 2A79). **(C)** Application of calix[4]arene reversibly blocks Shaker channel ionic current.

We employed organic synthesis, molecular dynamics and electrophysiology techniques to demonstrate that calix[4]arenes with free phenolic OH groups at the lower rim and positively-charged groups at the upper rim constitute a versatile class of reversible ligands for K_v1.x channels. Synthesis of a panel of calix[4]arenes with variable upper and lower rim substituents enabled the systematic development of K_v1.x channel-compatible ligands. Molecular modeling predicted calix[4]arene binding to the pore domain (Figure 1.4B). Electrophysiology experiments demonstrated the calix[4]arene ligands are reversible blockers of K_v1.x channels (Figure 1.4C). We probed the mechanism of calix[4]arene-channel interactions and found these ligands modify the voltage-dependent motions of the Shaker K_v channel in addition to inhibiting ionic current. We then designed a second generation of ligands to target the pore region of K_v channels and improve K_v1.x subtype specificity. Ultimately, the development of this new class of calix[4]arene compounds might lead to novel therapeutic agents against autoimmune disorders, diabetes, epilepsy, and cardiac diseases.[14]

Phosphoinositides are chemical regulators of ion channels

The control of endogenous modulators of ion channel function may also provide a way to treat ion-channel related diseases. Phosphoinositides (PIPs) serve as endogenous chemical regulators of ion channels. These phospholipids are concentrated on the cytosolic surface of virtually all cellular membranes and even though PIPs constitute less than 15% of all lipids in eukaryotic membranes, they play integral roles in the cell.[15, 16] Phosphatidylinositiol 4,5-bisphosphate ($PI(4,5)P_2$) represents roughly 99% of all doubly phosphorylated phosphoinositides within the cell and directly binds a variety of ion channels including inwardly rectifying K^+ (K_{ir}) channels, voltage dependent K^+ (K_v) channels, and transient receptor potential (TRP) channels.[17, 18, 19] $PI(4,5)P_2$-sensitive ion channels are regulated by cytosolic lipid kinases, phosphatases and phospholipases which maintain resting pools of $PI(4,5)P_2$ at the plasma membrane as well as generate $PI(4,5)P_2$-derived-secondary messengers.

The connection between electrical signals at the plasma membrane sensed by voltage-gated ion channels and chemical signals regulated by PIP mediated processes seemed unclear until the discovery of a voltage-gated PIP phosphatase, *Ciona intestinalis* voltage-sensor containing phosphatase.[20] Ci-VSP contains a voltage sensing domain like voltage-gated ion channels and a cytosolic phosphatase domain resembling PTEN, a phosphoinositide phosphatase and potent tumor suppressor protein[21] (Figure 1.5A). Ci-VSP is a voltage-regulated phosphoinositide phosphatase that catalyzes the hydrolysis of the D5 phosphate group of both phosphatidylinositol 3,4,5-trisphosphate ($PI(3,4,5)P_3$) and $PI(4,5)P_2$ (Figure 1.5B).

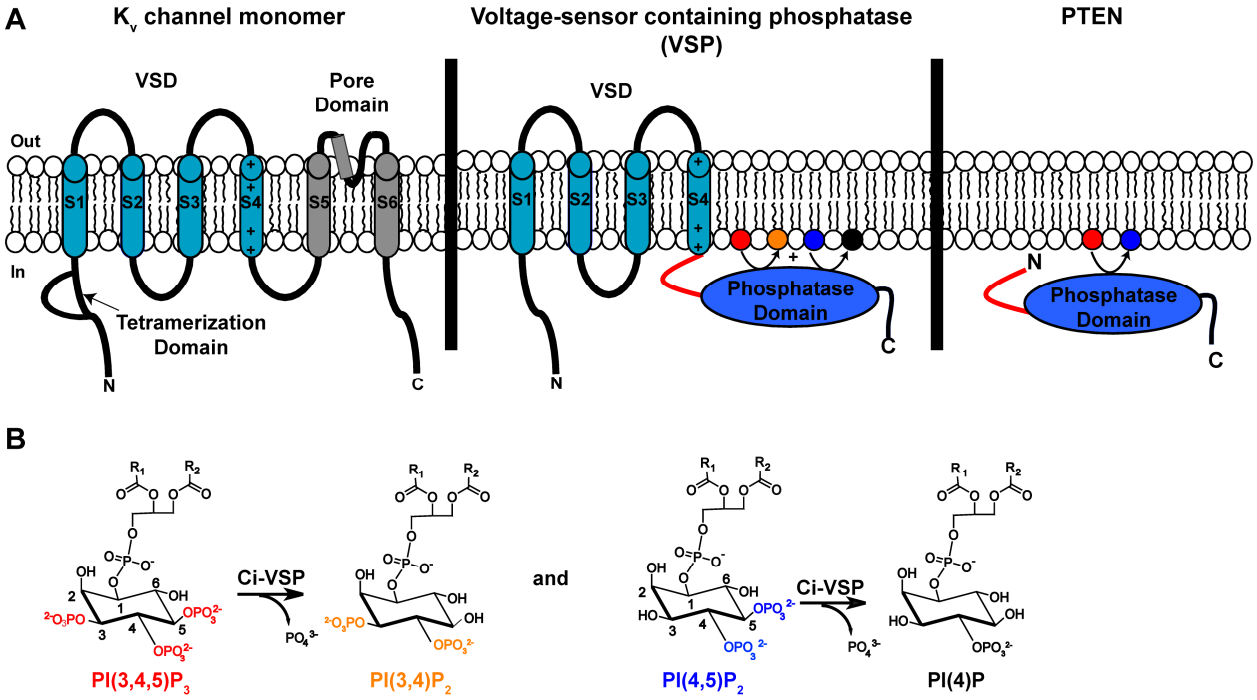

Figure 1.5. Overview of Ci-VSP topology and activity. (A) Comparison of Ci-VSP topology (middle) with K_v channels (left) and PTEN (right). Ci-VSP contains four transmembrane segments (S1-S4) that are homologous to the voltage sensing domain (VSD) of a K_v channel. The cytosolic domain of Ci-VSP shares 29.5% sequence identity with PTEN. Helices are represented by cylinders with VSDs shaded in light blue, pore domains shaded in gray, and phosphatase domains shaded in dark blue. **(B)** Ci-VSP is a voltage-regulated phosphoinositide phosphatase that catalyzes the hydrolysis of the D5 phosphate group of PI(3,4,5)P_3 and PI(4,5)P_2.

In Chapter 3 of this dissertation, I review phosphoinositide signaling, describe the functional characterization of Ci-VSP and its homologs, and review how VSPs can be used as tools to manipulate and dissect phosphoinositide signaling pathways.

Voltage sensing moves beyond voltage-gated ion channels

Until recently, ion channels were the only proteins known to sense changes in membrane potential. This changed with the discovery of Ci-VSP, which couples a voltage sensing domain (VSD) to a phosphatase and tensin homologue (PTEN)-like domain.[20] More recently, the voltage-gated proton channel (H_v) was cloned and found to contain a VSD, but it lacks a traditional pore domain.[22, 23] Figure 1.6 shows the diversity that exists both in membrane topology and subunit organization of the voltage-gated protein family.

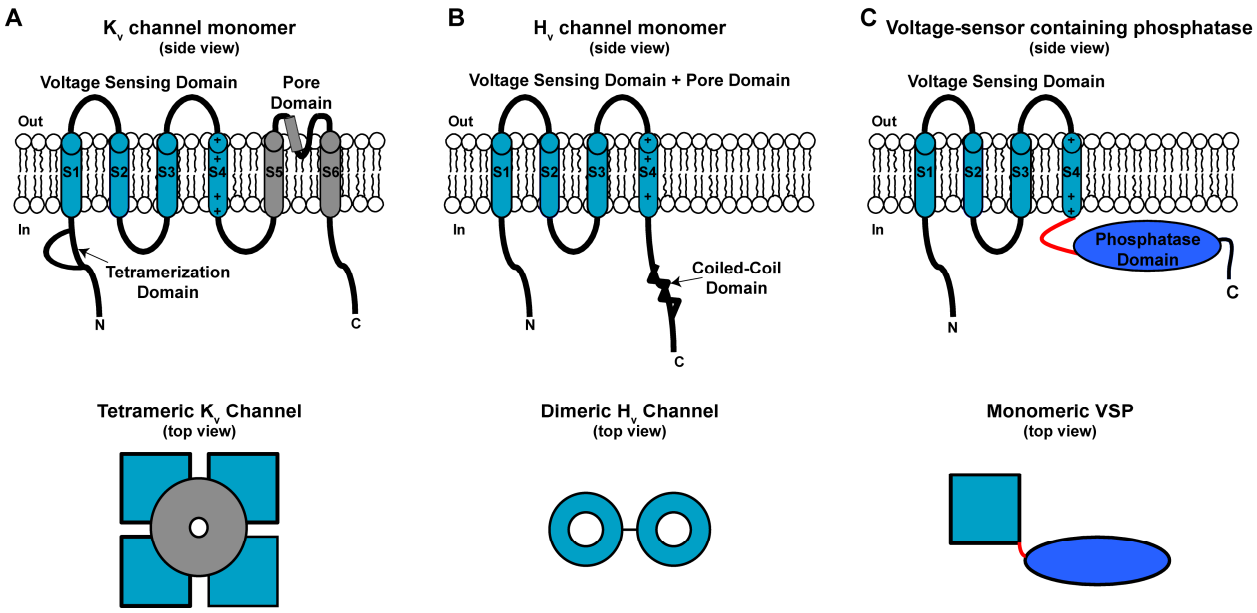

Figure 1.6. Membrane topology and subunit organization of voltage-gated proteins. (A) Voltage-gated K^+ (K_v) channel subunits contain six transmembrane segments which form the voltage sensing domain (VSD) and pore domain (top). These subunits form functional tetramers (bottom). **(B)** The H_v channel subunit contains four transmembrane domains which form both the VSD and pore domain (top). These subunits dimerize to form a functional two-pore channel (bottom). **(C)** Voltage-sensor containing phosphatases (VSPs) contain four transmembrane domains that form the VSD and are linked to cytosolic phosphatase domain (top). VSPs are functional monomers (bottom). In (A)-(C), helices are represented by cylinders with VSDs shaded in light blue, pore domains shaded in gray, and phosphatase domains shaded in dark blue.

The existence of Ci-VSP and H_v indicates that VSDs are functional modules[6, 24] that control distinct effectors. To date, voltage sensor-effector coupling has been studied in the context of four subunit channels, where a common pore is cooperatively gated by four VSDs.[5] In the H_v channel, the VSD acts as both a voltage sensor and pore. H_v is a functional dimer with each subunit containing its own pore domain, and the two VSDs working cooperatively to gate H^+ flux through both pore domains. [25, 26]

In chapter 4 of this dissertation, I describe our efforts to functionally characterize Ci-VSP in living cells. We combined electrophysiology and fluorescence methods to determine the oligomerization state of Ci-VSP, monitor the functional transitions that result in Ci-VSP mediated changes in phosphoinositide pools and study the mechanism of coupling between the Ci-VSP VSD and phosphatase domains. We demonstrated that Ci-VSP is a functional monomer which undergoes complex voltage-dependent conformational changes to control a cytosolic phosphoinositide phosphatase domain.[27]

Recent reports show that Ci-VSP catalyzes multiple PIP hydrolysis reactions in living cells.[28, 29] In chapter 5 of this dissertation, I describe the development of fluorescent-based

methods to study Ci-VSP substrate specificity and monitor Ci-VSP-mediated changes multiple PIP pools in a single cell.

Summary

Electrical and chemical signaling pathways provide ways for a cell to sense its surroundings and maintain homeostasis. Ion channels are key players in these pathways and the development of tools to modify ion channel function allows us to dissect complicated pathways. Figure 1.7 highlights two ways to control ion channel function using either small molecule or protein-based tools which I have developed during my Ph.D. research. The design and testing of small molecule calix[4]arene ligands as modulators of K_v channels has led to a new set of tools to control cell excitability by specifically targeting K_v channels. The functional characterization of Ci-VSP, a voltage-gated phosphoinositide phosphatase, allows us to electrically control phosphoinositide signaling pathways in the cell and therefore control the chemical regulators of ion channels.

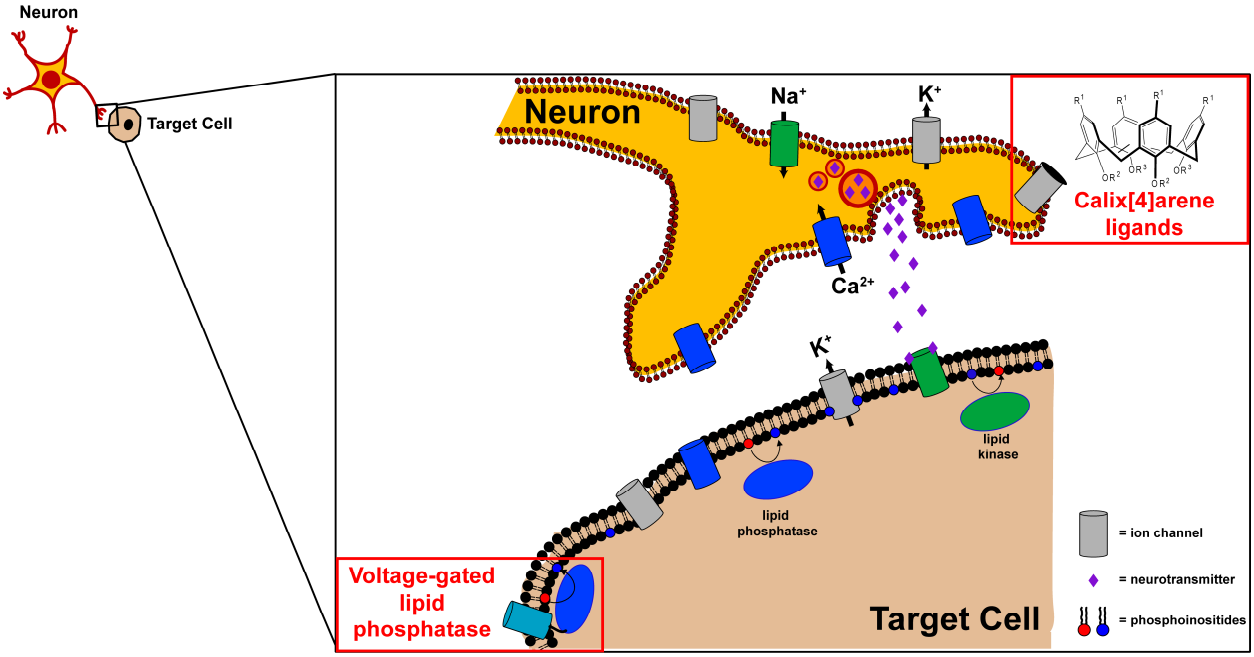

Figure 1.7. Tools to modulate ion channels and regulate cell communication. A neuron can communicate with neighboring cells using both electrical and chemical signals as shown in Figure 1.1. Red boxes indicate two tools that can be used to modulate ion channel function. Calix[4]arene ligands serve as small-molecule blockers of voltage-gated potassium channels which serve to limit the electrical signaling of the cell. Voltage-gated lipid phosphatases like Ci-VSP can change the phospholipid concentrations in the membrane to modulate phosphoinositide sensitive ion channels.

References

1. Yellen, G., The voltage-gated potassium channels and their relatives. *Nature* **2002,** 419, (6902), 35-42.

2. Yu, F. H.; Catterall, W. A., The VGL-chanome: A protein superfamily specialized for electrical signaling and ionic homeostasis. *Sci. STKE* **2004,** 253, re15-.

3. Wulff, H.; Castle, N. A.; Pardo, L. A., Voltage-gated potassium channels as therapeutic targets. *Nat Rev Drug Discov* **2009,** 8, (12), 982-1001.

4. Li, M.; Jan, Y. N.; Jan, L. Y., Specification of subunit assembly by the hydrophilic amino-terminal domain of the Shaker potassium channel. *Science* **1992,** 257, (5074), 1225-1230.

5. Tombola, F.; Pathak, M. M.; Isacoff, E. Y., How does voltage open an ion channel? *Annu. Rev. Cell Dev. Biol.* **2006,** 22, (1), 23-52.

6. Long, S. B.; Campbell, E. B.; MacKinnon, R., Crystal structure of a mammalian voltage-dependent Shaker family K^+ channel. *Science* **2005,** 309, (5736), 897-903.

7. Long, S. B.; Tao, X.; Campbell, E. B.; MacKinnon, R., Atomic structure of a voltage-dependent K^+ channel in a lipid membrane-like environment. *Nature* **2007,** 450, (7168), 376-382.

8. Jiang, Y., et al., X-ray structure of a voltage-dependent K^+ channel. *Nature* **2003,** 423, (6935), 33-41.

9. MacKinnon, R., Potassium channels. *FEBS Lett.* **2003,** 555, (1), 62-65.

10. Gradl, S. N., et al., Protein surface recognition by rational design: Nanomolar ligands for potassium channels. *J. Am. Chem. Soc.* **2003,** 125, (42), 12668-12669.

11. Martos, V., et al., Calix[4]arene-based conical-shaped ligands for voltage-dependent potassium channels. *Proc. Natl. Acad. Sci. U. S. A.* **2009,** 106, (26), 10482-10486.

12. Baldini, L.; Casnati, A.; Sansone, F.; Ungaro, R., Calixarene-based multivalent ligands. *Chem. Soc. Rev.* **2007,** 36, (2), 254-266.

13. Martos, V.; Castreño, P.; Valero, J.; de Mendoza, J., Binding to protein surfaces by supramolecular multivalent scaffolds. *Curr. Opin. Chem. Biol.* **2008,** 12, (6), 698-706.

14. Coghlan, M. J.; Carroll, W. A.; Gopalakrishnan, M., Recent developments in the biology and medicinal chemistry of potassium channel modulators: Update from a decade of progress. *J. Med. Chem.* **2001,** 44, (11), 1627-1653.

15. Niggli, V., Regulation of protein activities by phosphoinositide phosphates. *Annu. Rev. Cell Dev. Biol.* **2005,** 21, 57-79.

16. Di Paolo, G.; De Camilli, P., Phosphoinositides in cell regulation and membrane dynamics. *Nature* **2006,** 443, 651.

17. McLaughlin, S.; Wang, J.; Gambhir, A.; Murray, D., PIP_2 and proteins: Interactions, organization, and information flow. *Annu. Rev. Biophys. Biomol. Struct.* **2002,** 31, (1), 151-175.

18. Gamper, N.; Shapiro, M. S., Regulation of ion transport proteins by membrane phosphoinositides. *Nat. Rev. Neurosci.* **2007,** 8, (12), 921-934.

19. Suh, B.-C.; Hille, B., PIP_2 is a necessary cofactor for ion channel function: How and why? *Annual Review of Biophysics* **2008,** 37, (1), 175-195.

20. Murata, Y., et al., Phosphoinositide phosphatase activity coupled to an intrinsic voltage sensor. *Nature* **2005,** 435, (7046), 1239-1243.

21. Leslie, N. R.; Downes, C. P., PTEN: The down side of PI 3-kinase signaling. *Cell. Signal.* **2002,** 14, (4), 285-295.

22. Sasaki, M.; Takagi, M.; Okamura, Y., A voltage sensor-domain protein is a voltage-gated proton channel. *Science* **2006,** 312, (5773), 589-92.

23. Ramsey, I. S.; Moran, M. M.; Chong, J. A.; Clapham, D. E., A voltage-gated proton-selective channel lacking the pore domain. *Nature* **2006,** 440, (7088), 1213-6.

24. Lu, Z.; Klem, A. M.; Ramu, Y., Ion conduction pore is conserved among potassium channels. *Nature* **2001,** 413, (6858), 809-13.

25. Tombola, F.; Ulbrich, M. H.; Isacoff, E. Y., The voltage-gated proton channel H_v1 has two pores, each controlled by one voltage sensor. *Neuron* **2008,** 58, (4), 546-556.

26. Tombola, F.; Ulbrich, M. H.; Kohout, S. C.; Isacoff, E. Y., The opening of the two pores of the H_v1 voltage-gated proton channel is tuned by cooperativity. *Nat. Struct. Mol. Biol.* **2010,** 17, (1), 44-50.

27. Kohout, S. C.; Ulbrich, M. H.; Bell, S. C.; Isacoff, E. Y., Subunit organization and functional transitions in Ci-VSP. *Nat. Struct. Mol. Biol.* **2008,** 15, (1), 106-108.

28. Halaszovich, C. R.; Schreiber, D. N.; Oliver, D., Ci-VSP Is a depolarization-activated phosphatidylinositol-4,5-bisphosphate and phosphatidylinositol-3,4,5-trisphosphate 5'-phosphatase. *J. Biol. Chem.* **2009,** 284, (4), 2106-2113.

29. Murata, Y.; Okamura, Y., Depolarization activates the phosphoinositide phosphatase Ci-VSP, as detected in Xenopus oocytes coexpressing sensors of PIP_2. *J Physiol* **2007,** 583, (3), 875-889.

Chapter 2

Calix[4]arene-based ligands for voltage-gated potassium channels[1]

[1] A portion of this work was published in the following article:
Martos, V., Bell, S.C., Santos, E., Isacoff, E.Y., Trauner, D., de Mendoza, J., Calix[4]arene-based conical-shaped ligands for voltage-dependent potassium channels. *Proc. Natl. Acad. Sci. U. S. A.* **2009,** 106, (26), 10482-10486.

Introduction

Potassium (K^+) channels are essential membrane proteins in all cell types. In the human body, these proteins regulate neuronal excitability, heart beat, hormone secretion, and epithelial transport of electrolytes.[1]

The plasma membrane serves as a barrier to electrochemical homeostasis with greater concentrations of Na^+ and Ca^{2+} in the extracellular fluid and greater concentrations of K^+ in the cytoplasm. Electrical signaling is mediated by the flux of Na^+ K^+ and Ca^{2+} down their concentration gradients through ion channels across the plasma membrane.[2] At rest, the inside of the cell has a negative membrane potential. The flux of Na^+ and Ca^{2+} through cation channels causes an increase of positive charge in the intracellular space, depolarizing the cell and enhancing electrical excitability. To decrease electrical excitability, K^+ selective channels conduct K^+ out of the cytosol to repolarize the cell to its resting membrane potential. Potassium channels are responsible for stabilizing the resting potential of a cell and serve as "off" switches for many electrical signaling processes.

K^+ channels are multimeric proteins. The human genome encodes 78 K^+ channel alpha subunits.[3-5] Alternative gene-splicing, post-translational modifications, and hetero-multimeric oligomerization further adds to the diversity within the K^+ channel superfamily.[6] Although other parts of the channel differ in structure, the pore-forming region is highly homologous among members of the K^+ channel family. The pore-forming region is composed of a P-loop region containing the consensus amino acid sequence TXGYGD flanked by at least two transmembrane segments.[7]

K^+ channels can be divided into three groups based on their membrane topology and biophysical properties (Figure 2.1). In the 2-pore-loop K^+ (K_{2P}) channel subfamily, alpha subunits each containing four transmembrane segments and two pore-forming regions dimerize to form functional channels. These so-called "leak" K^+ channels help maintain negative resting potentials in both in excitable and non-excitable cells.[8] Members of the inwardly rectifying K^+ (K_{ir}) channel subfamily are composed of alpha subunits containing 2 transmembrane segments flanking single pore-forming region. K_{ir} channel subunits tetramerize to form functional channels. K_{ir} channels are prominently expressed in the heart, vascular and skeletal muscle, and brain and are responsible for maintaining the resting potential and controlling action potentitals.[9] K_{ir} channels also can be regulated by phospholipids, nucleotides, polyamines, ions, and cytosolic proteins.

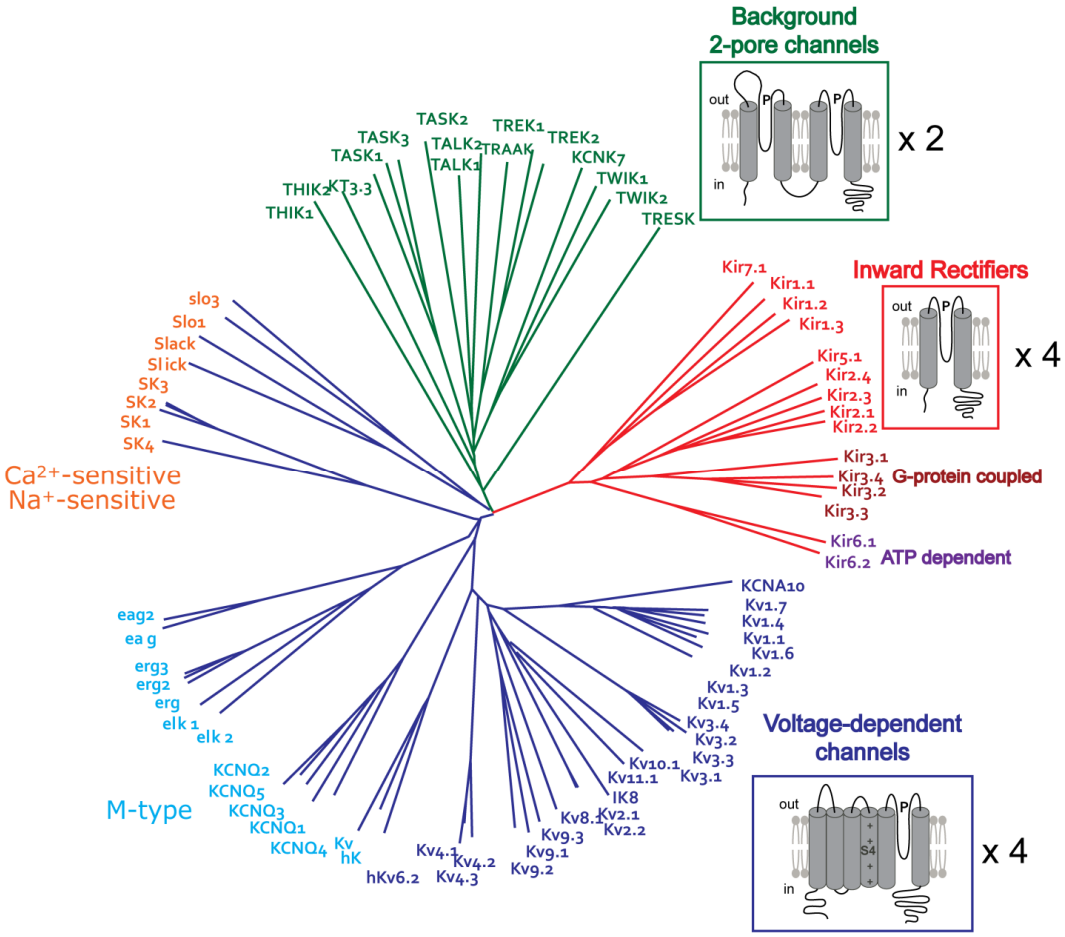

Figure 2.1. Classification of human K^+ channels. Tree diagram of potassium channels encoded by the human genome. Channels can be further classified according to their topology and response to different stimuli. Color code: two-pore K^+ channels (green), inwardly rectifying K^+ channels (red), and voltage-dependent K^+ channels (blue). Figure adapted from [10].

Voltage-dependent K^+ (K_v) channels represent the largest family of K^+ channels and the human genome contains 40 genes encoding these tetrameric channels.[11] Each alpha subunit is comprised of six transmembrane helices (S1-S6) (Figure 2.2A). The N-terminus of an alpha subunit contains a cytosolic tetramerization domain which mediates association with other K_v alpha subunits to form homotetramers or heterotetramers.[12] The first four transmembrane helices of an alpha subunit (S1-S4) form the voltage sensing domain (VSD). The S5 and S6 helices along with a short pore helix form the pore domain of the channel. K_v channels translate changes in the membrane electric field into the controlled permeation of K^+ ions. The S4 helix contains a series of positively-charged residues separated by two hydrophobic residues that move in response to changes in the membrane electric field. These movements are directly coupled to the opening and closing of the channel (Figure 2.2B). Some members of the K_v channel subfamily are regulated by additional stimuli including phospholipids and other cations.

The Shaker channel, a member of the K_v1.1x channel family from *Drosophila melanogaster*, was the first cloned K_v channel and has been studied extensively.[13] Decades of

functional studies on the Shaker channel using a variety of methods have resulted in models for the channel opening and closing and has served as the foundation for ion channel research [reviewed in [13]].

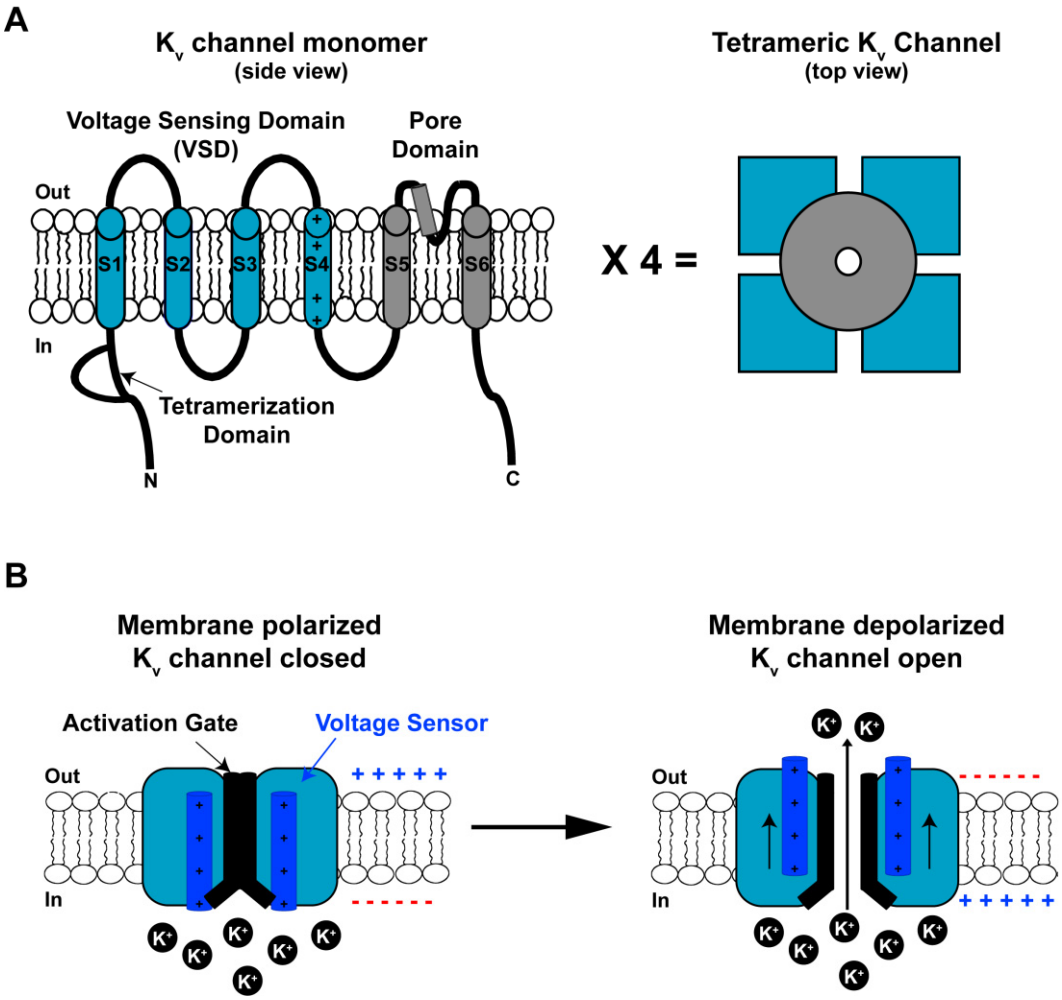

Figure 2.2. K_v channel topology and function. (A) Architecture of a K_v channel alpha subunit and tetrameric K_v channel. Helices are represented by cylinders with voltage sensing domains shaded in blue and pore domains shaded in gray. **(B)** Schematic of K_v channel function. At rest, the channel is closed. Membrane depolarization elicits movement of the voltage sensor which is translated into channel opening and allows for the flux on K^+ ions through the channel.

X-ray crystal structures of the K_v channel $K_v1.2$ from rat [14, 15] and other related K_v channels[16] show that the alpha subunits assemble as tetramers to form a pore comprising the turret loop, the pore-helix and the K^+ selectivity filter (Figure 2.3).[17] This structural information has allowed for the development of rationally designed ligands to modulate K_v channel function.[4, 5]

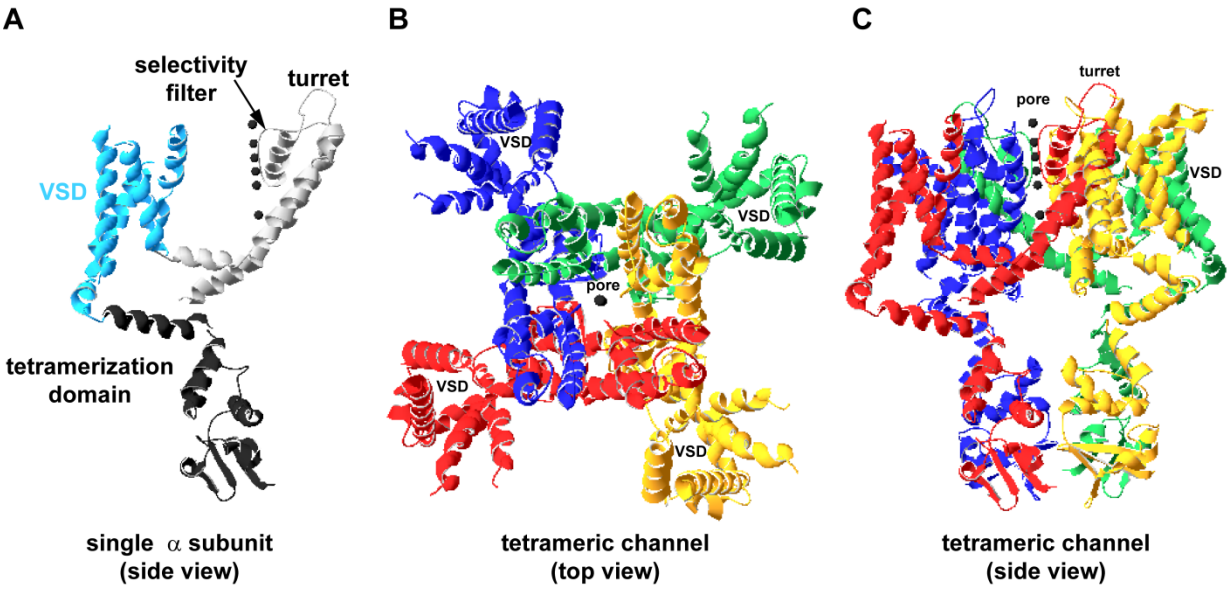

Figure 2.3. Crystal structure of $rK_v1.2$. (A) Side view of single $rK_v1.2$ subunit. Tetramerization domain (black), voltage sensing domain (blue) (VSD), and pore domain (gray) are highlighted. **(B)** Top view (extracellular side) of tetrameric $rK_v1.2$ channel. Each alpha subunit is shown in a different color. (C) Side view of tetrameric $rK_v1.2$ channel. Each alpha subunit shown in a different color. Potassium ions are shown as black spheres in all panels. Coordinates obtained from PDB file 2A79. All images created using Swiss PDB Viewer (http://spdbv.vital-it.ch/).

K_v channels are drug targets

K^+ channels are differentially expressed in virtually all cell types throughout the human body and are responsible for setting the resting potential of these cells.[6] Genetic defects resulting in either a loss or gain of K^+ channel function can lead to a variety of diseases termed channelopathies.[6, 11] As K^+ channels act as "off" switches for many signaling cascades, drugs that can control K^+ channel function can also serve as therapeutics for diseases characterized by hyper-excitability of the cell.[6]

Recently, the International Union of Basic and Clinical Pharmacology (IUPHAR) has assembled an online database which compiles detailed pharmacological, functional and pathophysiological information for many classes of membrane proteins including K_v channels.[18] This database is an invaluable resource for the biophysical properties of most ion channels. Members of the $K_v1.x$ subfamily are differentially expressed as homotetramers and heterotetramers in the nervous system, heart, vasculature, and immune system.[11] The resulting K_v channels are drug targets for a variety of diseases (Table 2.1).

Table 2.1 Properties and Therapeutic Implications for Selected Kv1.x channels. (adapted from [11] with additional information from [18]). Abbreviations: central nervous system (CNS), MS: multiple sclerosis (MS), not determined (ND), not reported NR).

Channel subunit	Tissue distribution in humans	Channelopathy	Therapeutic implications
K_v1.1	CNS, node of Ranvier, kidney	Episodic ataxia, primary hypomagnesaemia	Target for epilepsy, neuropathic pain, MS, and spinal cord injury
K_v1.2	CNS	NR	Target for seizure disorders
K_v1.3	T and B cells, macrophages, microglia, osteocytes, platelets, CNS, testis	Associated with impaired glucose sensitivity and lower insulin sensitivity.	Target for MS, rheumatoid arthritis, type I diabetes, contact dermatitis and T-cell mediated immune diseases
K_v1.4	CNS, heart skeletal, and smooth muscle, pancreas	NR	ND
K_v1.5	Cardiac myocytes, CNS, microglia, Schawn cells, macrophages, and vascular and smooth muscle	NR	Target for anti-arrthymias associated with atrial fibrillation
K_v1.6	Spinal cord, CNS, oligodendrocyte progenitor cells, astrocytes, pulmonary artery smooth muscle	NR	ND

The alpha subunits K_v1.x channels share over 50% identity in the pore forming region thus rendering these targets particularly challenging to differentiate (Figure 2.4). However, ligands that can target residues in the turret region of a specific K_v1.x channel may prove to be subtype specific therapeutics.

Figure 2.4. Multiple sequence alignment of pore-forming region of K_v1.x channels. Areas of sequence dissimilarity are shown in red. Sequence alignment created using CLC sequence viewer (www.clcbio.com/free/).

The K_v1.3 channel is expressed as homotetramers in human T lymphocytes and is a validated drug target for T-cell mediated autoimmune diseases including rheumatoid arthritis and type-1 diabetes.[19] At the molecular level, T-cell maturation associated with adaptive immunity is mediated by calcium signaling cascades.[20] Ca^{2+} enters the T-cell through various Ca^{2+} specific and nonspecific cation channels causing a depolarization of the cell. In order to maintain a driving force for Ca^{2+} entry into the cell, two types of K^+ channels are activated. K_v1.3 channels open in response to membrane depolarization and calcium-activated K^+ (K_{Ca}3.1) channels open in response to increased intracellular Ca^{2+}. The ratio of K_v1.3 to K_{Ca}3.1 channels present in T-cell membranes increases as T-cells mature making K_v1.3 channels more prominent drug targets for autoimmune diseases mediated by mature T-cells.[21]

Naturally-occurring peptides from poisonous animals as well as synthetic compounds have been reported as inhibitors for K_v1.3 channels.[3] Despite the high affinity of some of these inhibitors, none makes full use of the four-fold symmetry of these homotetrameric channels. Along these design principles, Gradl *et al.* reported that water-soluble ligands with four-fold symmetry and endowed with short positively-charged peptide arms anchored to a flat, rigid tetraphenylporphyrin core efficiently blocked the K_v1.3 channel in a reversible but non-specific way (Figure 2.5A).[4] Although porphyrins fulfill the symmetry requirement, they are flat scaffolds that do not ideally complement the conical pore-entrance of the K_v channels. Initially, Gradl *et al*. proposed a "lid" model where each arm of the tetraphenylporphyrin core contacted a different alpha subunit of the K_v channel tetramer (Figure 2.5B).[4] Later experiments employing solid state nuclear magnetic resonance (NMR) and molecular dynamics showed that the porphyrins do not sit like a lid on top of the channel, but instead are oriented parallel to the channel axis, with one positively charged side arm interacting with the selectivity filter (Figure 2.5C).[22] The insertion of a single positively charged arm of the porphyrin ligand into the K_v channel selectivity filter mimics the mode of action of K^+ channel specific peptidic toxins.[21]

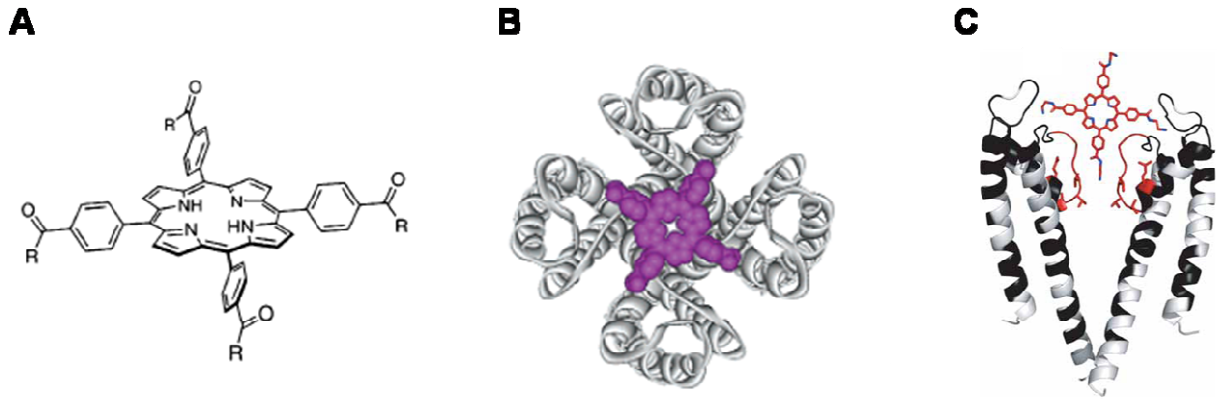

Figure 2.5. Porphyrin-based ligands for K_v channels. **(A)** Porphyrin scaffold used for K_v ligands (from[4]). **(B)** Space-filling model of porphyrin scaffold (magenta) from **(A)** modeled on X-ray crystal structural of tetrameric KcsA K^+ channel.(from [4]). **(C)** Structural model of porphyrin ligand bound to KcsA-K_v1.3 chimeric channel (from [22]).

Calix[4]arenes as ligands for K_v1.x channels

Calix[4]arenes have been used as platforms for multivalent ligands to efficiently bind proteins and nucleotides.[23] This building block of supramolecular chemistry contains a series of four phenol macrocyclic oligomers linked through methylene bridges which form basket-like structures with wider upper and narrower lower edges (Figure 2.6).[24] Differential substitution of the upper and lower rims allows for the generation of ligands that can specifically interact with a given target.

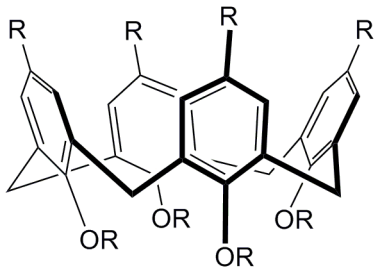

Figure 2.6. Calix[4]arene scaffold

Gordo *et. al* recently described calix[4]arene ligands for the tetramerization domain of the p53 transcription factor (p53TD).[25] The wildtype p53TD forms tetramers held together by electrostatic interactions between R337 and D352 on adjacent subunits (Figure 2.7A). Mutant forms of the p53TD often carry the R337H mutation which destabilizes the TD oligomerization. Gordo *et. al* synthesized a calix[4]arene ligand endowed with guanidinium substituents on the upper rim to mimic the arginine residue at position 337 and hydrophobic loops on the lower rim to interact with the hydrophobic core of the tetrameric p53TD complex (Figure 2.7B). NMR

structural studies and molecular modeling demonstrated that the calix[4]arene ligand could recover tetramerization of the p53TD-R337H protein (Figure 2.7C).[25]

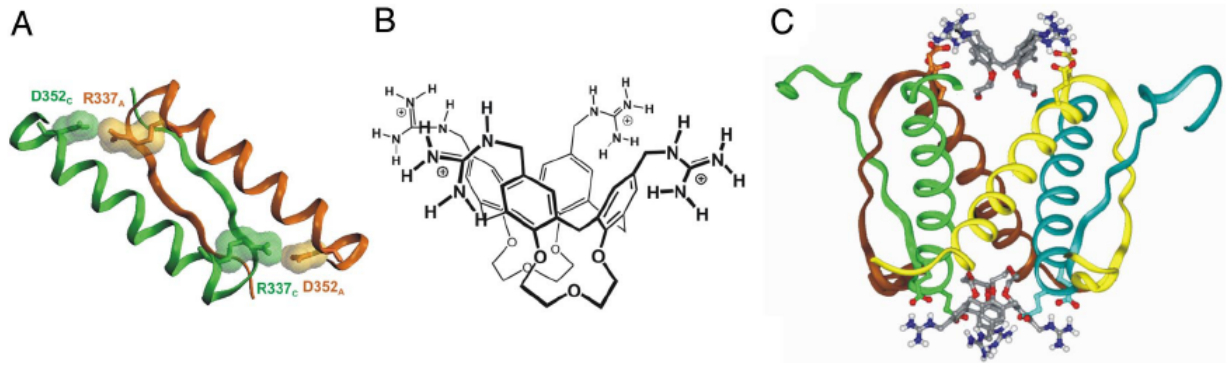

Figure 2.7. Calix[4]arene ligands for p53 tetramerization domain. **(A)** R337 and D352 residues located on adjacent p53 tetramerization domains (p53TD) form inter-subunit hydrogen-bonded ion pairs to stabilize tetrameric p53TD complex. **(B)** Chemical structure of calix[4]arene ligand used in study. **(C)** Model of calix[4]arene ligand from **(B)** stabilizing p53TD-R337H tetramer. (Figure adapted from [25])

Calix[4]arenes ligands could also provide the basis for a new class of ligands targeting tetrameric K_v channels. Unlike the flat porphyrin based ligands for K_v channels, calix[4]arenes display conical shapes which would likely complement the shape of the extracellular vestibule of a K_v channel. Next, The four-fold symmetry of the calix[4]arene scaffold would complement the architecture of a homotetrameric K_v channel. Finally, the calix[4]arene core provides a versatile scaffold for differential substitution of the upper and lower rims to achieve K_v channel subtype specificity. Structural information about the K_v1.x subfamily provided a starting point for the rational design of calix[4]arene ligands that complemented the extracellular face of homotetrameric K_v1.x channels.

Thus, ligands **1-8** were synthesized and evaluated (Figure 2.8). Structures **1-7** are free-OH calix[4]arenes, to avoid steric hindrance at the entrance of the channel, whereas **8** contains two short loops that cannot enter the channel simultaneously but could allow the molecule to adjust in a slightly distorted way, which cannot be possible with longer or less structured side chains, such as in **9** and **10**. Additionally, cationic substituents (guanidines) were attached to the upper rim of the calix[4]arenes to ideally complement the mainly negatively charged extracellular surface groups of the channel at the "turret loop" and the extracellular face of the selectivity filter (Figure 2.4), specifically residue D379 in K_v1.2, thus improving binding affinity and selectivity by both electrostatic interactions and hydrogen bonding.

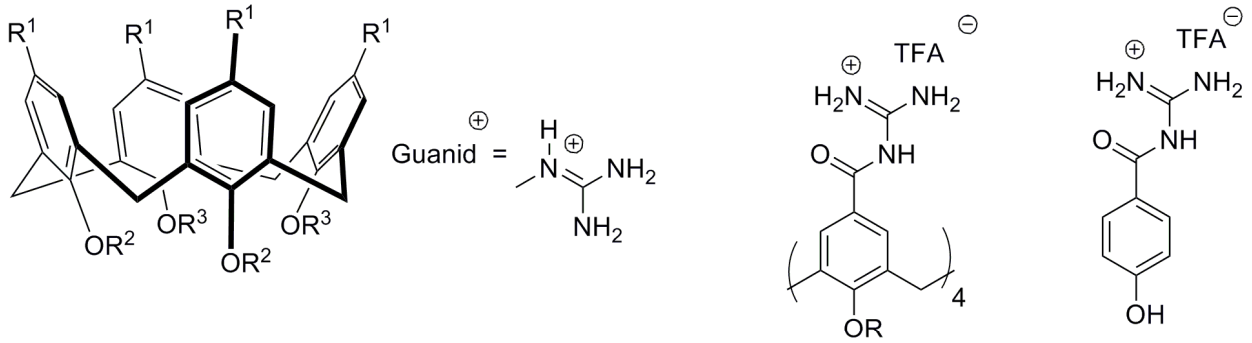

1 R^1 = COGuanid$^+$ Cl^-, R^2 = R^3 = H
2 R^1 = $CONHCH_2CH_2NH_3^+Cl^-$, R^2 = R^3 = H
3 R^1 = CO-Lys-OMe^+ TFA^-, R^2 = R^3 = H
4 R^1 = CO-Arg-OMe^+ TFA^-, R^2 = R^3 = H
5 R^1 = CO-Ala-OMe, R^2 = R^3 = H
6 R^1 = COOH, R^2 = R^3 = H
7 R^1 = R^2 = R^3 = H
8 R^1 = COGuanid$^+$ TFA^-, R^2-R^3 = $CH_2CH_2OCH_2CH_2$
12 R^1 = COOH, R^2 = R^3 = $CH_2C_6H_5$

9 R = $CH_2CH_2CH_3$
10 R = $CH_2C_6H_5$

11

Figure 2.8. Calix[4]arene ligand structures. Chemical formulae of calix[4]arenes **1-10** and phenol **11**. Figure from [5].

Results and Discussion

Synthesis of calix[4]arene ligands

The synthesis of OH-free calix[4]arenes was based on the common tetracarboxylic acid precursor **12**, allowing an easy introduction of the guanidine function, as well as any amino acid derivative or peptide chain by simple amide formation (Figure 2.9A). Thus, compound **12** was guanidilated following procedures by Schmuck et al.,[26] followed by simultaneous debenzylation and guanidine deprotection to afford **1**. Cationic ligands **2-4** and the neutral compound **5** were obtained from an activated O-succinimidoyl intermediate, followed by deprotection (*Materials and Methods* and Figure 2.9A). The tetraanionic negative control **6** resulted from O-debenzylation of **12**. O-Alkyl calix[4]arenes **8**-**10** were synthesized by similar procedures from the corresponding carboxylic acids (Figure 2.9B). Finally, phenol derivative **11** was selected as a non-calix[4]arene negative control, and readily prepared in two steps from 4-benzyloxybenzoic acid.

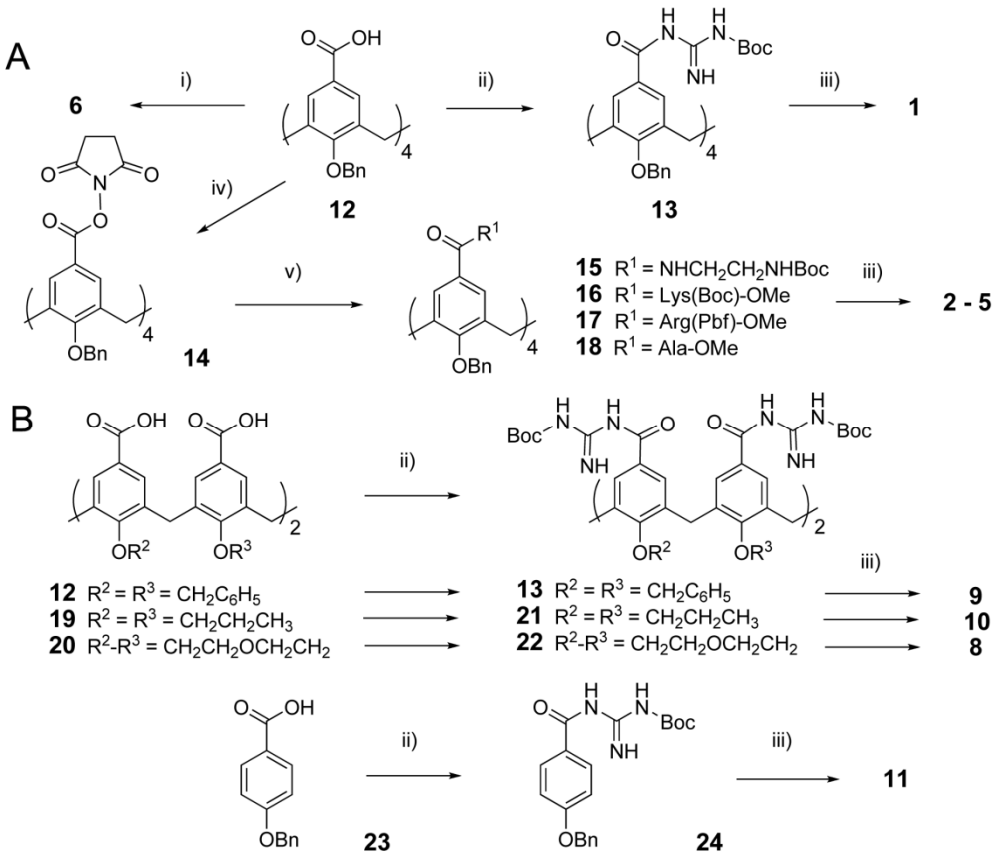

Figure 2.9. Synthetic scheme. (A) Synthesis of calix[4]arenes **1-6**. **(B)** Synthesis of calix[4]arenes **8-10** and phenol **11**. Reagents and conditions: i) HCl-AcOH (1:2), sealed tube, reflux 48 h; ii) PyBOP, NMM, DMF, Boc-guanidine, r. t.; iii) TFA-CH_2Cl_2, r. t. or reflux; iv) N-hydroxysuccinimide, DCC, DMF-CH_2Cl_2, r. t.; v) Et_3N, protected amine, DMF-CH_2Cl_2, r. t. For abbreviations, yields and details see *Materials and Methods*. Figure from [5].

Molecular dynamics

Docking studies employing the coordinates of the crystal structure of the $K_v1.2$ potassium channel[14] indicated that the conical platform of OH-free calix[4]arenes was best suited to deeply penetrate the extracellular outer vestibule of the channel (Figure 2.10). Protein-ligand stabilities were assessed by analyzing the trajectories obtained in 1500 ps molecular dynamics simulations in vacuo at 300K with positional restraints. Additional details are provided in the Materials and Methods section. To evaluate protein-ligand binding affinity, we computed both the Xscore empirical scoring function and the variation in the guanidinium-carboxylate (D379) distances versus time. Xscore was used to evaluate, for each trajectory, 128 structures collected every 12 ps. The values obtained for the three calixarenes were very similar and only slightly fluctuated during the molecular dynamics simulations. The average Xscore value of all the complexes formed with **1** was 6.65 (Figure 2.20). The complexes in which **4** and **8** intervened had values of 6.30 and 6.32 respectively (Figure 2.20). This demonstrated high and similar protein-ligand affinity in the three cases.

To estimate the variation of the hydrogen bond guanidinium-carboxylate distances, we measured all the NH-OC distances at every step. The two values corresponding to a same guanidinium-carboxylate interaction were averaged. Thus the result depended on the fine orientation of both interactions. Comparison of the plots versus time pointed out a slightly larger fluctuation of the hydrogen bond distances in **1**. In this ligand the four interactions oscillated between 1.6 and 2.4 Å during the whole trajectory (Figure 2.21). In compound **4** the four of them were highly fixed at a distance of 1.6-1.7 Å (Figure 2.22). Three of the interactions in compound **8** were maintained at this distance but the remaining highly fluctuated between values of 1.6 and more than 3 Å (Figure 2.23). This was due to the tilted disposition of the calixarene on the $K_v1.2$ surface, which caused one of the guanidinium groups of the calixarene to be not as close to the corresponding aspartate. Thus, **4** was the ligand with most favorable hydrogen bonding distances followed by **8**. In any case, the three compounds showed to maintain all the guanidinium-carboxylate groups at standard hydrogen bonding distances.

In conclusion, the three ligands bind the protein with high affinity by establishing four hydrogen bonds and by maintaining the lower rim embedded in the channel pore. The two crown ether bridges do not avoid the interaction of **8** with $K_v1.2$ but cause the ligand to be slightly twisted with respect to **1** and **4**.

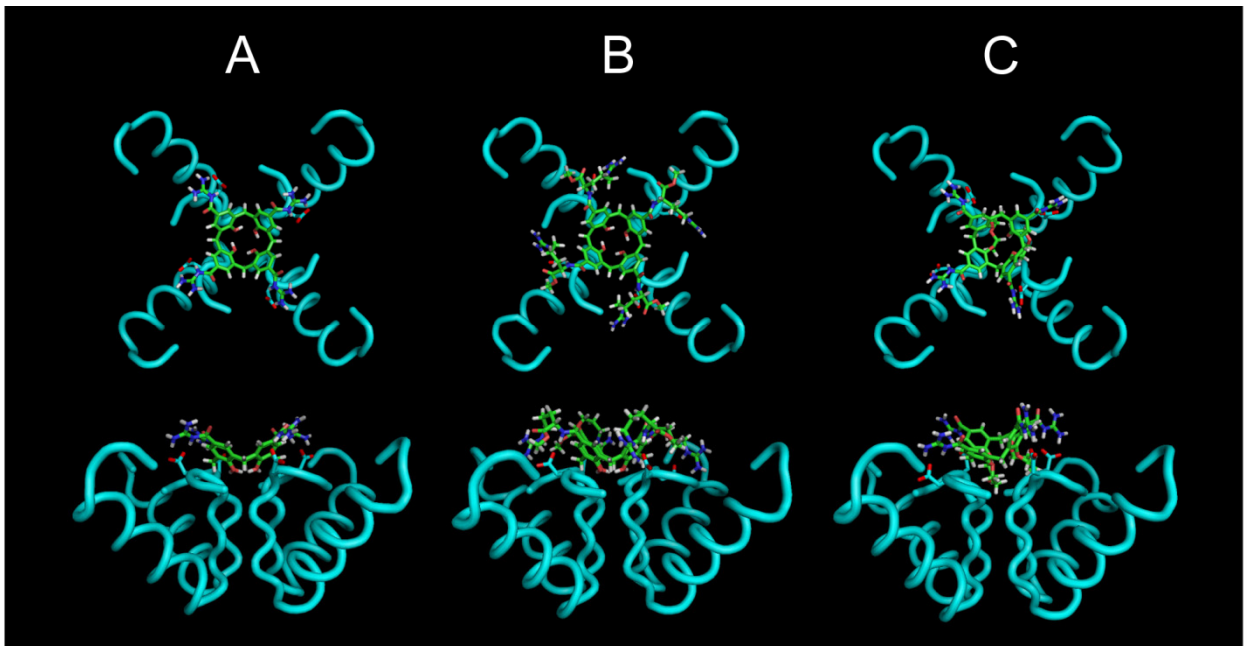

Figure 2.10. Molecular dynamics. Top and side wireframe views of calix[4]arenes **1 (A)**, **4 (B)**, and **8 (C)** docked into the X-ray structure of the $rK_v1.2$ potassium channel. Only the backbone helices of the alpha subunits are shown in cyan. The D379 side chains are represented, showing the four ion-pair, hydrogen bonded contacts with the guanidinium residues of the calix[4]arene. Structures were optimized *in vacuo* at 300K applying positional restraints to $K_v1.2$. Figure from[5].

Electrophysiological screen of calix[4]arene compounds

The interaction of the calix[4]arene compounds with K_v channels was investigated using electrophysiological methods on *Xenopus laevis* oocytes expressing the Shaker potassium channel, a prototypical member of the K_v1.x subfamily. Ionic currents were measured in cells expressing the Shaker channel in the presence of each calix[4]arene compound. Figure 2.11A summarizes the percent inhibition elicited by application of 50 μM of compounds **1-11** was compared to that induced by tetraethylammonium (TEA), a nonspecific open pore K^+ channel blocker. TEA reversibly binds to the external region of the pore forming region of the Shaker channel (IC_{50} >90 mM), and served as a good control to compare block by calix[4]arenes **1-10** which were designed to be more specific for the K_v1.x channel subfamily.[27, 28] Figure 2.11B shows the typical reversible inhibition response by 50 μM compound **4**.

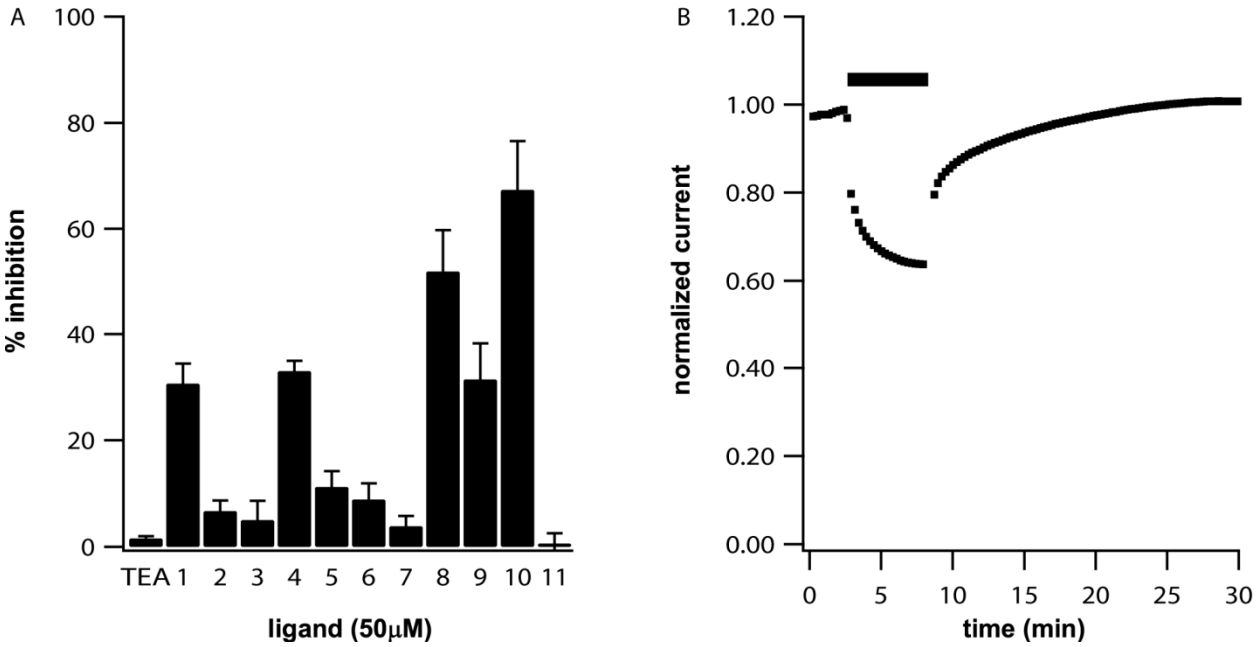

Figure 2.11. Electrophysiological screen of calix[4]arene ligands. (A) % inhibition elicited by application of 50 μM of compounds **1-11** and tetraethylammonium cation (TEA) to *Xenopus laevis* oocytes expressing the Shaker channel. ($n \geq 4$ for each condition; error bars indicate SEM). **(B)** Reversible reduction of Shaker ionic current in response to application of 50 μM ligand **4** (normalized current vs. time). Black bar indicates time of exposure to ligand **4**. Note that inhibition and recovery occur in two distinct phases. Figure from [5].

At 50 μM, compounds **1-11** caused different levels of reduction in Shaker ionic current, which in most cases was reversible. Compounds functionalized either with carboxylates (ligand **6**), ammonium (ligands **2** and **3**) or neutral (ligands **5** and **7**) functional groups at the upper rim, did not exert significant reduction in Shaker ionic current. On the contrary, ligands **1** and **4** containing guanidinium groups at the upper rim of a free-OH calix[4]arene scaffold, aimed at interacting with negatively charged residues in the extracellular vestibule of the channel, proved

promising ligands, as anticipated by the modeling studies. When applying O-alkyl derivatives **9** and **10** to oocytes expressing the Shaker channel, decreases in ionic current were also seen, but these effects were not reversible and cell health was visually compromised. Lower rim alkylation with hydrophobic residues can result in amphiphilic structures that may act as detergents for oocytes' integrity and might cause non-specific interactions with the membrane lipids or other hydrophobic portions of the Shaker channel which could not be restored by application of the aqueous recording solution used for the washout. Quite remarkably, but once again in agreement with the computer modeling studies, ligand **8**, carrying two crown ether loops at the lower rim, caused reduction in Shaker ionic currents in a reversible manner and even to a larger extent than the free-OH analogues **1** and **4**. It is known that crown ether bridges at vicinal lower rim positions in a calix[4]arene strongly contribute to keep the conical shape of the macrocycle, preventing collapse into the so-called pinched conformations.[29] The conical shape is also maintained in the free-OH derivatives, due to the cyclic array of hydrogen bonds. At the same time, the crown ether bridges on **8** do not create a severe steric effect, since the ligand can comfortably fit at the top of the channel in a slightly tilted orientation, as indicated by molecular modeling (Figure 2.10).

Changes in the counter-anions (either chloride or trifluoroacetic acid) had no measurable effect on the channel binding properties of the calix[4]arenes. Furthermore, the presence of < 2% dimethyl sulfoxide (DMSO) in the bath solution was not harmful to the cells. Finally, the effect of the multivalency effect present in the calix[4]arene macrocycle was evidenced by the fact that a simple guanidilated phenol such as **11** showed no inhibition at 50 μM. Even at four times the concentration employed for ligand **1**, thus at the same effective concentration, phenol **11** induced a minor increase in current flow (Figure 2.12). Among the most active ligands (**1**, **4**, and **8**), ligand **1** had a limited solubility and ligand **8** with bulkier substituents on the lower rim did dock into the pore in a tilted orientation. Therefore, in the rest of our work, we focused on ligand **4**.

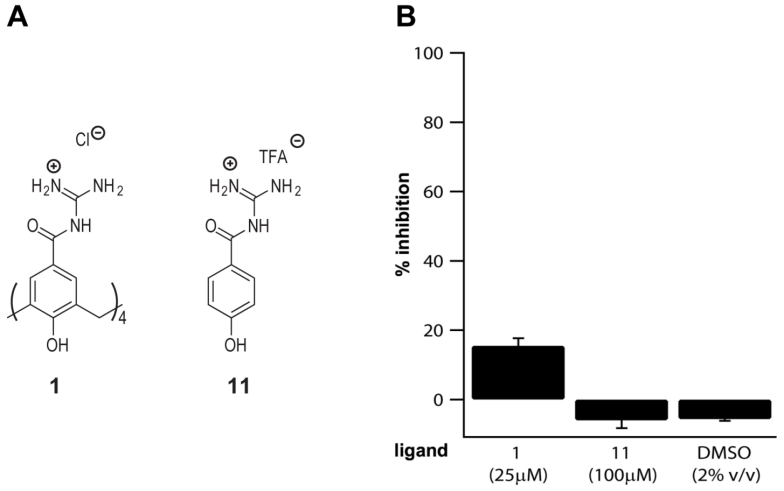

Figure 2.12. Comparison of monomer vs. calix[4]arene compounds. **(A).** Chemical structures of ligands **1** and **11**. **(B).** *Xenopus laevis* oocytes expressing the Shaker channel were incubated with either 25 μM ligand **1** (n = 4), 100 μM ligand **11** (n = 5), or DMSO (2% v/v), (n = 4). Error bars indicate SEM. Figure adapted from [5].

Calix[4]arene inhibition includes gating modification

Ligand **4** showed a concentration dependent inhibition of both Shaker and $K_v1.3$, two related members of the $K_v1.x$ subfamily of ion channels sharing 47% sequence identity (Figure 2.13). While the inhibition was greater in $K_v1.3$, the apparent affinity was similar for the two channels. The Hill coefficients for Shaker and $K_v1.3$ (1.0± 0.3 and 1.1± 0.7, respectively) were close to 1, fitting with the proposed molecular model in which a single calix[4]arene docks in the outer mouth of the pore and interacts with residue D379 ($K_v1.2$ sequence numbering), which is shared by all $K_v1.x$ subfamily members (Figure 2.4). Even at saturating concentrations of calix[4]arene **4**, Shaker ionic current was not completely inhibited (Figure 2.13), suggesting, an incomplete occlusion of the pore.

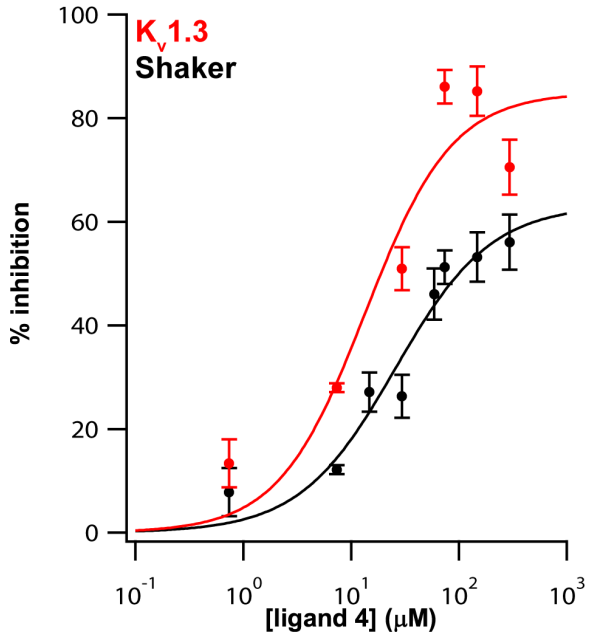

Figure 2.13. Concentration dependent effects of ligand 4. Inhibition curve on macroscopic ionic currents in *Xenopus laevis* oocytes expressing Shaker channels (black circles) or $K_v1.3$ channels (red circles). ($n \geq 3$ for each data point; error bars indicate SEM). Data fit to a single Boltzmann as described in methods section. Fit data: Shaker: max = 63±10, K_d = 25±11 μM, h = 1.0±0.3. $K_v1.3$: max = 85±16, K_d = 14±9 μM, h = 1.1±0.7. Figure from [5].

The effect of ligand **4** could not be entirely attributed to pore block. The rate of channel opening was slowed (Figure 2.15A) and the voltage dependence of channel opening was shifted in the positive direction (Figure 2.14A) by ligand **4**, suggesting that binding relatively stabilizes the resting state or an intermediate state preceding opening in the activation pathway. The onset of current inhibition and of the gating effect occurred in parallel, with reduction in current amplitude tracked by the slowing of channel opening (Figure 2.14B).

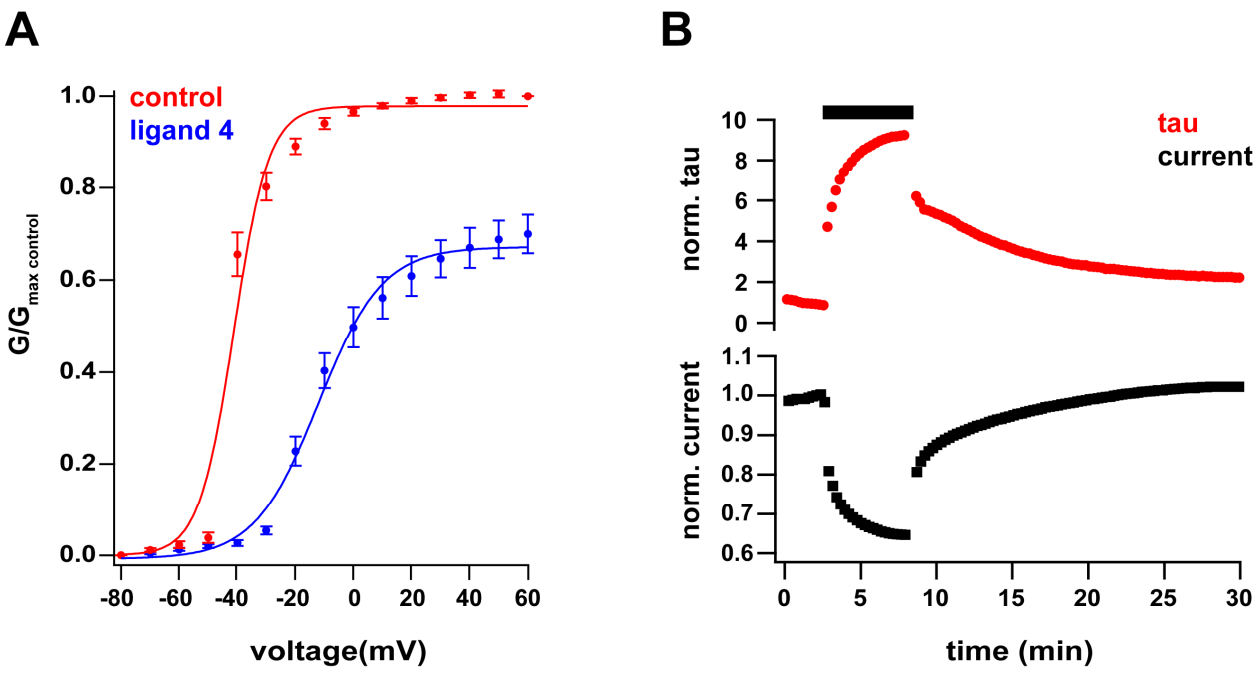

Figure 2.14. Electrophysiological analysis of kinetic effects of ligand 4. (A) Ligand **4** (50 μM) shifts the voltage dependence of channel opening to the right. Conductance measured from inward tails in 98 mM external K^+. (n = 4, error bars indicate SEM). Data fit to a single Boltzmann as described in Methods section. Control solution before exposure (red): max = 0.98±0.05, V_{mid} = -41±2 mV, slope = 6±1.3. During ligand **4** application (blue): max = 0.68±0.02, V_{mid} = -12±1 mV, slope = 11±1.2. **(B)** Time course of reduction of current amplitude (black) parallels slowing of channel opening (red) following application of 50 μM ligand **4** (represented by black bar). Figure adapted from [5].

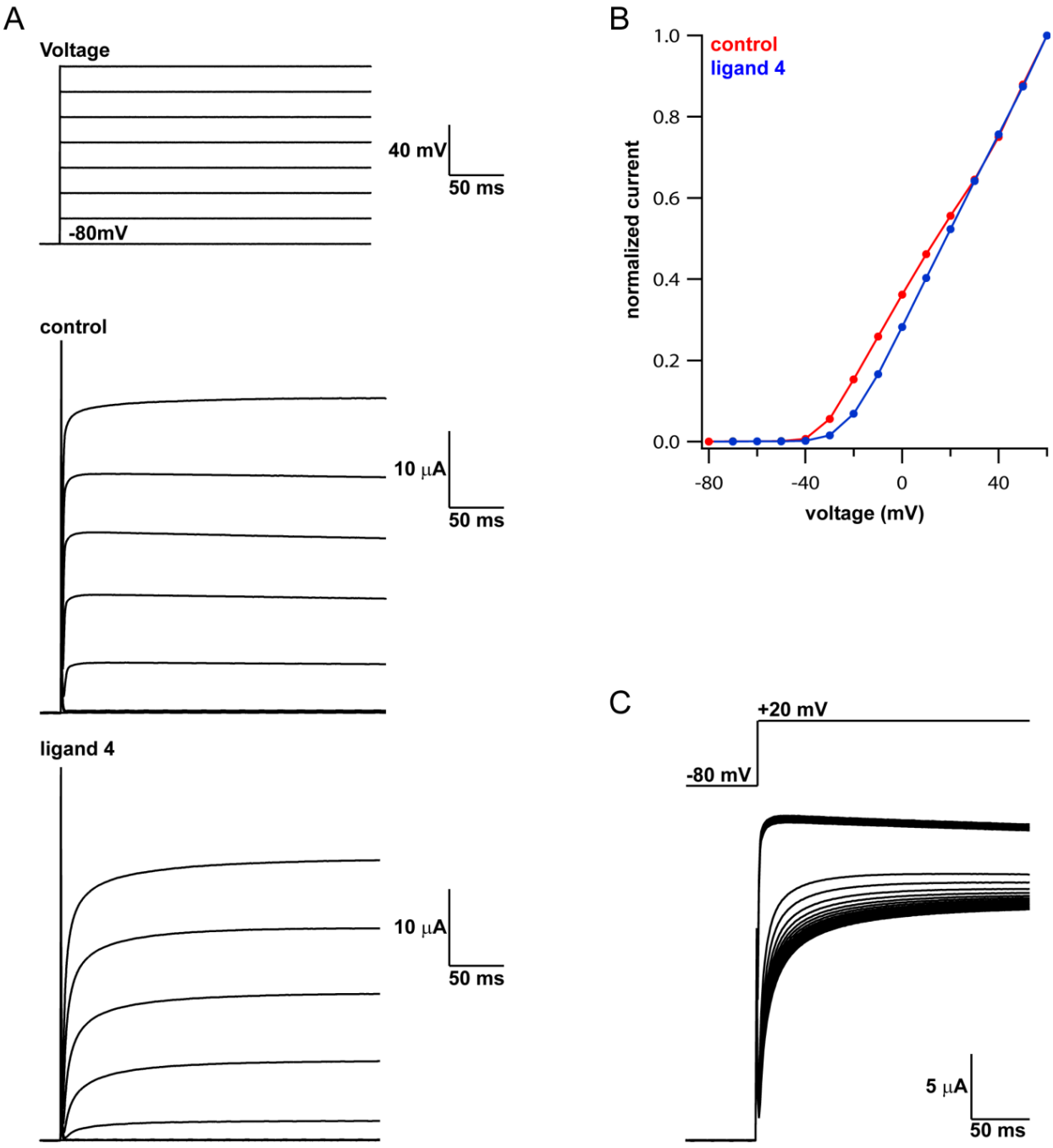

Figure 2.15. Kinetic and voltage-dependent effects of ligand 4. **(A)** Opening kinetics are slower in presence of 50 μM ligand **4** (lower traces) compared to control (upper traces). **(B)** Effect of ligand **4** on Shaker Current-Voltage (I-V) relationship. Representative I-V trace measured from a Xenopus laevis oocyte expressing Shaker before (red) and after application of 50 μM ligand **4** (blue). **(C)** Progressive slowing of opening kinetics accompanies progressive inhibition of current amplitude upon application of 50 μM ligand **4** (steps from holding potential of -80 mV to +20mV). Figure adapted from [5].

We wondered whether the gating effect reflects an influence of ligand **4** on the protein motions underlying voltage sensing. To address this we used voltage clamp fluorometry[30] to measure structural rearrangements in the S4 voltage sensor. Recordings were carried out in the W434F mutation, which locks the channel in the P-type inactivated state, preventing the conduction of K^+ but permitting free motion of S4.[31, 32] A single cysteine mutation was also introduced in the extracellular portion of the Shaker S4 segment (A359C) to allow for site-specific conjugation with tetramethylrhodammine-6-maleimide, an environmentally sensitive fluorophore, and monitor the movement of the voltage sensing domain.[33, 34] Ligand **4** (200 µM) was found to slow the rate of S4 motion at the top of the voltage dependence curve where channels open (Figure 2.16A). Furthermore, application of ligand 4 also slightly shifted the voltage-dependency of S4 movement (Figure 2.16B). This result is consistent with the observation that channel opening is slowed by application of ligand **4** (Figure 2.15A and C). To further probe the interaction of ligand **4** with the Shaker channel, we conducted competition experiments with known pore-blockers.

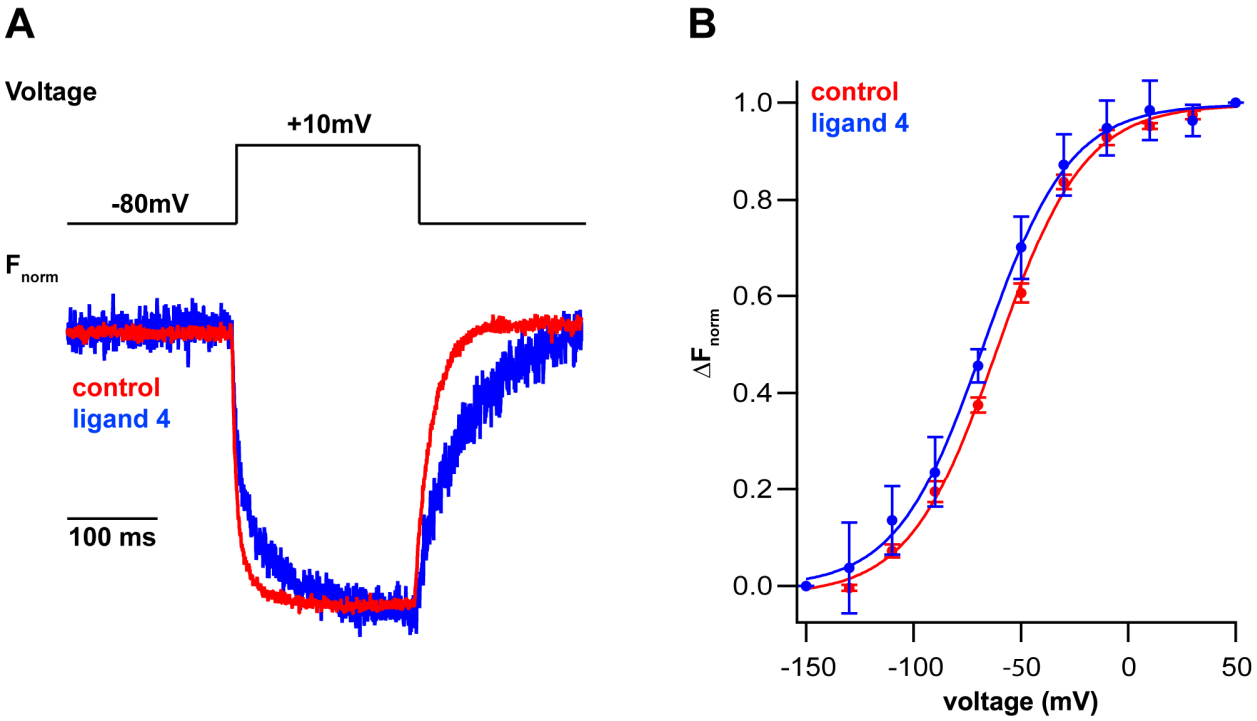

Figure 2.16. Fluorescence analysis of kinetic effects of ligand 4. (A) Representative normalized fluorescence traces showing Shaker voltage sensor movement in the absence (red) and presence (blue) of ligand **4**. A slowing in kinetics upon depolarization is seen upon application of ligand **4** (200 µM). **(B)** Fluorescence vs. voltage (FV) curves for Shaker voltage sensor movement recorded at position 359 by voltage clamp fluorometry in the absence (red) and presence (blue) of ligand **4** (200 µM) (n=3 for each condition). Data fit to single Boltzmann as described in methods section, error bars indicate SEM: control: V_{mid} = -61±1 mV, slope = 20±1, ligand **4** treatment: V_{mid} = -67±1 mV, slope = 20±1. Figure adapted from [5].

Competition experiments to probe ligand 4 binding to Shaker pore region

To further probe the location of ligand **4** binding on the Shaker channel, we conducted competition experiments with Agitoxin-2 ($AgTX_2$), a well-known Shaker channel pore blocker. $AgTX_2$ is a 38 amino-acid peptide toxin from scorpion venom previously shown to be a reversible and high affinity ($K_i = 0.64$ nM) pore blocker the Shaker channel.[35] Structural studies and computer simulations indicate that $AgTX_2$ interacts with the extracellular vestibule of the Shaker channel and physically blocks the pore by inserting a lysine residue into the selectivity filter of the channel. [36, 37] Using two-electrode voltage clamp methods in *Xenopus laevis* oocytes expressing the Shaker channel, we set out to test the hypothesis that ligand **4** bound to the pore of the Shaker channel.

Previously, we had observed that saturating concentrations (200 μM) of ligand **4** caused only 56% inhibition of Shaker ionic current (Figure 2.13). We proposed two models for this phenomenon. Model 1 predicts that application of saturating concentrations of ligand **4** blocks all Shaker channels in the membrane. In this scenario, application of saturating concentrations of $AgTX_2$ would not cause an additional decrease in Shaker ionic current. Model 2 predicts that application of saturating concentrations of ligand **4** does not block all Shaker channels in the membrane. This scenario would leave some channels accessible for $AgTX_2$ block resulting in an additional decrease in Shaker ionic current.

We first separately tested the effects of ligand **4** and $AgTX_2$ on Shaker channel activity. As previously seen, bath application of 200 μM ligand **4** caused 57 $\pm$ 3% ionic current inhibition. Interestingly, application of 10 μM $AgTX_2$ (100 times the IC_{90} level[35]) did not cause 100% inhibition of Shaker current. Previous research in the Isacoff lab had shown that two-electrode voltage-clamp methods using $AgTX_2$ as a Shaker blocker gave variable results. In order to more accurately measure the effects of toxin block, outside-out patch clamp experiments work best.[38] However, for the sake of time, the competition experiments were conducted under two-electrode voltage clamp conditions. The presence of ligand **4** did not completely prevent $AgTX_2$ binding indicating that saturating concentrations of ligand **4** do not block all Shaker pores (Figure 2.17).

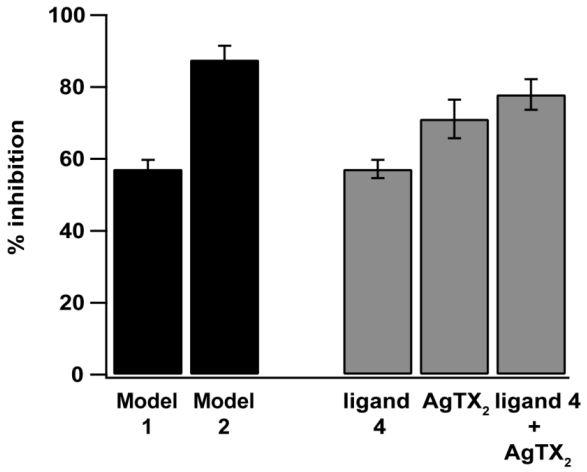

Figure 2.17. Agitoxin competition experiments. Black bars indicate Model 1 and 2 predictions (see main text for detailed descriptions) Gray bars indicate experimental data. *Xenopus laevis* oocytes expressing Shaker channels were incubated in 200 μM ligand 4, 1μM $AgTX_2$, or 200 μM ligand 4 followed by 1μM $AgTX_2$ (n=9 for each condition, error bars indicate SEM)

Together with the gating modifier properties of ligand **4** observed previously, these results suggest that the current calix[4]arene scaffold may have limited specificity for the pore region of the K_v1.x channels. We next began planning a second generation of calix[4]arene ligands with enhanced the affinity for the pore region of the Kv1.x channels.

Design of second-generation calix[4]arene ligands for K_v channels

Our initial concentration dependence experiments (Figure 2.13) showed that ligand **4** had a slightly higher affinity for K_v1.3 over the Shaker channel. Therefore, we decided to focus our attention on designing ligands specifically for K_v1.3, a validated target for immunosuppressant drugs.[20] The new approach has 2 main goals:

1. Increase specificity for the pore region of the K_v1.3 channel by functionalizing the lower rim with an alkyl amine to interact with the selectivity filter (ligands **25a-c**).

2. Further derivative the upper rim of ligand **4** to include peptide arms that complement residues in the turret region of K_v1.3 (ligand **26**).

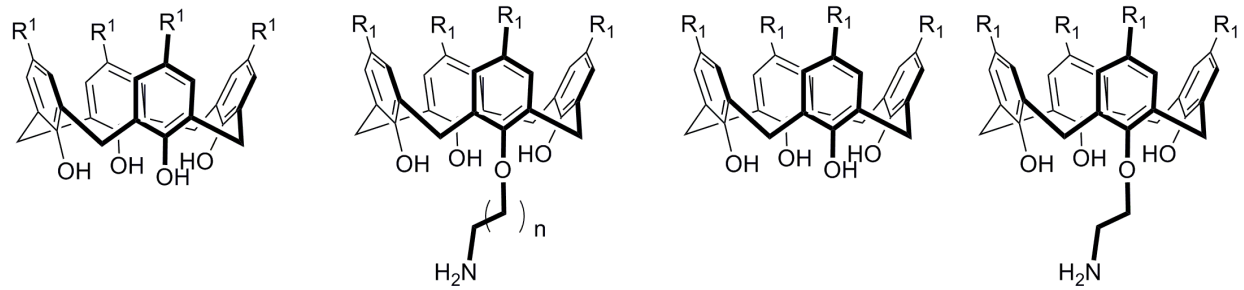

4 R^1 = CO-Arg-OMe^+ TFA^- **25a-c** R_1 = CO-Arg-OMe^+ TFA- n = 1, 2 or 3 **26** R_1 = CO-peptide **27** R_1 = CO-peptide

Figure 2.18. Second generation calix[4]arene ligands for increased K_v1.3 channel specificity.

Our inspiration for ligands **25a-c** came from structures of K^+ channel-blocking toxins like Agitoxin and charybdotoxin. The majority of these peptide toxins contain a "functional dyad" of a central lysine residue that inserts into the selectivity filter and physically occludes the K^+ permeation pathway and an aromatic residue approximately 5-7Å away from the central lysine that interacts with aromatic residues in the upper pore region (Figure 2.19).[20, 39]

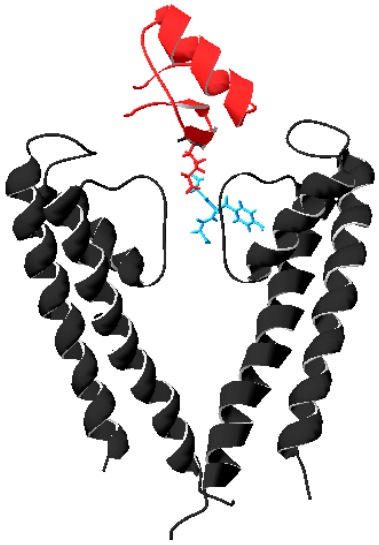

Figure 2.19. Channel-toxin interactions. NMR solution structure of complex of charybdotoxin interacting with bacterial K+ channel KcsA[40] (PDB ID 2A9H). Toxin in red with lysine residue inserted into channel selectivity filter. Pore region of KcsA channel in black (only 2/4 subunits shown for clarity. Residues of GYG selectivity filter in blue. Image created using Swiss PDB Viewer (http://spdbv.vital-it.ch/).

We rationalized that the introduction of an alkylamine to one of the lower-rim phenols of the calix[4]arene could mimic the central lysine residue of the toxin and the calix[4]arene core could favorably interact with the aromatic residues in the outer vestibule of the channel. Preliminary molecular modeling experiments measuring the interactions between ligands **25a-c**

and the pore region of the $rK_v1.2$ channel have suggested that a calix[4]arene endowed with an ethylamine chain on the lower rim as in ligand **25a** will most favorably interact with residues in the selectivity filter of the K_v channel. Synthesis of ligand **25a** is currently underway. Once synthesis is complete, electrophysiological testing and competition experiments will be conducted to assess the specificity of this ligand for the pore region of the $K_v1.x$ channels. With increased specificity for the pore region of the K_v channels, we can further derivative the upper rim of ligand **25a** with peptide substituents to achieve $K_v1.3$ specificity (ligand **27**).

To design the peptide substituents for ligand **26**, we performed sequence alignments of all members of the $K_v1.x$ subfamily to identify regions of high homology in the extracellular vestibule of the pore region of the proteins and locate "hot spots" where the sequence of $K_v1.3$ was unique from other $K_v1.x$ channel isoforms (Figure 2.4). As the turret region contains large areas of sequence divergence among members of the $K_v1.x$ subfamily, we decided to design peptide substituents that would interact favorably with residues D423, T425, and G427 in $K_v1.3$. Synthesis of calix[4]arene ligands possessing positively-charged and hydrogen-bonding peptide chains attached to the upper rim is currently underway.

Conclusions

We have shown that guanidilated calix[4]arenes with free phenolic OH groups at the lower rim, as well as bis-crowned calix[4]arenes endowed with four acylguanidinium groups at their upper rims, constitute a versatile class of reversible ligands for $K_v1.x$ channels. Electrophysiological experiments demonstrated that tetraacylguanidinium or tetraarginine members of the series with small lower rim O-substituents are reversible inhibitors of $K_v1.x$ channel function. Molecular modeling predicted that calix[4]arene ligands **1**, **4**, and **8** dock in the outer mouth of the pore of K_v channels. Apparent binding constants in the micromolar range and Hill coefficients of 1 were consistent with a single site of binding predicted through molecular modeling studies. Saturating concentrations of ligand **4** cause incomplete channel inhibition and in addition to current inhibition, ligand **4** shift the voltage dependence of gating and slowed both the opening of the gate and the voltage sensing motion of S4.

These gating effects are consistent with recent observations of opening rearrangements in the turret,[41] but did not definitively prove ligand **4** specifically interacted with the K_v pore. Competition studies between ligand 4 and Agitoxin, a known K_v channel pore blocker, also failed to prove that ligand **4** specifically interacted with the pore domain, but inspired a second generation of ligands designed to target the pore region of the K_v channels and improve $K_v1.x$ subtype specificity. Ultimately, the development of this new class of compounds might lead to novel therapeutic agents against various ailments such as autoimmune disorders, diabetes, epilepsy, or cardiac diseases.[42]

Experimental Contributions

This research was a collaboration among the laboratories of Professors Dirk Trauner, Javier de Mendoza, and Ehud Y. Isacoff. Vera Martos designed and synthesized all small molecules under the direction of Professor Javier de Mendoza then came to the Isacoff laboratory, where in collaboration with Sarah C. Bell, she conducted preliminary electrophysiology experiments. Sarah C. Bell performed the molecular biology work for ion channel constructs and conducted electrophysiology and fluorescence experiments under the direction of Ehud Y. Isacoff. Eva Santos performed computational studies under the direction of Javier de Mendoza. Sarah C. Bell and Vera Martos contributed equally to this work.

Materials and Methods

Synthesis. All reactions were carried out under argon with dry solvents unless otherwise noted. All commercially available reagents were used without further purification. The solvents were dried and distilled. 25,26,27,28-Tetrahydroxycalix[4]arene **(7)**[43], 25,26,27,28-tetrabenzyloxycalix[4]arene-5,11,17,23-tetracarboxylic acid (**12**)[44], 25,26,27,28-tetra-*n*-propoxycalix[4]arene-5,11,17,23-tetracarboxylic acid (**19**)[45], and 25,26-27,28-biscrown-3-calix[4]arene-5,11,17,23-tetracarboxylic acid (**20**)[46], were synthesized according to described procedures.

Chromatography. Reactions were monitored by thin layer chromatography (TLC) performed on DC-Fertigplatten SIL G-25 UV_{254} (Macherey-Nagel GmbH) or by analytical high performance liquid chromatography with a RP-C_{18} column (Symmetry300^{TM} C18 5 μm 4.6x150 mm, 1 ml/min flux and 220 nm UV detection) on a high performance liquid chromatograph (HPLC: Agilent Technologies Series 1200). Semi-preparative-HPLC purification was performed on Waters HPLC 600 equipment with a quaternary pump (17 mL/min, 220 nm). Standard column chromatography was done on silica gel by SDS (chromagel 60 ACC, 40-60 mm).

Analysis. Yields refer to chromatographically pure compounds. ^{1}H NMR and ^{13}C NMR spectra were recorded on a Bruker Avance 400 UltraShield spectrometer (^{1}H: 400 MHz ^{13}C: 125 MHz) and are reported in parts per million relative to the residual solvent peak. Data for ^{1}H are reported as follows: chemical shift (δ ppm), multiplicity (s = singlet, d = doublet, t = triplet, q = quadruplet, m = multiplet), coupling constant in Hz, and integration. Exact masses were measured on a Waters LCT Premier liquid chromatograph coupled to a time-of-flight mass spectrometer (HPLC/MS-TOF) with electrospray ionization (ESI). Melting points were measured with a Büchi B-540 apparatus.

General procedure for the synthesis of compounds 13, 21, 22, and 24. A solution of (benzotriazol-1-yloxy)tripyrrolidinophosphonium hexafluorophosphate (PyBOP, 0.33 g, 0.62 mmol) and *N*-methylmorpholine (NMM, 0.08 mL, 0.67 mmol) in dry DMF (4 mL) was added to a solution of the calix[4]arene tetraacid precursor (**12**, **19, 20** or **23**) (0.16 mmol), *N*-(*tert*-butoxycarbonyl)guanidine (0.1 g, 0.62 mmol), and NMM (0.08 mL, 0.67 mmol) in dry DMF (4 mL). The reaction mixture was stirred at room temperature (from 24 h to several days), and then poured into water. The resulting colorless precipitate was filtered and dried. The crude compound was purified by flash chromatography in silica gel.

25,26,27,28-Tetrabenzyloxycalix[4]arene-5,11,17,23-tetrakis[*tert*-butylamino(benzamido)methylcarbamate] (13). The reaction mixture was stirred for 24 h and pure $CHCl_3$ was employed as eluent for the chromatographic purification. The product was obtained in a 72 % yield.
^{1}H NMR ($CDCl_3$): δ 7.30-7.23 (m, 28H, ArH), 4.99 (s, 8H, CH_2Bn), 4.15 (d, J = 14.5 Hz, 4H, ArCH*Hax*Ar), 3.22 (d, J = 14.5 Hz, 4H, ArCH*Heq*Ar), 1.53 (s, 36H, C(CH_3)$_3$).
13C NMR (DMSO-d_6): δ 159.2 (CGua), 137.3 (CAr), 130.3 (CAr), 128.6 (CAr), 31.7 (ArCH_2Ar), 28.4 (C(*C*H_3)$_3$).
Exact Mass (ESI+) *m/z* of $[M + H]^+$ calc: 1525.6720 uma, found: 1525.6753 uma.
m.p.: > 350 ºC.

25,26,27,28-Tetra-*n*-propoxycalix[4]arene-5,11,17,23-tetrakis[*tert*-butylamino(benzamido)methylcarbamate] (21). The reaction mixture was stirred for 4 days and was purified by flash column chromatography eluting with ether/hexane (1:9). The yield of pure product was 42 %. Product **21** was sparingly soluble in all common deuterated solvents, therefore its purity was checked by HPLC (50 to 95% CH_3CN in H_2O + 0.1% TFA for 15 min followed by a 95 to 100% gradient over 5 min).
Exact Mass (ESI+) *m/z* $[M + H]^+$ calc.: 1333.6833 uma, found: 1333.6896 uma.
m.p.: > 330 ºC dec.

25,26-27,28-Biscrown-3-calix[4]arene-5,11,17,23-tetrakis[*tert*-butylamino(benzamido) methylcarbamate] (22). The reaction mixture was stirred for 3 days and the purification was achieved by chromatography with ether/hexane (1:4) as eluent. Yield was 38 %.
^{1}H NMR ($CDCl_3$): δ 7.80 (s, 8H, ArH), 5.09 (d, J = 12.2 Hz, 2H, ArCH*Hax*Ar), 4.51 (d, J = 12.2 Hz, 2H, ArCH*Hax*Ar), 4.32-4.22 (m, 12H, CH_2O), 3.89 (t, J = 10.4 Hz, 4H, CH_2O), 3.39 (tr, J = 13.6 Hz, 4H, ArCH*Heq*Ar), 1.51 (s, 36H, $C(CH_3)_3$).
^{13}C NMR (CD_3OD): δ 158.9 (COGua), 152.4 (CGua), 138.3 (CAr), 129.0 (CHAr), 127.3 (CHAr), 75.1 (CH_2), 74.3 (CH_2), 28.1 ($C(CH_3)_3$).
Exact Mass (ESI+) *m/z* $[M + H]^+$ calc.: 1419.5720 uma, found: 1419.5770 uma.
m.p.: > 350 ºC.

4-(Benzyloxy)-*N*-(*N*-(*tert*-butoxycarbonyl)carbamimidoyl)benzamide (24). The reaction mixture was stirred for 24 h and pure $CHCl_3$ was employed as eluent for the chromatographic purification. The product was obtained in a 60 % yield.
^{1}H NMR ($CDCl_3$): δ 8.06 (d, J = 8.5 Hz, 2H, ArH), 7.47-7.32 (m, 5H, ArH), 7.01 (d, J = 8.5 Hz, 2H, ArH), 5.14 (s, 2H, OCH_2Bn), 1.45 (s, 9H, $C(CH_3)_3$).
^{13}C NMR ($CDCl_3$): δ 153.6 (COGua), 141.4 (CGua), 131.1 (CAr), 125.4 (CHAr), 123.4 (CHAr), 123 (CHAr), 122.9 (CO), 122.2 (CHAr), 109.2 (CHAr), 64.8 (CH_2), 22.7 ($C(CH_3)_3$).
Exact Mass (ESI+) *m/z* $[M + H]^+$ calc.: 370.1767 uma, found: 370.1779 uma.
m.p.: > 350 ºC.

5,11,17,23-Tetrakis(succinimidoxycarbonyl)-25,26,27,28-tetrabenzyloxycalix[4]arene (14). To a suspension of the acid precursor **12** (0.310 g, 0.32 mmol) in dry CH_2Cl_2 and DMF (1:2, 18 mL) were added *N*-hydroxysuccinimide (0.204 g, 1.77 mmol) and 1,3-dicyclohexylcarbodiimide (0.372 g, 1.80 mmol). The reaction was stirred at room temperature for 24 h. Then, the solvent was evaporated to dryness and the residue was sonicated in a mixture of MeOH and CH_2Cl_2 (1:1, 30 mL). The solid product was filtered and obtained as a grey solid (0.35 g, 62 % yield).
^{1}H NMR ($CDCl_3$): δ 7.48 (s, 8H, ArH), 7.40-7.21 (m, 20H, ArH), 5.04 (s, 8H, CH_2Bn), 4.12 (d, J = 14.4 Hz, 4H, ArCH*Hax*Ar), 3.00 (d, J = 14.4 Hz, 4H, ArCH*Heq*Ar), 2.83 (s, 16H, CH_2).
^{13}C NMR ($CDCl_3$): δ 170.3 (CONR), 161.3 (CO_2), 161.0 (CAr), 136.3 (CAr), 130.7 (CHAr), 130.4 (CHAr), 128.7 (CHAr), 128.5 (CHAr), 119.7 (CAr), 77.2 (CH_2Bn), 30.9 ($ArCH_2Ar$), 25.5 (CH_2).
Exact Mass (ESI+) *m/z* $[M + Na]^+$ calc.: 1371.3699 uma, found: 1371.3693 uma.
m.p.: > 300 ºC dec.

General procedure for the synthesis compounds 15-18. Compound **14** (0.2 g, 0.15 mmol) was dissolved in a solution of dry CH_2Cl_2 and DMF (1:2, 10 mL). Triethylamine (0.25 mL, 1.78

mmol) and the protected amine (1.78 mmol) were added to the solution. The reaction was stirred at room temperature for 48 h. The solvent was evaporated and the residue dissolved in CH_2Cl_2. The organic phase was washed once with 1N HCl and twice with H_2O. After drying with anhydrous Na_2CO_3 and filtering, the solvent was eliminated *in vacuo* and the products were purified by flash column chromatography in silica gel.

25,26,27,28-Tetrabenzyloxycalix[4]arene-5,11,17,23-tetrakis(*N-tert*-butyl-2-benzamidoethylcarbamate) (15). The reaction was performed with *N*-(*tert*-butoxycarbonyl)-ethylenediamine and for the purification the eluent was a gradient of acetone/CH_2Cl_2 from 1:3 to 1:1. Product **15** was obtained as a colorless solid (51% yield).
^{1}H NMR ($CDCl_3$): δ 7.37-7.21 (m, 20H, ArH), 7.04 (s, 8H, ArH), 6.84 (br s, 4H, NH), 4.98 (s, 8H, C*H*$_2$Bn), 4.1 (d, *J* = 13.6 Hz, 4H, ArCH*Hax*Ar), 3.44-4.12 (m, 16H, CH_2); 2.86 (d, *J* = 13.6 Hz, 4H, ArCH*Heq*Ar), 1.44 (s, 36H, C(CH_3)$_3$).
^{13}C NMR ($CDCl_3$): δ 168.7 (CONH), 158.1 (CAr), 136.8 (CAr), 135.3 (CAr), 130.1 (CHAr), 128.4 (CHAr), 127.6 (CHAr), 79.6 (*C*(CH_3)$_3$), 69.7(CH_2Bn), 41.1 (CH_2), 40.4 (CH_2), 31.9 (ArCH_2Ar), 28.5 (C(*C*H_3)$_3$).
Exact Mass (ESI+) *m/z* [M + Na]$^+$ calc.: 1551.7539 uma, found: 1551.7468 uma.
m.p.: 145-150 ºC.

25,26,27,28-Tetrabenzyloxycalix[4]arene-5,11,17,23-tetrakis[carbonyl-L-(*N-tert*-butoxycarbonyl)lysine methyl ester] (16). H-L-Lys(Boc)-OMe·HCl was employed as the amine reagent and chromatographic purification was performed with acetone/CH_2Cl_2 1:4 as the eluent. The product was obtained as a colorless solid (45% yield).
^{1}H NMR ($CDCl_3$): δ 7.45-7.1 (m, 28H, ArH), 4.98 (s, 8H, CH_2Bn), 4.55 (m, 4H, CHα), 4.12 (d, 4H, *J*= 13.3 Hz, ArC*Hax*HAr), 3.76 (s, 12H, CO_2CH_3), 3.15-3.07 (m, 8H, CH_2ε), 2.95 (d, 4H, *J* = 13.3 Hz, ArCH*Heq*Ar), 1.90-1.75 (m, 8H, CH_2δ), 1.73-1.50 (m, 8H, CH_2ß), 1.52-1.30 (m, 44H, CH_2γ, C(CH_3)$_3$).
^{13}C NMR ($CDCl_3$): δ 173.2 (*C*O_2CH_3), 167.0 (CONH), 157.7 (CAr), 156.1 (C), 136.6 (CAr), 136.3 (CAr), 135.2 (CAr), 130.1 (CHAr), 129.8 (CHAr), 129.5 (CHAr), 128.5 (CHAr), 128.3 (CHAr), 53.9 (CHα), 52.8 (CH_3O), 40.5 (CH_2ε), 31.5 (ArCH_2Ar), 30.3 (CH_2ß), 29.3 *C*(*CH*$_3$)$_3$, 26.7 (CH_2δ), 22.9 (CH_2γ).
Exact Mass (ESI+) *m/z* [M + 2Na]$^{2+}$ calc.: 987.9748 uma, found: 987.9746 uma.
m.p.: 150-153 ºC.

25,26,27,28-Tetrabenzyloxycalix[4]arene-5,11,17,23-tetrakis[carbonyl-L-*N*-(2,2,4,6,7-pentamethyldihydrobenzofuran-5-sulfonyl)arginine methyl ester] (17). The diprotected amino acid employed was H-L-Arg(Pbf)-OMe·HCl and chromatographic purification was performed eluting with acetone/CH_2Cl_2 1:9. The product was obtained as a colorless solid (70% yield).
^{1}H NMR (CD_2Cl_2): δ 7.40-7.22 (m, 28H, ArH), 5.07-4.88 (m, CH_2Bn), 4.12 (d, 4H, *J* = 13.7 Hz, ArC*Hax*HAr), 3.76 (s, 12H, CO_2CH_3), 3.2 (m, 8H, CH_2δ), 2.98 (d, 4H, *J* = 13.7 Hz, ArCH*Heq*Ar), 2.97 (s, 8H, CH_2-Pbf), 2.58 (s, 12H, CH_3-Pbf), 2.5 (s, 12H, CH_3-Pbf), 2.08 (s, 8H, CH_3-Pbf), 1.92-1.82 (m, 8H, CH_2ß), 1.58-1.48 (m, 8H, CH_2γ), 1.46 (s, 24H, CH_3-Pbf).
^{13}C NMR (DEPTQ135, CD_2Cl_2): δ 172.7 (*C*O_2CH_3), 167.5 (CONH), 158.7 (CAr), 156.4 (CGua), 138.4 (CAr), 136.4 (CAr), 132.3 (CAr), 132.3 (CAr), 129.9 (CHAr), 128.4 (CHAr), 128.3 (CHAr), 124.5 (CAr), 123.9 (CAr), 117.6 (CAr), 86.5 (C), 53.8 (CH_α), 52.5 (CO_2CH_3), 43.3

($CH_2\delta$), 40.4 ($CH_2ß$), 40.0 ($ArCH_2Ar$), 29.3 ($CH_2\gamma$), 28.7 (CH_3-Pbf), 19.3 (CH_3-Pbf), 18.1 (CH_3-Pbf), 12.5 (CH_3-Pbf).
Exact Mass (ESI+) *m/z* $[M + 2Na]^{2+}$ calc.: 1347.5541 uma, found: 1347.5502 uma.
m.p.: 170-172 ºC.

25,26,27,28-Tetrabenzyloxycalix[4]arene-5,11,17,23-tetrakis(carbonyl-L-alanine methyl ester)- (18). The protected amino acid employed was H-L-Ala-OMe·HCl and chromatographic purification was performed with acetone/CH_2Cl_2 2:2.5 as eluent. The pure product is a colorless oil (46% yield).
^{1}H NMR ($CDCl_3$): δ 7.35-7.18 (m, 20H, ArH), 7.09 (s, 4H, ArH), 6.99 (s, 4H, ArH), 6.64 (d, J = 7.0 Hz, 4H, NH), 6.63 (s, 4H, NH), 4.99 (d, J = 15.3 Hz, 8H, CH_2Bn), 4.55 (q, J = 7.0 Hz, 4H, CHα), 4.10 (d, J = 13.6 Hz, 4H, ArCH*Hax*Ar), 3.77 (s, 12H, CO_2CH_3), 2.91 (d, J = 13.6 Hz, 4H, ArCH*Heq*Ar), 1.46 (d, J = 7.0 Hz, 12H, CH_3).
^{13}C NMR (DEPTQ135, $CDCl_3$): δ 173.73 (CO_2CH_3), 166.9 (CONH), 157.9 (CAr), 136.6 (CAr), 135.2 (CAr), 125.1 (CAr), 129.8 (CHAr), 128.4 (CHAr), 128.3 (CHAr), 128.0 (CHAr), 127.05 (CHAr), 76.8 (CH_2), 52.3 (CO_2CH_3), 48.7 (CHα), 31.4 ($ArCH_2Ar$), 18.1 (CH_3).
Exact Mass (ESI+) *m/z*. $[M + Na]^+$ calc.: 1323.5154 uma, found: 1323.5146 uma.
m.p.: 268-671 ºC.

General procedure to obtain compounds 1-5, 8-11. Trifluoroacetic acid (10^3 eq.) was added to a solution of the corresponding protected compounds **13**, **15-18, 21-23** (1 eq.) dissolved in the same volume of CH_2Cl_2. The reaction was stirred at room temperature or carried out under reflux, depending on the substrates, and analytical HPLC was employed to monitor the reaction: 5-95% CH_3CN in H_2O + 0.1% TFA in 20 min.

25,26,27,28-Tetrahydroxycalix[4]arene-5,11,17,23-tetrakis[*N*-(diaminomethyl)benzamide] hydrochloride (1). Compound **13** (50 mg, 0.033 mmol) was refluxed for 24 hours. The solvent was evaporated and the residue was dissolved in a solution of 1N HCl (1.5 mL). The aqueous phase was then washed twice with CH_2Cl_2 (1.5 mL), the solvent was evaporated and the residue was lyophilized to afford **1** as a colorless compound (23 mg, 90% yield).
^{1}H NMR (DMSO-d_6): δ 11.02 (s, 4H, OH), 8.49 (br s, 4H, NHGua), 8.40 (br s, 4H, NHGua), 7.71 (s, 8H, ArH), 4.36 (br s, 4H, ArCH*Hax*Ar), 3.48 (br s, 4H, ArCH*Heq*Ar).
^{13}C NMR (DMSO-d_6): δ 167.44 (COGua), 161.7 (CGua), 157.7 (CAr), 130.1 (CAr), 129.5 (CHAr), 120.9 (CAr), 32.4 ($ArCH_2Ar$).
Exact Mass (ESI+) *m/z* $[M + H - 4HCl]^+$ calc.: 765.2857 uma, found: 765.2887 uma.
m.p.: > 350 ºC.

25,26,27,28-Tetrahydroxycalix[4]arene-5,11,17,23-tetrakis[*N*-(2-aminoethyl)benzamide] hydrochloride (2). Reaction with **15** (115 mg, 0.075 mmol) at room temperature for 70 min. Work-up as described above for **1** afforded **2** as a colorless compound (53 mg, 73% yield).
^{1}H NMR (D_2O): δ 7.55 (s, 8H, ArH), 3.90 (br s, 4H, $ArCH_2Ar$), 3.51 (t, J = 5.8 Hz, 8H, CH_2CH_2), 3.11 (t, 8H, J = 5.8 Hz, 8H, CH_2CH_2).
^{13}C NMR (DMSO-d_6): δ 170.23 (CONH), 153.32 (CAr), 128.53 (CH), 128.37 (CAr), 125.9 (CAr), 39.39 (CH_2), 37.2 (CH_2).
Exact Mass (ESI+) *m/z* $[M + H - 4HCl]^+$ calc.: 769.3673 uma, found: 769.3709 uma.
m.p.: 160-170 ºC.

25,26,27,28-Tetrahydroxycalix[4]arene-5,11,17,23-tetrakis(carbonyl-L-lysine-methyl ester) trifluoroacetate (3). Reaction with **16** (40 mg, 0.02 mmol) at room temperature for 18 h. The solvent was evaporated to complete dryness (until all traces of acid were removed) and the residue was dissolved in water. Work-up as for **1** gave pure **3** as a colorless solid (27 mg, 80% yield).
^{1}H NMR (CD_3OD): δ 7.68 (s, 8H, ArH), 4.54-4.50 (m, 4H, CHα), 4.05 (br s, 8H, $ArCH_2Ar$), 3.70 (s, 12H, CO_2CH_3), 2.91 (t, J = 7.6 Hz, 8H, $CH_2\varepsilon$), 2.01-1.81 (m, 8H, $CH_2\delta$), 1.73-1.63 (m, 8H, $CH_2\beta$), 1.58-1.48 (m, 8H, $CH_2\gamma$).
^{13}C NMR (DMSO-d_6): δ 172.9 (CO_2CH_3), 168.8 (CONH), 153.4 (CAr), 128.53 (CHAr), 127.7 (CAr), 126.27 (CAr), 52.8 (CHα), 51.4 (CO_2CH_3), 39.1 ($CH_2\varepsilon$), 30.3 ($CH_2\beta$), 26.7 ($CH_2\gamma$), 22.9 ($CH_2\delta$).
Exact Mass (ESI+) *m/z* $[M + 2H - 4CH_3COOH]^{2+}$ calc.: 585.2919 uma, found: 585.2932 uma.
m.p.: > 250 ºC dec.

25,26,27,28-Tetrahydroxy-calix[4]arene-5,11,17,23-tetrakis(carbonyl-L-arginine methyl ester) trifluoroacetate (4). Reaction was performed with precursor **17** (50 mg, 0.019 mmol) at room temperature for 13 h. The solvent was evaporated to complete dryness (until all traces of acid were removed) and the pure product was obtained by crystallization in CH_3CN (20 mg, 60% yield).
^{1}H NMR (CD_3OD): δ 7.7 (s, 8H, Ar*H*), 4.55-4.50 (m, 4H, CHα), 3.65 (s, 12H, CO_2CH_3), 3.24-3.18 (m, 8H, $CH_2\delta$), 1.99-1.78 (m, 8H, $CH_2\beta$), 1.70-1.60 (m, 8H, $CH_2\gamma$).
^{13}C NMR (CD_3OD): δ 172.7 (CO_2CH_3), 168.9 (CONHR), 157.4 (CGua), 156.4 (CAr), 128.6 (CHAr), 127.7 (CAr), 126.3 (CAr), 52.6 (CHα), 51.6 (CO_2CH_3), 40.5 ($CH_2\delta$), 30.6 ($ArCH_2Ar$), 28.0 ($CH_2\beta$), 25.2 ($CH_2\gamma$).
Exact Mass (ESI+) *m/z* $[M + 2H - 2CF_3COOH]^{2+}$ calc.: 755.2971 uma, found: 755.2971 uma.
m.p.: 245-247 ºC.

25,26,27,28-Tetrahydroxycalix[4]arene-5,11,17,23-tetrakis(carbonyl-L-alanine methyl ester) (5). Reaction with compound **18** was performed in a TFA:CH_3Cl (1:1) mixture, at reflux in a closed tube for 1 h. The solvent was evaporated and the residue was sonicated in MeOH, filtered and lyophilized. The product was obtained as a colorless solid (15 mg, 100 % yield).
^{1}H NMR (CD_3OD): δ 7.67 (s, 8H, ArH), 4.52 (m, 4H, CHα), 4.04 (br s, 8H, CH_2Ar), 3.71 (s, 12H, OCH_3), 1.45 (s, 12H, CH_3).
^{13}C NMR (CD_3OD): δ 173.8 (CO_2CH_3), 168.4 (CONHR), 153.1 (CAr), 128.7 (CHAr), 127.7 (CAr), 126.7 (CAr), 51.3 (CHα), 48.6 (CO_2CH_3), 15.6 (CH_3).
Exact Mass ESI(-) *m/z* $[M - H]^-$ calc.: 939.3300 uma, found: 939.3343 uma.
m.p.: > 350 ºC dec.

25,26-27,28-Biscrown-3-calix[4]arene-5,11,17,23-tetrakis[*N*-(diaminomethyl)benzamide] trifluoroacetate (8). The reaction with precursor **22** was stirred at room temperature for 13 h. The solvent was evaporated and the crude was triturated in EtOAc. The product was obtained as a colorless solid (28 mg, 90% yield).
^{1}H NMR (CD_3OD): δ 7.81 (d, J = 13.3 Hz, 8H, ArH), 5.37 (d, J = 12.4 Hz, 2H, ArCH*Hax*Ar), 4.70 (d, J = 12.4 Hz, 2H, ArCH*Hax*Ar), 4.5 (d, J = 12.4 Hz, CH_2O), 4.37-4.23 (m, 8H, CH_2O), 3.89 (t, 4H, CH_2O), 3.5 (d, J = 12.7 Hz , 2H, ArCH*Heq*Ar), 3.43 (d, J = 12.7 Hz, 2H, ArCH*Heq*Ar).

^{13}C NMR (CD_3OD): δ 168.2 (CONH), 159.7 (CGua), 157.3 (CAr), 136.1 (CAr), 126.3 (CHAr), 76.6 (CH_2), 74.4 (CH_2), 30.1 (Ar*C*H_2Ar), 29.1(Ar*C*H_2Ar).
Exact Mass (ESI+) *m/z* $[M + H - CF_3COOH]^+$ calc.: 1247.3593 uma, found: 1247.3546 uma.
m.p.: > 350 ºC.

25,26-27,28-Tetrabenxyloxycalix[4]arene-5,11,17,23-tetrakis[*N*-(diaminomethyl)benzamide] trifluoroacetate (9). The reaction with compound **13** was stirred at 0-5 ºC (to avoid *O*-debenzylation) for 26 h. The reaction was quenched with distilled water, and the solvent was evaporated at room temperature. The residue was dissolved in MeOH and the solvent was eliminated *in vacuo* again. The pure compound was obtained as a colorless solid (90% yield).
^{1}H NMR (CD_3CN): δ 8.10 (br s, 6H, NH), 7.83 (br s, 6H, NH), 7.38-7.28 (m, 20H, ArH), 7.23 (s, 8H, ArH), 6.08 (br s, 1H, 8H), 5.08 (s, CH_2Bn), 4.28 (d, *J* = 14.3 Hz, 4H, ArCH*Hax*Ar), 3.07 (d, *J* = 14.3 Hz, 4H, ArCH*Heq*Ar).
^{13}C NMR (CD_3OD): δ 167.5 (CONH), 160.4 (CGua), 156.2 (CAr), 136.2 (CAr), 130.2 (CHAr), 128.7 (CHAr), 128.6 (CHAr), 128.3 (CHAr), 125.1 (CAr), 76.9 (CH_2Bn), 30.8 (CH_2).
Exact Mass (ESI+) *m/z* $[M + H - 4CF_3COOH]^+$ calc.: 1125.4848 uma, found: 1125.4806 uma.
m.p.: > 350 ºC.

25,26-27,28-Tetra-*n*-propoxycalix[4]arene-5,11,17,23-tetrakis[*N*-(diaminomethyl)benzamide] trifluoroacetate (10). Reaction was stirred overnight at room temperature. The solvent was evaporated and the residue sonicated in CH_3CN. The resulting precipitate was filtered and the product obtained as a colorless solid (90% yield).
^{1}H NMR (CD_3CN): δ 8.21 (br s, 6H, NH), 7.80 (br s, 6H, NH), 7.30 (s, 8H, ArH), 4.52 (d, *J* = 13.9 Hz, 4H, ArCH*Hax*Ar), 3.97 (t, *J* = 7.3 Hz, 8H, OC*H*$_2$CH$_2$CH$_3$), 3.36 (d, 8H, *J* = 13.9 Hz, ArCH*Heq*Ar), 1.99-1.89 (q, *J* = 7.3 Hz, 8H, OCH$_2$C*H*$_2$CH$_3$), 1.0 (t, *J* = 7.3 Hz, 12H, OCH$_2$CH$_2$C*H*$_3$).
^{13}C NMR (CD_3CN): δ 167.9 (CONH), 161.7 (CGua), 156.2 (CAr), 135.7 (CAr), 128.8 (CHAr), 124.9 (CAr), 77.4 (O*C*H$_2$CH$_2$CH$_3$), 30.5 (Ar*C*H_2Ar), 23.2 (OCH$_2$*C*H$_2$CH$_3$), 9.6 (OCH$_2$CH$_2$*C*H$_3$).
Exact Mass (ESI+) *m/z* of $[M + H - CF_3COOH]^+$ calc.: 1275.4521, found: 1275.4561 uma.
m.p.: > 330 ºC dec.

***N*-(diaminomethyl)-4-hydroxybenzamide trifluoroacetate (11).** This compound was prepared following the same procedure as for compound **1**, except for purification on semi-preparative HPLC: the crude was dissolved in CH_3CN (32 mg/mL), and a gradient of CH_3CN in water + 0.1% CF_3COOH (5-60% for 15 min and 60 to 95% for 3 min). The product is obtained as a colorless solid (43% yield).
^{1}H NMR (CD_3OD): δ 8.57 (s, 1H, OH), 7.97 (d, *J* = 8.8 Hz, 2H, ArH *meta*), 6.98 (d, *J* = 8.8 Hz, 2H, ArH *ortho*).
^{13}C NMR (CD_3OD): δ 167.7 (CGua), 163.3 (CONH), 130.5 (CHAr), 121.8 (CAr), 115.49 (CHAr).
Exact Mass (ESI+) *m/z*. $[M + H - CF_3COOH]^+$ calc.: 202.0592 uma, found: 202.0584 uma.
m.p.: 282-285 ºC.

25,26,27,28-Tetrahydroxycalix[4]arene-5,11,17,23-tetracarboxylic acid (6). This known compound[47, 48], was synthesized by a novel procedure. Benzyl derivative **12** (52 mg, 0.054

mmol) was suspended in 8 mL of a 1:2 mixture of conc. HCl and acetic acid. The reaction was stirred and heated at reflux for 48 h in a sealed tube. Solvents were evaporated and the residue was dissolved in THF-H_2O (3:1) and purified by semi-preparative HPLC (2.5 mg/mL, 30-36% CH_3CN in H_2O+0.1% CF_3COOH gradient in 15 min). The pure product was obtained (19 mg, 60% yield) as a grey powder.
^{1}H NMR (DMSO-d_6): δ 7.66 (s, 8H, ArH), 3.9 (br s, 4H, $ArCH_2Ar$).
^{13}C NMR (DMSO-d_6): δ 167.4 (COOH), 156.7 (CArOH), 130.9 (CHAr), 128.9 (CAr), 122.7 (CAr), 31.24 (CH_2).
Exact Mass ESI(-) *m/z* $[M]^-$ calc: 599.1190 uma, found: 599.1182 uma.
m.p.: > 350 ºC.

Molecular dynamics. Simulations were performed with K_v1.2 in the presence of **1**, **4**, and **8** at 300K in *vacuo*. The starting tetramer K_v1.2 was obtained from the x-ray structure [Protein Data Bank ID code 2a79],[14] excluding chain A and part of chain B (32-131 residues). Thus, the integral membrane component of K_v1.2 was considered. To form each of the three complexes the calixarene was docked manually on the surface of K_v1.2, the four guanidinium groups in the upper rim interacting through hydrogen bonds with the carboxylates of Asp-379 surrounding the channel pore. The lower rim of the calixarene laid on the middle of the pore. The Maestro interface (Schrodinger Inc.) was used to construct the complexes. Simulations were carried out by using Batchmin, the computational back-end of the Macromodel package (Schrodinger Inc.). Amber* force field was chosen to model the systems. Each complex was relaxed following a protocol already reported by Magis *et al.*[49] in the design of K_v1.2 potassium channel blockers. The protocol consisted of an energy minimization followed by molecular dynamics simulation applying positional restraints. The restraint force constants for residues located at a distance lower than 7 Å from the ligand were set to 5 kcal mol^{-1} Å^{-2} for the Cα and to 0.005 kcal mol^{-1} Å^{-2} for non-hydrogen atoms other than the Cα. For residues located at a distance greater than 7 Å from the ligand, the respective values were 50 kcal mol^{-1} Å^{-2} and 5 kcal mol^{-1} Å^{-2}. No restraints were applied to the ligand. The Polak-Ribiere conjugate-gradient (PRCG) algorithum[50] was used to initially minimize the structures. Next, a molecular dynamics of 1500 ps was carried out with a time step of 1 fs. The charges applied came from the force field. Van der Waals interactions were truncated at a cutoff distance of 7 Å. Electrostatic interactions were truncated at a distance of 12 Å. The cutoff distance for the hydrogen bonds was 4 Å. Temperature was maintained constant by using a standard velocity Verlet algorithm.[51] Maestro and XSCORE[51, 52] programs were used to analyze the trajectories.

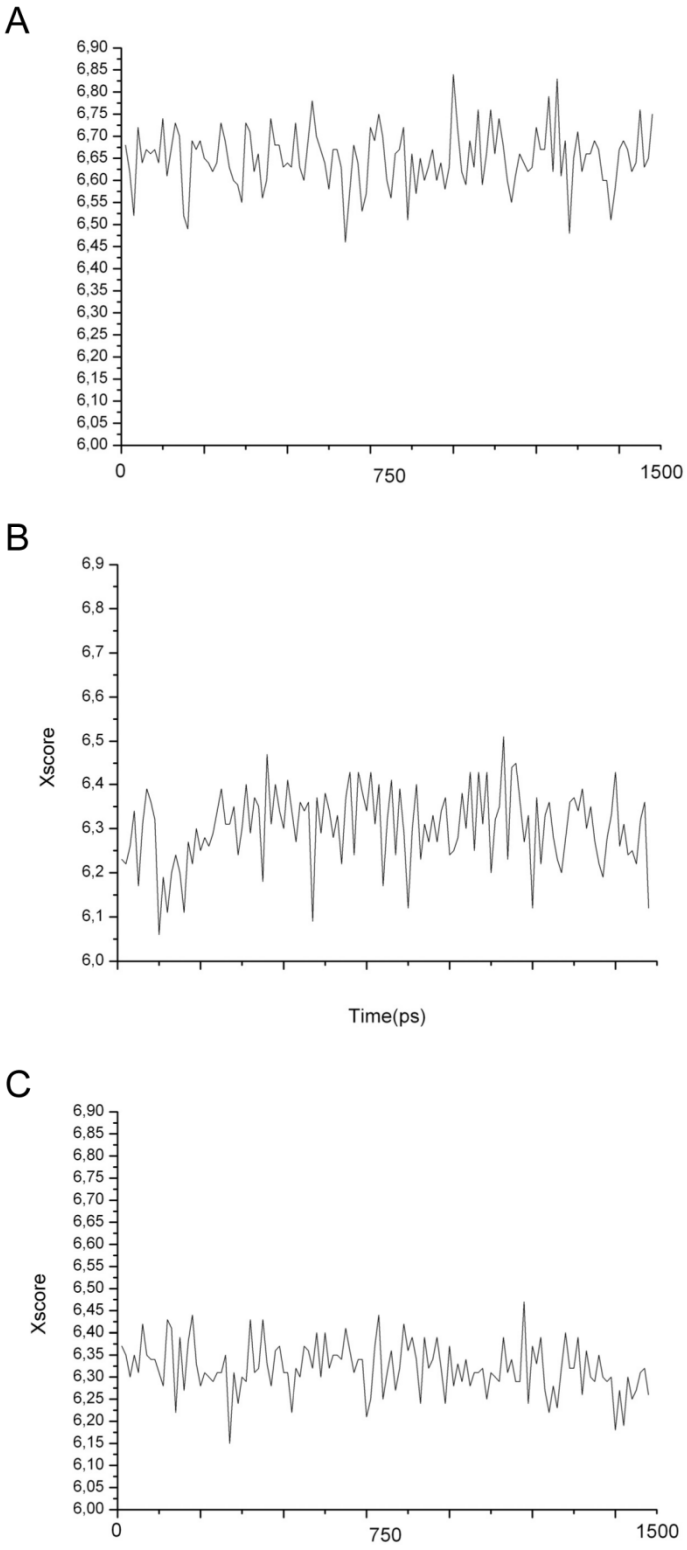

Figure 2.20. Average Xscore values between the protein and the ligands. (A) Ligand **1**. **(B)** Ligand **4**. **(C)** Ligand **8**.

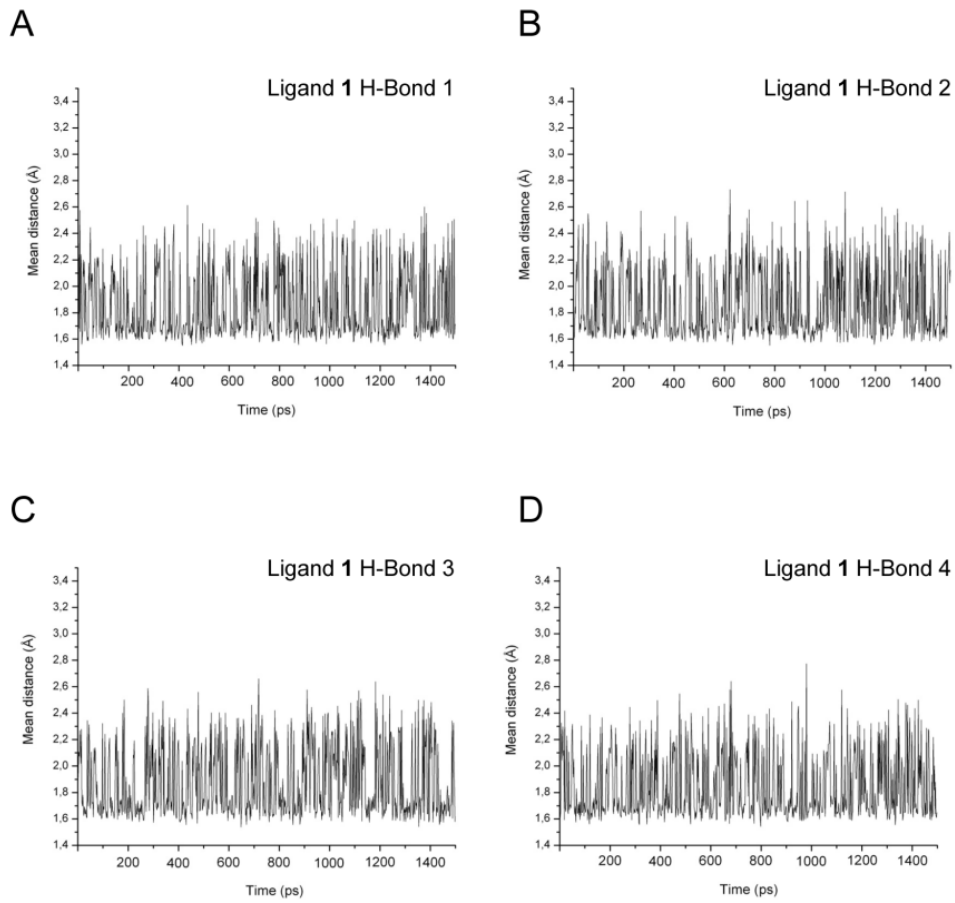

Figure 2.21. Average hydrogen bond distances between the guanidinium groups in ligand 1 and the carboxylate units of the protein. The two NH-OC distances corresponding to each guanidinium-carboxylate interaction were measured at each step. The results shown correspond to the average of the two values obtained. From **(*A*)** to **(*D*)**, the four guanidinium-carboxylate interactions.

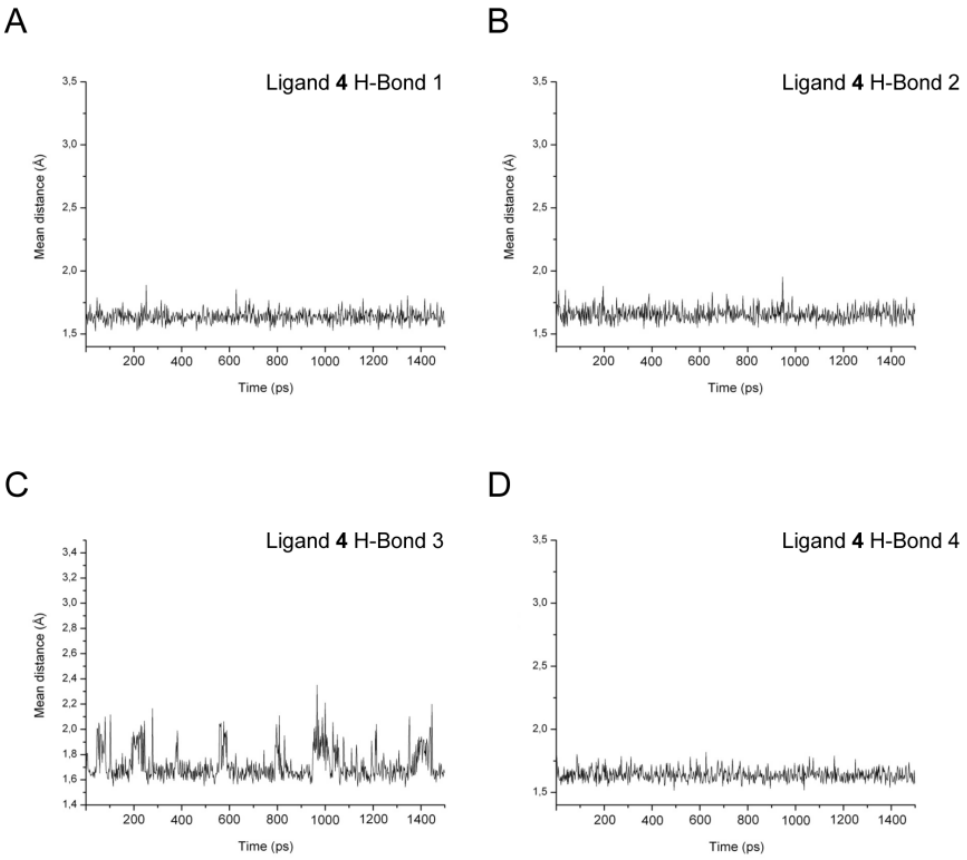

Figure 2.22. Average hydrogen bond distances between the guanidinium groups in ligand 4 and the carboxylate units of the protein. The two NH-OC distances corresponding to each guanidinium-carboxylate interaction were measured at each step. The results shown correspond to the average of the two values obtained. From **(*A*)** to **(*D*)**, the four guanidinium-carboxylate interactions.

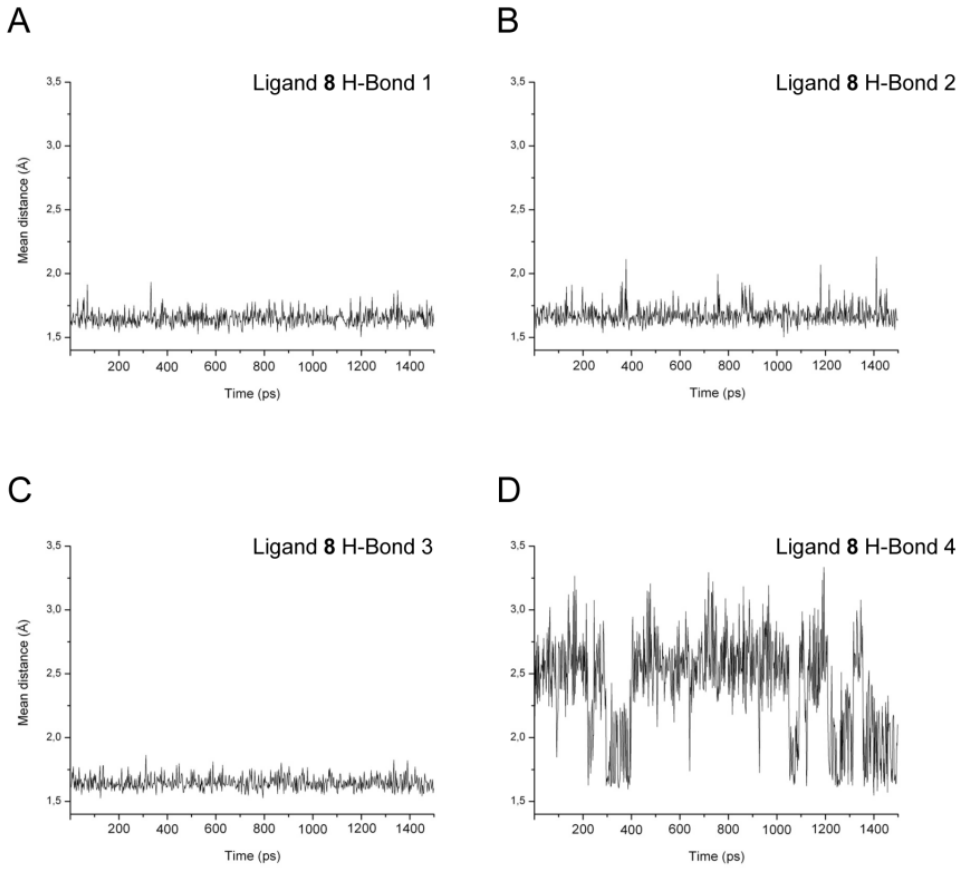

Figure 2.23. Average hydrogen bond distances between the guanidinium groups in ligand 8 and the carboxylate units of the protein. The two NH-OC distances corresponding to each guanidinium-carboxylate interaction were measured at each step. The results shown correspond to the average of the two values obtained. From **(*A*)** to **(*D*)**, the four guanidinium-carboxylate interactions.

Channel Expression. The Shaker clone Sh H4 IR [Delta](6-46) (*N*-type inactivation removed) in the pBluescript2 KS+ vector was used for all experiments unless otherwise noted. All point mutations were made by performing site-directed mutagenesis using the QuikChange protocol (Stratagene) from the Sh H4 IR clone.

The $rK_v1.3$ construct was in the pGEM-HE vector. Fluorescence experiments were conducted with the Sh H4 IR W434F (non-conducting channel) A359C (maleimide attachment site) construct which contained two additional mutations (C245V and C462A) to prevent background labeling of native cysteines in the Shaker channel.

All DNA was confirmed by DNA sequencing. RNA was transcribed using mMessage mMachine T7 transcription kit (Ambion).

Surgically extracted *Xenopus laevis* oocytes were injected with 0.5-4 ng channel RNA (50 nl). The cells were incubated in ND-96 (96 mM NaCl, 2 mM KCl, 1.8 mM $CaCl_2$, 1 mM

$MgCl_2$, 50 mg mL^{-1} gentamicin, 2.5 mM Na pyruvate, and 5 mM HEPES, pH 7.6) at 12-18°C for 12-48 h prior to experiments.

Electrophysiology. All electrophysiology experiments were conducted at room temperature. Two electrode voltage clamp (TEVC) experiments were performed using a Dagan CA-1B amplifier (Dagan Corporation), Digidata-1440A board, and pClamp10 software. The oocytes were placed in a perfusion dish to allow for pre-wash, wash, and post-wash recordings. All recordings were performed in ND-96 recording solution (96 mM NaCl, 2 mM KCl, 1.8 mM $CaCl_2$, 1 mM $MgCl_2$, 10 mM HEPES, pH 7.2) unless otherwise noted. For each experiment, the oocyte was voltage-clamped at -80 mV followed by a continuous train of 100 or 300 ms pulses to +20 mV every 15 seconds.

Current Voltage (I-V) relationships (Figure 2.15 B) were measured using the same experimental conditions as above, except that the oocyte was voltage-clamped at -80 mV followed by a depolarizing train of +10 mV steps lasting 300 ms then returned to -80 mV. Current was measured from -80 mV to +60 mV. The resulting data was normalized to the current measured at +60 mV.

All compounds were dissolved in ND-96 recording solution to make a 500 μM stock solution. When needed, a maximum of 5% (v/v) DMSO was added to the stock solution to facilitate solubilization. For inhibition experiments, small quantities of the calixarene stock solutions were manually applied and mixed in a stagnant bath containing the oocyte. For all recordings, DMSO was present at levels less than 2% (v/v). Oocytes were bathed in the calixarene solution until the current measurements taken at +20 mV reached steady-state. The compounds were washed away with ND-96 recording solution administered using a gravity perfusion system at approximately 80 mL/h.

All ionic current measurements taken at +20 mV were leak-subtracted using the following formula:

$$I_{LS} = I_{+20mV} - 0.25*(I_{-80mV})$$

The percent inhibition (B) was determined using the following formula, using leak subtracted current measured at +20 mV for steady state levels before and after addition of the calix[4]arene:

$$B = 100*[(I_{initial} - I_{ligand})/ I_{initial}]$$

For dose-response experiments (Figure 2.13), varying concentrations of ligand **4** were applied to oocytes expressing either the Shaker or $rK_v1.3$ channel. Each experiment was repeated with at least three different oocytes, and the data were then averaged. Then, the average reduction in ionic current elicited by application of ligand **4** (B) was plotted as a function of the $\log_{10}$ of ligand **4** concentration. The plotted data were then fit using Igor Pro software with the modified Hill equation:

$$B = B_{max} * [L]^h/(K_d^h + [L]^h)$$

where L represents the concentration of calix[4]arene used in the experiment, K_d the equilibrium dissociation constant and h the Hill Coefficient.

Tail currents (Figure 2.14A) were measured using the I-V protocol described above with cells being incubated in a high potassium ND-96 recording solution (98 mM KCl, 1.8 mM $CaCl_2$, 1 mM $MgCl_2$, 10 mM HEPES, pH 7.2). Measurements taken from four different oocytes were averaged and inverted to obtain conductance (G) values and then normalized to the maximum conductance measured before the application of ligand **4** and then plotted as a function of the step voltage. The plotted data were then fit using Igor Pro software with a standard sigmoid equation where G/G_{max} represents the normalized conductance, V represents the step voltage, V_{mid} the midpoint voltage and m the slope.

Voltage clamp fluorometry experiments were conducted according to [34]. Briefly, oocytes were injected with 4 ng Sh H4 IR W434F-A359C (C245V, C462A) cRNA. After 1 h, endogenous cysteines on the oocytes surface were treated with tetraglycine-maleimide [53] for 20 min at 18ºC. Cells then were extensively washed with ND-96 and incubated at 18ºC for 3-4 days. On the day of experiments, oocytes were incubated with 12.5 μM tetramethylrhodamine-6-maleimide (Invitrogen) for 30 min at 0ºC and then extensively washed with ND-96. After labeling, cells were kept at 12ºC. Recordings were done in ND-96 recording solution at room temperature. Oocytes were voltage clamped at -80 mV and fluorescence changes were evoked by a series of +20 mV steps from -150 mV to +50 mV (300 ms step length). The voltage step protocol was then repeated after an 8-minute incubation with 200μM ligand **4**. For fluorescence vs. voltage (FV) curves (Figure 2.15B) steady state fluorescence levels were measured at the end of each voltage step and then plotted as a function of the step voltage. Measurements were then normalized to the maximum ΔF measured. Data for each condition were then averaged. The averaged data were then fit using Igor Pro software with a sigmoid equation where ΔFnorm represents the normalized ΔF measurement , V represents the step voltage, V_{mid} the midpoint voltage and m the slope.

Agitoxin competition experiments were conducted in ND-96 recording solution supplemented with 50μg/mL bovine serum albumin (BSA) (Sigma Aldrich) to minimize non-specific toxin binding to the recording chamber. Recombinant Agitoxin-2 ($AgTx_2$) (Alomone labs) was dissolved in H_2O to afford a 10 μM stock solution which was kept on ice during experiments. Oocytes expressing Shaker channels were incubated in 200 μM ligand **4**, 1 μM $AgTX_2$, or 200 μM ligand **4** followed by 1 μM $AgTX_2$. The % inhibition after application of each reagent was calculated using the formula above and data for each condition were averaged. Error bars represent SEM.

Acknowledgements

This work was supported by the Spanish Ministry of Science and Education (MEC) (project CTQ2005-08948-C02-01/BQU), Consolider Ingenio 2010 (Grant CSD2006-0003), the ICIQ Foundation and the National Institutes of Health (5R01NS035549 to EYI). V. M. thanks MEC and the ICIQ Foundation for pre-doctoral fellowships. Thanks to Dr. Matt Banghart for preliminary electrophysiology experiments to assess the applicability of the calix[4]arene scaffold as a new class of K_v channel ligands, to Dr. Francesco Tombola for assistance with electrophysiological experiment design and data analysis, to Dr. Maximilian Ulbrich for help

with data analysis, and to Dr. Harald Janovjak for help with molecular modeling and data analysis.

References

1. Yu, F. H.; Catterall, W. A., The VGL-chanome: A protein superfamily specialized for electrical signaling and ionic homeostasis. *Sci. STKE* **2004,** 253, re15-.

2. Yellen, G., The voltage-gated potassium channels and their relatives. *Nature* **2002,** 419, (6902), 35-42.

3. Wulff, H.; Zhorov, B. S., K^+ channel modulators for the treatment of neurological disorders and autoimmune diseases. *Chem. Rev.* **2008,** 108, (5), 1744-1773.

4. Gradl, S. N., et al., Protein surface recognition by rational design: Nanomolar ligands for potassium channels. *J. Am. Chem. Soc.* **2003,** 125, (42), 12668-12669.

5. Martos, V., et al., Calix[4]arene-based conical-shaped ligands for voltage-dependent potassium channels. *Proc. Natl. Acad. Sci. U. S. A.* **2009,** 106, (26), 10482-10486.

6. Lawson, K.; McKay, N. G., Modulation of potassium channels as a therapeutic approach. *Curr. Pharm. Des.* **2006,** 12, (4), 459-470.

7. Hille, B., *Ion Channels of Excitable Membranes*. 3rd ed.; Sinauer: Sunderland, MA, 2001.

8. Bayliss, D. A.; Barrett, P. Q., Emerging roles for two-pore-domain potassium channels and their potential therapeutic impact. *Trends Pharmacol. Sci.* **2008,** 29, (11), 566-575.

9. Hibino, H., et al., Inwardly rectifying potassium channels: Their structure, function, and physiological Roles. *Physiol. Rev.* **2010,** 90, (1), 291-366.

10. Yu, F. H.; Yarov-Yarovoy, V.; Gutman, G. A.; Catterall, W. A., Overview of molecular relationships in the voltage-gated ion channel superfamily. *Pharmacol. Rev.* **2005,** 57, (4), 387-395.

11. Wulff, H.; Castle, N. A.; Pardo, L. A., Voltage-gated potassium channels as therapeutic targets. *Nat Rev Drug Discov* **2009,** 8, (12), 982-1001.

12. Li, M.; Jan, Y. N.; Jan, L. Y., Specification of subunit assembly by the hydrophilic amino-terminal domain of the Shaker potassium channel. *Science* **1992,** 257, (5074), 1225-1230.

13. Tombola, F.; Pathak, M. M.; Isacoff, E. Y., How does voltage open an ion channel? *Annu. Rev. Cell Dev. Biol.* **2006,** 22, (1), 23-52.

14. Long, S. B.; Campbell, E. B.; MacKinnon, R., Crystal structure of a mammalian voltage-dependent Shaker family K^+ channel. *Science* **2005,** 309, (5736), 897-903.

15. Long, S. B.; Tao, X.; Campbell, E. B.; MacKinnon, R., Atomic structure of a voltage-dependent K^+ channel in a lipid membrane-like environment. *Nature* **2007,** 450, (7168), 376-382.

16. Jiang, Y., et al., X-ray structure of a voltage-dependent K^+ channel. *Nature* **2003,** 423, (6935), 33-41.

17. MacKinnon, R., Potassium channels. *FEBS Lett.* **2003,** 555, (1), 62-65.

18. Harmar, A. J., et al., IUPHAR-DB: the IUPHAR database of G protein-coupled receptors and ion channels. *Nucl. Acids Res.* **2009,** 37, (suppl_1), D680-685.

19. Beeton, C., et al., $K_v1.3$ channels are a therapeutic target for T cell-mediated autoimmune diseases. *Proc. Natl. Acad. Sci. U. S. A.* **2006,** 103, (46), 17414-17419.

20. Panyi, G., et al., K channel blockers: novel tools to Inhibit T cell activation leading to specific immunosuppression. *Curr. Pharm. Des.* **2006,** 12, 2199-2220.

21. Norton, R. S.; Pennington, M. W.; Wulff, H., Potassium channel blockade by the sea anemone toxin ShK for the treatment of multiple sclerosis and other autoimmune diseases. *Curr. Med. Chem.* **2004,** 11, (23), 3041-3052.

22. Ader, C., et al., A structural link between inactivation and block of a K^+ channel. *Nat. Struct. Mol. Biol.* **2008,** 15, (6), 605-612.

23. Baldini, L.; Casnati, A.; Sansone, F.; Ungaro, R., Calixarene-based multivalent ligands. *Chem. Soc. Rev.* **2007,** 36, (2), 254-266.

24. Martos, V.; Castreño, P.; Valero, J.; de Mendoza, J., Binding to protein surfaces by supramolecular multivalent scaffolds. *Curr. Opin. Chem. Biol.* **2008,** 12, (6), 698-706.

25. Gordo, S., et al., Stability and structural recovery of the tetramerization domain of p53-R337H mutant induced by a designed templating ligand. *Proc. Natl. Acad. Sci. U. S. A.* **2008,** 105, (43), 16426-16431.

26. Schmuck, C.; Machon, U., Amino acid binding by 2-(guanidiniocarbonyl)pyridines in aqueous solvents: A comparative binding study correlating complex stability with stereoelectronic factors. *Chem.--Eur. J.* **2005,** 11, (4), 1109-1118.

27. Heginbotham, L.; MacKinnon, R., The aromatic binding site for tetraethylammonium ion on potassium channels. *Neuron* **1992,** 8, (3), 483-491.

28. Blaustein, R. O.; Cole, P. A.; Williams, C.; Miller, C., Tethered blockers as molecular `tape measures' for a voltage-gated K^+ channel. *Nat. Struct. Mol. Biol.* **2000,** 7, (4), 309-311.

29. Arduini, A., et al., Calix[4]arenes blocked in a rigid cone conformation by selective functionalization at the lower rim. *J. Org. Chem.* **1995,** 60, (5), 1454-1457.

30. Mannuzzu, L. M.; Moronne, M. M.; Isacoff, E. Y., Direct physical measure of conformational rearrangement underlying potassium channel gating. *Science* **1996,** 271, (5246), 213-216.

31. Loots, E.; Isacoff, E. Y., Protein rearrangements underlying slow inactivation of the Shaker K^+ channel. *J. Gen. Physiol.* **1998,** 112, (4), 377-389.

32. Perozo, E.; MacKinnon, R.; Bezanilla, F.; Stefani, E., Gating currents from a nonconducting mutant reveal open-closed conformations in Shaker K^+ channels. *Neuron* **1993,** 11, (2), 353-358.

33. Glauner, K. S.; Mannuzzu, L. M.; Gandhi, C. S.; Isacoff, E. Y., Spectroscopic mapping of voltage sensor movement in the Shaker potassium channel. *Nature* **1999,** 402, (6763), 813-817.

34. Mannuzzu, L. M.; Isacoff, E. Y., Independence and cooperativity in rearrangements of a potassium channel voltage sensor revealed by single subunit fluorescence. *J. Gen. Physiol.* **2000,** 115, (3), 257-268.

35. Garcia, M. L., et al., Purification and characterization of three inhibitors of voltage-dependent K^+ channels from Leiurus Quinquestriatus var. Hebraeus venom. *Biochemistry* **1994,** 33, (22), 6834-6839.

36. Eriksson, M. A. L.; Roux, B., Modeling the structure of agitoxin in complex with the Shaker K+ channel: A computational approach based on experimental distance restraints extracted from thermodynamic mutant cycles. *Biophys. J.* **2002,** 83, (5), 2595-2609.

37. Garcia, M. L.; Gao, Y.-D.; McManus, O. B.; Kaczorowski, G. J., Potassium channels: from scorpion venoms to high-resolution structure. *Toxicon* **2001,** 39, (6), 739-748.

38. Tombola, F.; Pathak, M. M.; Isacoff, E. Y., Voltage-sensing arginines in a potassium channel permeate and occlude cation-selective pores. *Neuron* **2005,** 45, (3), 379-388.

39. Dauplais, M., et al., On the convergent evolution of animal toxins. *J. Biol. Chem.* **1997,** 272, (7), 4302-4309.

40. Yu, L., et al., Nuclear magnetic resonance structural studies of a potassium channel-charybdotoxin complex. *Biochemistry* **2005,** 44, (48), 15834-15841.

41. Pathak, M. M., et al., Closing in on the resting state of the Shaker K^+ channel. *Neuron* **2007,** 56, (1), 124-140.

42. Coghlan, M. J.; Carroll, W. A.; Gopalakrishnan, M., Recent developments in the biology and medicinal chemistry of potassium channel modulators: Update from a decade of progress. *J. Med. Chem.* **2001,** 44, (11), 1627-1653.

43. Gutsche, C. D.; Levine, J. A., Calixarenes. 6. Synthesis of a functionalizable calix[4]arene in a conformationally rigid cone conformation. *J. Am. Chem. Soc.* **1982,** 104, (9), 2652-2653.

44. Zhou, H., et al., Structure-activity studies on a library of potent calix[4]arene-based PDGF antagonists that inhibit PDGF-stimulated PDGFR tyrosine phosphorylation. *Org. Biomol. Chem.* **2006,** 4, (12), 2376-2386.

45. Sansone, F., et al., Synthesis and structure of chiral calix[4]arenes functionalized at the upper rim with L-alanine units. *Eur. J. Org. Chem.* **1998,** 1998, (5), 897-905.

46. Sansone, F., et al., A new chiral rigid cone water soluble peptidocalix[4]arene and its inclusion complexes with α-amino acids and aromatic ammonium cations. *Tetrahedron Lett.* **1999,** 40, (25), 4741-4744.

47. Dalgarno, S. J., et al., Large diameter non-covalent nanotubes based on the self-assembly of para-carboxylatocalix[4]arene. *New J. Chem.* **2007,** 31, (11), 1891-1894.

48. Yilmaz, M.; Vural, U. S., Synthesis of new substituted calix[4]arenes and their complexes with iron(III). *Synth. React. Inorg. Met.-Org. Chem.* **1991,** 21, (8), 1231 - 1241.

49. Magis, C., et al., Structure-based secondary structure-independent approach to design protein ligands:application to the design of K_v1.2 potassium channel blockers. *J. Am. Chem. Soc.* **2006,** 128, (50), 16190-16205.

50. Polak, E.; G, R., Note on convergence of conjugate direction methods. *Rev Fr Inf Rech Oper* **1969,** 16, 35-43.

51. Swope, W. C.; Andersen, H. C.; Berens, P. H.; Wilson, K. R., A computer simulation method for the calculation of equilibrium constants for the formation of physical clusters of molecules: Application to small water clusters. *J. Chem. Phys.* **1982,** 76, (1), 637-649.

52. Wang, R.; Lu, Y.; Fang, X.; Wang, S., An extensive test of 14 scoring functions using the PDBbind refined set of 800 protein-ligand complexes. *J. Chem. Inf. Comput. Sci.* **2004,** 44, (6), 2114-2125.

53. Borah, H. N.; Boruah, R. C.; Sandhu, J. S., Microwave-induced one-pot synthesis of N-carboxyalkyl maleimides and phthalimides. *J. Chem. Res., Synop.* **1998**, (5), 272-+.

Chapter 3

The role of voltage in regulating phosphoinositide signaling pathways

Phosphoinositides are major players in cell signaling pathways

Phosphatidylinositol (PI) and its phosphorylated derivatives known as phosphoinositides (PI(n)P), are concentrated on the cytosolic surface of virtually all cellular membranes.[1] Even though PI and PIPs together constitute less than 15% of all lipids in eukaryotic membranes, they play integral roles in the cell.[1, 2] Figure 3.1 shows the structure of PI (Figure 3.1A), highlights the eight different phosphoinositides, the known kinase and phosphatase reactions that interconvert these species (Figure 3.1B), and the known subcellular locations of each PIP (Figure 3.1C).[3] Each PIP has a unique distribution throughout all cellular membranes thus distinguishing organelle membranes from the plasma membrane (Figure 3.1C).[1]

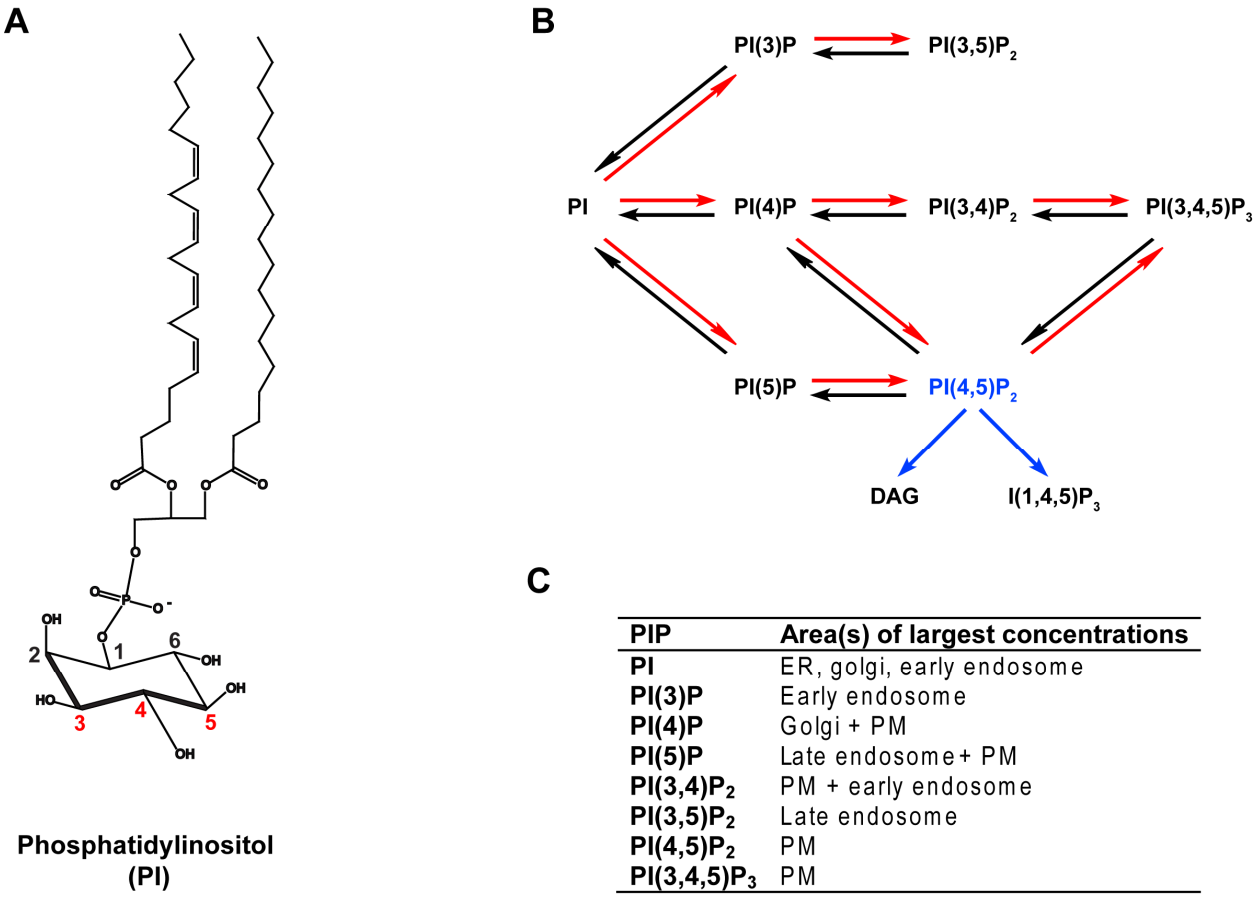

PIP	Area(s) of largest concentrations
PI	ER, golgi, early endosome
PI(3)P	Early endosome
PI(4)P	Golgi + PM
PI(5)P	Late endosome + PM
$PI(3,4)P_2$	PM + early endosome
$PI(3,5)P_2$	Late endosome
$PI(4,5)P_2$	PM
$PI(3,4,5)P_3$	PM

Figure 3.1. Phosphatidylinositol and its analogs. (A) Chemical structure of phosphatidylinositol (PI). Sites of PI phosphorylation at the D3, D4 and D5 positions of the inositol ring are highlighted in red. **(B)** Interconversion of PI and its derivatives. Arrows represent reactions catalyzed by phosphoinositide kinases (red), phosphoinositide phosphatases (black), and phospholipases (blue). **(C)** Table showing compartmentalization of PIPs in the cell. Abbreviations: Plasma membrane (PM), Endoplasmic reticulum (ER). Figure adapted from [4].

PIPs serve a variety of functions in the cell, serving as membrane recognition sites for many cytosolic proteins as well as second messengers that modulate membrane protein function.[5] For a thorough review of the enzymes responsible for maintaining resting levels of each PIP in the plasma membrane and organelle membranes, please see[6]. The localization of a particular PIP is regulated by a series of lipid kinases and phosphatases that can reversibly add or remove phosphate groups to the D-3,4, or 5 position of the inositol ring of phosphatidylinositol.[7]

Phosphatidylinositol 4-phosphate (PI(4)P) and phosphatidylinositol 4,5-bisphophate ($PI(4,5)P_2$) each comprise 5% of the total lipid pools in the cell and are found primarily in the inner leaflet of the plasma membrane.[1, 8] These two species represent the majority of PIPs located at the plasma membrane. Phosphatidylinositol 3,4-bisphosphate ($PI(3,4)P_2$) and phosphatidylinositol 3,4,5-trisphosphate ($PI(3,4,5)P_3$) are also found primarily in the inner leaflet of the plasma membrane and each comprises approximately 0.005% of the total PIP pools in the cells, with these pools being tightly regulated by cellular signaling pathways.[2, 8]

Membrane and cytosolic proteins can bind phosphoinositides

Both cytosolic proteins and the cytosolic domains of membrane proteins bind phosphoinositides. These interactions are mediated by electrostatic interactions between the negatively charged phosphate groups on the inositol ring of the PIP and basic residues on the protein's surface.[1] The PIP interacting regions of proteins can be unstructured, as is the case in numerous cytoskeleton binding proteins where clusters of basic amino acids create a positively charged surface which binds the negatively charged head group of a PIP.[4, 9] Alternatively, PIP binding domains can form a structured PIP binding pocket, as is the case in proteins containing pleckstrin homology (PH) domains. More than 250 human proteins contain PH domains, each composed of approximately 120 amino acids. Structural information for many PH domains shows that they contain a common β-sandwich motif with a basic residue-rich PIP binding pocket.[4] Biochemical and *in vivo* studies have demonstrated that most PH domains do not possess strong binding affinity or specificity for particular PIPs and reside primarily in the cytosol, not bound to PIPs in the plasma or organelle membranes.[9] However, many of these proteins have been shown to interact with $PI(4,5)P_2$ *in vivo*, as it is the most abundant PIP in the plasma membrane. Fusions of green fluorescent protein (GFP) and other fluorescent proteins (FPs) to certain PH domains can be used as reporters of PIP pools in the cell.[10] The first and best characterized FP-PH domain is from PLC-δ1 and serves as a sensor for $PI(4,5P)_2$ and inositol-1,4,5-trisphopshate ($I(1,4,5)P_3$).

Roles of $PI(4,5)P_2$ in the cell

$PI(4,5)P_2$ is one of the major PIPs in the plasma membrane, represents roughly 99% of all doubly phosphorylated phosphoinositides within the cell, and has an effective concentration of 10 μM at the plasma membrane.[9] $PI(4,5)P_2$ plays major roles in a variety of cellular processes shown in Figure 3.2 that have been extensively reviewed.[1, 2, 9, 11, 12]

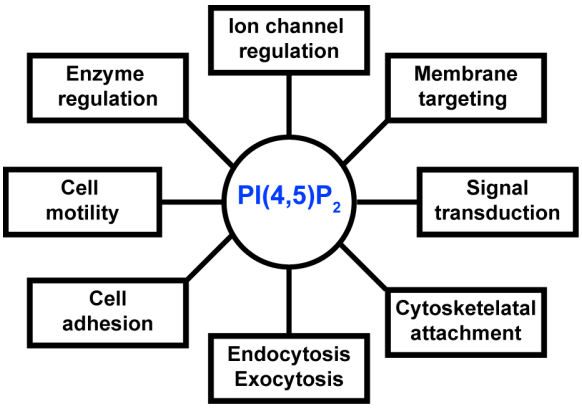

Figure 3.2. Roles of $PI(4,5)P_2$ in the cell. For more thorough summaries of each $PI(4,5)P_2$ role listed above, please see [1, 2, 9].

Over the past 15 years, the role of $PI(4,5)P_2$ as a direct modifier of ion channels has been extensively studied.[5, 11] As $PI(4,5)P_2$ is the major PIP in the plasma membrane, it has been shown to directly regulate a variety of ion channels including inwardly rectifying K^+ (K_{ir}) channels, voltage dependent K^+ (K_v) channels, and transient receptor potential (TRP) channels.[5]

$PI(4,5)P_2$ serves a variety of functions in cellular signal transduction. $PI(4,5)P_2$ is the substrate for phospholipase C (PLC), a key enzyme in many signal transduction pathways in the cell.[13] PLC activity is regulated through the action of g-protein coupled receptors (GPCRs). When active, PLC catalyzes the hydrolysis of $PI(4,5)P_2$ into the soluble second messenger inositol-1,4,5-trisphosphate ($I(1,4,5)P_3$) and the membrane bound second messenger diacylglycerol (DAG). These second messengers then initiate the release of intracellular Ca^{2+} stores and promote protein kinase C activation causing amplification of various signaling pathways in the cell.[13]

Furthermore, $PI(4,5)P_2$ serves as the substrate for PI-3-kinase, a key regulatory enzyme associated with the signaling pathways regulating cell growth, cell survival and cell movement.[14] PI-3-kinase catalyzes the phosphorylation of $PI(4,5)P_2$ at the D3 position of the inositol ring to form $PI(3,4,5)P_3$. While $PI(3,4,5)P_3$ is usually found at very low concentrations in a resting cell, high levels of $PI(3,4,5)P_3$ result in the recruitment of protein kinases and phosphatases involved in cell growth and migration signaling pathways to the plasma membrane. Up-regulation of or defects in these pathways has been implicated in certain types of human cancers and diabetes, respectively.[14]

Phosphoinositide phosphatases turn off signaling cascades

While kinases such as PI-3-kinase upregulate phosphoinositide signaling pathways, phosphoinositide phosphatases serve to downregulate these pathways. Phosphoinositide phosphatases are similar to protein tyrosine phosphatases and contain the same conserved $C\text{-}X_5\text{-}R$ catalytic domain.[15] Their involvement in the regulation of phosphoinositides in complex cellular processes including cell growth and development, metabolism, responses to extracellular

signals, membrane trafficking, and apoptosis has expanded the field of phosphoinositide phosphatase research.[15] In particular, much emphasis has been placed on understanding the role of the phosphate and tensin homolog (PTEN), a D3 phosphoinositide phosphatase that selectively dephosphorylates the D3 phosphate group of $PI(3,4,5)P_3$. PTEN is directly involved in the regulation of cell growth and the control of cell size, and mutations in PTEN have been directly related to cancers and genetic diseases.[15] The Sac1 family of phosphoinositide phosphatases has important roles in membrane trafficking, secretion, and cytoskeletal organization, and have shown preference for monophosphorylated PIP substrates.[16] Furthermore, the myotubularin phosphoinositide phosphatases specifically dephosphorylate PI(3)P and/or $PI(3,5)P_2$. In particular, mutations in the myotubularin MTMR2 have been associated with type 4B Charcot-Marie-Tooth syndrome, an inherited demyelating neuropathy.[17]

The growing importance of phosphoinositide phosphatase activity in human health and disease has initiated the development of both *in vitro* and *in vivo* assays to study phosphoinositide phosphatase specificity and activity. Traditionally, radiolabeled ^{32}P or ^{3}H lipid substrates have been used in the study of the phosphoinositide phosphatase activity, but radioactivity assays provide little information about substrate specificity.[18] Furthermore, fluorescent dyes have not been amenable to the *in vitro* study of lipid phosphatases due to the light scattering of lipid suspensions.[19] However, in recent years, the availability and use of fluorescent phospholipids and the development of colorimetric assays that can selectively detect the removal of inorganic phosphate groups, have made it possible to understand more about the specificity and activity of phosphoinositide phosphatases. Dixon and co-workers have pioneered the use of colorimetric assays and fluorescent phospholipids substrates to specifically study phosphoinositide phosphate substrate specificity and phosphatase activity *in vitro*. These two methods have been thoroughly developed and are often used in tandem in order to fully characterize a phosphoinositide phosphatase.[15, 20] Both experimental techniques are described in detail in reference [21]. Until recently, phosphoinositide modulation of membrane proteins and phosphoinositide signaling pathways appeared to be only distantly related through the action of cytosolic lipid kinases and phosphatases. However, the recent discovery of a voltage-gated phosphoinositide phosphatase serves a link between voltage sensing and phosphoinositide signaling

Discovery of a voltage-gated phosphoinositide phosphatase

In 2005, Murata and colleagues reported the isolation and initial characterization of a voltage-gated phosphoinositide phosphatase from the ascidian *Ciona intestinalis*.[22] This 576 amino acid voltage-sensor containing phosphatase was named Ci-VSP and contained sequence homology with both voltage-gated ion channels and phosphatases. Voltage gated ion channel subunits typically contain six transmembrane segments. The first four segments (S1-S4) comprise the voltage-sensing domain, with the S4 segment containing a series of positively charged residues separated by hydrophobic residues. These "charge-carrying" residues move through the membrane electric field in response to changes in voltage across the plasma membrane.[23, 24] S4 movements are then translated into conformational rearrangements in the protein that regulate its function. The fifth and sixth transmembrane segments (S5-S6) of voltage-gated ion channel subunits comprise the pore domain. All voltage-gated ion channels are functional tetramers.

Like voltage gated ion channels, the first 240 amino acids of Ci-VSP form a voltage-sensing domain, comprised of four transmembrane segments (S1-S4), with the fourth segment (S4) containing a series of positively charged residues separated by hydrophobic residues (Figure 3.3). Ci-VSP lacks a pore domain, but instead contains a cytosolic phosphatase domain that has 29.5% sequence identity with the phosphatase and tensin homolog PTEN, a protein and phosphoinositide phosphatase shown to be a putative tumor suppressor protein.[25] Sequence alignments with amino acids 240-576 of Ci-VSP reveal that Ci-VSP contains a catalytic sequence (CX_5R) that is conserved throughout many members of the protein tyrosine phosphatase super family of proteins. Ci-VSP also contains a 16 amino acid sequence linking the VSD and phosphatase domain that contains several basic residues and shares 43% sequence identity with the putative $PI(4,5)P_2$ binding domain located on the N-terminus of PTEN.[26]

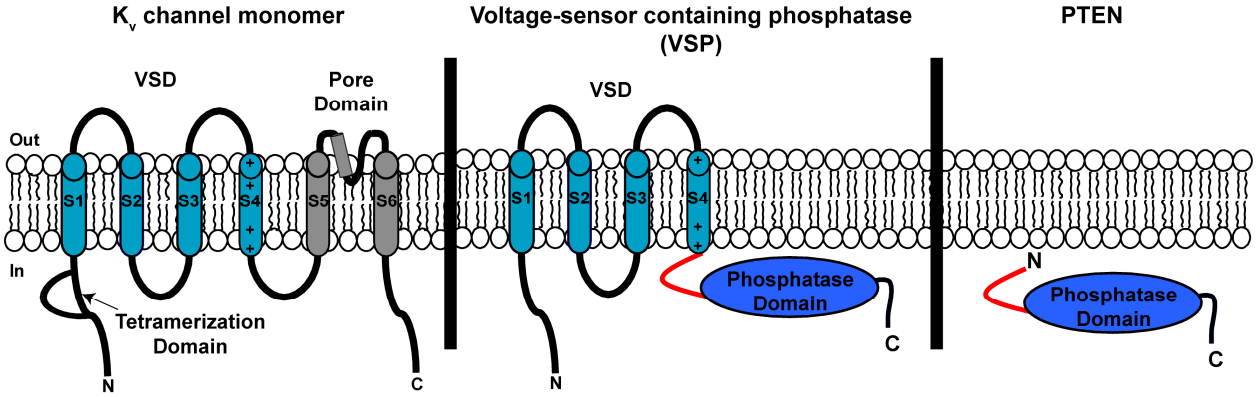

Figure 3.3. Ci-VSP shares homology with voltage gated potassium (K_v) channels and PTEN. Comparison of Ci-VSP topology (middle) with K_v channels (left) and PTEN (right). Ci-VSP contains 4 transmembrane segments (S1-S4) that are homologous to the voltage sensing domain (VSD) of a voltage-gated potassium channel. The cytosolic domain of Ci-VSP shares 29.5% sequence identity with PTEN. Helices are represented by cylinders with VSDs shaded in light blue, pore domains shaded in gray, and phosphatase domains shaded in dark blue. Red line represents putative $PI(4,5)P_2$ binding domain.

Characterization of Ci-VSP VSD movement

To test whether the proposed VSD of Ci-VSP was indeed a voltage sensor, Murata *et al.* expressed either the full length Ci-VSP protein or only the VSD domain in *Xenopus laevis* oocytes and measured gating currents. These currents resembled gating currents of the Shaker voltage-gated potassium channel, a well-studied K_v channel, but the voltage-dependence of Ci-VSP charge movement was shifted almost 100 mV in the positive direction compared with Shaker.[22] Moreover, neutralization of two of the proposed charge carrying residues in the VSD of Ci-VSP eliminated measureable gating currents. These experiments indicated that the four transmembrane segments in Ci-VSP are a functional VSD.

Biochemical studies of Ci-VSP activity

To test whether the proposed phosphatase domain of Ci-VSP was a phosphoinositide phosphatase like PTEN, Murata and co-workers conducted biochemical studies with the isolated Ci-VSP phosphatase domain.[22] Amino acids 240-576 of Ci-VSP share 29.5% sequence homology with PTEN, a D3-phosphoinositide phosphatase that has highest levels of activity against $PI(3,4,5)P_3$. The initial characterization of Ci-VSP activity focused on activity against $PI(3,4,5)P_3$.

Murata and co-workers first used a colorimetric *in vitro* assay involving malachite green that is commonly used to study PTEN phosphatase activity. In this *in vitro* assay, the phosphatase and its proposed substrate are incubated in a buffer containing malachite green dye and ammonium molybdate.[27] The molybdate binds to the inorganic phosphate group and the resulting change in the pH of the solution causes a change in the absorbance of the malachite green, a basic pH indicator, in solution.[28] The resulting phosphomolybdate malachite green complex has a characteristic absorbance at 620 nm and can be monitored as a function of time and in order to determine the efficiency of phosphatase activity.[19] Using the malachite green assay, Murata and co-workers determined the V_{max} (0.292 nmol $min^{-1}\mu g^{-1}$) and K_m (36 μM) for the isolated phosphatase domain of Ci-VSP against $PI(3,4,5)P_3$.[22] The estimated turnover rate for Ci-VSP is 3.2s[29]. These values are similar to those for PTEN (V_{max} = 7.31 nmol $min^{-1}\mu g^{-1}$ and K_m<50μM).[30, 31] Furthermore C363 was identified as the nucleophilic cysteine required for $PI(3,4,5)P_3$ hydrolysis.

To determine the substrate specificity of the isolated Ci-VSP phosphatase domain, thin layer chromatography (TLC) utilizing fluorescently labeled $PI(3,4,5)P_3$ and $PI(4,5)P_2$ was used. The utility of the TLC analysis relies in the ability to determine the specific phosphate group that is hydrolyzed from a multiply phosphorylated phosphoinositide[32] and this approach has been used to determine the substrate specificity of PTEN as well as other phosphoinositide phosphatases.[32] Murata and co-workers showed that the phosphatase domain of Ci-VSP could dephosphorylate $PI(3,4,5)P_3$ to make a bisphosphorylated PIP_2, but the precise identity of this product was not yet determined.[22]

Characterization of voltage-dependent Ci-VSP phosphatase activity in living cells

Traditional methods of assaying voltage-gated ion channel function rely on heterologously expressing the channel in *Xenopus laevis* oocytes or other exogenous systems and then using electrophysiological techniques to precisely vary membrane potential and monitor current flux through the channel. As Ci-VSP is a voltage sensitive protein without a channel, indirect methods of measuring phosphoinositide phosphatase activity were developed. $PI(3,4,5)P_3$ is present in very low concentrations in the plasma membrane, but $PI(4,5)P_2$ is the most abundant PIP in the plasma membrane[1], and since Ci-VSP had been shown to produce some form of PIP_2 *in vitro*, reporters of $PI(4,5)P_2$ were used to study Ci-VSP voltage-dependent activity in cells.

Many classes of ion channels have been shown to be directly modulated by PI(4,5)P2.[5, 11] Murata *et al.* utilized three different $PI(4,5)P_2$ sensitive ion channels to measure the voltage-dependent phosphatase activity of Ci-VSP. The inwardly-rectifying potassium channel $K_{ir}2.1$ (IRK1) has one of the highest recorded specificities and affinities for $PI(4,5)P_2$, which acts as an agonist of channel activity.[33] Murata and co-workers made a point mutation in the putative $PI(4,5)P_2$ binding site (R228Q) to make the channel an effective reporter of Ci-VSP mediated changes in $PI(4,5)P_2$ concentrations.[34] In *Xenopus laevis* oocytes co-expressing Ci-VSP and IRK1-R228Q, membrane depolarization resulted in decreases of $PI(4,5)P_2$ and membrane hyperpolarization resulted in increases of $PI(4,5)P_2$ which were recorded as decreases or increases in IRK1-R228Q current. Similar results were seen using $K_{ir}3.2$ (GIRK) channels and voltage dependent KCNQ2/3 channels, which also show high affinity for $PI(4,5)P_2$ but have different voltage ranges of activation.[34-36]

Murata and co-workers concluded that Ci-VSP was a hyperpolarization activated phosphoinositide phosphatase which catalyzes the hydrolysis of $PI(3,4,5)P_3$ to make $PI(4,5)P_2$ (Figure 3.4). This proposed mechanism of activity opposes the well-characterized mechanism where most voltage-gated ion channels which are activated upon membrane depolarization.[37] Instead, the proposed mechanism of Ci-VSP activity was similar to the action of hyperpolarization-activation cation (I_h) channels.[38]

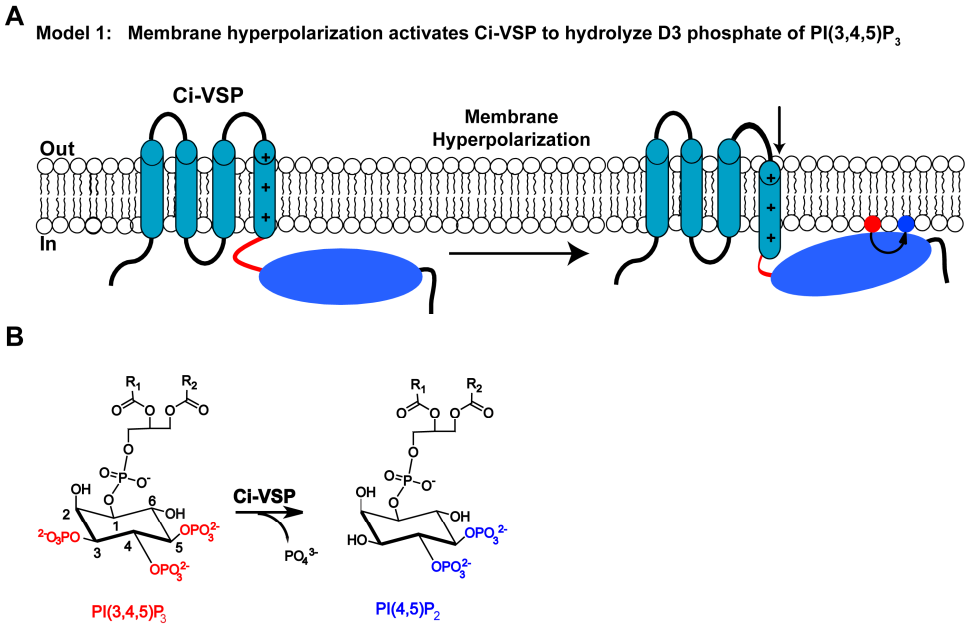

Figure 3.4. Hyperpolarization-activation model for Ci-VSP activity. (A) Cartoon depicting model 1 of Ci-VSP activation, where, upon membrane hyperpolarization, the VSD of Ci-VSP moves through the membrane electric field and activates the Ci-VSP phosphatase domain. **(B)** Proposed Ci-VSP mediated reaction from model 1 in which Ci-VSP acts as a D3-phosphoinositide phosphatase and hydrolyzes $PI(3,4,5)P_3$ to form $PI(4,5)P_2$.

The initial characterization of Ci-VSP voltage-dependent activity did not definitely prove whether Ci-VSP was depolarization or hyperpolarization activated.[22] $PI(3,4,5)P_3$ is a minor

phosphoinositide component of resting plasma membranes with concentrations that are less than 1000 times the concentrations of $PI(4,5)P_2$.[39] If Ci-VSP exclusively hydrolyzed $PI(3,4,5)P_3$ to form $PI(4,5)P_2$, the resulting changes in $PI(4,5)P_2$ would be much smaller than those observed using ion channels reporters of $PI(4,5)P_2$.[22] Furthermore, the discrepancy between the dynamic voltage range of Ci-VSP gating charge movement (roughly 0 mV to +120 mV) and the dynamic voltage range of Ci-VSP-mediated changes in $PI(4,5)P_2$ (-60 mV to +20 mV) suggested that the initial model of Ci-VSP activation did not fully explain recorded Ci-VSP activity. In 2007, Murata and Okamura employed the use of fluorescent reporters of $PI(3,4,5)P_3$ and $PI(4,5)P_2$ and channel reporters of $PI(4,5)P_2$ to determine that Ci-VSP was a depolarization-activated phosphatase.[40]

Fluorescent protein-pleckstrin homology (FP-PH) domain fusions have been used as tools to study phosphoinositide dynamics in living cells. The location of these protein domains shifts from the cytoplasm to the plasma membrane when the inner leaflet of the plasma membrane contains high concentrations of their PIP binding partner. This movement results in increased fluorescence signal at the plasma membrane. As concentrations of the PIP binding partner decrease, the FP-PH protein translocates to the cytosol, resulting in a decrease of fluorescence at the plasma membrane. These changes in fluorescence can be monitored using confocal or total-internal reflection (TIR) fluorescence microscopy.[41] Murata and Okamura co-expressed Ci-VSP with a fluorescently-tagged PH domain from phospholipase C-delta1 ($GFP\text{-}PH_{PLC}$) as a reporter of $PI(4,5)P_2$ in *Xenopus laevis* oocytes and used confocal microscopy to monitor Ci-VSP mediated changes in $PI(4,5)P_2$. They found that membrane depolarization resulted in Ci-VSP mediated decreases in $PI(4,5)P_2$ which was in agreement with previous experiments using $PI(4,5)P_2$ sensitive ion channels as reporters of Ci-VSP activity.[22] However, this result implied that Ci-VSP might also hydrolyze $PI(4,5)P_2$.

To directly test the activity of Ci-VSP against $PI(3,4,5)P_3$ in cells, Murata and Okamura co-expressed Ci-VSP with a fluorescently tagged PH domain from Brutons' tyrosine kinase ($GFP\text{-}PH_{Btk}$) shown to be a specific reporter of $PI(3,4,5)_3$ dynamics in living cells.[42, 43] To increase levels of $PI(3,4,5)P_3$ in the membrane, endogenous insulin receptors were stimulated resulting in upregulation of PI-3-kinase activity. In the presence of Ci-VSP, membrane depolarization caused a decrease in membrane fluorescence of the $GFP\text{-}PH_{Btk}$ probe and therefore a decrease in levels of $PI(3,4,5)P_3$ in the plasma membrane. This result supported previous biochemical data demonstrating that Ci-VSP hydrolyzes $PI(3,4,5)P_3$.[22] The dynamic voltage range of Ci-VSP mediated hydrolysis of $PI(3,4,5)P_3$ was not determined.

However, $PI(4,5)P_2$ might not be the biologically relevant product as depolarization also causes the Ci-VSP mediated hydrolysis of $PI(4,5)P_2$. The resulting PIP product was not identified, but was most likely PI(4)P, which is natively at concentrations equal to that of $PI(4,5)P_2$ in the inner leaflet of the plasma membrane.[4] PI(4)P serves as the major substrate for PI-5-kinases which are responsible for maintaining high levels of $PI(4,5)P_2$ in the plasma membrane.[6] To confirm that depolarization activated Ci-VSP to hydrolyze $PI(4,5)P_2$, Murata and Okamura returned to $PI(4,5)P_2$ ion channels as reporters of Ci-VSP activity. Coexpressing Ci-VSP with either $K_{ir}2.1$ or $K_{ir}3.2$ channels as high or low affinity reporters for $PI(4,5)P_2$, resulted in depolarization induced K_{ir} current run down that was attributed to Ci-VSP hydrolysis

of $PI(4,5)P_2$. The kinetics of Ci-VSP mediated $PI(4,5)P_2$ hydrolysis was voltage dependent with greater depolarizations leading to faster rates of $PI(4,5)P_2$.[40]

Murata and Okamura also used $PI(4,5)P_2$ sensitive KCNQ2/3 channels as reporters of Ci-VSP activity and demonstrated that depolarizations up to +100mV could elicit Ci-VSP-mediated hydrolysis of $PI(4,5P)_2$. This voltage range of activity more closely corresponded to the gating charge movement of Ci-VSP previously reported.[22, 40] Murata and Okamura concluded that Ci-VSP was a depolarization activated phosphatase (Figure 3.5). Like voltage-gated K^+ channels which translate changes in membrane potential into the controlled gating of a pore domain, Ci-VSP undergoes voltage-dependent conformational changes to control a phosphatase domain.

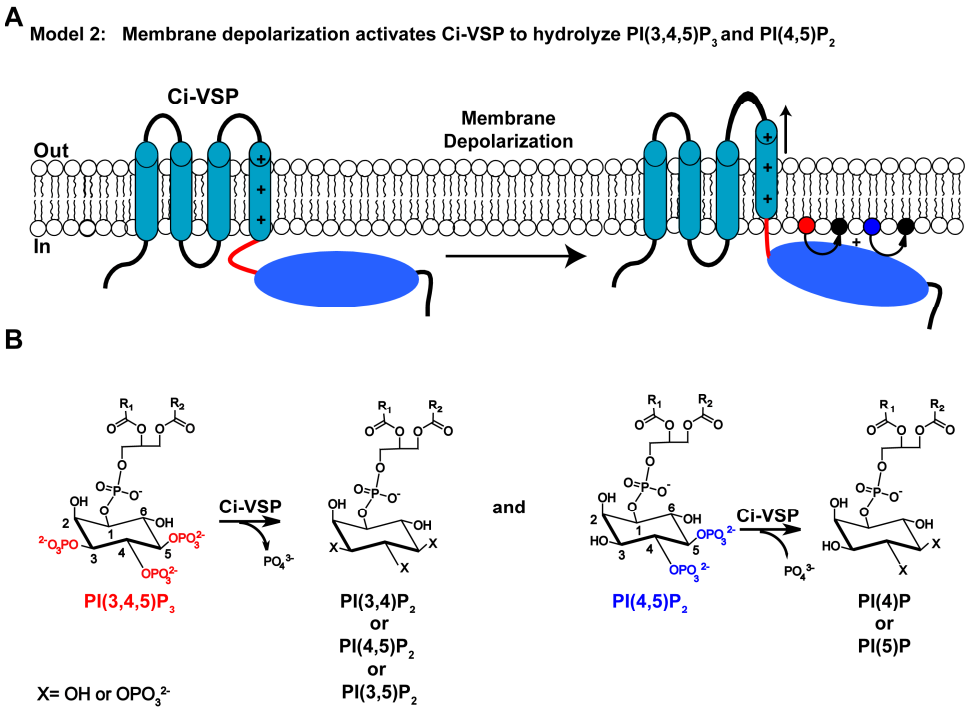

Figure 3.5. Depolarization-activation model for Ci-VSP activity. (A) Cartoon depicting model 2 of Ci-VSP activation, where, upon membrane depolarization, the VSD of Ci-VSP moves through the membrane electric field and activates the Ci-VSP phosphatase domain. **(B)** Proposed Ci-VSP mediated reactions from model 2 in which Ci-VSP acts as a D3- or D4- or D5-phosphoinositide phosphatase and hydrolyzes both $PI(3,4,5)P_3$ and $PI(4,5)P_2$ to form unknown products.

Ci-VSP acts as a D5-phosphoinositide phosphatase *in vitro* and in living cells

In 2008, Iwasaki and co-workers published a comparative biochemical study of the substrate specificities of PTEN and the Ci-VSP phosphatase domain.[44] PTEN specifically removed the D3 phosphate group from multiple substrates including $PI(3,4,5)P_3$, $PI(3,4)P_2$ and $PI(3,5)P_2$ with $PI(3,4,5)P_3$ being the most biologically relevant substrate.[26] Recent *in vivo*

experiments had shown that Ci-VSP is able to hydrolyze both $PI(3,4,5)P_3$ and $PI(4,5)P_2$[40] asking the question whether the active site of Ci-VSP could accommodate different PIP substrates.

Using the malachite green assay, Iwasaki *et al.* showed that PTEN had the greatest specificity for $PI(3,4,5)P_3$ and some activity against $PI(3,4)P_2$ and $PI(3,5)P_2$, but not monophosphorylated PIPs.[44] The cytosolic domain of Ci-VSP was active against a variety of PIPs including $PI(3,4,5)P_3$, $PI(4,5)P_2$, $PI(3,4)P_2$ and $PI(3,5)P_2$.[44] The specificity of Ci-VSP was highest for $PI(3,4,5)P_3$, being twice that for $PI(4,5)P_2$. Interestingly, the $PI(3,4,5)P_3$ specificity of Ci-VSP was almost 10-fold less than the $PI(3,4,5)P_3$ specificity of PTEN. As $PI(4,5)P_2$ is the most common PIP in the plasma membrane[4], Iwasaki *et al.* suggested that Ci-VSP hydrolysis of $PI(4,5)P_2$ might be the more biologically relevant activity.[44]

By incorporating ^{32}P at either the D4 or D5 position of the inositol ring of $PI(4,5)P_2$, incubating the cytosolic domain of Ci-VSP with both substrates, and conducting TLC experiments coupled with autoradiography, Iwasaki *et al.* demonstrated that Ci-VSP dephosphorylates the 5-phosphate group of $PI(4,5)P_2$. The potential D3-phosphatase activity of Ci-VSP against $PI(3,4)P_2$ or $PI(3,5)P_2$ was not determined.

The active sites amino acid sequences of Ci-VSP and PTEN only differ at one position where Ci-VSP has a glycine (G365) and PTEN has an alanine (A126) (Figure 3.6).

```
PTEN     92 DH.....AIHCKAGKGRTG
Ci-VSP  331 DH.....AIHCKGGKGRTG
```

Figure 3.6. Comparison of PTEN and Ci-VSP active sites. Partial sequence alignment of active site residues in PTEN (top) and Ci-VSP(bottom). Areas of sequence identity are shaded in blue.

Iwasaki *et al.* proposed that G365 in Ci-VSP was crucial for Ci-VSP's preferential D5-phosphatase activity and tested the substrate specificity of Ci-VSP G365A using TLC analysis. Ci-VSP-G365A showed activity against $PI(3,4)P_2$, $PI(3,5)P_2$ inferring that this mutant had D3 phosphatase activity like PTEN. Ci-VSP-G365A did not have significant activity against $PI(4,5)P_2$ suggesting that an alanine at position 365 prevents D5-phosphatase activity. Interestingly, Ci-VSP-G365A did not show significant activity against $PI(3,4,5)P_3$. Iwasaki and co-workers also stated that Ci-VSP could dephosphorylate both the D3 and D5 phosphate group from $PI(3,4,5)P_3$, but did not present any data to confirm their statement.[44]

To test the hypothesis that Ci-VSP G365A did not hydrolyze $PI(4,5)P_2$ *in vivo*, Iwasaki *et al*. co-expressed Ci-VSP-G365A with either $K_{ir}3.2$ or GFP-PH_{PLC} as reporters of $PI(4,5)P_2$ in *Xenopus laevis* oocytes. Membrane depolarization caused wild type Ci-VSP to deplete $PI(4,5)P_2$ and reduce $K_{ir}3.2$ currents and decrease GFP-PH_{PLC} membrane fluorescence. Membrane depolarization did not cause any Ci-VSP-G365A mediated changes in Kir3.2 currents or decreases in GFP-PH_{PLC} membrane fluorescence suggesting that this mutant did not hydrolyze $PI(4,5)P_2$. The effects of the G365A mutation on Ci-VSP activity against $PI(3,4,5)P_3$ were not tested. Iwasaki *et al.* concluded that G365 in Ci-VSP can allow for both the D3 and D5 phosphoinositide phosphatase activity of Ci-VSP.

Halaszovich *et al.* used total internal reflection fluorescence (TIRF) microscopy to study Ci-VSP activity in Chinese Hamster Ovary (CHO) cells. By coexpressing Ci-VSP with FP-PH domain reporters of each possible Ci-VSP substrate and product, and combining TIRF microscopy and patch clamping techniques, they determined that Ci-VSP acts as a depolarization activated dual function D5 phosphoinositide phosphatase (Figure 3.7).[45] Halaszovich *et al.* demonstrated that membrane depolarization activates Ci-VSP to hydrolyze $PI(4,5)P_2$ and produce PI(4)P. This confirmed the previous biochemical data suggesting that Ci-VSP was a D5 phosphoinositide phosphatase.[44] Also, membrane depolarization caused a Ci-VSP mediated decrease in $PI(3,4,5)P_3$ with concomitant generation of $PI(3,4)P_2$. This behavior is similar to the reported phosphoinositide phosphatase activity of the PTEN homolog PLiP which bears the same CX_5R catalytic motif as PTEN, yet preferentially hydrolyzes the D5 phosphate of PI(5)P.[31]

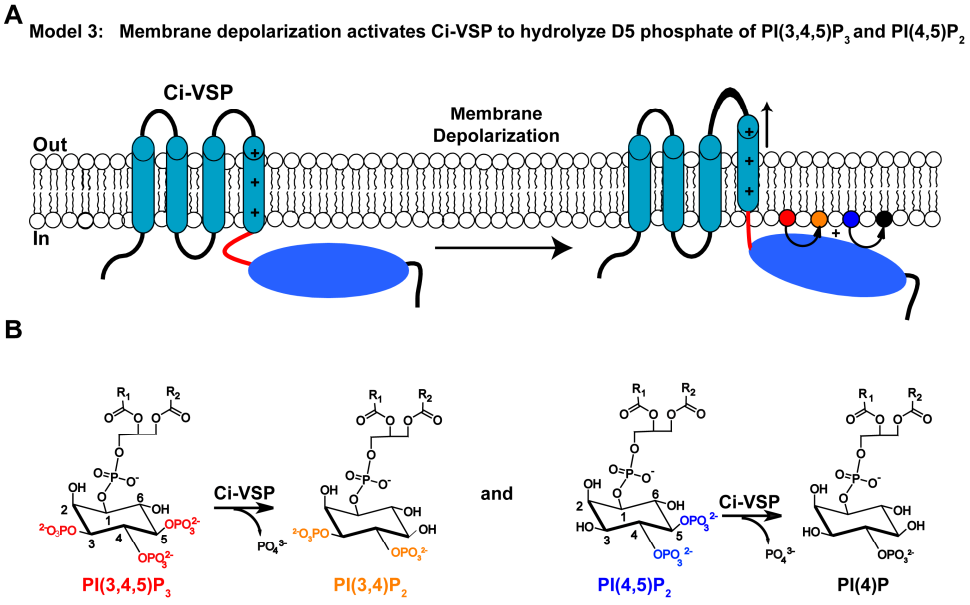

Figure 3.7. Depolarization activated D5 phosphoinositide phosphatase model for Ci-VSP activity. (A) Cartoon depicting model 3 of Ci-VSP activation, where, upon membrane depolarization, the VSD of Ci-VSP moves through the membrane electric field and activates the Ci-VSP phosphatase domain. **(B)** Proposed Ci-VSP mediated reactions from model 3 in which Ci-VSP acts as a D5 phosphoinositide phosphatase and hydrolyzes $PI(3,4,5)P_3$ to form $PI(3,4)P_2$ and hydrolyzes $PI(4,5)P_2$ to form PI(4)P.

Ci-VSP subunit organization and electrochemical coupling

Kohout *et al.* demonstrated that Ci-VSP is a functional monomer that undergoes multiple conformational states which control lipid phosphatase activity (Figure 3.8).[46] This work is described in detail in chapter 4 of this dissertation.

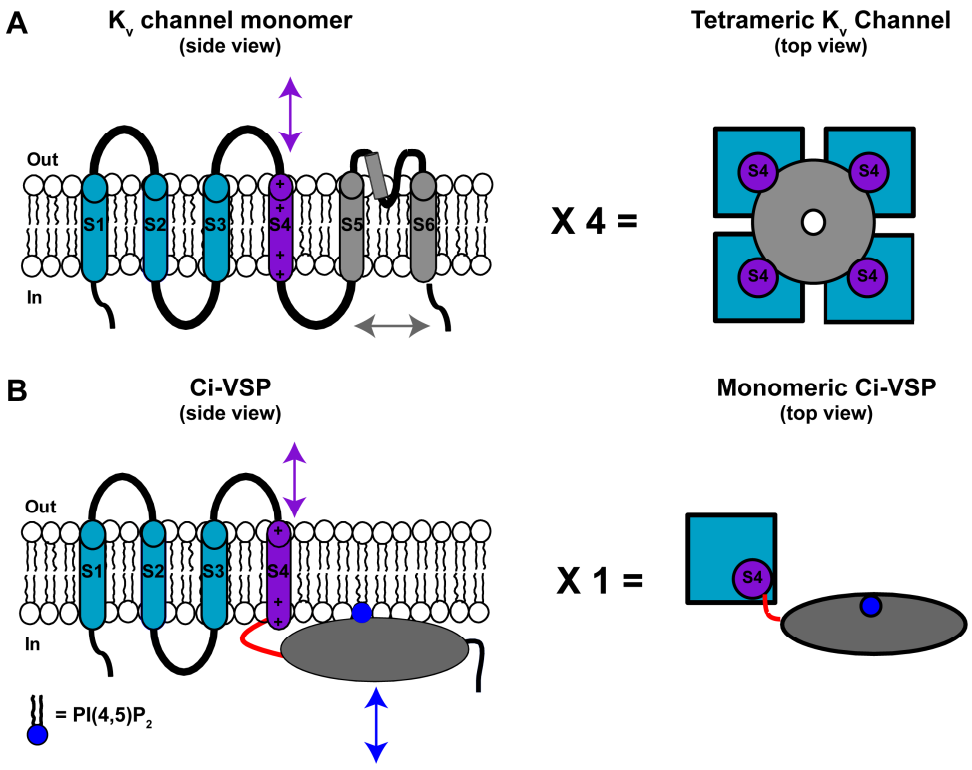

Figure 3.8. Model for coupling VSDs to effector domains. **(A)** Side and top views of K_v channel monomer (left) and tetrameric K_v channel (right). **(B)** Side and top views of Ci-VSP monomer (left) and functional monomeric phosphatase (right). $PI(4,5)P_2$ in dark blue). In both **(A)** and **(B)**, arrows indicate both S4 and "gating" motions. Figure adapted from[46].

Other groups have demonstrated the tight coupling between the VSD and catalytic domains in Ci-VSP where mutations in either domain affect the function of the other.[40, 47-49] Much research has focused on understanding the role of the 16 amino acid linker connecting the two domains in Ci-VSP. This region contains a series of basic amino acids that resemble the putative $P(4,5)P_2$ binding motif in the N-terminus of PTEN.[30] Deletions or charge neutralizations in the linker region in Ci-VSP reduce or eliminate Ci-VSP phosphatase activity.[22, 48, 49] Recently, Kohout *et al.* identified a late stage of VSD motion that requires both $PI(4,5)P_2$ and basic residues in the linker region.[48] They proposed that both $PI(4,5)P_2$ and these basic residues are responsible for stabilizing the active state of Ci-VSP. As Ci-VSP depletes $PI(4,5)P_2$ from the plasma membrane, the active state becomes destabilized which uncouples the two domains and turns off the enzyme. This work is described in detail in Appendix 1 of this dissertation and reference [48].

Functional characterization of Ci-VSP orthologs

Ci-VSP and other phosphoinositide phosphatases share a highly conserved catalytic site motif (CX_5R) which places these proteins in the protein tyrosine phosphatase (PTP) super family. Members of the PTP family are key regulators of virtually all cellular processes.[50]

Kumanovics and colleagues first reported the convergence between voltage sensing domains and phosphoinositide phosphatases in 2003. They suggested that the voltage-sensor could be a modular domain and that orthologs of PTEN which contained four transmembrane domains in addition to a PTEN-like phosphatase domain may be voltage sensitive proteins.[51] Indeed, the functional characterization of Ci-VSP indicates that other PTEN orthologs may be voltage-sensitive. Basic Local Alignment Search Tool (BLAST) analyses of Ci-VSP and its orthologs indicate a high degree of sequence conservation across numerous species with almost identical catalytic site sequences (Figure 3.9).[52]

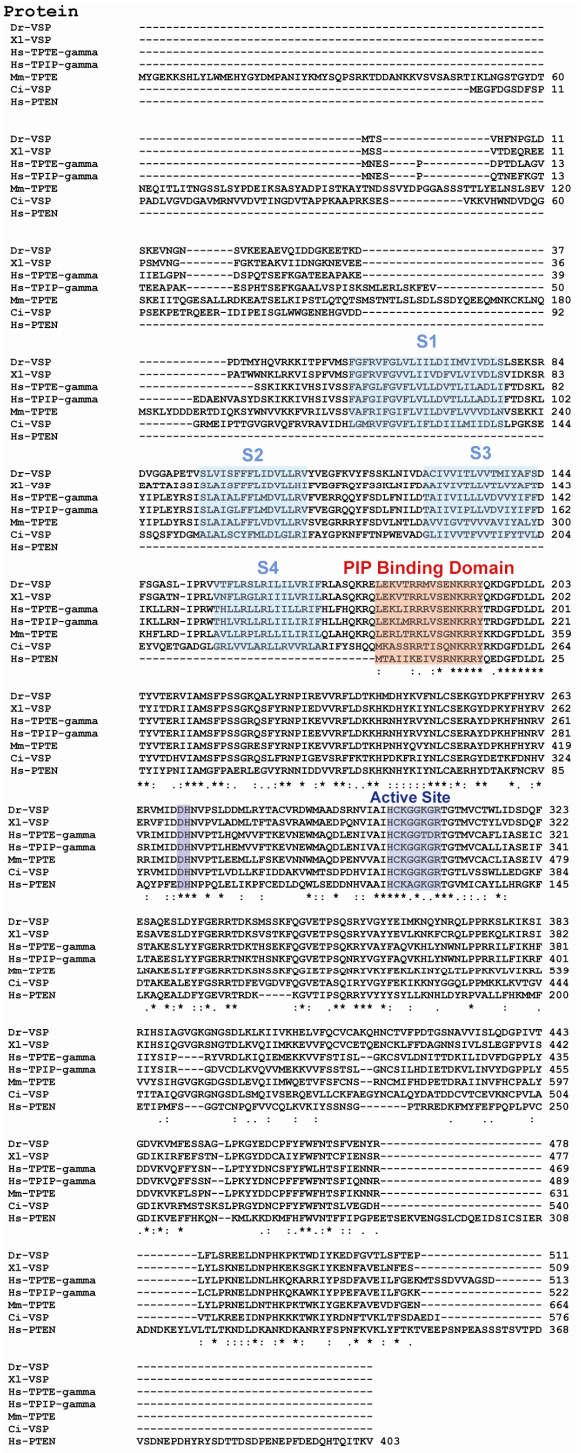

Figure 3.9. Sequence alignment of VSPs. Alignment performed using CLUSTALW 2.1 (http://www.ebi.ac.uk/Tools/clustalw/index.html). Transmembrane segments predicted using DAS Transmembrane Prediction Server (http://www.sbc.su.se/~miklos/DAS/maindas.html). Asterisk(*) indicates sequence identity. Dots (. or :) indicate sequence similarity.

To date, two other voltage-gated phosphoinositide phosphatases have been reported. Hossain *et al*. characterized a voltage sensor containing phosphatase from *Danio rario*, which they named Dr-VSP.[47] Like Ci-VSP, Dr-VSP shows gating currents and voltage dependent phosphoinositide phosphatase activity against $PI(3,4,5)P_3$ *in vitro* and $PI(4,5)P_2$ *in vivo*. However, gating current experiments revealed that the voltage-dependency of Dr-VSP is shifted almost 40 mV to the right and voltage dependent transitions are slower when compared with Ci-VSP.[47]

Two groups have reported the discovery and characterization of a VSP in the *Xenopus laevis* genome, Xl-VSP, which shares 40% overall sequence identity with Ci-VSP.[53, 54] Xl-VSP has been shown to dephosphorylate $PI(4,5)P_2$ *in vivo*, but further characterization of its voltage dependency or substrate specificity has not yet been reported.

Ci-VSP orthologs are also found in mammals and these proteins possess four transmembrane segments resembling a VSD and a cytosolic phosphatase domain resembling PTEN.[52] This group of proteins was named the transmembrane phosphatase and tensin homology (TPTE) family and contains 3 putative VSPs: transmembrane phosphatase with tensin homology (TPTE or PTEN2), human transmembrane phosphoinositide 3-phosphatase and tensin homolog 2 (TPIP or TPTE2), and mouse transmembrane phosphatase with tensin homology (mTPTE or PTEN2).[55] While the voltage-dependent activity of these proteins has yet to be determined, several groups have characterized their tissue distribution and membrane localization and utilized biochemical techniques to characterize the activity of the isolated phosphatase domains. These results are summarized in Table 3.1. Interestingly, the native human TPTEγ whose active site differs by two amino acids from other putative VSPs, is not active against a wide range of PIPs (N. Leslie, personal communication). However, the enzyme can be "reactivated" by mutating the active site residues to match those in PTEN, and this "reactivated" TPTE shows activity against $PI(3,4,5)P_3$.[56] Further functional characterizations of putative VSPs in living cells are needed to learn more about the role of membrane voltage in regulating phosphoinositide phosphatase activity.

Table 3.1. Characterization of confirmed and putative VSPs. Abbreviations: plasma membrane (PM), Endoplasmic reticulum (ER). NR indicates information has not been reported.

Organism	Protein	Tissue distribution	Membrane localization	Substrate(s)	Product(s)	Reference(s)
Ciona intestinalis	Ci-VSP	Testis (sperm tails), neural complex	PM	$PI(3,4,5)P_3$ $PI(4,5)P_2$	$PI(3,4)P_2$ PI(4)P	[22, 40, 45]
Danio rario	Dr-VSP	testis	PM	$PI(3,4,5)P_3$ $PI(4,5)P_2$	NR	[29, 47]
Xenopus laevis	Xl-VSP	testis	NR	$PI(4,5)P_2$	NR	[53, 54]
Homo sapiens	TPTEγ (PTEN 2γ)	testis	PM and Golgi	NR	NR	[55, 57, 58]
Homo sapiens	TPTEγ-R	NR	NR	$PI(3,4,5)P_3$	NR	[56]
Homo sapiens	TPIPγ (TPTE2γ)	testis, brain, stomach	ER and Golgi	NR	NR	[55, 58]
Mus musculus	TPTE (PTEN 2)	Testis, neural tissue	Golgi	$PI(3,5)P_2$ $PI(3,4,5)P_3$ PI(3)P $PI(3,4)P_2$	NR	[59, 60]

Physiological significance of VSPs

All confirmed and putative VSPs show high levels of expression in the testis (Table 3.1), suggesting that these proteins may play roles in spermatogenesis, development, and function.[29, 52] To further study the role of VSPs in fertilization, Ratzan and Jaffe recently proposed the use of Xl-VSP to study the role of voltage sensitive phosphatases in sperm-egg fusion in transgenic frogs.[54] There have also been recent reports demonstrating the role of phosphoinositide signaling pathways in the early events of mammalian fertilization.[61] As VSPs are expressed in the testis, they may play a role in the signal transduction pathways underlying sperm capacitation, the process by which the sperm becomes competent to fertilize the egg.[62] Potassium (Ksper) and calcium (Catsper) channels expressed in sperm have recently been reported to play crucial roles in sperm capacitation and these effects have been directly studied using sperm patch clamping techniques.[63] Ksper, is responsible for capacitation-induced sperm membrane hyperpolarization and has recently been shown to be directly activated by $PI(4,5)P_2$.[64] VSPs may serve as regulators of Ksper, where VSP mediated hydrolysis of $PI(4,5)P_2$ may decrease Ksper activity and slow the process of capacitation.

Furthermore, VSPs may be involved in the fast block to polyspermy, an electrically mediated process by which membrane depolarization of an already fertilized egg prevents a second sperm from fusing with the egg membrane.[65] The resulting depolarization of the sperm membrane may activate VSPs to reduce $PI(4,5)P_2$ levels and down-regulate capacitation

signaling pathways. Further experiments in both heterologous and native systems will reveal the role of VSPs in regulating sperm function.

Development of Ci-VSP-based optical probes of membrane voltage

Understanding how activity flows through neural circuits is critical for understanding sensory processing, motor control and memory formation. A key breakthrough would be the development of an optical voltage indicator that can be targeted to specific neurons. The Isacoff lab reported the first use of FlaSH, a fusion between the voltage sensitive Shaker channel and GFP, that serves as a genetically encoded optical voltage reporter.[66] Other channel-GFP sensors followed, but all suffer from two major problems: i) even if made non-conducting with a mutation, their expression in neurons will perturb function because they will co-assemble with native subunits to form the multi-subunit functional channels, and ii) currently available voltage sensors like FlaSH have limited applicability in the study of neuronal processes due to their low expression levels in mammalian systems, low targetability to neuronal membranes, and low signal-noise ratios.[67, 68]

Because Ci-VSP is a monomer[46] and is foreign to mammalian cells, it is unlikely to interact with native proteins. Furthermore, substitution of the S4 segment of Ci-VSP for the S4 segment of a voltage-gated potassium channel can reconstitute ion channel gating, which demonstrates the portability of this motiff.[69] Several research groups have taken advantage of the unique properties of the Ci-VSP VSD to create new classes of genetically encoded voltage-sensitive fluorescent proteins (VSFPs) to measure membrane voltage. These sensors have been extensively reviewed in reference [70]. These probes combine a sensor, in this case the voltage sensing domain of Ci-VSP, which undergoes conformational changes in response to membrane voltage, with a fluorescent protein reporter whose optical output is modulated by sensor movement (Figure 3.10). These probes demonstrate the transferability of Ci-VSP voltage sensitivity to other proteins, and open many opportunities to control protein function using voltage.

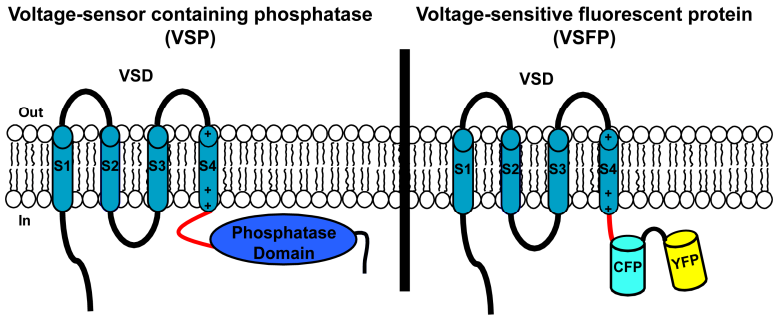

Figure 3.10. Ci-VSP based fluorescent voltage sensors. Cartoon showing construction of optical probes of membrane voltage (VSFPs) based on Ci-VSP. In these probes, the phosphatase domain of Ci-VSP is replaced with a pair of fluorescent proteins whose signal is dependent on Ci-VSP VSD movement.

VSPs as reversible tools to study PI(4,5)P_2 ion channel interactions

Determination of the voltage range and substrate specificity of Ci-VSP and its orthologs has allowed for the use of these proteins as rapid, tunable, and reversible manipulators of phosphoinositide concentrations in living cells. In particular, Ci-VSP and it orthologs have been used to manipulate PI(4,5)P_2 concentrations at the plasma membrane to study the direct interactions of PI(4,5)P_2 with ion channels in the context of living cells (Figure 3.11). Many classes of ion channels are either directly regulated by PI(4,5)P_2 or modulated by PIP signaling cascades that change PI(4,5)P_2 concentrations at the plasma membrane.[5]

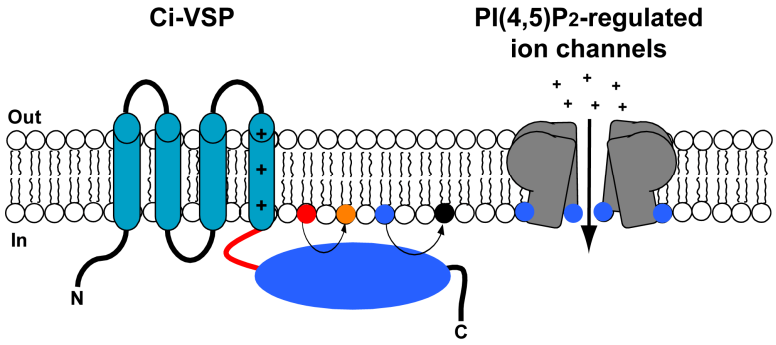

Figure 3.11. Ci-VSP as a reversible tool for studying PI(4,5)P_2 regulated ion channels. Cartoon showing how Ci-VSP activity can used to manipulate PI(4,5)P_2 concentrations at the plasma membrane to aid in the study of PI(4,5)P_2 regulation of ion channels.

Klein *et al.* used Ci-VSP as a tool to reversibly remove PI(4,5)P_2 from the plasma membrane to demonstrate that PI(4,5)P_2 was endogenous lipid regulator of the transient receptor potential vanilloid-type1 (TRPV1) channel, an important channel in the transduction of painful thermal and chemical stimuli.[71] The results of this study indicate that Ci-VSP can be further used as a valuable tool to manipulate and study the influence of phosphoinositides on the molecular basis of pain perception.[72]

Falkenburger *et al.* used Dr-VSP as a tool to develop kinetic models[73, 74] for the synthesis of PI(4,5)P_2 and its interactions with KCNQ 2/3 channels which help control neuronal excitability.[75] This work demonstrates that VSPs can be valuable tools in the study of the mechanisms that govern PI(4,5)P_2 availability at the plasma membrane without production of other secondary messengers such as DAG and I(1,4,5)P_3.

VSPs offer two advantages over recently reported chemically inducible systems for manipulating phosphoinositide concentrations at the plasma membrane.[76, 77] Chemically inducible PIP manipulation systems rely on rapamycin induced heterodimerization of FK506 binding protein (FKBP) and the rapamycin binding fragment of mTOR (FRB). A plasma membrane localization sequence is fused to FRB and a cytosolic D5 phosphoinositide phosphatase specific for PI(4,5)P_2 is fused to the FKBP construct. Upon application of rapamycin, FRB and FKBP heterodimerize to bring the phosphatase to the membrane and catalyze the chronic depletion of PI(4,5)P_2. The first advantage of VSP-induced changes in PIP concentrations is that they are controllable and reversible, while chemically inducible systems are irreversible. Secondly, from an experimental standpoint, VSPs are single proteins that are

not native to most cell membranes and can be easily controlled using traditional electrophysiology techniques while chemically inducible systems require optimization of expression of two protein constructs. Furthermore, the application of rapamycin may inhibit cellular processes including cytoskeletal organization, transcription and protein synthesis.[78]

Ci-VSP and its orthologs can be invaluable tools in the determination of phosphoinositide regulators of ion channels and the dissection of complicated phosphoinositide signaling pathways.

Room for improvement

As Ci-VSP has been shown to change at least four different PIP concentrations upon membrane depolarization, there is still much work to be done to improve its utility as a tool for studying phosphoinositide mediated processes. Mutagenesis studies directed at limiting Ci-VSP substrate specificity to a single substrate would allow this enzyme to be used as a tool to precisely study the effects of a single PIP. Efforts toward these goals are described in chapter 5 of this dissertation. Furthermore, the creation of chimeric proteins which fuse the Ci-VSP VSD to a PIP phosphatase with known substrate specificity may allow for the creation of a family of voltage-sensitive enzymes with a wide range of substrate specificities that could be used for studying specific PIP pathways.

Conclusions

The discovery and characterization of Ci-VSP and its orthologs offers new insights into the coupling between voltage sensing domains and effectors, provides new insights into the interplay between changes in membrane voltage and phosphoinositide signaling pathways, and allows for the development of new tools to dissect complex neural circuits and phosphoinositide signaling cascades. Further research on the VSP family of proteins will no doubt lead to a better understanding of the general mechanisms governing voltage-regulation of proteins. Furthermore, VSP-based tools will aid in studying the role phosphoinositide signaling pathways in cellular homeostasis and disease states.

References

1. Di Paolo, G.; De Camilli, P., Phosphoinositides in cell regulation and membrane dynamics. *Nature* **2006,** 443, 651.

2. Niggli, V., Regulation of protein activities by phosphoinositide phosphates. *Annu. Rev. Cell Dev. Biol.* **2005,** 21, 57-79.

3. Tolias, K., Cantley, LC, Pathways for phosphoinositide synthesis. *Chem. Phys. Lipids* **1999,** 98, 69-77.

4. Lemmon, M. A., Phosphoinositide recognition domains. *Traffic* **2003,** 4, (4), 201-213.

5. Suh, B.-C.; Hille, B., PIP_2 is a necessary cofactor for ion channel function: How and why? *Annual Review of Biophysics* **2008,** 37, (1), 175-195.

6. Roth, M. G., Phosphoinositides in constitutive membrane traffic. *Physiol. Rev.* **2004,** 84, (3), 699-730.

7. Tolias, K. F.; Cantley, L. C., Pathways for phosphoinositide synthesis. *Chem. Phys. Lipids.* **1999,** 98, (1-2), 69-77.

8. Leslie, N. R.; Downes, C. P., PTEN: The down side of PI 3-kinase signaling. *Cell. Signal.* **2002,** 14, (4), 285-295.

9. McLaughlin, S.; Wang, J.; Gambhir, A.; Murray, D., PIP_2 and proteins: Interactions, organization, and information flow. *Annu. Rev. Biophys. Biomol. Struct.* **2002,** 31, (1), 151-175.

10. Várnai, P.; Balla, T., Visualization and manipulation of phosphoinositide dynamics in live cells using engineered protein domains. *Pflügers Archiv European Journal of Physiology* **2007,** 455, (1), 69-82.

11. Gamper, N.; Shapiro, M. S., Regulation of ion transport proteins by membrane phosphoinositides. *Nat. Rev. Neurosci.* **2007,** 8, (12), 921-934.

12. Gamper, N.; Shapiro, M. S., Target-specific PIP_2 signaling: how might it work? *The Journal of Physiology* **2007,** 582, (3), 967-975.

13. Rhee, S. G., Regulation of phosphoinositide-specific phospholipase C. *Annu. Rev. Biochem.* **2001,** 70, (1), 281-312.

14. Cantley, L. C., The phosphoinositide 3-kinase pathway. *Science* **2002,** 296, (5573), 1655-1657.

15. Taylor, G., Dixon, JE, PTEN and myotubularins: families of phosphoinositide phosphatases. *Methods Enzymol* **2003,** 366, 43-56.

16. Wishart, M., Taylor, GS, Slama, JT, Dixon, JE, PTEN and myotubularin phosphoinositide phosphatases: bringing bioinformatics to the lab bench. *Curr Opin Cell Biol* **2001,** 13, 172-181.

17. Robinson, F., Dixon, JE, The phosphoinositide-3-phosphatase MTMR2 Associates with MTMR13, a membrane-associated pseudophosphatase also mutated in Type 4B Charcot-Marie-Tooth Disease. *J. Biol. Chem.* **2005,** 280, (36), 31699-31707.

18. Gray, A., Olsson, H, Batty, IH, Priganica, L, Downes, CP, Nonradioactive methods of the assay of phosphoinositide 3-kinases and phosphoinositide phosphatases and selective detection of signaling lipids in cell and tissue extracts. *Anal. Biochem.* **2003,** 313, 234-245.

19. Maehama, T., Taylor, GS, Slama, JT, Dixon, JE, A sensitive assay for phosphoinositide phosphatases. *Anal. Biochem.* **2000,** 279, 248-250.

20. Murata, Y., Iwasaki, H, Sasaki, M, Inaba, K, Okumura, Y, Phosphoinositide phosphatase activity coupled to an intrinsic voltage sensor. *Nature* **2005,** 435, 1239-1243.

21. Taylor, G., Dixon, JE, Assaying phosphoinositide phosphatases. *Methods Mol. Biol.* **2004,** 284, 217-227.

22. Murata, Y., et al., Phosphoinositide phosphatase activity coupled to an intrinsic voltage sensor. *Nature* **2005,** 435, (7046), 1239-1243.

23. Aggarwal, S. K.; MacKinnon, R., Contribution of the S4 segment to gating charge in the Shaker K^+ channel. *Neuron* **1996,** 16, (6), 1169-1177.

24. Papazian, D. M., et al., Electrostatic interactions of S4 voltage sensor in Shaker K^+ channel. *Neuron* **1995,** 14, (6), 1293-1301.

25. Leslie, N. R.; Maccario, H.; Spinelli, L.; Davidson, L., The significance of PTEN's protein phosphatase activity. *Adv. Enzyme Regul.* **2009,** 49, (1), 190-196.

26. Maehama, T.; Dixon, J. E., The tumor suppressor, PTEN/MMAC1, dephosphorylates the lipid second messenger, phosphatidylinositol 3,4,5-trisphosphate. *J. Biol. Chem.* **1998,** 273, (22), 13375-13378.

27. Martin, B., Pallen, CJ, Wang, JH, Graves, DJ, Use of flourinated tyrosine phosphatases to probe the substrate specificity of the low molecular weight phosphatase activity of calcineurin. *J. Biol. Chem.* **1985,** 260, 14932-14937.

28. Quan, A., Robinson, PJ, Rapid purification of native dynamin I and colorimetric GTPase assay. *Methods Enzymol* **2005,** 404, 556-69.

29. Okamura, Y., Biodiversity of voltage sensor domain proteins. *Pflügers Archiv European Journal of Physiology* **2007,** 454, (3), 361-371.

30. Maehama, T.; Taylor, G. S.; Dixon, J. E., PTEN and myotubularin: novel phosphoinositide phosphatases. *Annu. Rev. Biochem.* **2001,** 70, 247-79.

31. Pagliarini, D. J.; Worby, C. A.; Dixon, J. E., A PTEN-like phosphatase with a novel substrate specificity. *J. Biol. Chem.* **2004,** 279, (37), 38590-38596.

32. Rudge, S., Anderson, DM, Emr, SD, Vacuole size control: Regulation of PtdIns(3,5) P_2 levels by vacuole-associated Vac14-Fig4 complex, a Ptd(3,5) P_2-specific phosphatase. *Mol. Bio. Cell* **2004,** 15, 24-36.

33. Rohacs, T.; Chen, J.; Prestwich, G. D.; Logothetis, D. E., Distinct specificities of inwardly rectifying K^+ channels for phosphoinositides. *J. Biol. Chem.* **1999,** 274, (51), 36065-36072.

34. Zhang, H., et al., Activation of inwardly rectifying K^+ channels by distinct PtdIns(4,5)P_2 interactions. *Nat. Cell Biol.* **1999,** 1, (3), 183-8.

35. Zhang, H., et al., PIP_2 activates KCNQ channels, and its hydrolysis underlies receptor-mediated inhibition of M currents. *Neuron* **2003,** 37, (6), 963-975.

36. Huang, C.-L.; Feng, S.; Hilgemann, D. W., Direct activation of inward rectifier potassium channels by PIP_2 and its stabilization by $G_{\beta\gamma}$. *Nature* **1998,** 391, (6669), 803-806.

37. Tombola, F.; Pathak, M. M.; Isacoff, E. Y., How Far Will You Go to Sense Voltage? *Neuron* **2005,** 48, (5), 719-725.

38. Robinson, R. B.; Siegelbaum, S. A., Hyperpolarization-activated cation currents: From molecules to physiological function. *Annu. Rev. Physiol.* **2003,** 65, (1), 453-480.

39. McLaughlin, S.; Murray, D., Plasma membrane phosphoinositide organization by protein electrostatics. *Nature* **2005,** 438, (7068), 605-611.

40. Murata, Y.; Okamura, Y., Depolarization activates the phosphoinositide phosphatase Ci-VSP, as detected in Xenopus oocytes coexpressing sensors of PIP_2. *J Physiol* **2007,** 583, (3), 875-889.

41. Balla, T.; Varnai, P., Visualization of cellular phosphoinositide pools with GFP-fused protein domains. In *Current Protocols in Cell Biology*, John Wiley & Sons, Inc.: 2009; Vol. 42, pp 24.4.1-24.4.27.

42. Fukuda, M.; Kojima, T.; Kabayama, H.; Mikoshiba, K., Mutation of the pleckstrin homology domain of Bruton's Tyrosine Kinase in immunodeficiency impaired inositol 1,3,4,5-tetrakisphosphate binding capacity. *J. Biol. Chem.* **1996,** 271, (48), 30303-30306.

43. Salim, K., et al., Distinct specificity in the recognition of phosphoinositides by the pleckstrin homology domains of dynamin and Bruton's tyrosine kinase. *EMBO (Eur. Mol. Biol. Organ.) J.* **1996,** 15, (22), 6241-6250.

44. Iwasaki, H., et al., A voltage-sensing phosphatase, Ci-VSP, which shares sequence identity with PTEN, dephosphorylates phosphatidylinositol 4,5-bisphosphate. *Proc. Natl. Acad. Sci. U. S. A.* **2008,** 105, (23), 7970-7975.

45. Halaszovich, C. R.; Schreiber, D. N.; Oliver, D., Ci-VSP Is a depolarization-activated phosphatidylinositol-4,5-bisphosphate and phosphatidylinositol-3,4,5-trisphosphate 5'-phosphatase. *J. Biol. Chem.* **2009,** 284, (4), 2106-2113.

46. Kohout, S. C.; Ulbrich, M. H.; Bell, S. C.; Isacoff, E. Y., Subunit organization and functional transitions in Ci-VSP. *Nat. Struct. Mol. Biol.* **2008,** 15, (1), 106-108.

47. Hossain, M. I., et al., Enzyme domain affects the movement of the voltage sensor in ascidian and zebrafish voltage-sensing phosphatases. *J. Biol. Chem.* **2008,** 283, (26), 18248-18259.

48. Kohout, S. C., et al., Electrochemical coupling in the voltage-dependent phosphatase Ci-VSP. *Nat. Chem. Biol.* **2010,** 6, (5), 369-375.

49. Villalba-Galea, C. A.; Miceli, F.; Taglialatela, M.; Bezanilla, F., Coupling between the voltage-sensing and phosphatase domains of Ci-VSP. *J. Gen. Physiol.* **2009,** 134, (1), 5-14.

50. Alonso, A., et al., Protein tyrosine phosphatases in the human genome. *Cell* **2004,** 117, (6), 699-711.

51. Kumanovics, A.; Levin, G. A. L.; Blount, P., Family ties of gated pores: evolution of the sensor module. *FASEB J.* **2002,** 16, (12), 1623-1629.

52. Worby, C. A.; Dixon, J. E., Phosphoinositide phosphatases: Emerging roles as voltage sensors? *Molecular Interventions* **2005,** 5, (5), 274-277.

53. Segal-Hayoun, Y.; Cohen, A.; Zilberberg, N., Molecular mechanisms underlying membrane-potential-mediated regulation of neuronal $K_{2P}2.1$ channels. *Mol. Cell. Neurosci.* **2010,** 43, (1), 117-126.

54. Ratzan, W. J.; Okamura, Y.; Jaffe, L. A., A voltage sensitive phosphatase from Xenopus Laevis testis. *Biophys. J.* **2009,** 96, (3, Supplement 1), 594a-594a.

55. Tapparel, C., et al., The TPTE gene family: cellular expression, subcellular localization and alternative splicing. *Gene* **2003,** 323, 189-199.

56. Leslie, N. R.; Yang, X.; Downes, C. P.; Weijer, C. J., PtdIns(3,4,5)P_3-dependent and -independent roles for PTEN in the control of cell migration. *Curr. Biol.* **2007,** 17, (2), 115-125.

57. Chen, H., et al., A testis-specific gene, TPTE, encodes a putative transmembrane tyrosine phosphatase and maps to the pericentromeric region of human chromosomes 21 and 13, and to chromosomes 15, 22, and Y. *Hum. Genet.* **1999,** 105, (5), 399-409.

58. Walker, S. M.; Downes, C. P.; Leslie, N. R., TPIP: a novel phosphoinositide 3-phosphatase. *Biochem. J.* **2001,** 360, (2), 277-283.

59. Guipponi, M., et al., The murine orthologue of the Golgi-localized TPTE protein provides clues to the evolutionary history of the human TPTE gene family. *Hum. Genet.* **2001,** 109, (6), 569-575.

60. Wu, Y., et al., PTEN 2, a Golgi-associated testis-specific homologue of the PTEN tumor suppressor lipid phosphatase. *J. Biol. Chem.* **2001,** 276, (24), 21745-21753.

61. Jungnickel, M. K.; Sutton, K. A.; Wang, Y.; Florman, H. M., Phosphoinositide-dependent pathways in mouse sperm are regulated by egg ZP3 and drive the acrosome reaction. *Dev. Biol.* **2007,** 304, (1), 116-126.

62. Abou-haila, A.; Tulsiani, D. R., Signal transduction pathways that regulate sperm capacitation and the acrosome reaction. *Arch. Biochem. Biophys.* **2009,** 485, (1), 72-81.

63. Navarro, B.; Kirichok, Y.; Chung, J. J.; Clapham, D. E., Ion channels that control fertility in mammalian spermatozoa. *Int. J. Dev. Biol.* **2008,** 52, (5-6), 607-13.

64. Tang, Q. Y., et al., Phosphatidylinositol (4,5)-bisphosphate (PIP_2) activates Slo3 currents and its hydrolysis underlies the EGF-induced current inhibition. *J. Biol. Chem.* **2010**.

65. Jaffe, L. A., Fast block to polyspermy in sea urchin eggs is electrically mediated. *Nature* **1976,** 261, (5555), 68-71.

66. Siegel, M. S.; Isacoff, E. Y., A genetically encoded optical probe of membrane voltage. *Neuron* **1997,** 19, (4), 735-741.

67. Baker, B. J., et al., Three fluorescent protein voltage sensors exhibit low plasma membrane expression in mammalian cells. *J. Neurosci. Methods* **2007,** 161, (1), 32-38.

68. Knöpfel, T.; Díez-García, J.; Akemann, W., Optical probing of neuronal circuit dynamics: genetically encoded versus classical fluorescent sensors. *Trends Neurosci.* **2006,** 29, (3), 160-166.

69. Alabi, A. A., et al., Portability of paddle motif function and pharmacology in voltage sensors. *Nature* **2007,** 450, (7168), 370-375.

70. Patti, J. T.; Isacoff, E. Y. *Measuring membrane voltage with fluorescent proteins*, Cold Spring Harbor Laboratory Press: in press.

71. Klein, R. M.; Ufret-Vincenty, C. A.; Hua, L.; Gordon, S. E., Determinants of molecular specificity in phosphoinositide regulation. *J. Biol. Chem.* **2008,** 283, (38), 26208-26216.

72. Stucky, C. L., et al., Roles of transient receptor potential channels in pain. *Brain Res. Rev.* **2009,** 60, (1), 2-23.

73. Falkenburger, B. r. H.; Jensen, J. B.; Hille, B., Kinetics of PIP_2 metabolism and KCNQ2/3 channel regulation studied with a voltage-sensitive phosphatase in living cells. *The Journal of General Physiology* **2010,** 135, (2), 99-114.

74. Falkenburger, B. r. H.; Jensen, J. B.; Hille, B., Kinetics of M1 muscarinic receptor and G protein signaling to phospholipase C in living cells. *The Journal of General Physiology* **2010,** 135, (2), 81-97.

75. Shapiro, M. S., et al., Reconstitution of muscarinic modulation of the KCNQ2/KCNQ3 K^+ channels that underlie the neuronal M current. *J. Neurosci.* **2000,** 20, (5), 1710-1721.

76. Suh, B.-C.; Inoue, T.; Meyer, T.; Hille, B., Rapid chemically induced changes of PtdIns(4,5)P_2 gate KCNQ ion channels. *Science* **2006,** 314, (5804), 1454-1457.

77. Varnai, P.; Thyagarajan, B.; Rohacs, T.; Balla, T., Rapidly inducible changes in phosphatidylinositol 4,5-bisphosphate levels influence multiple regulatory functions of the lipid in intact living cells. *The Journal of Cell Biology* **2006,** 175, (3), 377-382.

78. Dowling, R. J. O.; Topisirovic, I.; Fonseca, B. D.; Sonenberg, N., Dissecting the role of mTOR: Lessons from mTOR inhibitors. *Biochimica et Biophysica Acta (BBA) - Proteins & Proteomics* **2010,** 1804, (3), 433-439.

Chapter 4

Functional characterization of the voltage-gated phosphatase Ci-VSP[2]

[2] A portion of this work has been published and is reprinted with permission from *Nature Structural and Molecular Biology*:

"Subunit organization and functional transitions in Ci-VSP"
Susy C. Kohout, Maximilian H. Ulbrich, Sarah C. Bell and Ehud Y. Isacoff, *Nature Structural and Molecular Biology* 2008, 15, 106-108.

Introduction

Until recently, ion channels were the only proteins known to sense changes in membrane potential. This changed with the discovery of *Ciona intestinalis* voltage-sensor containing phosphatase, Ci-VSP, which couples a voltage sensing domain (VSD) to a phosphatase and tensin homologue (PTEN)-like domain (Figure 4.1).[1] More recently, the voltage-gated proton channel (H_v) was cloned and found to contain a VSD, but to lack a traditional pore domain.[2, 3] The existence of Ci-VSP and H_v indicates that VSDs are functional modules[4, 5] that control distinct effectors. To date, voltage sensor-effector coupling has been studied in the context of four subunit channels, where a common pore is cooperatively gated by four VSDs.[6] However, PTEN is a monomer[7], raising the possibility that in Ci-VSP, an isolated VSD can endow voltage dependence onto a single effector domain.

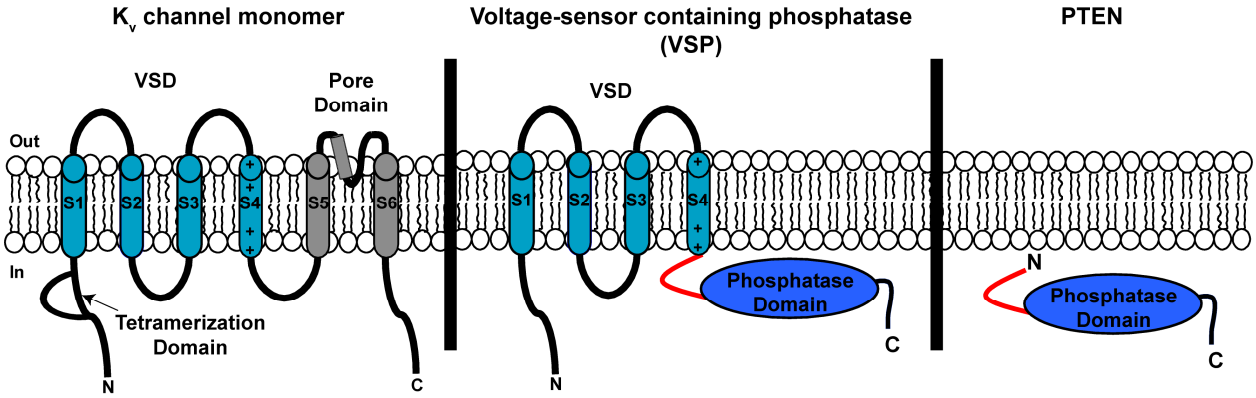

Figure 4.1. Ci-VSP shares homology with voltage gated potassium (Kv) channels and PTEN. Comparison of Ci-VSP topology (middle) with Kv channels (left) and PTEN (right). Ci-VSP contains 4 transmembrane segments (S1-S4) that are homologous to the voltage sensing domain (VSD) of a voltage-gated potassium channel. The cytosolic phosphatase domain of Ci-VSP shares 29.5% sequence identity with PTEN. Helices are represented by cylinders with VSDs shaded in light blue, pore domains shaded in gray, and phosphatase domains shaded in dark blue. Red line represents putative $PI(4,5)P_2$ binding domain.

This initial characterization of Ci-VSP left many questions about the assembly and function of Ci-VSP unanswered. We set out to address the following questions using electrophysiological and fluorescence methods in living cells:

1. What is the oligomerization state of Ci-VSP?
2. What reactions does Ci-VSP catalyze in cells?
3. What functional transitions in Ci-VSP are responsible for activity?
4. What is the mechanism of coupling between the Ci-VSP VSD and phosphatase domains?

Results and Discussion

Oligomerization state of Ci-VSP

Voltage-gated ion channel subunits each contain a VSD and pore domain and assemble as functional tetramers with the four VSDs flanking a central pore. While Ci-VSP contains a functional VSD, the pore domain is replaced with a cytosolic phosphatase domain that resembles PTEN, which is a functional monomer.[7] To determine the number of subunits in Ci-VSP, we employed a single molecule microscopy technique developed in the Isacoff lab (Figure 4.2).[8]

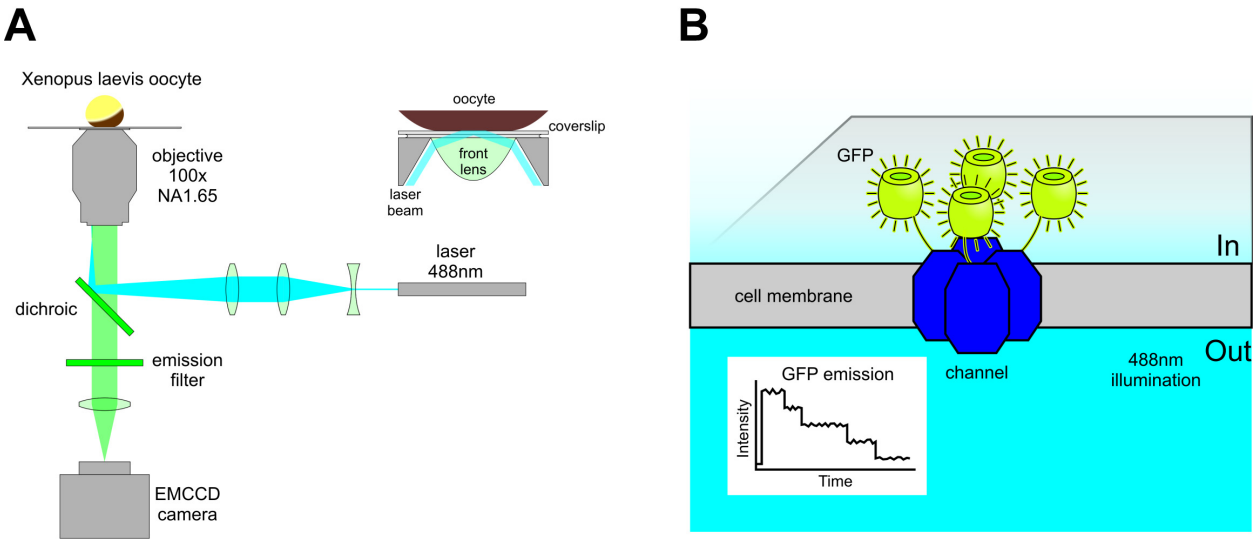

Figure 4.2. Single molecule subunit counting method. (A) Total internal reflection fluorescence (TIRF) set-up for subunit counting experiments. *Xenopus laevis* oocytes expressing low levels of a mEGFP-tagged membrane protein subunit are imaged using high numerical aperture (NA) objective coupled to a CCD camera. **(B)** Cartoon depicting fluorescently tagged tetrameric membrane protein imaged using set up TIRF set-up described in **(A)**. Bleaching of each mEGFP chromophore will result in the decrease in total mEGFP intensity in a step-wise manner as a function of time (depicted by graph).

In this method, subunits of the membrane protein of interest are fused to a monomeric enhanced green fluorescent protein[9] (mEGFP) and then expressed in *Xenopus laevis* oocytes at low density. Total internal reflection fluorescence (TIRF) microscopy is used to selectively visualize the mEGFP-tagged proteins located at the plasma membrane at the single molecule level. In multi-subunit ion channels with mEGFP fused to each subunit, we can detect as many steps of mEGFP photobleaching as there are subunits.[8] We constructed a Ci-VSP-mEGFP fusion protein and used this method to determine the oligomerization state of Ci-VSP. In our initial experiments, we expressed Ci-VSP-mEGFP alone, but lateral diffusion permitted the evaluation of only a minority of fluorescent spots.

In the second approach, we reduced lateral diffusion by fusing the C terminus of the potassium channel $K_v1.4$ and co-expressing Ci-VSP-mEGFP-$K_v1.4$C with the synaptic protein PSD-95, which binds to $K_v1.4$C. We imaged 15x15 μm^2 areas of membrane which had ~50 spots—enough for statistical analysis, but with low probability that two proteins would lie within the same diffraction-limited spot. The emission intensities of the fluorescent spots were extracted from short movies (Figure 4.3A and *Materials and Methods*). In oocytes expressing Ci-VSP-mEGFP alone, 93 $\pm$ 1% (n = 3) of the immobile spots bleached in a single step, while the remainder bleached in two steps. In oocytes expressing Ci-VSP-mEGFP-$K_v1.4$C and PSD-95, where larger numbers of spots were immobile, 94 $\pm$ 1% (n=5) of the immobile fluorescent spots bleached in a single step, while the remainder bleached in two steps (Figure 4.3B). We compared this result to the distributions of bleaching steps previously found for ion channels labeled with one, two, and four mEGFP molecules per protein. The results from Ci-VSP match closely the distribution found for a Ca^{2+} channel, which carried only one mEGFP at its C terminus (Figure 4.3C) and stood in marked contrast to the distributions seen in tetrameric cyclic nucleotide-gated (CNG) channels, in which the majority of fluorescent spots consisted of three or four bleaching steps (Figure 4.3B), and NMDA receptors with two of the four subunits fused to mEGFP, which mainly exhibit spots with two bleaching steps (Figure 4.3C). The results clearly indicate that, unlike voltage-gated channels, Ci-VSP is not an obligate tetramer, instead residing in the membrane as a monomer.

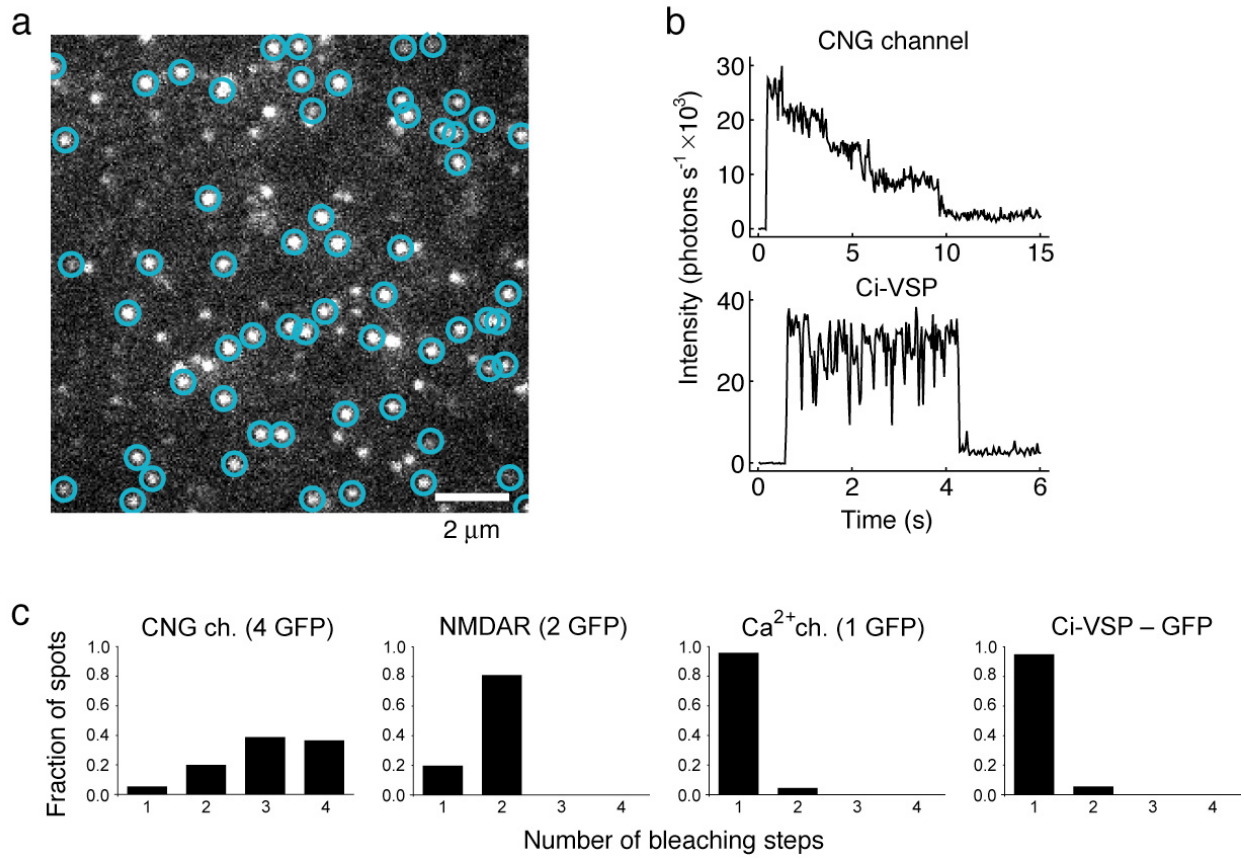

Figure 4.3. Ci-VSP is a monomer at low density. (A) Image from TIRF movie of oocyte coexpressing Ci-VSP-mEGFP-K_v1.4C and PSD-95, showing fluorescent spots in membrane, some of which fit criteria for analysis (blue circles). **(B)** Tetrameric CNG channel, with mEGFP on each subunit, bleaches in four steps (top), but Ci-VSP-mEGFP-K_v1.4C bleaches in a single step (bottom). **(C)** Frequency of single and multiple bleaching events from fluorescent spots in oocytes expressing Ci-VSP compared to reference proteins[8]: CNG channel (one mEGFP/subunit = four/channel), the NMDA receptor (mEGFP on NR2B = two/channel), the Ca^{2+} channel (one mEGFP per linked tetramer = one/channel). Ci-VSP resembles Ca^{2+} channel. Figure from[10].

Monitoring voltage-dependent Ci-VSP activity in living cells

Murata and co-workers first proposed that membrane hyperpolarization causes Ci-VSP-mediated increases in phosphatidylinositol 4,5-bisphosphate ($PI(4,5)P_2$) at the plasma membrane which they attributed to the Ci-VSP hydrolysis of phosphatidylinositol 3,4,5-trisphsophate ($PI(3,4,5)P_3$).[1] The cytosolic domain of Ci-VSP shares 29.5% sequence identity with PTEN, a putative tumor suppressor protein that is a D3-phosphoinositide phosphatase.[11] In a subsequent publication, Murata and Okamura demonstrated membrane depolarization caused Ci-VSP mediated decreases in membrane concentrations of both $PI(3,4,5)P_3$ and $PI(4,5)P_2$, but they did not determine the products of these reactions.[12]

While it was unclear whether Ci-VSP could catalyze multiple reactions, we chose to monitor Ci-VSP mediated changes in $PI(4,5)P_2$, as this lipid is a proposed substrate and/or product of the enzyme and is one of the most concentrated phosphoinositides (PIPs) present in the plasma membrane.[13]

We began our study of the voltage dependence of Ci-VSP activity by using an inwardly rectifying potassium $K_{ir}2.1$ (IRK1) channel, which directly binds $PI(4,5)P_2$,[14] as a downstream reporter of Ci-VSP phosphatase activity. We introduced a mutation (R228Q) in the putative $PI(4,5)P_2$ binding site of IRK1 in order to lower the channels' affinity for $PI(4,5)P_2$ and increase its response time to Ci-VSP mediated changes in $PI(4,5)P_2$.[15] The IRK1-R228Q (IRK1Q) reporter had been previously used by Murata *et al.* as a Ci-VSP-sensitive ion channel reporter of $PI(4,5)P_2$.[1] The IRK1Q channel is tetrameric and requires four molecules of $PI(4,5)P_2$ to stabilize the open state of the channel (Figure 4.4A). In the presence of higher extracellular concentrations of K^+ IRK1Q will conduct K^+ ions into the cell. This K^+ flux through the IRK1Q channel can be recorded using electrophysiology techniques.

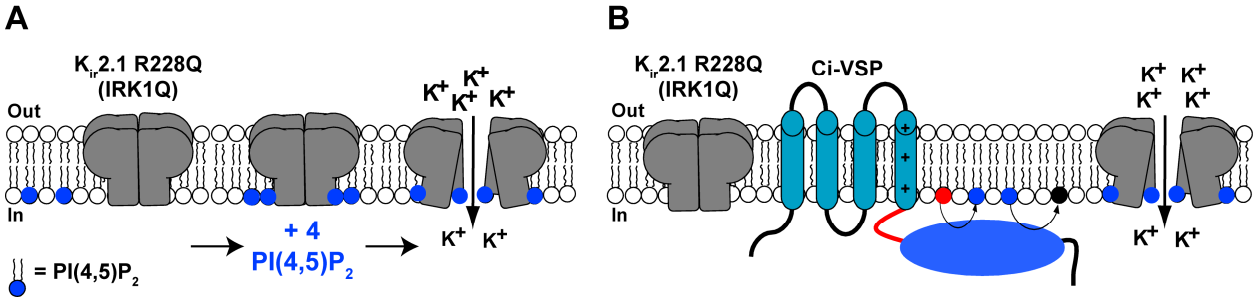

Figure 4.4. Schematic for IRK1Q activity assay. (A) $PI(4,5)P_2$ acts as an agonist of IRK1Q channels where four molecules of $PI(4,5)P_2$ are required for channel activation. **(B)** IRK1Q activity is modulated by voltage-dependent Ci-VSP production and/or depletion of $PI(4,5)P_2$ thus serving as a downstream reporter of Ci-VSP activity.

We co-expressed Ci-VSP and IRK1Q in *Xenopus laevis* oocytes and used two-electrode voltage clamping (TEVC) techniques to change the cell membrane voltage and measure the IRK1Q current (Figure 4.4B). Using the voltage protocol shown in Figure 4.5A, we varied the membrane voltage to regulate Ci-VSP activity, thus changing the $PI(4,5)P_2$ concentrations at the plasma membrane. We then monitored these changes by measuring IRK1Q currents.

In control cells expressing only IRK1Q, the current did not change in response to changes in membrane potential (Figure 4.5A, middle). However, in cells expressing both Ci-VSP and IRK1Q, membrane depolarization resulted in decreased $PI(4,5)P_2$ levels due to Ci-VSP activity and led to the subsequent decrease in IRK1Q current (Figure 4.5A, bottom). Ci-VSP activity modulated IRK1Q current in a voltage-dependent manner where membrane depolarizations resulted in smaller IRK1Q currents and membrane hyperpolarizations resulted in larger IRK1Q currents. By plotting steady-state levels IRK1Q current as a function of holding voltage, we

were able to infer the voltage dependence of Ci-VSP mediated changes in $PI(4,5)P_2$ (Figure 4.5B).

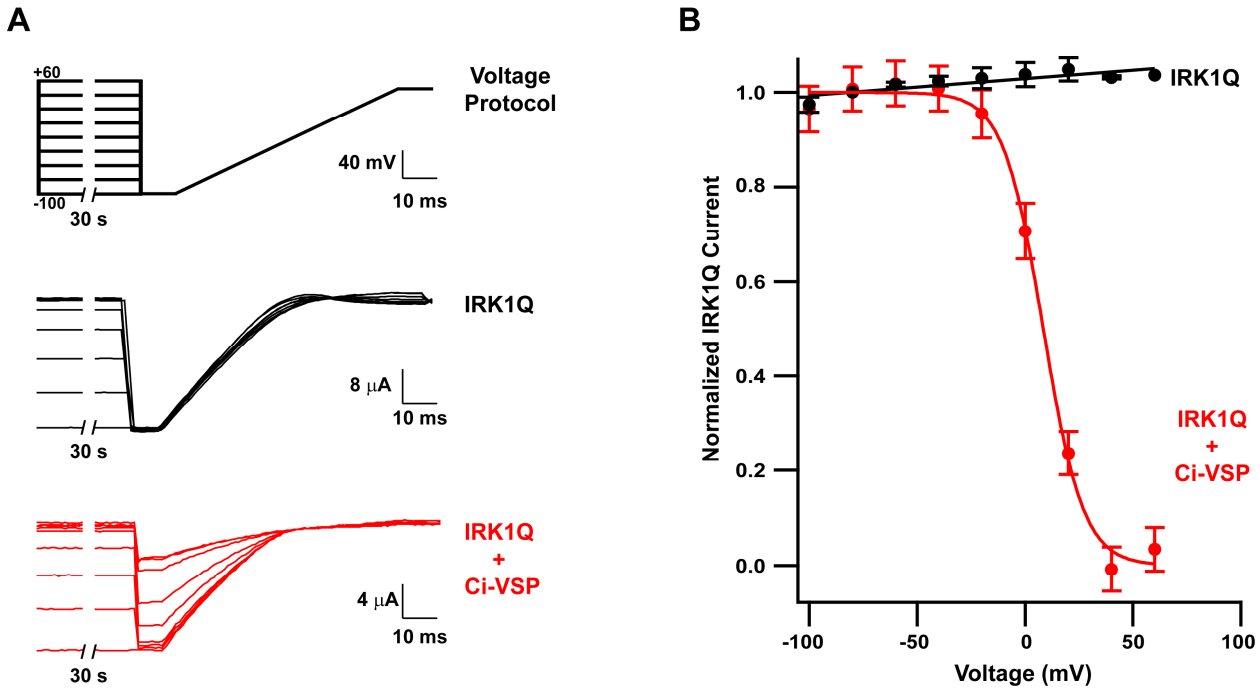

Figure 4.5. Ci-VSP modulates IRK1Q activity in a voltage dependent manner. (A) Voltage protocol (top) and representative traces of IRK1Q alone (middle) or IRK1Q and Ci-VSP (bottom). **(B)** IRK1Q current vs. voltage graph shows the steady-state Ci-VSP-mediated voltage dependent modulation of IRK1Q current (red). Red line indicates single Boltzmann fit. Control cells only expressing IRK1Q did not respond to changes in membrane voltage (black). Error bars indicate SEM. For fit data, see Table 4.1.

This assay was also used to confirm the functionality of the Ci-VSP-mEGFP-K_v1.4C construct used for oligomerization experiments. The mEGFP-K_v1.4C tag did not significantly affect the activity of Ci-VSP (Figure 4.6).

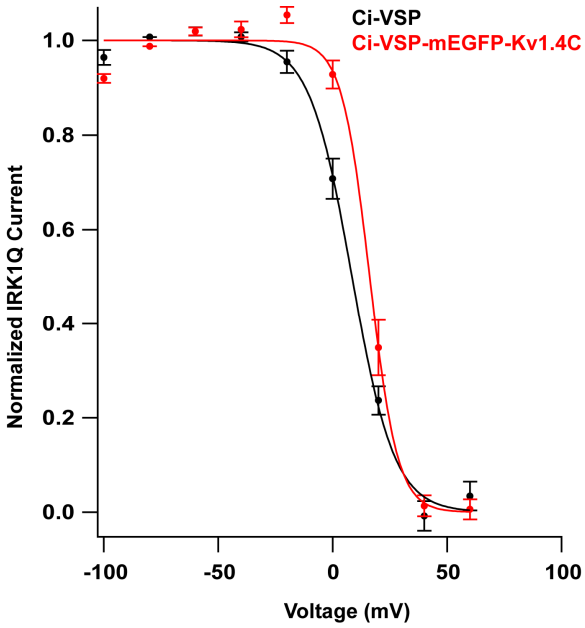

Figure 4.6. Validation of functional Ci-VSP-mEGFP-K_v1.4C protein. Comparison of voltage-dependent activity of Ci-VSP-mEGFP-K_v1.4C construct (red) used in single molecule experiments with Ci-VSP (black) using IRK1Q activity assay. Solid lines represent single Boltzmann fits. Error bars indicate SEM. For fit data, see Table 4.1.

To confirm that IRK1Q was a dynamic reporter of Ci-VSP activity, we conducted kinetic experiments at the extremes of the voltage range of IRK1Q sensitivity to Ci-VSP. Oocytes expressing both Ci-VSP and IRK1Q were clamped at either +60 mV (Figure 4.7A) or -100 mV (Figure 4.7B). Membrane depolarization caused depletion of $PI(4,5)P_2$ and subsequent run down of IRK1Q current in less than one minute (Figure 4.7A). Membrane hyperpolarization caused production of $PI(4,5)P_2$ and subsequent saturation of IRK1Q current in approximately six minutes (Figure 4.7B). In both cases, absence of lag indicates that the voltage-driven changes in Ci-VSP activity lead to changes in $PI(4,5)P_2$ concentrations that are within the dynamic range of the reporter, IRK1Q.

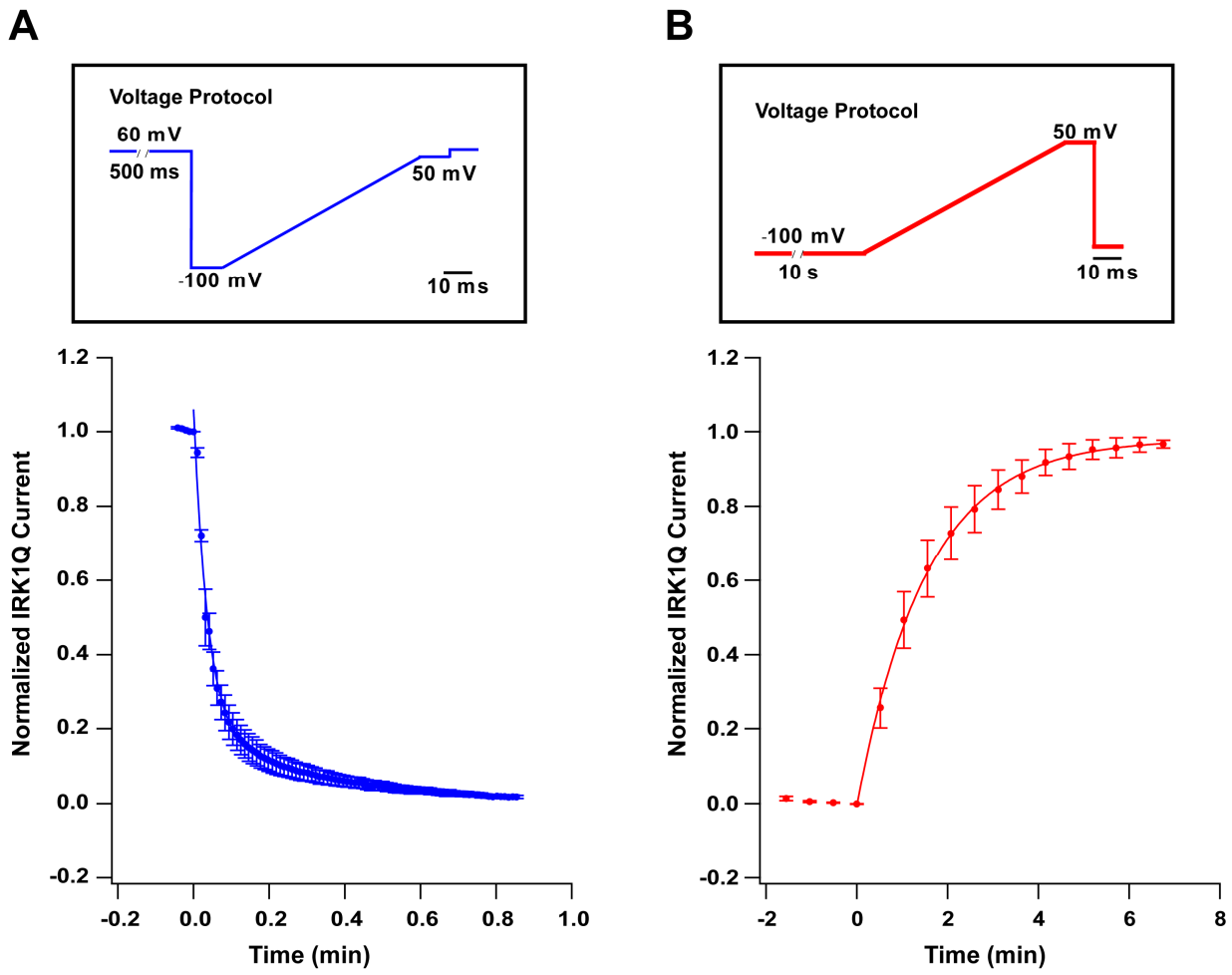

Figure 4.7. Dynamic range of IRK1Q assay. (A) Ci-VSP mediated depletion of $PI(4,5)P_2$ as measured using IRK1Q activity assay occurs rapidly (< 1 min) when oocyte is voltage clamped at +60 mV. Blue line indicates double exponential fit. **(B)** Ci-VSP mediated production of $PI(4,5)P_2$ occurs slowly (~6 min) when oocyte is voltage clamped at -100 mV. Red line indicates single exponential fit. For both **(A)** and **(B)** voltage protocols shown in boxes. Average response from 4 cells shown for each condition, error bars indicate SEM.

Furthermore, we observed that the rate of Ci-VSP mediated hydrolysis of $PI(4,5)P_2$ was voltage dependent with greater depolarizations leading to faster depletion of $PI(4,5)P_2$ and faster run down of IRK1Q currents (Figure 4.8). The level Ci-VSP-mediated IRK1Q current run down was also voltage dependent with greater depolarizations leading to greater levels of IRK1Q current run down. Comparing our results with rates of Ci-VSP voltage sensor movement (milliseconds) and *in vitro* Ci-VSP phosphoinositide phosphatase activity (0.292 nmol/min/µg protein[1], we concluded that Ci-VSP hydrolyzes $PI(4,5)P_2$ upon membrane depolarization.

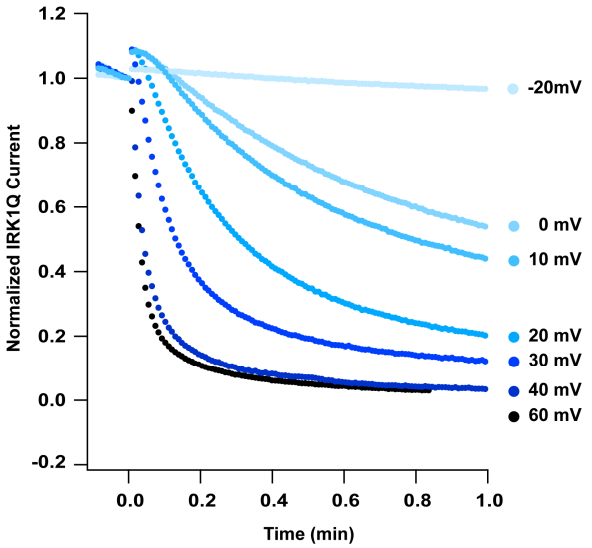

Figure 4.8. Rates and steady state levels of Ci-VSP-mediated PI(4,5)P_2 hydrolysis are voltage-dependent. Representative traces for cells voltage clamped at different membrane voltages are shown. Increased depolarization leads to increases in the rate of PI(4,5)P_2 hydrolysis as reported using the IRK1Q assay.

This result was in agreement with recently published work from Murata and Okamura suggesting that membrane depolarization activates Ci-VSP hydrolysis of PI(4,5)P_2[12]. But, neither approach eliminated the possibility that Ci-VSP also produced PI(4,5)P_2 upon membrane hyperpolarization. At membrane potentials where Ci-VSP is not fully activated, there is a voltage-dependent lag in the amount of time needed to cause changes in IRK1Q current (Figure 4.8). This lag may result from the voltage dependence of turning off Ci-VSP or indicate equilibrium between the endogenous pathways regulating PI(4,5)P_2 levels and Ci-VSP activity.

In summary, the IRK1Q channel is a robust reporter of dynamic Ci-VSP mediated changes in PI(4,5)P_2. Our experiments indicate that Ci-VSP depletes PI(4,5)P_2 upon membrane depolarization.

Functional transitions in Ci-VSP

In another approach to study the coupling of the VSD to the catalytic domain, we used voltage clamp fluorometry (VCF), where we mutate a single residue to cysteine in the positively-charged S4 segment and attach tetramethylrhodamine maleimide (TMRM), an environment-sensitive fluorophore.[16] Voltage-driven conformational rearrangements of S4 are detected as changes in TMRM fluorescence intensity. This technique has been used extensively to characterize the voltage-dependent conformational changes of the Shaker potassium channel, a prototypical member of the K_v1.1 subfamily.[17] The proposed external end of S4 in Ci-VSP has over 70% sequence homology with that of Shaker, making Ci-VSP a good candidate for VCF experiments. Furthermore, Ci-VSP does not contain any surface accessible cysteine residues which could form disulfide bonds with the introduced cysteine and interrupt the native structure

of the protein. We chose labeling positions in Ci-VSP that were homologous to labeling positions in Shaker that served as reporters of VSD movement[6] (Figure 4.9A).

We first engineered cysteine residues at three different locations near the proposed S4 segment of Ci-VSP (Figure 4.9A) and measured the effects of the introduced cysteines on voltage-dependent Ci-VSP phosphatase activity using the IRK1Q assay. Cysteine substitution at positions 207 and 208 did not significantly affect Ci-VSP activity and cysteine substitution at position 214 caused a slight leftward shift in the voltage-dependence of Ci-VSP activity (Figure 4.9B).

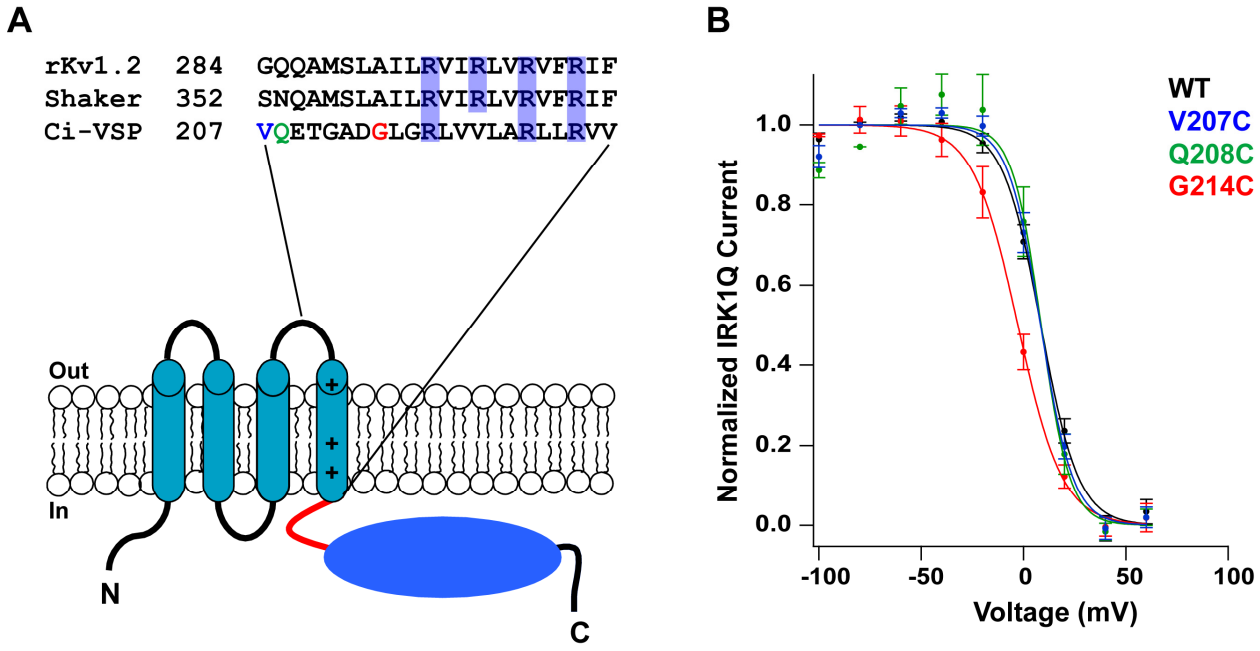

Figure 4.9. Cysteine substitution does not impair Ci-VSP activity. (A) Ci-VSP topology with sequence of S3-S4 linker and S4 highlighted. Partial sequence alignment of S4 segments from K_v channels and Ci-VSP with basic residues highlighted in blue. **(B)** IRK1Q activity vs. voltage (AV) curves for Ci-VSP (black), Ci-VSP-V207C (blue), Ci-VSP-Q208C (green), and Ci-VSP-G214C (red). Solid lines indicate single Boltzmann fits. Error bars indicate SEM. For fit data see Table 4.1.

TMRM-labeled G214C mutant showed robust changes in fluorescence as a function of voltage that were in the same voltage range of gating charge measurements for Ci-VSP suggesting that this reporter site closely monitored Ci-VSP VSD motion[1] (Figure 4.10A). Moreover, the voltage-dependent activity of Ci-VSP-G214C was well characterized (Figure 4.10B) and we decided to continue our VCF experiments and activity with Ci-VSP-G214C.

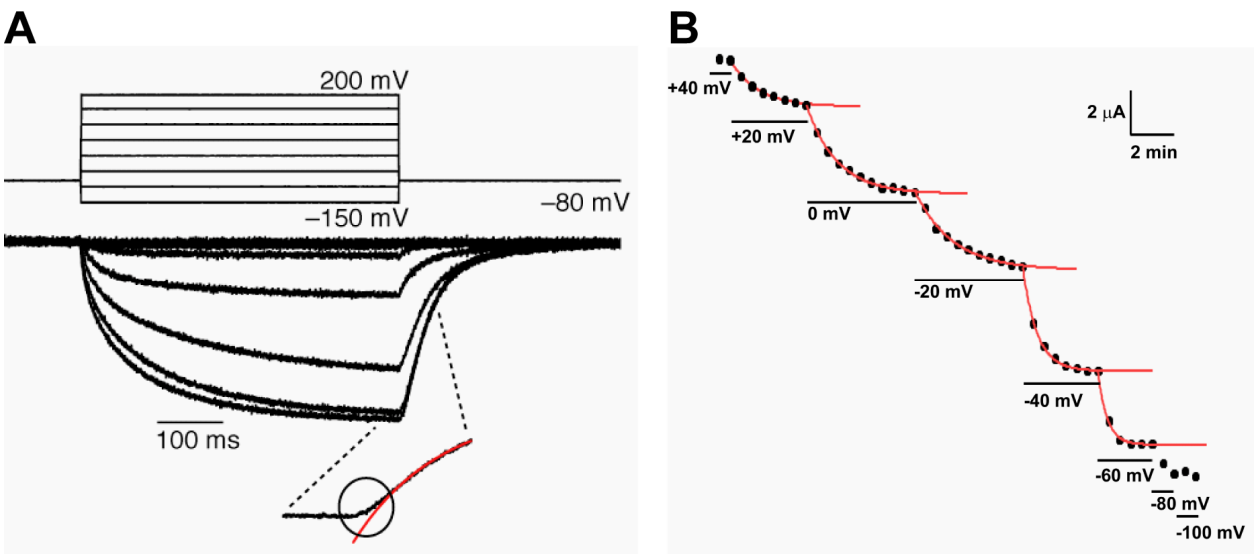

Figure 4.10. Voltage dependent motions and activity of Ci-VSP-G214C. (A) G214C-TMRM single fluorescence traces (bottom) evoked by voltage steps (top; only 50 mV increments shown; delayed ΔF during repolarization circled in inset). Note that VSD motions occur on the millisecond time scale. **(B)** Voltage dependent Ci-VSP-G214C activity vs. time using IRK1Q assay. Note that up to hundreds of seconds are needed for the amplitude of IRK1Q current to settle to new levels at each new holding voltage. Red lines indicate single exponential fits. Figures adapted from[10].

The VSDs of voltage-gated channels go through at least two independent rearrangements and one cooperative one involving the four VSDs.[18-22] We asked whether Ci-VSP, as a monomer, would undergo only a single step transition or have multiple steps. VSD protein motion was detected using VCF[23], following attachment of tetramethylrhodamine-maleimide (TMRM) to a cysteine substituted at G214. Protein motion was monitored from changes in fluorescence (ΔF) evoked by voltage steps (Figure 4.10A), yielding steady-state fluorescence-voltage (FV) relations (Figure 4.11). As found earlier for gating charge[1], VSD motion was detected over a wide range of voltage (FV), distinct from the steeper voltage dependence of IRK1Q activation (AV) (Figure 4.11). The difference between the FV and AV could reflect the indirect nature of the activity assay (e.g. IRK1Q is activated by four $PI(4,5)P_2$ molecules), or it could indicate that a two-state model is not sufficient to describe the system. The recent discovery that Ci-VSP may catalyze the dephosphorylation of both $PI(3,4,5)P_3$ and $PI(4,5)P_2$[12] supports the notion that a two-state model is insufficient.

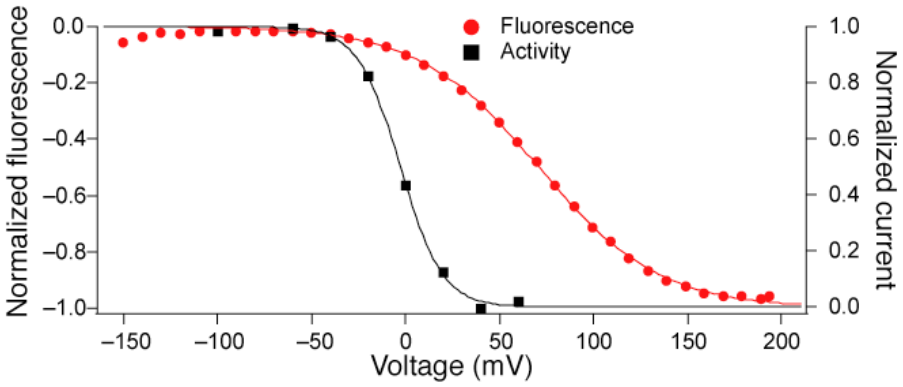

Figure 4.11. Superposition of Ci-VSP-G214C activity and VSD motions. Steady-state voltage dependence of IRK1Q current (enzymatic activity) (black) and of fluorescence (VSD motion) (red) for G214C-TMRM. Solid lines represent single Boltzmann fits. Error bars (smaller than symbols) indicate SEM. For fit data, see Tables 4.1 and 4.2. Figure from[10].

To determine whether protein activation evolves in more than one step, we capitalized on the real-time report of protein motion by VCF. While small depolarizations evoked fast ΔFs that were well-fit by a single exponential both during the step and upon repolarization (data not shown), the ΔFs evoked by larger depolarizations required two exponentials and had a delay phase in the ΔF upon repolarization (Figure 4.10A, inset). This behavior resembles that of the four VSD containing Shaker K^+ channel.[24] To further investigate this behavior, we attached TMRM to another position in the S3-S4 linker, Q208C (Figure 4.9A). As with G214C-TMRM, small depolarizations evoked fast, single exponential ΔFs from Q208C-TMRM (Figure 4.12, pink). Larger depolarizations successively recruited three additional components (Figure 4.12). The complex ΔFs indicate that the VSD undergoes multiple structural rearrangements over a wide range of voltages.

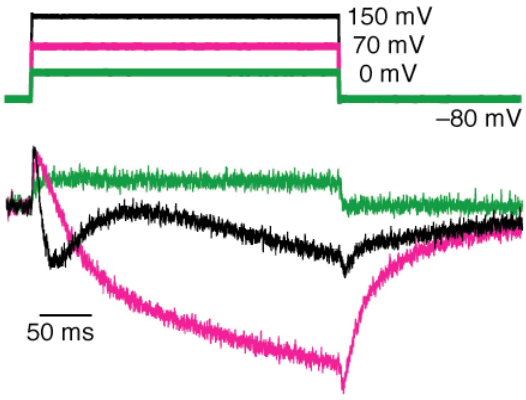

Figure 4.12. Ci-VSP VSD adopts multiple conformations. Multi-component fluorescence evoked by steps to indicated voltages for Q208C-TMRM. Figure from[10].

VSD charge mutations influence VSD transitions and phosphatase activity

To further investigate the coupling between the Ci-VSP VSD and phosphatase domain, we measured the effects of charge neutralization or charge introduction in the proposed Ci-VSP S4 segment in the G214C background. We first tested R217Q[25] and found this to shift the FV to the left by 131 mV. The large shift in the FV for the charge neutralization, R217Q, argues in favor of the alignment shown in Figure 4.13A, because mutating the first charge-carrying residue (R1) in the Shaker channel (Shaker R362) produces a similar leftward shift in voltage dependence, due to a destabilization of its interactions within the VSD where it is situated at negative voltages.[26, 27] The R217Q mutation also shifted Ci-VSP-G214C-R217Q activity to the left by 41 mV compared with the AV curve for Ci-VSP-G214C (Figure 4.13B). The sequence alignment is also supported by the decrease in fluorescence seen in G214C-TMRM in response to depolarization (Figure 4.10A), which is consistent with G214 being the homolog of Shaker A359, three residues before R1.[28]

Similarly, we introduced an arginine at position 220 which corresponds to R2 in Shaker. We observed a 71 mV rightward shift in the FV curve (Figure 4.13B, blue) and a 6 mV shift in the AV curve (Figure 4.13C, blue) further supporting our alignment. Interestingly, the R217Q mutation decreased the slope of the AV curve and the V220R mutation increased the slope of the AV curve (Table 4.1), yet these mutations did not affect the slopes of FV curves (Table 4.2)

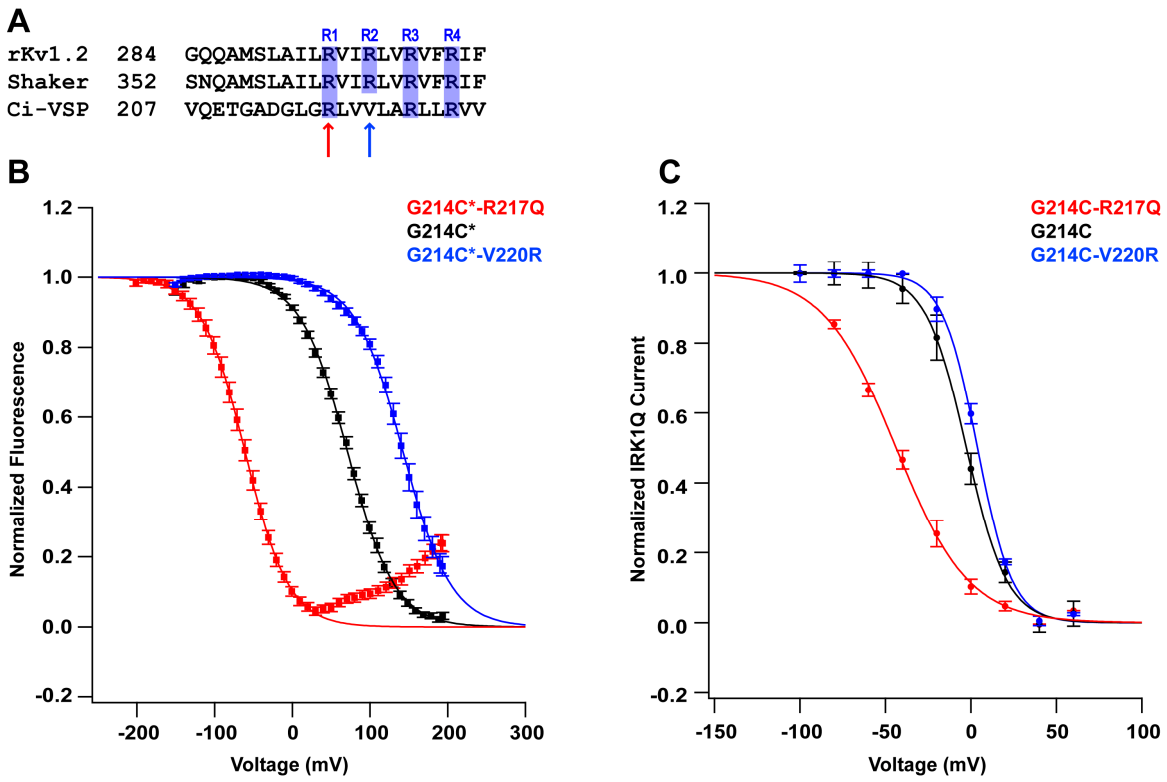

Figure 4.13. S4 charge mutations affect voltage dependence of Ci-VSP VSD movement and phosphatase activity. (A) Sequence alignment of S4 segments of K_v channels and Ci-VSP; basic residues shaded in blue. **(B)** Fluorescence vs. Voltage (FV) curves for VSD charge mutants measured using VCF. Asterisk denotes labeling with TMRM. **(C)** Activity vs. Voltage (AV) curves for VSD charge mutants measured using IRK1Q assay. Soild lines represent single Boltzmann fits. Error bars indicate SEM. For fit data, see Tables 4.1 and 4.2.

Through the course of our VCF experiments, we identified a labeling position (V207C) where one component of the FV curve was in the same voltage range as the IRK1Q AV curve for Ci-VSP-V207C. We hypothesized that the VSD motions recorded at position 207 could be directly coupled to activity. To test our hypothesis, we again turned to the R217Q mutation which shifted both Ci-VSP VSD motions and phosphatase activity to the left (Figure 4.13A and B). The R217Q mutation shifted the AV curve for Ci-VSP V207C by 49 mV to the left and changed the slope of the AV curve by 10.8 (Figure 4.14A and Table 4.1). These effects are similar to those seen in the G214C background. On the contrary, the R217Q mutation shifted the FV curve 104 mV to the right (Figure 4.14B and Table 4.2). We concluded that the VSD motions recorded by V207C were not directly coupled to Ci-VSP phosphatase activity.

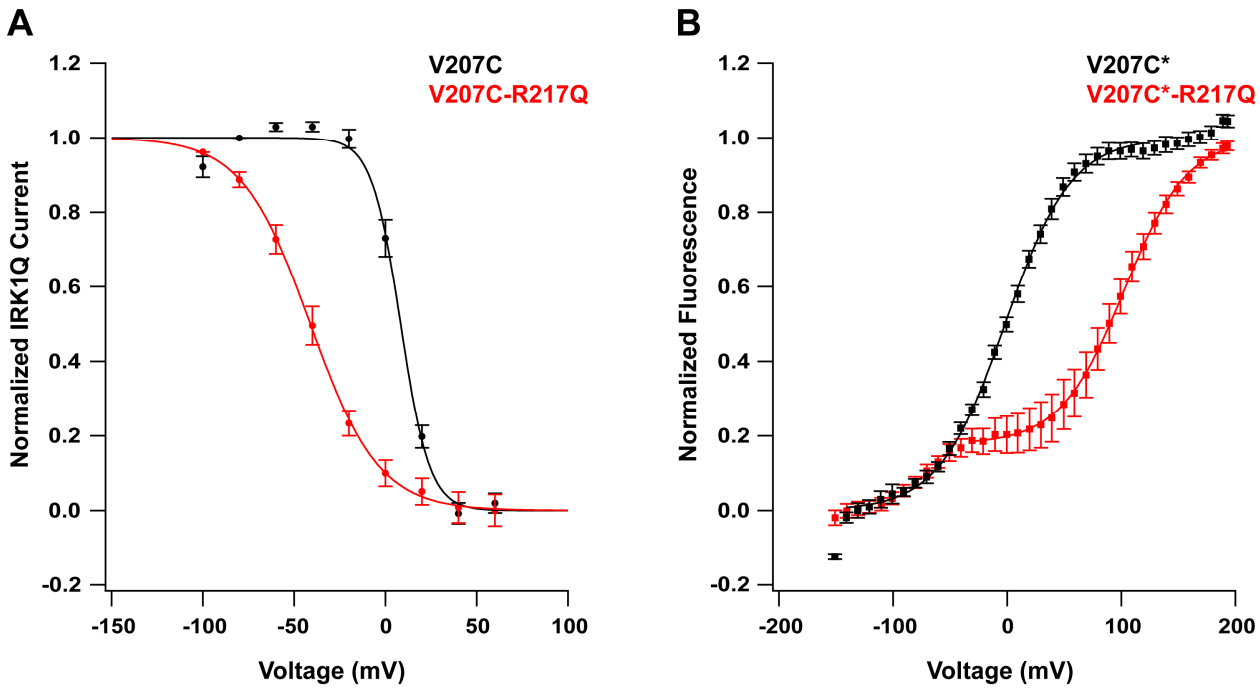

Figure 4.14. VSD motions reported by V207C are not directly coupled to activity. (A) AV curves for V207C (black) and V207C-R217Q (red) using IRK1Q assay. $V_{1/2}$ shift = -49.4 mV. **(B)** FV curves for V207C-TMRM and V207C-TMRM-R217Q. Asterisk indicates labeling with TMRM. $V_{1/2}$ shift = +104 mV. For both (A) and (B) solid lines represent single Boltzmann fits. Error bars indicate SEM. For all fit data, see Tables 4.1 and 4.2.

Cooperativity experiments

While our subunit counting was carried out at low density, the fluorescence and activity analyses were performed at high density. Is it possible that the complex behavior of Ci-VSP emerges from multimerization at high density? We used fluorescence coinjection to address this question. We asked whether coexpression of wild-type (WT) Ci-VSP with a voltage-shifted mutant would yield two independent populations of proteins, as expected for a monomer, or if they would influence each other in a manner consistent with coassembly and cooperativity.

To test cooperativity between adjacent Ci-VSP VSDs, RNAs encoding Ci-VSP-G214C-R217Q and WT were coinjected. This permitted us to view protein motion exclusively in the R217Q protein (since only this could be labeled by TMRM) and ask whether the presence of the WT protein in the same cell would influence it, as occurs between coexpressed Shaker channel subunits.[18, 22] Without cooperativity, the R217Q/G214C-TMRM fluorescence should be the same as if WT were not coexpressed. We found that R217Q/G214C-TMRM coexpressed with WT had the same voltage dependence as R217Q/G214C-TMRM alone (Figure 4.15B), indicating absence of cooperativity. In a second assay, we coexpressed G214C and R217Q/G214C so that both would be labeled with TMRM, enabling their conformational changes to be observed simultaneously. In this case, cooperativity would be predicted to produce a hybrid FV curve, whereas independence would produce a biphasic FV curve from the

linear combination of the individual F-Vs. For two different RNA ratios, we obtained FVs that could be accounted for as linear sums of the individual FVs (Figure 4.15C). These results indicate that, even at high density, there is no functional interaction between Ci-VSP monomers, supporting the notion that each Ci-VSP functions as a single, independent entity.

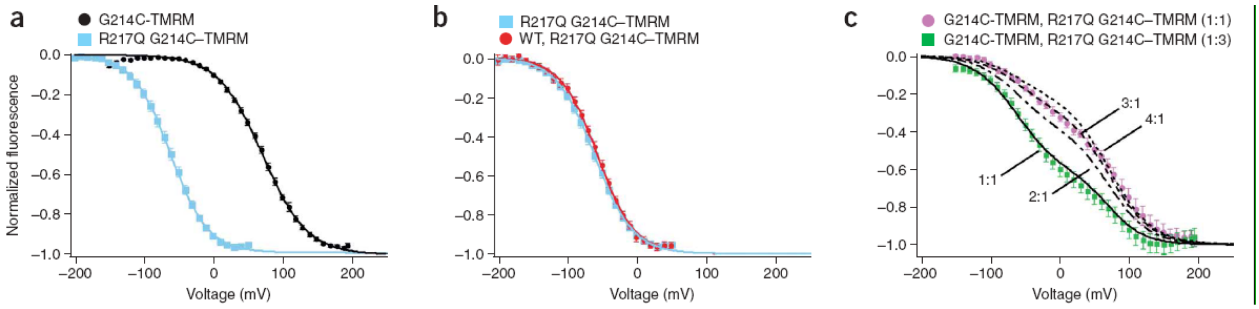

Figure 4.15. Ci-VSP monomers function independently. (A) FVs of G214C-TMRM (black) and R217Q/G214C-TMRM (blue). Solid lines are single Boltzmann fits. (B) FVs of R217Q/G214C-TMRM alone (blue) and R217Q/G214C-TMRM coinjected with WT (no added cysteine) (red). (C) Coinjection of two ratios of G214C-TMRM and R217Q/G214C-TMRM (magenta circles, 1:1; green squares, 1:3). FVs for the two ratios were well-fit by sum of two Boltzmanns with the V1/2 and slope values taken from the single Boltzmann fits to the individual F-Vs (from (a)) (see *Materials and Methods*). Fits from four fixed amplitude ratios in black. Figure from [10].

We attempted similar cooperativity experiments using the IRK1Q activity assay to determine whether two Ci-VSP mutants with different voltage dependencies of activity could influence each other. The maximum $V_{1/2}$ difference for AV curves observed using the IRK1Q assay was 77 mV when comparing Ci-VSP-G214C-R217Q and Ci-VSP-G214C-V220R. While this difference was less than the differences observed using VCF techniques, we hoped that co-injection of RNAs for Ci-VSP-G214C-R217Q and Ci-VSP-G214C-V220R with the IRK1Q reporter would produce a hybrid AV curve. Indeed, AV curve obtained for cells coinjected with a 1:1 ratio of RNAs for Ci-VSP-G214C-R217Q and Ci-VSP-G214C-V220R with IRK1Q displayed a hybrid AV curve that was both shifted in $V_{1/2}$ and slope compared with the independent activities of Ci-VSP-G214C-R217Q and Ci-VSP-G214C-V220R (Figure 4.16). However, the mechanism of multiple molecules of $PI(4,5)P_2$ binding to the IRK1Q reporter remained constant across all co-injection experiments and prevented us from definitively showing that the activities of Ci-VSP VSD mutants were not cooperative.

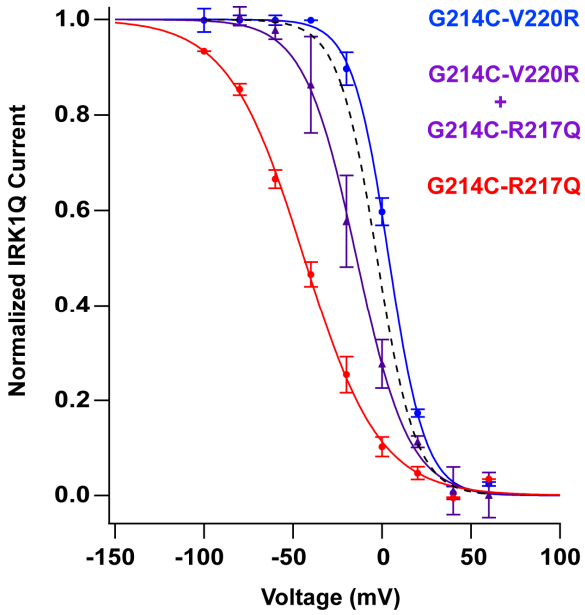

Figure 4.16. Co-injection IRK1Q activity assay experiments. AV curves obtained for Ci-VSP-G214C-R217Q (red); 1:1 coinjection of Ci-VSP-G214C-R217Q and Ci-VSP-G214C-V220R (purple), and Ci-VSP-G214C-V220R (blue). Black dotted line indicates Boltzmann fit from AV curve for CiVSP-G214C (Figure 4.13C). Solid lines represent Boltzmann fits. Error bars indicate SEM. For fit data, see Table 4.1.

Model for VSD-effector coupling

In channels, VSDs interact with the membrane pore domain and undergo at least one cooperative transition to open the channel (Figure 4.17A), while in Ci-VSP the VSD activates the cytoplasmic phosphatase, perhaps by docking it to the membrane (Figure 4.17B). We find that, unlike VSD-containing ion channels, Ci-VSP is an independent monomer, consistent with the finding that an isolated ion channel VSD is functional and structurally stable.[29] Strikingly, despite this architectural simplicity and the difference in effector, Ci-VSP undergoes multi-step rearrangements that resemble those of channels.[23, 24] Our results indicate that a single VSD can function in the membrane on its own, and that its orientation and essential features of its structural rearrangements are internally determined, consistent with the notion that VSDs function as loosely interacting modular domains.

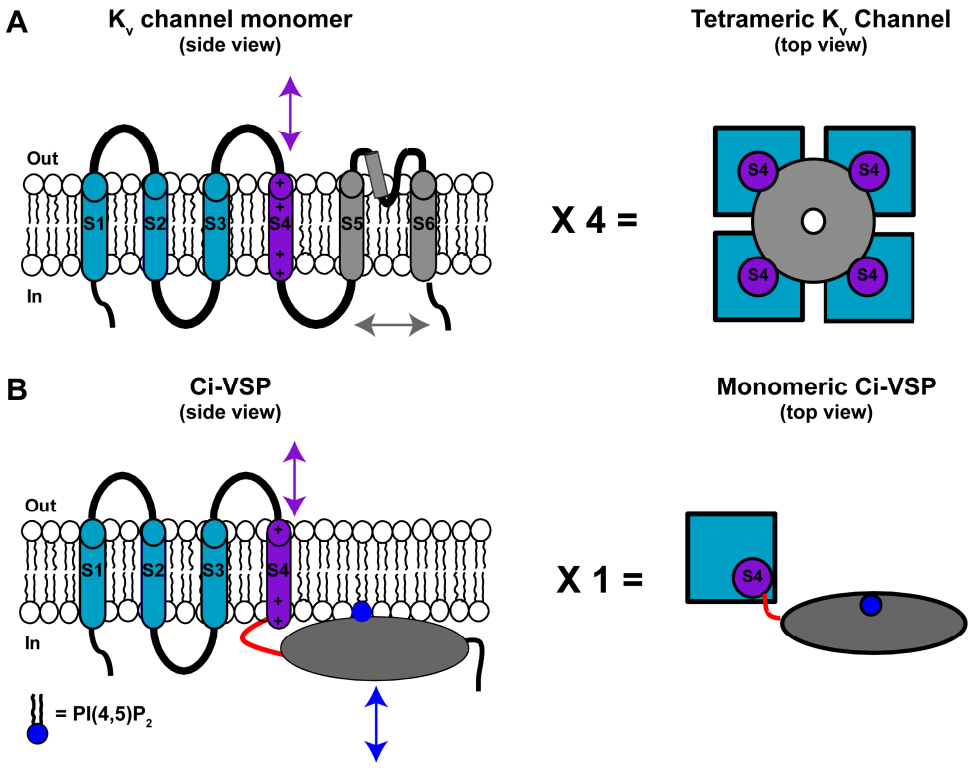

Figure 4.17. Model for coupling VSDs to effector domains. **(A)** Side and top views of K_v channel monomer (left) and tetrameric K_v channel (right). **(B)** Side and top views of Ci-VSP monomer (left) and functional monomeric phosphatase (right). $PI(4,5)P_2$ in dark blue). In both (A) and (B), arrows indicate both S4 and "gating" motions. Figure adapted from[10].

Mechanistic studies of electrochemical coupling in Ci-VSP

While we[10] and others[1, 12, 30, 31] have observed the tight coupling between the VSD and phosphatase domains of Ci-VSP, the mechanism by which the two domains are allosterically coupled is not well understood. We used mechanistic studies of PTEN activity as a guide in our efforts to better understand the mechanism Ci-VSP activity. The cytosolic domain of Ci-VSP (240-576) shares 29.5% sequence identity with PTEN (Figure 4.18A). The 16 amino acid linker connecting S4 and the phosphatase domain of Ci-VSP shares 43% sequence identity with the putative $PI(4,5)P_2$ binding domain (PBD) of PTEN (Figure 4.18B). Moreover, the catalytic domains of Ci-VSP and PTEN are 92% identical (Figure 4.18C). Combining biochemical and functional studies of Ci-VSP motions and activity in living cells, we studied the effects of mutations in the Ci-VSP PBD and catalytic domains as well as membrane concentrations of PIPs to further elucidate the mechanism of electrochemical coupling in Ci-VSP. This work is described in detail in Appendix 1 and reference [32].

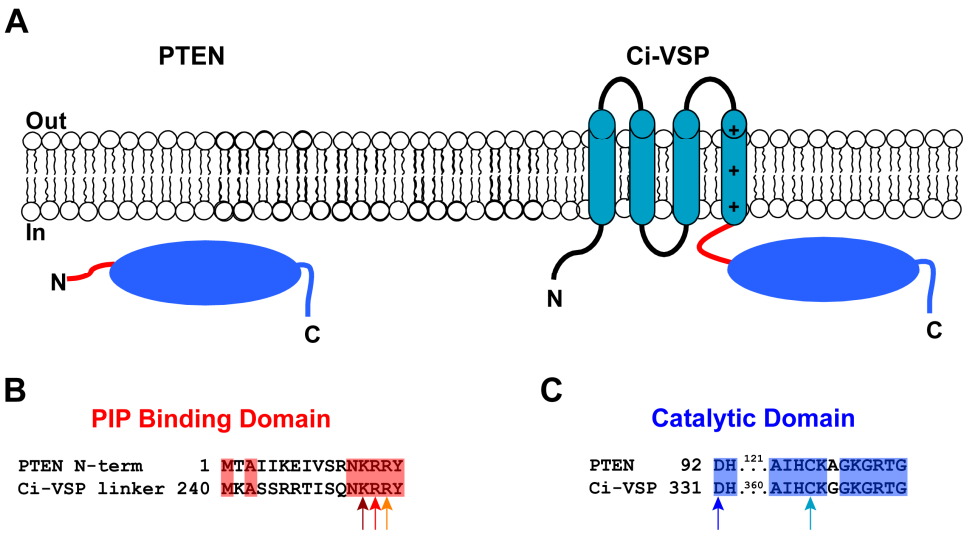

Figure 4.18. PTEN and Ci-VSP share regions of high homology. **(A)** Cartoon showing topology of PTEN and Ci-VSP. **(B)** Sequence alignment of putative PIP binding domain residues. **(C)** Sequence alignment of catalytic domain residues. The influence of residues highlighted by colored arrows in the electrochemical coupling of Ci-VSP is described in detail in Appendix 1 and reference [32].

Further characterization of voltage-dependent Ci-VSP phosphatase activity and substrate specificity

While the IRK1Q channel was a faithful reporter of $PI(4,5)P_2$ concentrations in *Xenopus laevis* oocytes, its utility in mechanistic studies of electrochemical coupling in Ci-VSP was not ideal. First, the dynamic voltage range of sensitivity for the IRK1Q reporter (approximately -100 mV to +60 mV) was not well-matched with the dynamic range of VSD motions measured by VCF and gating current measurements (approximately -20 mV to +100 mV) (Figure 4.11). This mismatch prevents the simultaneous study of how Ci-VSP VSD motion is directly coupled to phosphatase activity.

We tested the inwardly rectifying potassium channel $K_{ir}2.3$, (IRK3) with the hope that its dynamic range of activity would better match Ci-VSP VSD movement. IRK3 had been previously shown to have a lower apparent affinity for $PI(4,5)P_2$ of (29 μM) than IRK1 (5 μM).[33] This difference in $PI(4,5)P_2$ affinity is thought to be responsible for the increased sensitivity of IRK3 to phosphoinositide signaling pathways.[33, 34] The R228Q mutation in IRK1 has also been shown to lower the channels' affinity for $PI(4,5)P_2$ and respond more quickly to changes in $PI(4,5)P_2$ than the wild-type IRK channel.[15] We conducted a comparative study of IRK3 vs. IRK1Q as reporters of Ci-VSP activity. We rationalized that IRK3 may serve as a faster reporter of Ci-VSP mediated changes in $PI(4,5)P_2$ and the dynamic voltage range of IRK3 sensitivity to Ci-VSP activity may be shifted toward more positive voltages allowing us to access a voltage range for activity studies that was closer to the voltage range of VSD movement. The kinetics of IRK3 response to Ci-VSP mediated changes in $PI(4,5)P_2$ was not significantly different than the kinetics observed for IRK1Q (data not shown). Furthermore, the voltage range of IRK3

response to Ci-VSP mediated changes in $PI(4,5)P_2$ was not significantly different from that of the IRK1Q reporter (Figure 4.19). At this point, we decided to use only IRK1Q as a reporter of Ci-VSP mediated changes in $PI(4,5)P_2$.

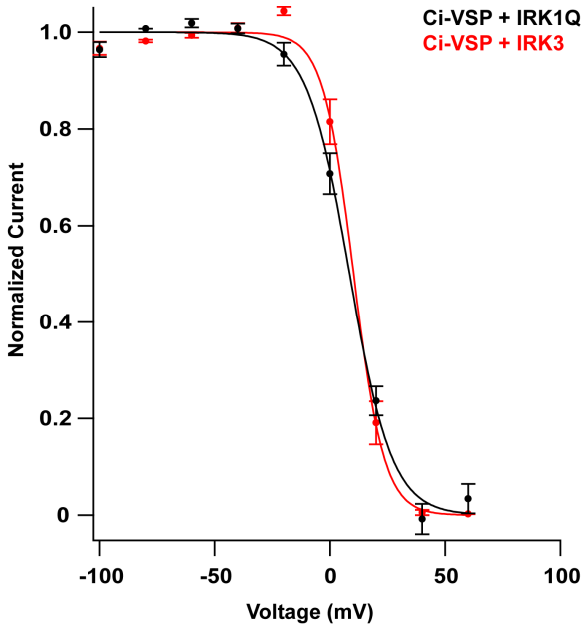

Figure 4.19. Comparison of IRK1Q and IRK3 as reporters of Ci-VSP activity. AV curves for Ci-VSP +IRK1Q (black), Ci-VSP +IRK3 (red). Solid lines represent single Boltzmann fits. Error bars indicate SEM. For fit data, see Table 4.1.

Another problem we faced with the IRK1Q assay was the nonlinearity between Ci-VSP production/hydrolysis of $PI(4,5)P_2$ and levels of IRK1Q current as four molecules of $PI(4,5)P_2$ are needed to activate one IRK1Q channel. Our initial activity experiments were conducted using a 10:1 Ci-VSP:IRK1Q ratio of injected RNAs. To control the ratio of Ci-VSP:IRK1Q protein expression so that one Ci-VSP would be attached to each IRK1Q subunit, we constructed fusion proteins where we appended Ci-VSP to the N or C-terminus of IRK1Q. While the appendage of Ci-VSP did not impair IRK1Q function, it slowed the response time to Ci-VSP activity by a factor of 2 and narrowed the voltage range of sensitivity compared with co-expression of Ci-VSP and IRK1Q separately (data not shown).

At this point, we decided to utilize fluorescent reporters of $PI(4,5)P_2$ and other PIPs to further characterize the voltage-dependence of phosphatase activity and substrate specificity of Ci-VSP. These efforts are described in detail in chapter 5 of this dissertation.

Experimental Contributions

Dr. Susy C. Kohout designed, conducted and analyzed the VCF experiments. Dr. Maximilian Ulbrich designed, conducted, and analyzed the single molecule subunit counting experiments. Sarah C. Bell designed, conducted and analyzed the *in vivo* activity assay. Professor Ehud Y. Isacoff helped design the VCF and *in vivo* activity assay experiments and supervised all research.

Materials and Methods

Molecular Biology. The Ci-VSP in the pSD64TF vector was kindly provided by Dr. Y. Okamura (National Institute for Physiological Sciences, Okazaki, Japan). Monomeric EGFP was fused to the C-terminal end of Ci-VSP using a short flexible linker (TSGGSGGSRGSGGSGG). The K_v1.4 C terminus (amino acids 586–654) was fused to the end of EGFP making the final Ci-VSP-GFP-K_v1.4C construct. The PSD-95 cDNA was kindly provided by Dr. P. Scheiffele (Columbia University, New York, NY). The IRK constructs were kindly provided by Dr. E. Reuveny (IRK1) (Weizmann Institute of Science, Rehovot, Israel) and Dr. L. Jan (IRK3) (University of California, San Francisco). All point mutations were made using QuikChange (Stratagene). All DNA was confirmed by DNA sequencing. RNA was transcribed using either T7 or SP6 mMessage mMachine (Ambion).

Single Molecule Counting of Subunits. We used a recently described method in which green fluorescent protein (mEGFP) is fused to a membrane protein, the fusion is expressed at low density in *Xenopus laevis* oocytes and total internal reflection fluorescence (TIRF) microscopy is used to visualize fluorescent spots and determine subunit stoichiometry by counting mEGFP bleaching steps. To do this, we engineered a fusion of mEGFP to the C terminus of Ci-VSP to ensure that every tagged subunit carries one chromophore. In addition, the C terminus of the potassium channel K_v1.4 was fused to the protein. By expressing the Ci-VSP-mEGFP-K_v1.4C with the synaptic protein PSD-95, which binds to the K_v1.4 C terminus, lateral diffusion of Ci-VSP in the membrane was reduced. The double tagged Ci-VSP-mEGFP-K_v1.4C was determined to function normally based on the IRK1Q activity assay (Figure 4.6).

Subunit counting experiments and analysis were conducted as described earlier.[8] Briefly, 50 nl mRNA at 0.02 μg μl^{-1} were injected into *Xenopus laevis* oocytes and incubated in ND-96 (96 mM NaCl, 2 mM KCl, 1.8 mM $CaCl_2$, 1 mM $MgCl_2$, 50 mg ml^{-1} gentamicin, 2.5 mM Na pyruvate and 5 mM HEPES, pH 7.6) at 12°C for 12–18 hours. Cells were then dropped onto a high refractive index coverslip and the fluorescence from the membrane was imaged with a high numerical aperture objective (Olympus 100x NA1.65). mEGFP was excited with a 488 nm laser, and high-quality dichroic mirrors and filters were used to maximize the yield of photons, which were detected with a state-of-the-art back-illuminated EMCCD camera (Andor iXon DV-897 BV). Movies of 500–800 frames were acquired using a frame rate of 20–33 Hz.

The center positions of the fluorescent spots were determined from the intensity peaks in the average of the first 5 illuminated frames of the movie. The time course of the fluorescence was extracted from regions of interest around these points as described in Ulbrich and Isacoff (2007).[8] Fluorescent spots that moved during the acquisition were excluded from the analysis. The traces were manually classified as containing one of two bleaching steps. A fraction of spots of about 10% could not be analyzed due to extreme fluctuations in intensity and therefore was not included in the population distributions.

Voltage clamp fluorometry. Voltage clamp fluorometry was performed as described previously[23]. Briefly, 50 nl mRNA at 0.4–0.8 μg-μl^{-1} were injected into *Xenopus laevis* oocytes and incubated in ND-96 at 18°C for 24–48 hours. For the fluorescence coinjection experiments,

the total concentration of mRNA was 0.4 μg-μl^{-1} and the ratio of G214C to R217Q/G214C was varied from 1:1 to 1:3. Injected oocytes were treated with a 1 mM solution of glycine maleimide[35] to block native cysteines before protein expression. A Nikon Diaphot inverted microscope with a 20X 0.75 NA fluorescence objective (Nikon) was used with a Dagan CA-1 amplifier (Dagan Corporation), illuminated with a 100 W mercury arc lamp and intensity was measured with a Hamamatsu HC120-05 photomultiplier tube. The amplifier, photomultiplier and Uniblitz shutter (Vincent Associates) were controlled by the Digidata-1200 board and PClamp8 software package (Axon Instruments). Light was filtered through an HQ535/50 excitation filter, an HQ610/75 emission filter and a Q565LP dichroic (Chroma Technology). Fluorescence signals were low pass filtered at 2 kHz through an eight-pole Bessel filter (Frequency Devices).

On the day of the experiment, cells were incubated in a high potassium solution (92 mM KCl, 0.75 mM$CaCl_2$, 1 mM $MgCl_2$, 10 mM HEPES, pH7.5) and 25 μM tetramethylrhodamine-6-maleimide (Invitrogen) for one hour on ice and in the dark. After extensive washing with ND-96, the cells were stored in ND-96, in the dark and at 12^{o}C until the time of the experiment. Recording solutions contained 110 mM N-methyl-D-glucamine (NMG) methanesulfonic acid (MES), 2 mM KMES, 2 mM $Ca(MES)_2$, 10 mM HEPES, pH 7.5.

Electrophysiological measure of activity. We measured catalytic activity using an electrophysiological assay. Ci-VSP catalytic activity was measured indirectly by detecting the catalytic product, phosphatidylinositol-4,5-bisphosphate ($PI(4,5)P_2$), via its activation of the inwardly-rectifying IRK1 R228Q K^+ channel (IRK1Q). The R228Q mutation of IRK1 was used to alter the sensitivity of the channel for $PI(4,5)P_2$ into an observable range.[15] Voltage was held at different levels with a test every 30 s consisting of a 10 ms step to –100 mV to measure inward current, followed by a 70 ms ramp to 50 mV, confirming that the current was due to IRK1Q and not leak (Figure 4.5). To reach steady-state currents at each voltage required multiple iterations of the protocol, reflecting the time it takes to establish a steady-state level of $PI(4,5)P_2$ at each level of Ci-VSP activity (Figure 4.10B).

For these experiments, 50 nl of mRNA for Ci-VSP and IRK1Q were coinjected into *Xenopus laevis* oocytes at a 10:1 ratio with a total RNA concentration of ~0.9 μg-μl^{-1}. Cells were incubated in ND-96 at 18^{o}C for 16–48 hours. The recording solutions contained 90 mM KMES, 3 mM $Mg(MES)_2$, 8 mM KOH, 10 mM HEPES, pH 7.4. Other conditions were the same as for VCF.

Data Analysis. All image analysis was done in Mathematica as described previously.[8] Kinetic and steady-state traces were analyzed using Igor Pro and Microsoft Excel software. Kinetic traces were fit with either single or double exponential equations. Steady-state voltage dependent traces were fit with Boltzmann equations. Data were normalized to the amplitude of the Boltzmann fits and the error bars indicate the standard error of the mean. Statistical signifance was assessed using the Student's t-test.

IRK1Q Activity Analysis. The activity experiments with IRK1Q were leak subtracted by assuming a voltage-independent linear leak. Current was measured at –100 mV after the test holding potential and leak was measured at +50 mV where the IRK channels should be blocked

by Mg^{2+} and polyamines and the following equation applied to calculate the leak subtracted (LS) current: $I_{LS} = I_{-100mV} + 2I_{+50mV}$. Multiple iterations of the protocol were tested per holding potential to reach steady-state levels of current. For voltages where steady-state currents could not be reached, the data were extrapolated using a single exponential. We examined the ability of IRK1Q currents to follow $PI(4,5)P_2$ concentration from maximal to minimal Ci-VSP activity. IRK currents were evoked once every 30 s by 10 ms test steps to –100 mV to measure inward current, followed by a 70 ms ramp to 50 mV to measure inward rectification. The initial holding potential was 60 mV to obtain a baseline of minimal IRK1Q current at the minimal $PI(4,5)P_2$ concentration. The holding potential was then switched to –100 mV, to drive the maximal increase in $PI(4,5)P_2$ concentration and IRK1Q current (see Figure 4.7B). This enabled us to follow the time course of IRK1Q current increase and determine if there was any delay that could be accounted for if the minimal $PI(4,5)P_2$ concentration fell below what is required to significantly activate IRK1Q. We observed no such delay, and found instead that the increase in current was well fit by a single exponential (Figure 4.7B). Alternatively, the protocol was reversed to start at the maximal PIP_2 concentration (holding potential of –100 mV) and switch to the minimal concentration (holding potential of 60 mV). Here too, no lag was observed and the time course of current decrease was well fit by exponentials (Figure 4.7A). The observations indicate that the IRK1Q report is within the dynamic range of changes in $PI(4,5)P_2$ concentration that result from voltage-driven changes in Ci-VSP activity.

IRK1Q Jump Protocol Activity Analysis (Figure 4.7 and 4.8). IRK1Q currents evoked by test steps from a holding potential of –100 mV, once every 5 s for 40 sweeps (data not shown) to establish a flat baseline. The interval between the test steps was then shortened to 580 ms. After 10 more sweeps at the holding potential of –100 mV, the holding potential was switched to +60 mV (protocol in box) and test steps were continued once every 580 ms, leading to an exponential decrease in IRK1Q current with no lag. Data fit with double exponential. Absence of lags indicates that the voltage-driven changes in Ci-VSP activity lead to changes in PIP_2 concentration that are within the dynamic range of the reporter, IRK1Q. Test steps to –100 mV evoked IRK1Q currents, whose leak-subtracted amplitudes (from the ramp) are plotted over time. Test steps from a holding potential of +60 mV evoked currents once every 10 s to establish a flat baseline of IRK1Q current. After 10 such sweeps, the holding potential was switched to –100 mV (protocol on top), leading to an exponential increase in IRK1Q current with no lag. Data fit with single exponential.

Analysis of fluorescence assay of independence versus cooperativity. The data analysis in Figure 4.15C was as follows: Single Boltzmann relations were fitted to the individual F-Vs obtained for G214C-TMRM alone and for R217Q/G214C-TMRM alone (Figure 4.15A and B). These single Boltzmanns were added linearly in four different ratios (solid line, 1:1; dashed-dotted line, 2:1; dashed line, 3:1; dotted line 4:1) and compared to two data sets. The data sets came from coinjection of the cRNAs for G214C-TMRM and R217Q/G214C-TMRM at two different ratios (Figure 4.15C), magenta circles, 1:1 and green squares, 1:3). G214C-TMRM was found to expresses better than R217Q/G214C-TMRM so that the coinjection favoring the more weakly expressing R217Q/G214C-TMRM by 3 fold only resulted in a slighter greater proportion of R217Q/G214C-TMRM (1:1.75). Data were fit to a double Boltzmann equation keeping the $V_{1/2}$ and slope values from the single injection data constant. The resulting amplitudes from

G214C-TMRM and R217Q/G214C-TMRM components were, respectively, 0.43 and 0.57 for green squares; 0.71 and 0.29 for magenta circles.

Table 4.1. IRK1Q activity assay (AV) curve fit data. Data obtained using long IRK1Q protocol described above. Data for each construct were normalized, averaged and plotted as a function of voltage step. Averaged data were fit to single Boltzmann using IGOR. $V_{1/2}$ represents the midpoint of the activity vs. voltage (AV) relationships, slope represents the slope of the fit, and n represents the number of individual cells tested.

Protein(s)	$V_{1/2}$ (mV)	slope	n
IRK1Q	ND	ND	9
Ci-VSP + IRK1Q	8.5 ± 1.3	9.3 ± 1.1	18
Ci-VSP-mEGFP-K_v1.4C + IRK1Q	16.2 ± 1.6	6.1 ± 1.6	11
Ci-VSP-V207C+IRK1Q	8.3 ± 1.8	7.9 ± 1.3	9
Ci-VSP-V207C-R217Q + IRK1Q	-41.1 ± 0.9	18.7 ± 0.8	9
Ci-VSP-Q208C + IRK1Q	8.6 ± 2.9	7.1 ± 1.9	10
Ci-VSP-G214C +IRK1Q	-2.8 ± 0.9	10.9 ± 0.9	11
Ci-VSP-G214C-R217Q + IRK1Q	-43.8 ± 2.1	21.3 ± 1.9	15
Ci-VSP-G214C-V220R + IRK1Q	3.8 ± 0.7	10.3 ± 0.7	3
Ci-VSP-G214C-R217Q + Ci-VSP-G214C-V220R + IRK1Q	-14.3 ± 1.6	14.7 ± 1.5	4
Ci-VSP + IRK3	10.2 ± 1.2	6.6 ± 0.7	6

Table 4.2. VCF assay (FV) fit data. Effects of VSD charge mutations on VSD motion, as gauged by FVs measured from TMRM attached to two cysteine substitution sites outside S4. Values of parameters from single Boltzmann fits to the entire fluorescence vs. voltage (F-V) relation except where noted in parentheses. Asterisk (*) denotes labeling with TMRM

Protein(s)	$V_{1/2}$ (mV)	slope	n
G214C*	71.2 ± 0.8	30.3 ± 0.7	13
G214C*-R217Q (-200mV to +30mV)	-60.7 ± 0.3	28.2 ± 0.3	11
G214C*-V220R	142.6 ± 1.8	30.8 ± 1.0	10
V207C* (-140mV to +120mV)	-1.9 ± 0.8	28.9 ± 0.8	13
V207C*-R217Q (-30mV to +190mV)	102.3 ± 0.6	28.0 ± 0.6	10
G214C* (Figure 4.15A)	70.8 ± 0.5	32.0 ± 0.5	13
G214C*-R217Q (Figure 4.15A)	–61.3 ± 0.4	27.7 ± 0.4	11
G214C*-R217Q + Ci-VSP (Figure 4.15B)	–56.7 ± 0.9	26.5 ± 0.8	6

Acknowledgments

This work was supported by a postdoctoral fellowship (to M.H.U.) from the American Heart Association, and by grant R01NS035549 from the National Institutes of Health. We thank Dr. F. Tombola, Dr. H. Janovjak, Dr. M. Pathak and Dr. S. Pautot for technical assistance and helpful discussions. We also thank Alex Kintzer, a chemical biology rotation student, for conducting initial experiments with the IRK3 and Ci-VSP-IRK1Q fusions.

References

1. Murata, Y., et al., Phosphoinositide phosphatase activity coupled to an intrinsic voltage sensor. *Nature* **2005,** 435, (7046), 1239-1243.

2. Sasaki, M.; Takagi, M.; Okamura, Y., A voltage sensor-domain protein is a voltage-gated proton channel. *Science* **2006,** 312, (5773), 589-92.

3. Ramsey, I. S.; Moran, M. M.; Chong, J. A.; Clapham, D. E., A voltage-gated proton-selective channel lacking the pore domain. *Nature* **2006,** 440, (7088), 1213-6.

4. Lu, Z.; Klem, A. M.; Ramu, Y., Ion conduction pore is conserved among potassium channels. *Nature* **2001,** 413, (6858), 809-13.

5. Long, S. B.; Campbell, E. B.; MacKinnon, R., Crystal structure of a mammalian voltage-dependent Shaker family K^+ channel. *Science* **2005,** 309, (5736), 897-903.

6. Tombola, F.; Pathak, M. M.; Isacoff, E. Y., How does voltage open an ion channel? *Annu. Rev. Cell Dev. Biol.* **2006,** 22, (1), 23-52.

7. Lee, J. O., et al., Crystal structure of the PTEN tumor suppressor: implications for its phosphoinositide phosphatase activity and membrane association. *Cell* **1999,** 99, (3), 323-34.

8. Ulbrich, M. H.; Isacoff, E. Y., Subunit counting in membrane-bound proteins. *Nat. Meth.* **2007,** 4, (4), 319-321.

9. Shaner, N. C.; Patterson, G. H.; Davidson, M. W., Advances in fluorescent protein technology. *J. Cell Sci.* **2007,** 120, (24), 4247-4260.

10. Kohout, S. C.; Ulbrich, M. H.; Bell, S. C.; Isacoff, E. Y., Subunit organization and functional transitions in Ci-VSP. *Nat. Struct. Mol. Biol.* **2008,** 15, (1), 106-108.

11. Maehama, T.; Dixon, J. E., The tumor suppressor, PTEN/MMAC1, dephosphorylates the lipid second messenger, phosphatidylinositol 3,4,5-trisphosphate. *J. Biol. Chem.* **1998,** 273, (22), 13375-13378.

12. Murata, Y.; Okamura, Y., Depolarization activates the phosphoinositide phosphatase Ci-VSP, as detected in Xenopus oocytes coexpressing sensors of PIP_2. *J Physiol* **2007,** 583, (3), 875-889.

13. Niggli, V., Regulation of protein activities by phosphoinositide phosphates. *Annu. Rev. Cell Dev. Biol.* **2005,** 21, 57-79.

14. Huang, C.-L.; Feng, S.; Hilgemann, D. W., Direct activation of inward rectifier potassium channels by PIP_2 and its stabilization by $G_{\beta\gamma}$. *Nature* **1998,** 391, (6669), 803-806.

15. Zhang, H., et al., Activation of inwardly rectifying K^+ channels by distinct PtdIns(4,5)P_2 interactions. *Nat. Cell Biol.* **1999,** 1, (3), 183-8.

16. Mannuzzu, L. M.; Moronne, M. M.; Isacoff, E. Y., Direct physical measure of conformational rearrangement underlying potassium channel gating. *Science* **1996,** 271, (5246), 213-216.

17. Pathak, M. M., et al., Closing in on the resting state of the Shaker K^+ channel. *Neuron* **2007,** 56, (1), 124-140.

18. Mannuzzu, L. M.; Isacoff, E. Y., Independence and cooperativity in rearrangements of a potassium channel voltage sensor revealed by single subunit fluorescence. *J Gen Physiol* **2000,** 115, (3), 257-68.

19. Schoppa, N. E.; Sigworth, F. J., Activation of Shaker potassium channels. III. An activation gating model for wild-type and V2 mutant channels. *J Gen Physiol* **1998,** 111, (2), 313-42.

20. Baker, O. S.; Larsson, H. P.; Mannuzzu, L. M.; Isacoff, E. Y., Three transmembrane conformations and sequence-dependent displacement of the S4 domain in shaker K+ channel gating. *Neuron* **1998,** 20, (6), 1283-94.

21. Ledwell, J. L.; Aldrich, R. W., Mutations in the S4 region isolate the final voltage-dependent cooperative step in potassium channel activation. *J Gen Physiol* **1999,** 113, (3), 389-414.

22. Pathak, M.; Kurtz, L.; Tombola, F.; Isacoff, E., The cooperative voltage sensor motion that gates a potassium channel. *J Gen Physiol* **2005,** 125, (1), 57-69.

23. Mannuzzu, L. M.; Moronne, M. M.; Isacoff, E. Y., Direct physical measure of conformational rearrangement underlying potassium channel gating. *Science* **1996,** 271, (5246), 213-6.

24. Cha, A.; Bezanilla, F., Characterizing voltage-dependent conformational changes in the Shaker K+ channel with fluorescence. *Neuron* **1997,** 19, (5), 1127-40.

25. Dimitrov, D., et al., Engineering and characterization of an enhanced fluorescent protein voltage sensor. *PLoS ONE* **2007,** 2, (5), e440.

26. Gandhi, C. S.; Isacoff, E. Y., Molecular models of voltage sensing. *J. Gen. Physiol.* **2002,** 120, (4), 455-63.

27. Tiwari-Woodruff, S. K.; Lin, M. A.; Schulteis, C. T.; Papazian, D. M., Voltage-dependent structural interactions in the Shaker K^+ channel. *J. Gen. Physiol.* **2000,** 115, (2), 123-38.

28. Gandhi, C. S.; Loots, E.; Isacoff, E. Y., Reconstructing voltage sensor-pore interaction from a fluorescence scan of a voltage-gated K+ channel. *Neuron* **2000,** 27, (3), 585-95.

29. Jiang, Y., et al., X-ray structure of a voltage-dependent K+ channel. *Nature* **2003,** 423, (6935), 33-41.

30. Villalba-Galea, C. A.; Miceli, F.; Taglialatela, M.; Bezanilla, F., Coupling between the voltage-sensing and phosphatase domains of Ci-VSP. *J. Gen. Physiol.* **2009,** 134, (1), 5-14.

31. Villalba-Galea, C. A.; Sandtner, W.; Starace, D. M.; Bezanilla, F., S4-based voltage sensors have three major conformations. *Proc. Natl. Acad. Sci. U. S. A.* **2008,** 105, (46), 17600-17607.

32. Kohout, S. C., et al., Electrochemical coupling in the voltage-dependent phosphatase Ci-VSP. *Nat. Chem. Biol.* **2010,** 6, (5), 369-375.

33. Du, X., et al., Characteristic interactions with phosphatidylinositol 4,5-bisphosphate determine regulation of K_{ir} channels by diverse modulators. *J. Biol. Chem.* **2004,** 279, (36), 37271-37281.

34. Shen, W., et al., Cholinergic modulation of $K_{ir}2$ channels selectively elevates dendritic excitability in striatopallidal neurons. *Nat. Neurosci.* **2007,** 10, (11), 1458-1466.

35. Borah, H. N.; Boruah, R. C.; Sandhu, J. S., Microwave-induced one-pot synthesis of N-carboxyalkyl maleimides and phthalimides. *Journal of Chemical Research-S* **1998**, (5), 272-+.

Chapter 5

Fluorescence methods to monitor multiple Ci-VSP reactions in living cells

Introduction

Ciona intestinalis voltage-sensor containing phosphatase (Ci-VSP) is the first reported voltage-gated phosphatase.[1] Ci-VSP contains four transmembrane segments (S1-S4) that form a voltage-sensing domain (VSD) resembling the VSD of a voltage-gated potassium (K_v) channel and a cytosolic phosphoinositide phosphatase domain that shares 29.5% sequence identity with the phosphatase and tensin homolog PTEN (Figure 1A). While the isolated Ci-VSP phosphatase domain is constitutively active against a variety of phosphoinositides (PIPs) *in vitro*[1, 2], recent research has shown that in living cells, Ci-VSP is a depolarization-activated D5-phosphoinositide phosphatase that hydrolyzes the D5 phosphate group of phosphatidylinositol- 3,4,5-trisphosphate ($PI(3,4,5)P_3$) and phosphatidylinositol-4,5-bisphosphate ($PI(4,5)P_2$) (Figure 1B).[3]

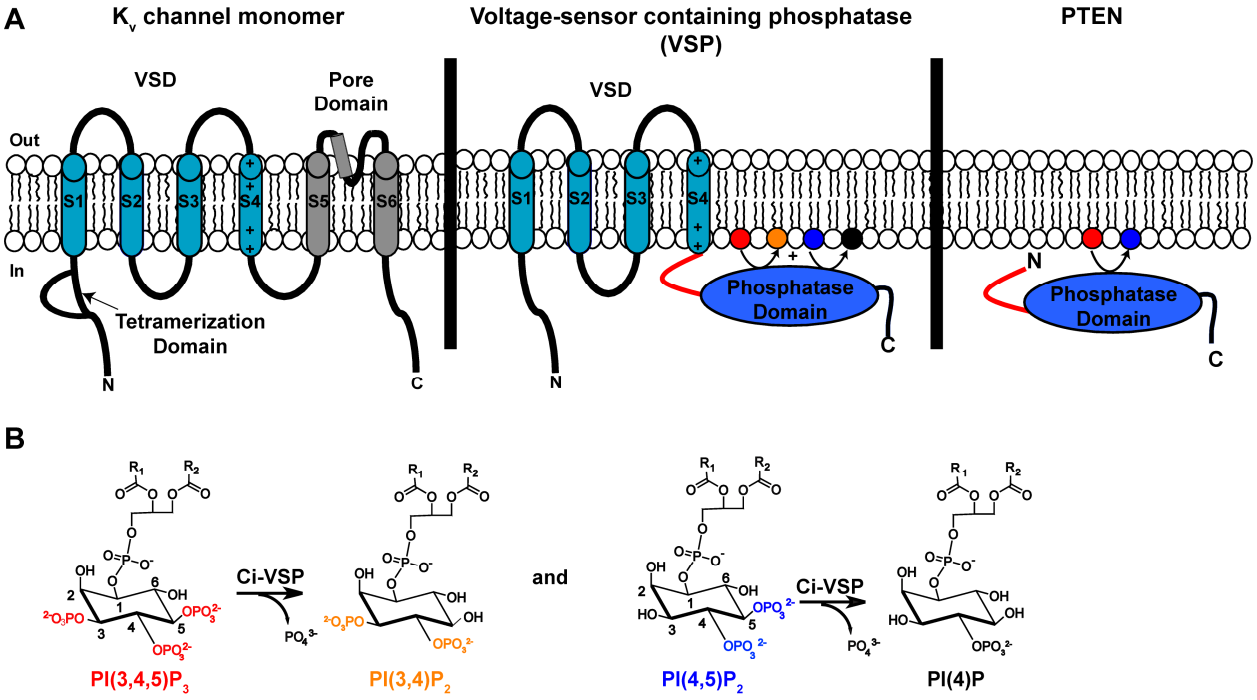

Figure 5.1. Ci-VSP topology and catalytic reactions. **(A)** Comparison of Ci-VSP topology (middle) with K_v channels (left) and PTEN (right). Ci-VSP contains 4 transmembrane segments (S1-S4) that are homologous to the voltage sensing domain (VSD) of a voltage-gated potassium channel. The cytosolic phosphatase domain of Ci-VSP shares 29.5% sequence identity with PTEN. **(B)** Proposed Ci-VSP mediated reactions in living cells in which Ci-VSP acts as a D5 phosphoinositide phosphatase and hydrolyzes $PI(3,4,5)P_3$ to create $PI(3,4)P_2$ and hydrolyzes $PI(4,5)P_2$ to form PI(4)P.

While the VSD and phosphatase domains of Ci-VSP are tightly coupled,[1, 4-6] the precise roles of these domains in regulating Ci-VSP catalysis and substrate specificity *in vivo* have not yet been elucidated. Current methods of assessing Ci-VSP activity *in vivo* have primarily relied on ion-channel based reporters that are sensitive to $PI(4,5)P_2$, a proposed substrate and/or

product of Ci-VSP. $PI(4,5)P_2$ is the major PIP in the plasma membrane and regulates a variety of ion channels including inwardly rectifying K^+ (K_{ir}) channels, voltage dependent K^+ (K_v) channels, and transient receptor potential (TRP) channels.[7]

We began our study of the voltage dependence of Ci-VSP activity using an inwardly rectifying potassium $K_{ir}2.1$-R228Q (IRK1Q) channel,[8] which directly binds $PI(4,5)P_2$, as a downstream reporter of Ci-VSP phosphatase activity. The IRK1Q channel is tetrameric and requires four molecules of $PI(4,5)P_2$ to stabilize the open state of the channel (Figure 5.2A). In the presence of greater extracellular concentrations of K^+ IRK1Q will conduct K^+ ions into the cell. This K^+ flux through the IRK1Q channel can be recorded using electrophysiology techniques.

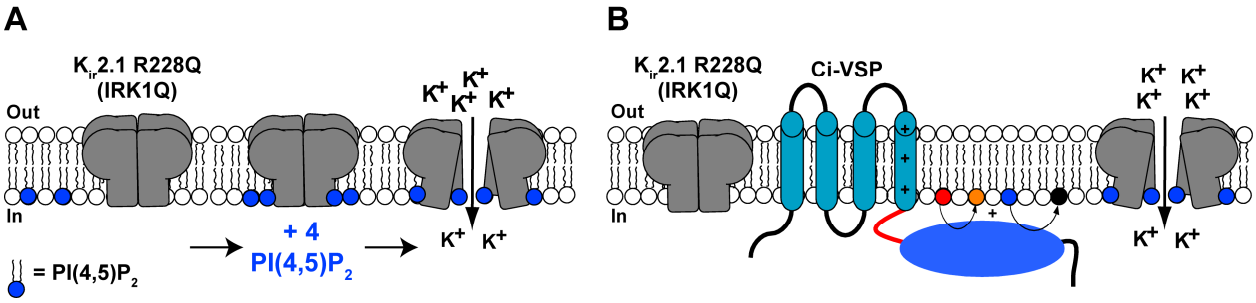

Figure 5.2. Schematic for IRK1Q activity assay. (A) $PI(4,5)P_2$ acts as an agonist of IRK1Q channels where four molecules of $PI(4,5)P_2$ are required for channel activation. **(B)** IRK1Q activity is modulated by voltage-dependent Ci-VSP depletion of $PI(4,5)P_2$ thus serving as a downstream reporter of Ci-VSP activity.

While the IRK1Q channel is a faithful reporter of $PI(4,5)P_2$ concentrations in *Xenopus laevis* oocytes, its utility in mechanistic studies of electrochemical coupling in Ci-VSP was not ideal. First, the dynamic voltage range of sensitivity for the IRK1Q reporter (approximately -100 mV to +60 mV) was not well-matched with the dynamic range of VSD motions measured by voltage-clamp fluorometry and gating current measurements (approximately -20 mV to +100 mV) (Figure 5.3).

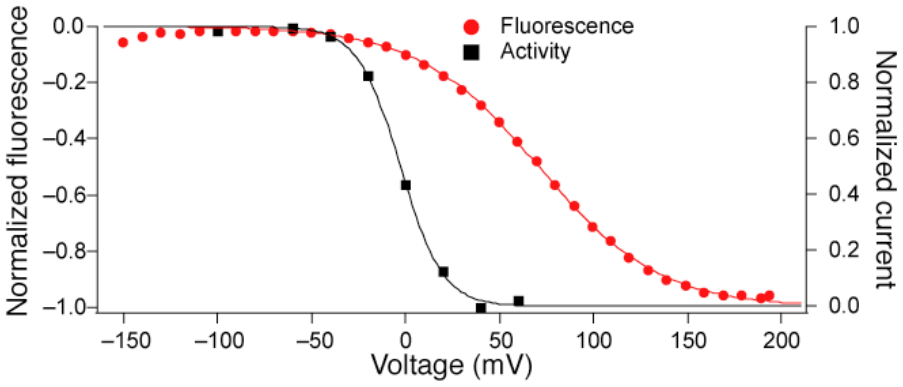

Figure 5.3. Superposition of Ci-VSP-G214C activity and VSD motions. Steady-state voltage dependence of IRK1Q current (enzymatic activity) (black) and of fluorescence (VSD motion) (red) for G214C-TMRM. Solid lines represent single Boltzmann fits. Error bars (smaller than symbols) indicate SEM. For fit data, see Tables 5.3. Figure from[9].

This mismatch complicated the study of how Ci-VSP VSD motion is directly coupled to phosphatase activity. Secondly, the 4:1 PIP:channel stoichiometry complicated our efforts to accurately measure the kinetics of Ci-VSP mediated changes in $PI(4,5)P_2$ pools. Finally, as Ci-VSP has recently been shown to change the concentrations of multiple PIP pools[3, 10], the IRK1Q channel report of $PI(4,5)P_2$ does not accurately follow all Ci-VSP mediated reactions.

In addition to ion channel regulation, $PI(4,5)P_2$ and other phosphoinositides mediate many cellular processes through their interactions with cytosolic proteins. These interactions are mediated by electrostatic interactions between the negatively charged phosphate groups on the inositol ring of the PIP and basic residues on the protein's surface.[11] The PIP interacting regions of proteins can be unstructured, as is the case in numerous cytoskeleton binding proteins where clusters of basic amino acids create a positively charged surface which binds the negatively charged head group of a PIP.[12, 13] Alternatively, PIP binding domains can form a structured PIP binding pocket, as is the case in proteins containing pleckstrin homology (PH) domains. This structured binding pocket allows for specific binding one or more phosphoinositide binding partners.

Fluorescent protein-pleckstrin homology (FP-PH) domain fusions have been extensively used as tools to study phosphoinositide dynamics in living cells.[14] When expressed in living cells, these cytosolic proteins reversibly bind to the membrane when high concentrations of its PIP binding partner are present. This movement results in increased fluorescence signal at the plasma membrane. As concentrations of the PIP binding partner decrease, the FP-PH protein translocates to the cytosol, resulting in a decrease of fluorescence at the plasma membrane. These fluorescence changes can be monitored using epifluorescence, confocal or total-internal reflection fluorescence (TIRF) microscopy.[15] As many PH domains specifically bind one or two PIP binding partners, a single FP-PH reporter can track a distinct PIP species in cells. Also, there are many green fluorescent protein (GFP) analogs that have spectrally separable properties[16] which allows for the use of multiple FP-PH domains to simultaneously monitor multiple PIP species in a single cell. Finally, the 1:1 reporter:PIP stoichiometry allows for more

accurate monitoring of the kinetics of Ci-VSP mediated changes in PIP pools than channel-based PIP reporters.

FP-PH domains have been used by two groups to study the substrate specificity of Ci-VSP in living cells.[3, 10] Most recently, Halaszovich *et al.* used TIRF microscopy to study Ci-VSP activity in Chinese Hamster Ovary (CHO) cells. By coexpressing Ci-VSP with FP-PH domain reporters of each possible Ci-VSP substrate and product, and combining TIRF microscopy and patch clamping techniques, they found that Ci-VSP acts as a depolarization activated dual-function D5 phosphoinositide phosphatase.[3] Halaszovich *et al.* demonstrated that membrane depolarization activates Ci-VSP to hydrolyze $PI(4,5)P_2$ and produce PI(4)P, thus confirming the previous biochemical data suggesting that Ci-VSP was a D5 phosphoinositide phosphatase (Figure 5.1B).[2] Also, membrane depolarization causes a Ci-VSP mediated decrease in $PI(3,4,5)P_3$ with concomitant generation of $PI(3,4)P_2$ (Figure 5.1B).

While Halaszovich and co-workers demonstrated the D5 phosphoinositide phosphatase activity of Ci-VSP, their method to monitor Ci-VSP activity in living cells has three limitations:

1. Temporal resolution of Ci-VSP activity was not achieved as images were collected at 3s intervals.

2. Single cell experiments measuring the effects of Ci-VSP activity on multiple PIP pools were not conducted.

3. Whole cell patch clamp techniques cause dialysis of cytosolic cofactors[17] that may be necessary for proper Ci-VSP function.

Here, we develop a new method combining electrophysiology and fluorescence microscopy to monitor Ci-VSP mediated changes in concentrations of multiple PIP species using FP-PH domains in *Xenopus laevis* oocytes. This method can be used to follow Ci-VSP mediated changes in multiple PIP pools in a single cell with millisecond time resolution minimal perturbation to the interior of the cell.

Method Development

FP-PH domains have been extensively characterized in mammalian cell systems and are used to study phosphoinositide dynamics in a variety of contexts.[18] However, there are few reports noting the utility of these sensors in *Xenopus laevis* oocytes. The oocyte is a robust heterologous expression system for membrane proteins and serves as model system for biophysical characterization of voltage-sensitive membrane proteins.[19] In the animal pole of the oocytes, there is a dark pigment layer that separates the yolk from the plasma membrane.[20] This pigment layer shields autofluorescence from the yolk of the oocyte, and allows for the direct imaging of fluorescent proteins near the plasma membrane. In 2004, Zhang and co-workers demonstrated that an EGFP-tagged PH domain from phospholipase C-δ1 ($EGFP\text{-}PH_{PLC}$) accurately followed changes $PI(4,5)P_2$ concentrations levels in the plasma membrane of *Xenopus laevis* oocytes.[21] Murata and Okamura co-expressed Ci-VSP with FP-PH domain reporters for

either $PI(4,5)P_2$ or $PI(3,4,5)P_3$ in *Xenopus laevis* oocytes and used confocal microscopy to monitor Ci-VSP mediated changes in these PIP concentrations. They found that membrane depolarization resulted in Ci-VSP mediated decreases in both $PI(4,5)P_2$ and $PI(3,4,5)P_3$ but did not determine the exact products of Ci-VSP activity.[10] The Isacoff lab has utilized *Xenopus laevis* oocytes for the expression of fluorescently tagged membrane proteins in numerous contexts.[22, 23]

The Isacoff lab has also pioneered the development of voltage-clamp fluorometry (VCF) in *Xenopus laevis* oocytes to study voltage dependent protein motion of voltage-gated ion channels and phosphatases.[6, 9, 24] VCF couples two-electrode voltage clamp (TEVC) techniques to control membrane voltage with fluorescence microscopy to gain a real-time optical report of voltage-dependent conformational changes at specific regions of a membrane protein (Figure 5.4).[25]

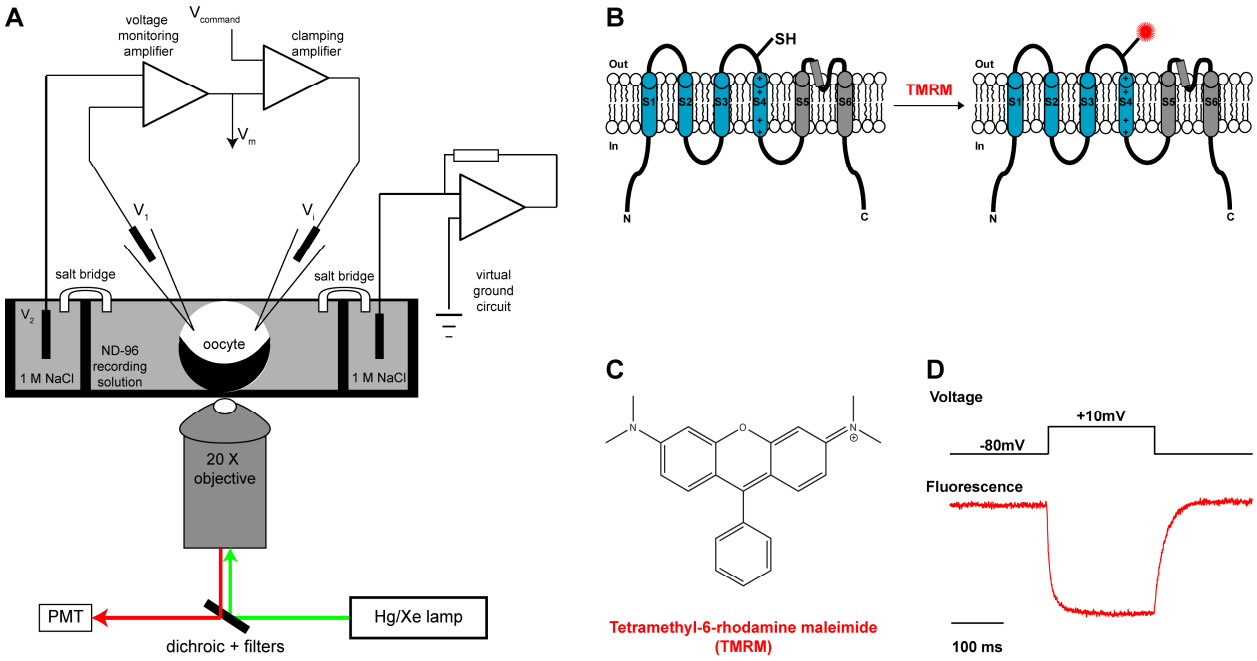

Figure 5.4. Voltage Clamp Fluorometry (VCF) method. (A) Electrophysiology set-up for VCF experiments. Diagram adapted from [26]. **(B)** Cartoon depicting tetramethyl-6-rhodamine maleimide (TMRM) labeling of Shaker channel bearing engineered cysteine residue near the S4 segment**. (C)** Chemical structure of TMRM. **(D)** Example fluorescence trace showing changes in TMRM fluorescence in response to depolarizing voltage step. TMRM fluorescence monitors voltage-dependent conformational changes.

In this method, a voltage-gated ion channel is genetically engineered to include a cysteine residue in a solvent-accessible region and the protein is expressed in a *Xenopus laevis* oocyte. Next, the cell is treated with a thiol-reactive probe containing an environmentally sensitive fluorophore such as tetramethylrhodamine-6-maleimide (Figure 5.4B). The oocyte is then voltage-clamped in a TEVC configuration. The TEVC configuration allows for precise control of membrane voltage across the entire oocyte membrane without dialysis of the cytosol. The

electrophysiology set-up is coupled to a fluorescence microscope equipped with a lamp and filters to excite the fluorophore and a photomultiplier tube (PMT) to measure changes in the fluorophore emission (Figure 5.4A). A voltage-dependent conformational change near the fluorophore will cause a change in the fluorescence intensity (Figure 5.4D). The kinetics of these fluorescence changes reflect the kinetics of voltage-dependent structural rearrangements in the ion channel and can be related to the kinetics of ion current flow through the channel which is measured by TEVC. This method has been used extensively to characterize the voltage-dependent conformational changes responsible for opening and closing the Shaker potassium channel.[24] Recently, we extended this methodology to characterize the voltage-gated phosphatase Ci-VSP.[6, 9]

We utilized the same VCF set-up to monitor Ci-VSP mediated changes in phosphoinositide concentrations at the plasma membrane. The experimental set up is shown in Figure 5.5. An oocyte expressing Ci-VSP and an FP-PH protein is voltage clamped using traditional VCF set-up. The oocyte is placed with the animal pole side facing the fluorescence microscope to minimize background fluorescence. FP-PH proteins are selectively illuminated using a Hg-Xe lamp equipped with filters and dichroics to selectively excite the FP of interest and collect only FP emissions using 20X objective. The microscope is coupled to a photomultiplier tube (PMT) to collect the total fluorescence at the plasma membrane. The total fluorescence signal will depend on the amount of FP-PH domain bound to its PIP binding partner at the plasma membrane. Ci-VSP mediated decreases in PIP concentrations will result in FP-PH domain translocation to the cytosol and will result in a smaller fluorescence signal (Figure 5.5). The total fluorescence signal is measured in with millisecond time resolution which allows for temporal precision in monitoring PIP dynamics. This new method allows for the measurement of fast Ci-VSP mediated changes in PIP concentrations that may have been missed by steady-state activity assays employing ion channel PIP reporters.

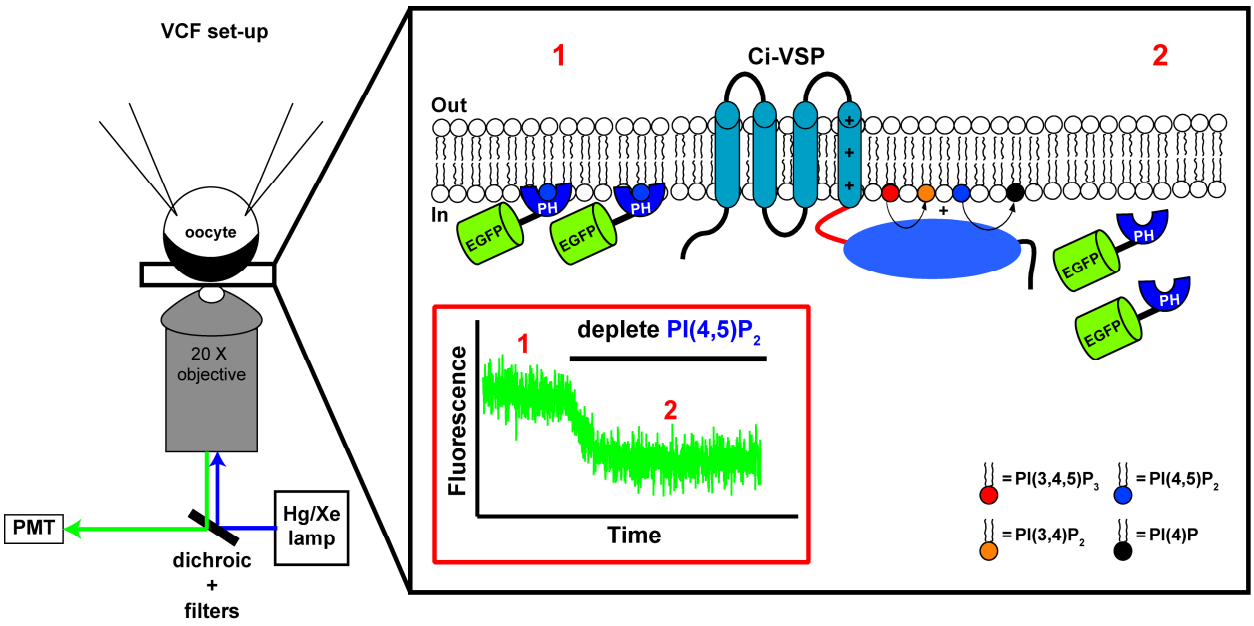

Figure 5.5. FP-PH domain method. *Xenopus laevis* oocytes are voltage clamped and imaged using a traditional VCF set-up (left). The black box shows a cartoon depicting the translocation of an EGFP-PH domain in response to Ci-VSP depletion of $PI(4,5)P_2$ with a sample fluorescence trace (red box). Red numbers represent times of high EGFP-PH membrane fluorescence (1) and low EGFP-PH membrane fluorescence (2).

Screening fluorescent PIP reporters in oocytes

Hundreds of phosphoinositide binding domains have been reported in the literature, but very few have been shown to be faithful reporters of a single phosphoinositide species. Discrepancies exist between the biochemical characterization of a PIP binding domain's PIP specificity and its utility as a reporter for the PIP species in phosphoinositide pathways in living cells. These discrepancies necessitate careful control experiments to confirm that a given PIP sensor will accurately monitor changes in the PIP species elicited by the phosphoinositide signaling pathway under study. A detailed treatment of this topic can be found in reference [15]. Table 5.1 summarizes the fluorescently-tagged PIP reporters (FP-PIP reporters) used in this study.

Table 5.1 FP-PIP reporters tested in oocytes. References are given for *in vivo* utility as sensor for plasma membrane concentrations of a given PIP. Abbreviations: tagRFP-T (tagRFP S158T)

PIP binding domain	Published PIP binding partner(s)	FPs Tested	References
PH_{OSH1}	PI(4)P	EGFP	27-29
$PH_{OSH2-2T}$	PI(4)P Possible $PI(4,5)P_2$	EGFP	30-32
PH_{PLC}	$PI(4,5)P_2$ $I(1,4,5)P_3$	EYFP EGFP tagRFP-T	33, 34
tubby-C-R332H	$PI(4,5)P_2$ Maybe $PI(3,4,5)P_3$	EYFP EGFP	35,36
PH_{TAPP1}	$PI(3,4)P_2$	EGFP	37, 38
PH_{AKT}	$PI(3,4)P_2$ $PI(3,4,5)P_3$	EGFP	39, 40
PH_{BTK}	$PI(3,4,5)P_3$	EGFP	41

For our screen, each FP-PIP reporter was expressed in *Xenopus laevis* oocytes alone or co-expressed with Ci-VSP-G214C to assess its utility as a reporter for specific PIP concentrations and Ci-VSP activity. All experiments were conducted using Ci-VSP-G214C so we could compare Ci-VSP mediated changes in PIP pools with Ci-VSP VSD motion using VCF techniques. Cells were voltage clamped at -80mV to record basal levels of FP-PIP reporter fluorescence at the membrane. Then cells were subjected to a 30s depolarizing pulse and the effects of membrane depolarization on FP-PIP reporter fluorescence were measured. Finally, the cells were repolarized to -80 mV to determine if the changes in FP-PIP reporter fluorescence were reversible. The profile of each probe in the presence and absence of Ci-VSP is summarized in Figure 5.6.

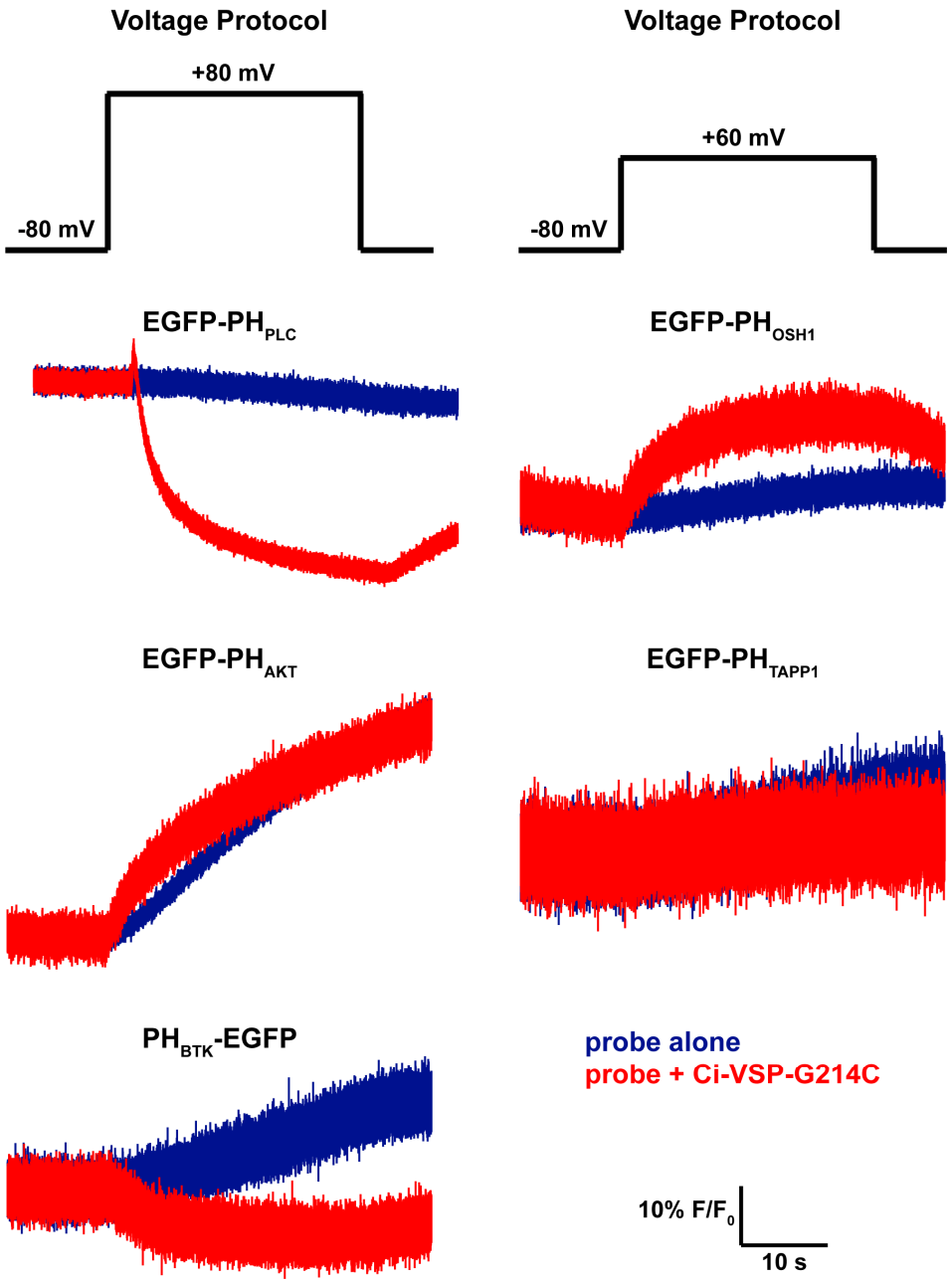

Figure 5.6. Representative voltage dependent profiles for each EGFP-PH PIP sensor. Representative F/F_0 fluorescence traces for *Xenopus laevis* oocytes expressing EGFP-tagged PH domains alone (blue) or with Ci-VSP-G214C (red). Cells were voltage clamped at -80mV and subjected to a 30s depolarizing to pulse to +60mV or +80 mV, then repolarized to -80mV.

We noticed that many of the FP-PH probes responded to membrane depolarization in the absence of Ci-VSP (Figure 5.6). Recently, there have been reports of an endogenous voltage-regulated G_q protein coupled receptor (GPCR) pathway in the *Xenopus laevis* oocyte.[42, 43] This pathway has been shown to activate the phospholipase C and result in the hydrolysis of $PI(4,5)P_2$

and the production of secondary messengers diacylglycerol (DAG) and inositol-1,4,5-trisphosphate ($I(1,4,5)P_3$). In most cases, the endogenous pathway had little effect on FP-PH domain movement compared to the effects of Ci-VSP catalysis, but in some cases the endogenous effects were indistinguishable from Ci-VSP mediated effects.

PI(4)P and $PI(4,5)P_2$ probe testing

We began our screen using FP-PH probes for PI(4)P and $PI(4,5)P_2$ as these lipids are the major PIP components in the inner leaflet of the plasma membrane.[7, 11] The PH domains from yeast oxysterol binding proteins homologs (PH_{OSHBP}) have been shown to track PI(4)P pools both in the Golgi apparatus and the plasma membrane.[15] We first tested a tandem dimer construct of the OSH2 PH domain (EGFP-$PH_{OSH2\text{-}2T}$) which had been reported to specifically bind PI(4)P at the plasma membrane in living cells.[32] However, in our hands, EGFP-$PH_{OSH2\text{-}2T}$ probe seemed to only report changes in $PI(4,5)P_2$ as membrane depolarization activation of Ci-VSP caused a decrease in the membrane fluorescence of the probe (data not shown). Recent literature has shown that the EGFP-$PH_{OSH2\text{-}2T}$ construct may bind both $PI(4,5)P_2$ and PI(4)P in the plasma membrane.[30] The EGFP-PH_{OSH1} was an effective sensor for PI(4)P in our experiments as it showed minimal response to endogenous voltage dependent GPCR pathways, and followed the Ci-VSP mediated production of PI(4)P upon membrane depolarization (Figure 5.6). The EGFP-PH_{OSH1} probe was used to track Ci-VSP production in PI(4)P in all future experiments.

The PH domain from phospholipase C-δ1 (PH_{PLC}) had been previously shown to be a robust reporter of $PI(4,5)P_2$ in *Xenopus laevis* oocytes.[10, 21] In our hands, the EGFP- PH_{PLC} probe had the largest signal-noise ratio of all the probes tested. EGFP- PH_{PLC} showed minimal response to endogenous depolarization activated $PI(4,5)P_2$ depleting pathways and a robust decrease in membrane fluorescence in response to Ci-VSP hydrolysis of $PI(4,5)P_2$. The EGFP-PH_{PLC} probe response to Ci-VSP activity was more than 100 times the response of the EGFP-PH_{PLC} probe to endogenous pathways (Figure 5.6). We also tested other FP-PH_{PLC} constructs and showed that they also followed Ci-VSP mediated changes in $PI(4,5)P_2$. We used the FP-PH_{PLC} constructs to track Ci-VSP mediated changes in $PI(4,5)P_2$ for the majority of our experiments.

$PI(3,4)P_2$ and $PI(3,4,5)P_3$ probe testing

As D3 phosphorylated PIPs represent less than 1% of the total PIP concentrations in a resting cell,[44] we worried that that we would not be able to follow Ci-VSP mediated changes in these lipid concentrations. Indeed, other research groups studying Ci-VSP activity in *Xenopus laevis* oocytes have stimulated an endogenous PI-3-kinase pathway to elevate $PI(3,4,5)P_3$ concentrations in the cell.[10] We tested 3 probes for D3 phosphorylated PIPs.

Salim *et al.* and Rameh *et al.* reported that the PH domain from Bruton's tyrosine kinase (PH_{BTK}) specificity binds $PI(3,4,5)P_3$ over $PI(4,5)P_2$, and $PI(3,4)P_2$.[45, 46] Varnai and co-workers have shown that a fluorescently tagged PH_{BTK} construct can accurately track membrane pools of

$PI(3,4,5)P_3$ in mammalian cells.[41] Murata and Okamura used PH_{BTK}-EGFP to follow Ci-VSP mediated decreases in $PI(3,4,5)P_3$ in *Xenopus laevis* oocytes, but they had to elevate membrane concentrations of $PI(3,4,5)P_3$ through insulin stimulation of endogenous PI-3-kinase pathways in order to monitor Ci-VSP activity against $PI(3,4,5)P_3$.[10]

We were able to follow Ci-VSP mediated changes in $PI(3,4,5)P_3$ concentrations using the PH_{BTK}-EGFP probe in unstimulated oocytes which demonstrates that Ci-VSP has a high affinity for this substrate (Figure 5.6). These results are in agreement with biochemical data that suggests Ci-VSP has the largest amount of activity against $PI(3,4,5)P_3$.[2] However, in cells only expressing PH_{BTK}-EGFP probe we noticed that the PH_{BTK}-EGFP probe membrane fluorescence drastically increased upon membrane depolarization (Figure 5.6). This increase suggests that there is a depolarization activated PI3-kinase pathway in the oocyte, yet there are no reports of this pathway in the literature. In our case, the depolarization-activated Ci-VSP hydrolysis of $PI(3,4,5)P_3$ monitored using the PH_{BTK}-EGFP probe was easily distinguishable from endogenous effects, and PH_{BTK}-EGFP was used as a $PI(3,4,5)P_3$ probe in future experiments.

The PH domain from the tandem-PH domain-containing protein 1 (TAPP1) specifically binds $PI(3,4)P_2$ over other phosphoinositides *in vitro*[37, 38] and the EGFP-PH_{TAPP1} construct is the only reported $PI(3,4)P_2$ sensor that localizes at the plasma membrane.[38] We were unable to accurately monitor Ci-VSP mediated changes in $PI(3,4)P_2$ concentrations in oocytes as this probe exhibited large membrane depolarization activated increases in fluorescence which were indistinguishable from Ci-VSP mediated production of $PI(3,4)P_2$ (Figure 5.6).

We next tested the PH domain from protein kinase B (PH_{AKT}) which binds both $PI(3,4,5)P_3$ and $PI(3,4)P_2$ but shows a three-fold higher affinity for $PI(3,4,5)P_2$ *in vitro*.[47] Similarly, the EGFP-PH_{AKT} probe, which is reported to monitor $PI(3,4)P_2$ and $PI(3,4,5)P_3$ concentrations in living cells,[39] also exhibited large increases in fluorescence upon membrane depolarization that could not be offset by Ci-VSP activity (Figure 5.6). Recent reports have suggested that Ci-VSP might also serve as a D3 phosphoinositide phosphatase and biochemical studies show that the Ci-VSP phosphatase domain is active against $PI(3,4)P_2$.[2] If $PI(3,4)P_2$ is both a substrate and product of Ci-VSP,[2] this information could explain why we were unable to measure Ci-VSP mediated changes in this lipid. Table 5.2 summarizes our screen of FP-PH domain phosphoinositide reporters in *Xenopus laevis* oocytes. With reliable fluorescence reporters for most plasma membrane PIPs in hand, we next tested the utility of these probes to monitor the voltage dependency and kinetics of Ci-VSP activity.

Table 5.2. Summary of fluorescent PIP probes tested in *Xenopus laevis* oocytes.

PIP binding domain	FPs	PIP specificity	Utility for Ci-VSP activity?
PH_{OSH1}	EGFP	PI(4)P	Yes
$PH_{OSH2-2T}$	EGFP	PI(4)P and $PI(4,5)P_2$	No
PH_{PLC}	EYFP,EGFP, tagRFP-T	$PI(4,5P)_2$	Yes
PH_{TAPP1}	EGFP	$PI(3,4)P_2$	No
PH_{AKT}	EGFP	$PI(3,4)P_2$ $PI(3,4,5)P_3$	No
PH_{BTK}	EGFP	$PI(3,4,5)P_3$	Yes

FP-PH domains report voltage-dependent Ci-VSP activity

We next tested the utility of each FP-PH protein as a reporter of the voltage-dependent activity of Ci-VSP. For these experiments, we utilized short voltage pulses to activate Ci-VSP without the concomitant activation of voltage dependent endogenous signaling pathways in the oocytes. Furthermore, we repolarized the cell for up to two minutes between depolarizing pulses to allow for the endogenous PIP kinases and phosphatases to replenish PIP levels. All experiments were conducted using Ci-VSP-G214C so that we could compare Ci-VSP mediated changes in PIP pools with Ci-VSP VSD motion. We tested the activity of Ci-VSP-G214C in the dynamic voltage range of VSD movement monitored by VCF (-40 mV to + 200mV). We witnessed voltage dependent increases in FP-PH domain movement with stronger depolarizations leading to larger changes in FP-PH domain fluorescence for all FP-PH domains tested. These fluorescence changes were correlated with Ci-VSP activity such that stronger depolarizations led to larger Ci-VSP mediated changes in PIP concentrations. Figure 5.7 shows that in cells expressing Ci-VSP-G214C and EGFP-PH_{OSH1}, stronger depolarizations led to increased membrane fluorescence of the EGFP-PH_{OSH1} which indicates greater Ci-VSP production of PI(4)P. While 200 ms depolarizing pulses elicited Ci-VSP activity, tens of seconds were needed for the FP-PH domain report of these changes to reach a steady state. Diffusion of the FP-PH domains to and from the membrane occurs on the millisecond to second time scale.[48]

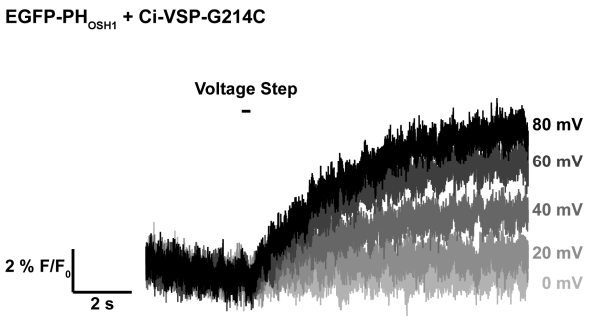

Figure 5.7. Increased membrane depolarization leads to greater Ci-VSP activity. F/F_0 fluorescence trace for oocyte expressing EGFP-PH_{OSH1} and Ci-VSP-G214C. Cell was voltage-clamped at -80mV then subjected to a train of 200 ms depolarizing voltage steps to voltages shown at right. Larger membrane depolarizations resulted in larger increases in EGFP-PH_{OSH1} signaling greater Ci-VSP production of PI(4)P.

By plotting the steady state FP-PH fluorescence levels (ΔF) as a function of step voltage, we constructed activity vs. voltage (AV) curves (Figure 5.8). These curves could be compared with the fluorescence vs. voltage (FV) curves constructed using VCF data which monitored VSD movement for Ci-VSP-G214C. We found that the AV curves were in the same dynamic voltage range as the FV curves for the voltage dependency of Ci-VSP VSD movement measured using TMRM labeled Ci-VSP- G214C (G214C*)(Figure 5.8).

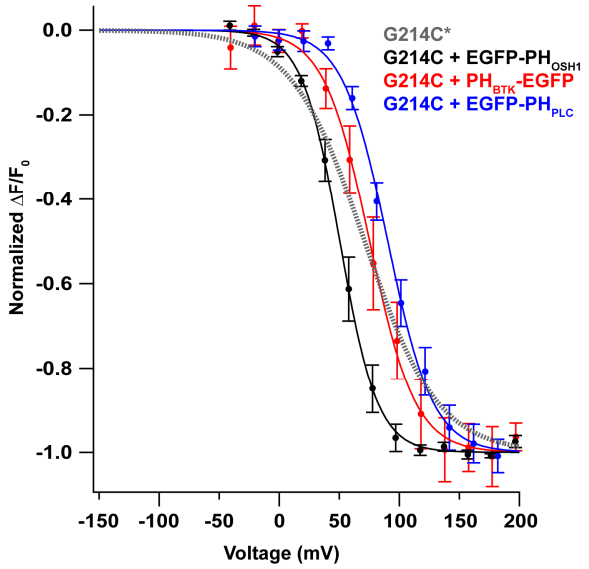

Figure 5.8. FP-PH domains report voltage dependent Ci-VSP activity. Oocytes co-expressing Ci-VSP-G214C and FP-PH domains were voltage clamped and subjected to a train of depolarizing pulses resulting in a voltage-dependent changes in FP-PH domain fluorescence mediated by Ci-VSP activity. VCF data for G214C* (gray line) shown for comparison of voltage dependency of VSD movement. Solid lines represent single Boltzmann fits. Error bars indicate SEM. For fit data, see Table 5.3.

To confirm that the FP-PH domains were accurately measuring Ci-VSP activity, we tested Ci-VSP-R217Q which we had previously shown to shift the voltage-dependent Ci-VSP hydrolysis of $PI(4,5)P_2$ using the IRK1Q assay (Figure 5.9A). We used EGFP-PH_{PLC} as a fluorescent probe for $PI(4,5)P_2$ and found that this probe could accurately follow the voltage-shifted activity of Ci-VSP-R217Q (Figure 5.9B). For both methods tested, the R217Q mutation shifted the midpoint ($V_{1/2}$) for the AV curves 41 mV leftward and caused an increased shallowness of the AV curve slope (Figure 5.9A and B).

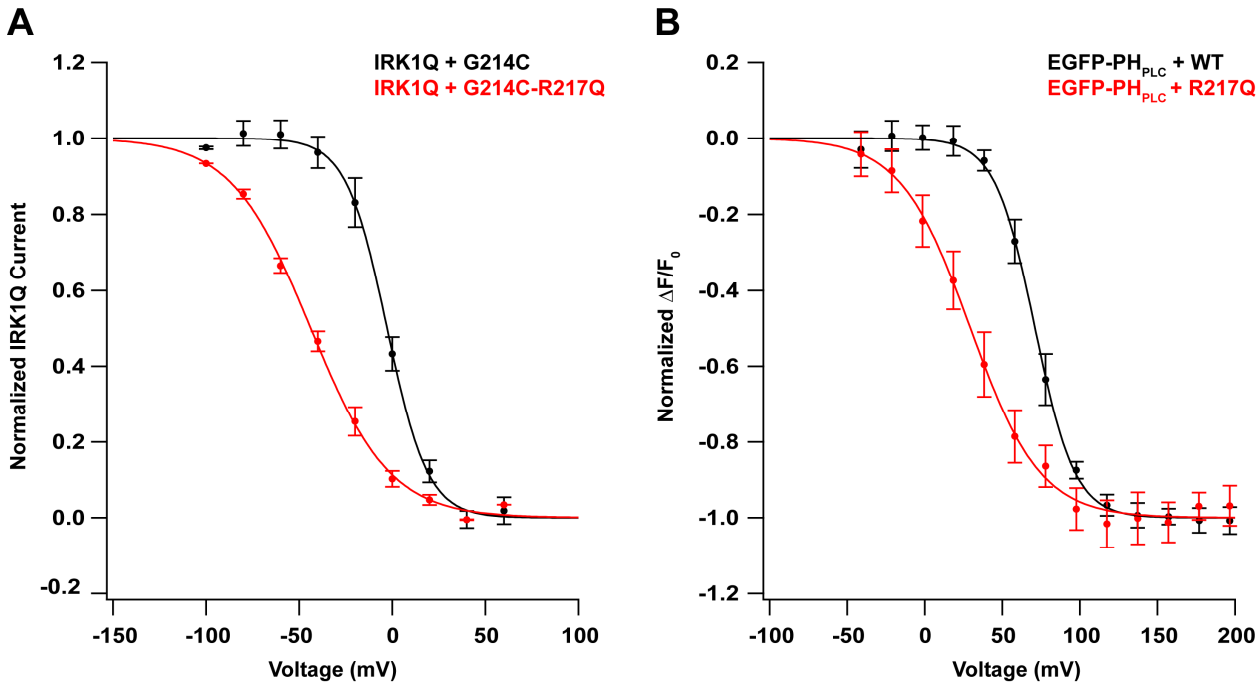

Figure 5.9. Comparison of IRK1Q and EGFP-PH_{PLC} reporters of Ci-VSP activity. (A) Activity vs. Voltage (AV) curves for VSD charge mutants measured using IRK1Q assay. **(B)** Activity vs. Voltage (AV) curves for VSD charge mutants using FP-PH domain assay. For (A) and (B), solid lines represent single Boltzmann fits and error bars indicate SEM. For fit data, see Table 5.3.

FP-PH domains report voltage step duration dependency of Ci-VSP activity

We next measured the effects of voltage step length on Ci-VSP activity. Villalba-Galea and colleagues recently reported that the Ci-VSP VSD adopts a "relaxed" conformation upon prolonged membrane depolarization that may resemble the inactivated state of an ion channel.[4, 49] However, the Ci-VSP phosphatase domain has shown to be constitutively active *in vitro* suggesting that as long as the phosphatase domain is close enough to PIP pools at the plasma membrane, it should be able to properly function.[1, 2] We wondered if prolonged membrane depolarization would also led to an "inactivation" of the phosphatase domain. To test this, we conducted time series experiments in which oocytes expressing both Ci-VSP-G214C and an FP-PH domain were subjected to a series of depolarizing pulses to +150 mV of varying duration. We allowed two minutes of membrane repolarization to -80mV between voltage steps to allow

endogenous PIP kinases and phosphatases to replenish PIP pools and allow the Ci-VSP VSD to return to its resting state. Figure 5.10 shows that in cells expressing Ci-VSP-G214C and EGFP-$PH_{OSH1,}$ longer voltage step durations up to 200 ms resulted in increased Ci-VSP production of PI(4)P. As we saw with the voltage dependency experiments, tens of seconds were needed for the FP-PH domain report of these changes to reach a steady state. We concluded that as long as $PI(4,5)P_2$ pools are replenished and the voltage sensor remains in its active state, then Ci-VSP can function properly.

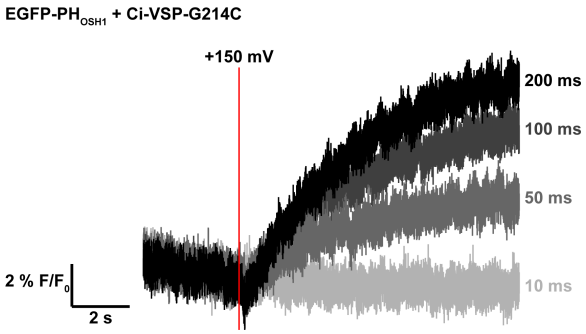

Figure 5.10. Longer membrane depolarization leads to greater Ci-VSP activity. F/F_0 fluorescence trace for oocyte expressing EGFP-PH_{OSH1} and Ci-VSP-G214C. Cell was voltage-clamped at -80mV then subjected to a train of +150 mV steps of lengths shown at right. Red line indicates beginning of voltage step. Longer membrane depolarizations resulted in larger increases in EGFP-PH_{OSH1} showing greater Ci-VSP production of PI(4)P.

Monitoring multiple Ci-VSP mediated reactions in a single cell

We next used the FP-PH domains to monitor the effects of Ci-VSP phosphatase activity on multiple PIP pools in a single cell. As our experimental set-up was equipped to only measure fluorescence from a single FP, we hoped that sequential imaging would allow us to monitor multiple FP signals. Again, we used short (200 ms) depolarizing pulses and waited at least two minutes between pulses to allow for recovery of PIP levels. We chose tagRFP-S158T (tagRFP-T)[50] and EGFP as our fluorescent sensors as the excitation and emission profiles for these proteins do not overlap which minimized FP signal bleed through with our filter set. We tested the reproducibility of each FP-PH domain report of Ci-VSP activity and found that each probe gave repeated robust fluorescence changes in response to Ci-VSP activity. To validate this method, we tested the Ci-VSP hydrolysis of $PI(4,5)P_2$ to make PI(4)P (Figure 5.11A). We had previously seen that Ci-VSP activity caused increases in PI(4)P and decreases in $PI(4,5)P_2$ levels at the plasma membrane (Figure 5.6), but wanted to see if we could monitor both PIP pools in a single cell. We coexpressed Ci-VSP-G214C and tagRFP-T-PH_{PLC} and EGFP-PH_{OSH1} in *Xenopus laevis* oocytes and measured the effects of Ci-VSP activity on the FP-PH domain movements. Cells were voltage clamped at -80 mV then subjected to a 200 ms pulse to +150 mV. Membrane depolarization resulted in changes in the FP-PH fluorescence which tracked the depletion of $PI(4,5)P_2$ and formation of PI(4)P and confirmed that Ci-VSP is a D5 phosphoinositide phosphatase (Figure 5.11B). As each PH domain has a different apparent affinity for its PIP binding partner, we were unable to use the kinetics of FP-PH domain

diffusion from the membrane to gain information about the absolute rates of Ci-VSP mediated changes in these PIPs.

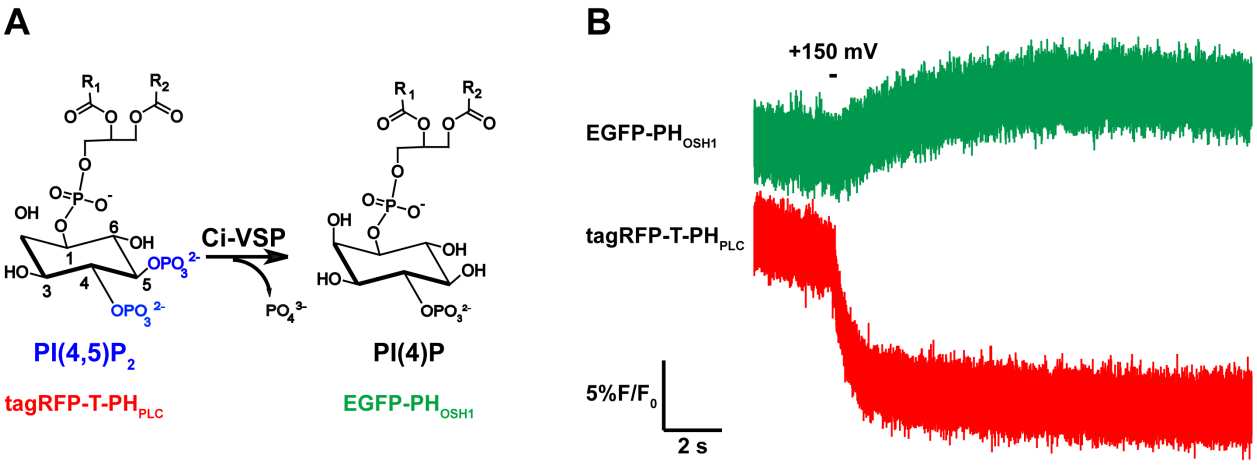

Figure 5.11. Single cell imaging of Ci-VSP D5 phosphatase activity. (A) Ci-VSP removes the D5 phosphate group of $PI(4,5)P_2$ to form PI(4)P. TagRFP-T-PH_{PLC} is used to track changes in $PI(4,5)P_2$ and EGFP-PH_{OSH1} is used to track changes in PI(4)P. **(B)** Sample trace from an oocyte expressing Ci-VSP-G214C and both FP-PH PIP probes described in (A). Cell was held at -80mV then subjected to a 200 ms pulse to +150mV. Membrane depolarization resulted in changes in the FP-PH fluorescence which tracks the depletion of $PI(4,5)P_2$ and formation of PI(4)P and confirms Ci-VSP reaction shown in **(A)**.

We have developed a robust fluorescence method utilizing FP-PH domains to monitor voltage-dependent Ci-VSP mediated changes in multiple PIP pools in *Xenopus laevis* oocytes. We can track these fluorescence changes with millisecond temporal precision and can follow multiple PIP pools in a single cell. We determined that the FP-PH domain report of Ci-VSP activity matches well with the voltage-dependency of Ci-VSP VSD movement which will aid in future mechanistic studies. We also found that larger depolarizations as well as longer depolarizations lead to greater Ci-VSP activity. We next applied our fluorescence method for monitoring Ci-VSP activity to answer the following questions:

1. Can Ci-VSP serve as a D3 phosphoinositide phosphatase in living cells?

2. Can mutations in the Ci-VSP catalytic site control the kinetics of Ci-VSP phosphatase activity ?

Characterization of possible Ci-VSP D3 phosphoinositide phosphatase activity

During our screen of FP-PH domain reporters, we noticed that the EGFP-PH_{PLC} probe showed a biphasic response to Ci-VSP activity (Figure 5.12A). As EGFP-PH_{PLC} is specific for $PI(4,5)P_2$ over all other PIPs, We hypothesized that this probe might be monitoring Ci-VSP mediated production and destruction of $PI(4,5)P_2$. Recently, Iwasaki *et al.* reported that Ci-VSP may act as a D3 and D5 phosphatase against $PI(3,4,5)P_3$ *in vitro*,[2] and we rationalized that the

EGFP-PH_{PLC} probe may be tracking the production of $PI(4,5)P_2$ via D3 hydrolysis of PI(3,4,5)P3 (reaction 1, Figure 5.12B) and the depletion of $PI(4,5)P_2$ via D5 hydrolysis (reaction 2, Figure 5.12B).

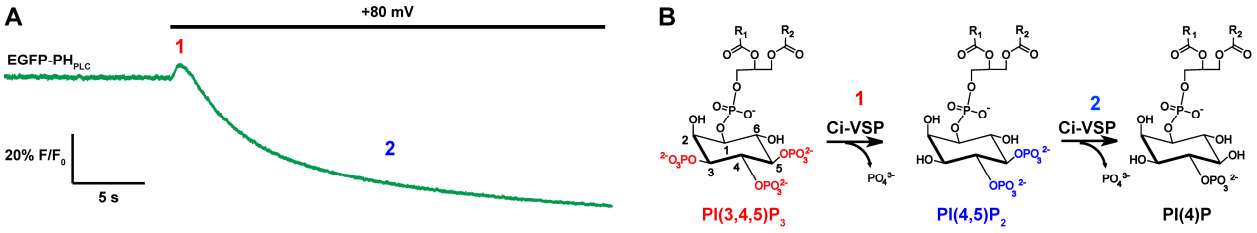

Figure 5.12. EGFP-PH_{PLC} may report two Ci-VSP reactions. (A) Representative trace from oocyte co-expressing Ci-VSP-G214C and EGFP-PH_{PLC} showing biphasic response of EGFP-PH_{PLC} to Ci-VSP activity upon depolarization. Ci-VSP may produce and deplete $PI(4,5)P_2$. **(B)** Model providing Ci-VSP mediated reactions to describe trace shown in (A). Ci-VSP may act as a D3 (reaction 1) and D5 (reaction 2) phosphoinositide phosphatase.

To test our hypothesis, we utilized a recently described $PI(4,5)P_2$ specific probe based on the $PI(4,5)P_2$ sensitive tubby transcription factor.[36] A fluorescent protein fusion to the C terminus of the tubby protein carrying a point mutation (R332H) in the PIP binding pocket (tubby-C-R332H-EYFP) had recently been shown to follow $PI(4,5)P_2$ pools in the cells.[35] This probe can be used to measure changes in $PI(4,5)P_2$ that may be independent of the PLC hydrolysis of $PI(4,5)P_2$ intro DAG and $I(1,4,5)P_3$ which may not be distinguished using PH_{PLC} probes. We constructed a green fluorescent protein tubby construct (tubby-C-R332H-EGFP) to monitor Ci-VSP mediated changes in $PI(4,5)P_2$. Ci-VSP activity caused decreases in the tubby-C-R332H-EGFP membrane fluorescence indicating a decrease in $PI(4,5)P_2$ at the plasma membrane (Figure 5.13). However, the tubby-C-R332H-EGFP signature lacked the upward component present for the EGFP-PH_{PLC} probe. The tubby protein has been shown to also bind $PI(3,4,5)P_3$ *in vitro*[36] suggesting this probe may be monitoring Ci-VSP mediated changes in both $PI(3,4,5)P_3$ and $PI(4,5)P_2$.

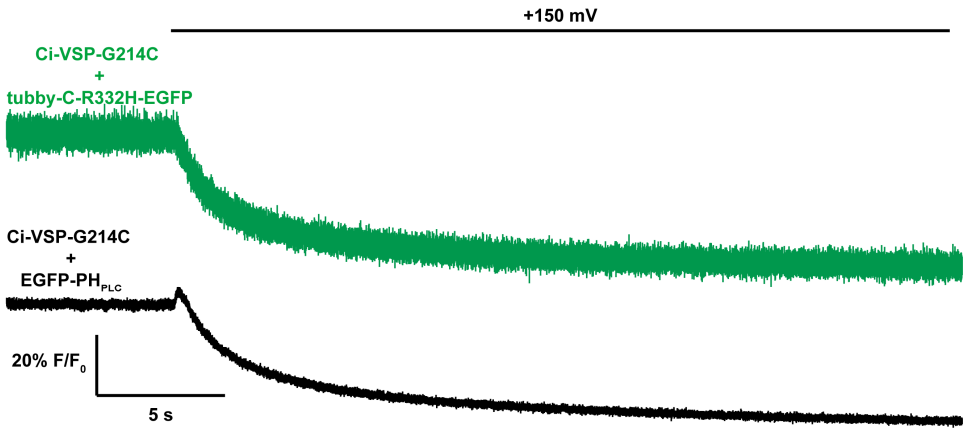

Figure 5.13. Ci-VSP activity against PI(4,5)P_2 using 2 fluorescent probes. Oocytes co-expressing Ci-VSP G214C and tubby-C-R332H-EGFP(top, green) or Ci-VSP-G214C and EGFP-PH_{PLC} (bottom, black) were voltage clamped at -80mV then subjected to a 30s pulse to +150 mV. Note that tubby-C-R332H-EGFP does not show biphasic response to Ci-VSP activity.

We wondered if the biophysical properties of EGFP were causing the upward effect. EGFP and structurally related proteins have pH dependent fluorescence where increases in intracellular pH cause increase in EGFP fluorescence. This pH effect is most pronounced with EYFP.[51] We also tested EYFP-PH_{PLC} and tagRFP-T-PH_{PLC} probe as sensors of Ci-VSP activity, but neither of these probes showed the upward component of the fluorescence signal in response to Ci-VSP activation. Furthermore, the EGFP-PH_{PLC} upward component had a voltage-dependence where larger depolarizations also led to increasing peak height (data not shown). We concluded that the biphasic response of EGFP-PH_{PLC} was caused by Ci-VSP and tried other experiments to determine whether Ci-VSP was a D3 phosphoinositide phosphatase.

We next used the sequential dual-color imaging technique to test whether Ci-VSP could deplete both PI(4,5)P_2 and PI(3,4,5)P_3 upon membrane depolarization in a single cell. Biochemical studies have shown that the Ci-VSP catalytic domain shows greater activity toward PI(3,4,5)P_3 than PI(4,5)P_2.[2] In living cells, PI(3,4,5)P_3 is present in minute concentrations compared with PI(4,5)P_2. We wondered if Ci-VSP mediated PI(4,5)P_2 hydrolysis would dominate in cells. We coexpressed Ci-VSP-G214C and tagRFP-T-PH_{PLC} and PH_{BTK}-EGFP and measured the effects of Ci-VSP activity on the FP-PH domain movements. Again, cells were voltage clamped at -80 mV then subjected to a 200 ms pulse to +150 mV. Membrane depolarization resulted in changes in the FP-PH fluorescence that tracked the Ci-VSP mediated depletion of both PI(3,4,5)P_3 and PI(4,5)P_2 (Figure 5.14). This result supports the depolarization activated D5 phosphoinositide phosphatase model for Ci-VSP proposed by Halaszovich *et al,*[3] but it still did not answer the questions of whether Ci-VSP could act as a D3 phosphoinositide phosphatase *in vivo* or which reaction dominated under physiological conditions.

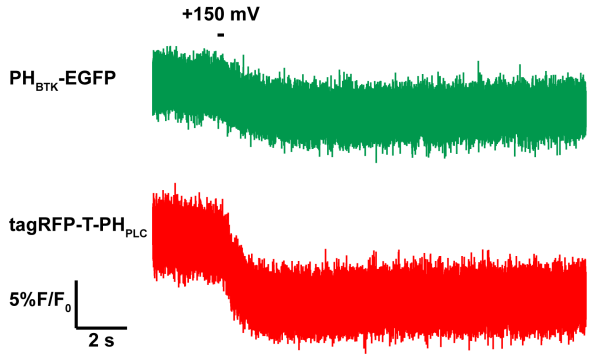

Figure 5.14. Ci-VSP hydrolyzes both PI(3,4,5)P_3 and PI(4,5)P_2 upon membrane depolarization. Representative F/F_0 trace from an oocyte expressing Ci-VSP-G214C and FP-PH probes for PI(3,4,5)P3 (PH_{BTK}-GFP) and PI(4,5)P_2 (TagRFP-T-PH_{PLC}). Cell was voltage clamped at -80mV then subjected to a 200 ms pulse to +150 mV. Membrane depolarization causes Ci-VSP to hydrolyze both PIP species.

We attempted to increase PI(3,4,5)P_3 levels in the cell using a chemically inducible PI3-kinase system[52] with the hope that larger pools of PI(3,4,5)P_3 would result in larger D3 phosphatase from Ci-VSP, but these experiments were unsuccessful.

We also worried that membrane depolarization was turning on voltage sensitive endogenously expressed phospholipase C in the oocyte which was hydrolyzing PI(4,5)P_2 pools and offsetting the Ci-VSP mediated increases in these pools. We next incubated oocytes expressing EGFP-PH_{PLC} and Ci-VSP in U73122, a potent PLC inhibitor[53] to reduce the effects of endogenous PI(4,5)P_2 depleting pathways, then applied a long depolarizing pulse to fully activate Ci-VSP. As expected, in control cells only expressing EGFP-PH_{PLC}, U73122 treatment reduced the effects of voltage sensitive PI(4,5)P_2 depleting pathways. Interestingly, U73122 treatment did not affect the upward component of the EGFP-PH_{PLC} response to Ci-VSP activity, but it did significantly reduce the downward component. (Figure 5.15). These results suggest that Ci-VSP may act as a D3 phosphoinositide phosphatase in living cells.

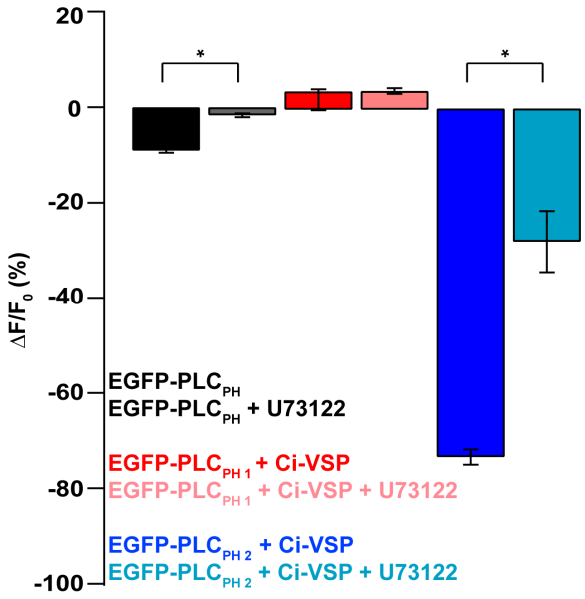

Figure 5.15. U73122 does not affect EGFP-PH$_{PLC}$ signal #1. Cells were voltage clamped at -80 mV then depolarized to +80 mV for 2 min. #1 denotes upward component of EGFP-PH$_{PLC}$ response to Ci-VSP activity and #2 denotes downward component of EGFP-PH$_{PLC}$ response to Ci-VSP activity (see figure 5.12 for more details). Bars show mean ($n \geq 6$) $\pm$ SEM for each condition. Asterisk denotes $p<0.05$.

In summary, the EGFP-PH$_{PLC}$ response to Ci-VSP activity may reveal that Ci-VSP acts as a D3 phosphoinositide phosphatase in living cells. Biochemical studies utilizing D3 phosphoinositides bearing ^{32}P-labeled phosphate groups should be conducted to confirm that the Ci-VSP phosphatase domain can remove the D3 phosphate group from PI(3,4,5)P_3 and PI(3,4)P_2. This information will then guide experiments to probe the functional importance of this reaction in living cells.

Characterization of Ci-VSP substrate specificity and kinetics using single FP-PIP sensors

While the different binding affinities of the FP-PIP probes prevented us from comparing the rates of Ci-VSP mediated changes in multiple PIP pools, we wondered if we could use a single FP-PIP sensor to compare the activities of two Ci-VSP mutants against a single PIP. For these studies, we also wanted to monitor the effects of Ci-VSP active site mutations on voltage-dependent activity. The cytosolic domain of Ci-VSP shares 29.5% overall sequence identity with PTEN, raising questions about the functional similarities of these proteins. Ci-VSP and PTEN share 93% sequence identity in their catalytic domains (Figure 5.16) and the key catalytic residues involved in PTEN function are crucial for Ci-VSP activity.[6]

```
PTEN     92 DH.....AIHCKAGKGRTG
Ci-VSP  331 DH.....AIHCKGGKGRTG
```

Figure 5.16. Comparison of PTEN and Ci-VSP active sites. Partial sequence alignment of active site residues in PTEN (top) and Ci-VSP (bottom). Areas of sequence identity are shaded in blue.

Iwasaki *et al.* recently proposed that G365 in Ci-VSP is crucial for Ci-VSP's preferential D5 phosphoinositide phosphatase activity.[2] Both biochemical and living cell studies showed that Ci-VSP-G365A did not have significant activity against $PI(4,5)P_2$, suggesting that an alanine at position 365 prevents D5-phosphatase activity. We performed functional studies with Ci-VSP-G365A to investigate its ability to tune the substrate specificity of Ci-VSP and to measure the kinetic effects of this mutation.

We first conducted voltage clamp fluorometry (VCF) experiments to monitor the effects of G365A on Ci-VSP VSD movement. We used position G214 near extracellular end of the S4 segment as our labeling site to monitor VSD motions. We had previously shown that mutations in the catalytic site that eliminate phosphatase activity also shift the voltage sensitivity and kinetics of voltage sensor movement.[6] However, the G365A mutation did not significantly shift the voltage dependency of VSD movement (Figure 5.17) or affect the kinetics of VSD movements (data not shown).

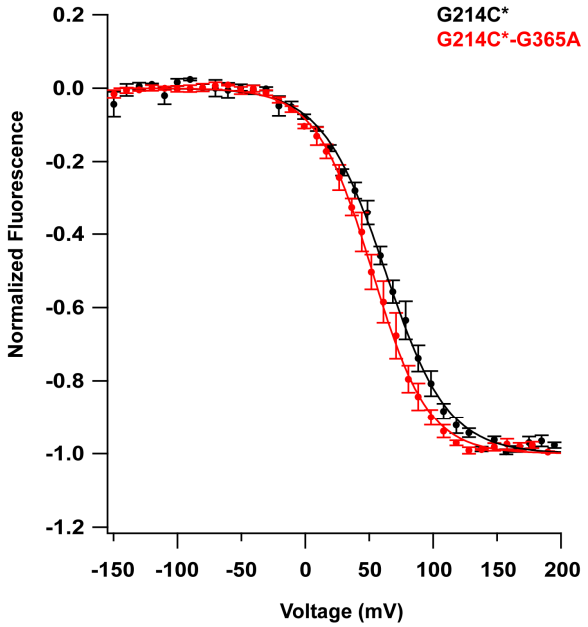

Figure 5.17. Effects of G365A on Ci-VSP VSD movement. FV curves for G214C. Asterisk denotes labeling with TMRM Solid lines represent single Boltzmann fits. Error bars indicate SEM. For fit data, see Table 5.3.

We next used FP-PH domain assay to study the effects of G365A on $PI(3,4,5)P_3$ hydrolysis and confirm that Ci-VSP-G214C-G365A did not hydrolyze $PI(4,5)P_2$ under stronger membrane depolarization. To compare the $PI(4,5)P_2$ hydrolysis of Ci-VSP-G214C with Ci-VSP-

G214C-G365A, we expressed each protein with EGFP-PH_{PLC} as a reporter for $PI(4,5)P_2$. Unlike previous reports, we found that Ci-VSP-G214C-G365A had delayed $PI(4,5)P_2$ hydrolysis (Figure 5.18A) and even at full activation, only had 20 % catalytic activity when compared with Ci-VSP-G214C (Figure 5.18B).

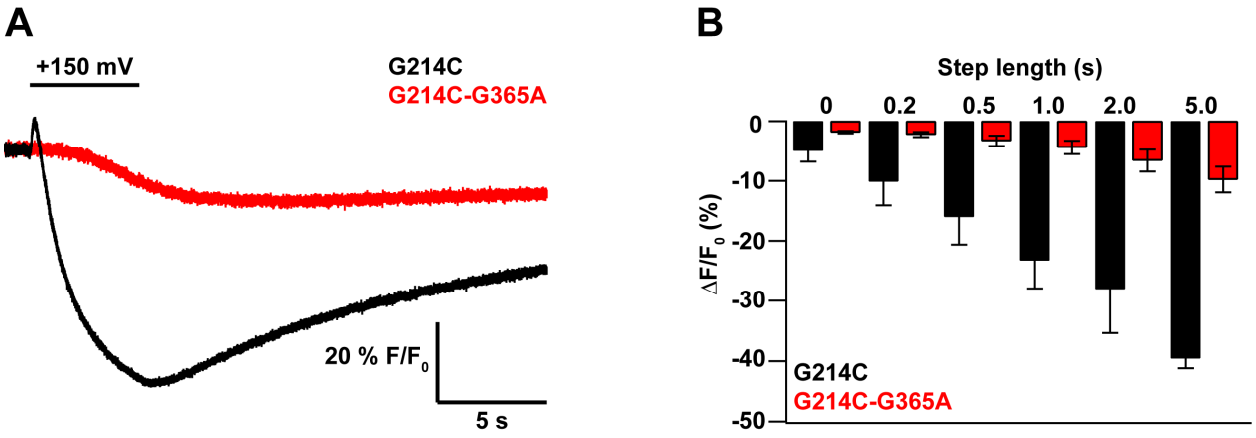

Figure 5.18. G365A mutation causes delayed and reduced $PI(4,5)P_2$ hydrolysis. (A) Representative F/F_0 fluorescence traces for oocytes co-expressing EGFP-PH_{PLC} with Ci-VSP-G214C (black) or EGFP-PH_{PLC} with Ci-VSP-G214C-G365A**.** Cells were voltage clamped at -80 mV then subjected to a 5 s depolarizing pulse to +150 mV. Note that G365A mutation delays $PI(4,5)P_2$ hydrolysis as measured by EGFP-PH_{PLC} reporter. (B) Comparison of steady-state EGFP-PH_{PLC} $\Delta F/F_0$ vs. step length for cells co-expressing EGFP-PH_{PLC} and Ci-VSP-G214C (black, n=4) or Ci-VSP-G214C-G365A (red, n=4). Bars represent mean $\pm$ SEM. Cells were voltage clamped at -80 mV then subjected to a train of pulses to +150 mV of varying duration. Note that even at longer depolarizations, Ci-VSP-G214C-G365A has reduced activity compared to Ci-VSP-G214C.

Interestingly, the biphasic EGFP-PH_{PLC} response to Ci-VSP activity remained for Ci-VSP-G214C-G365A, although it was much slower (Figure 5.18A). Other FP-PIP sensors of $PI(4,5)P_2$ and PI(4)P also showed delayed responses in the presence of Ci-VSP-G214C-G365A suggesting that this mutation delays $PI(4,5)P_2$ hydrolysis and PI(4)P production (data not shown). We next tested how the G365A mutation affected Ci-VSP $PI(3,4,5)P_3$ hydrolysis.

As the G365A mutant has a catalytic domain sequence identical to that of PTEN, a known D3 phosphoinositide phosphatase, we predicted that this mutant might have larger activity against $PI(3,4,5)P_3$. We tested this hypothesis by co-expressing Ci-VSP-G214C or Ci-VSP-G214C-G365A with PH_{BTK}-EGFP as a reporter for $PI(3,4,5)P_3$. We observed that the kinetics for Ci-VSP-G214C-G365A and Ci-VSP-G214C were not statistically different (Figure 5.19A). We did observe that the steady-state activity for Ci-VSP-G214C-G365A was significantly lower than Ci-VSP-G214C during short depolarizations, but the activities were not statistically different during longer depolarizations (Figure 5.19B). We concluded that the G365A mutation may slightly delay $PI(3,4,5)P_3$ hydrolysis but does not alter the substrate specificity of Ci-VSP.

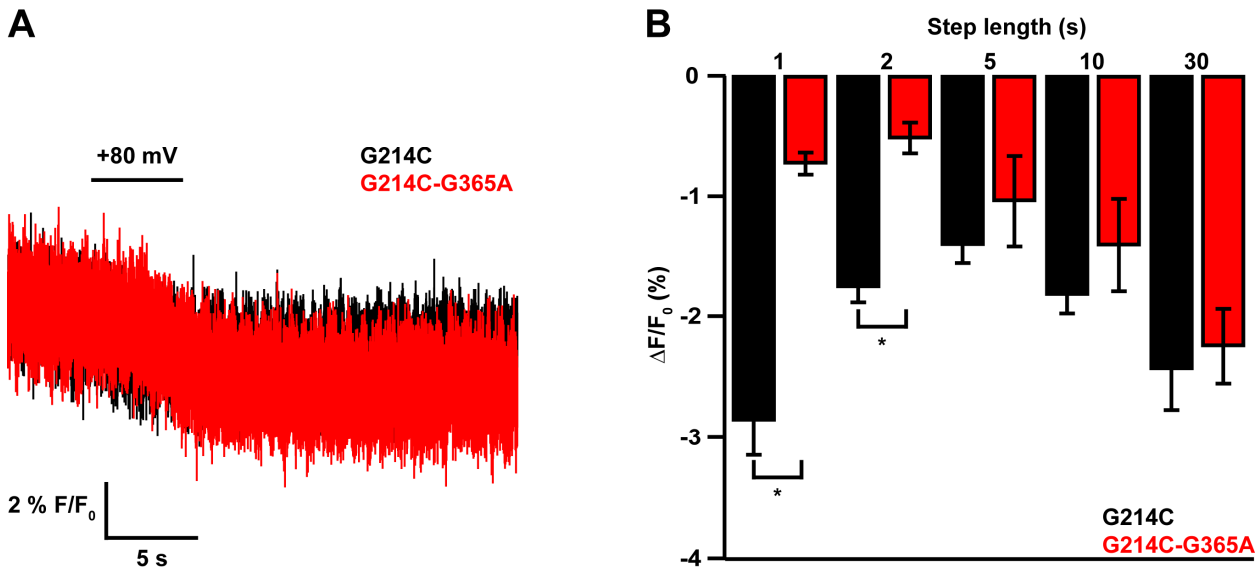

Figure 5.19. G365A mutation reduces PI(3,4,5)P_3 hydrolysis during short depolarizations. (A) Representative F/F_0 fluorescence traces for oocytes co-expressing PH_{BTK}-EGFP with Ci-VSP-G214C (black) or EGFP-PH_{PLC} with Ci-VSP-G214C-G365A**.** Cells were voltage clamped at -80 mV then subjected to a 5 s depolarizing pulse to +80 mV. Note that G365A mutation does not delay PI(3,4,5)P_2 hydrolysis as measured by PH_{BTK}-EGFP reporter. (B) Comparison of steady-state PH_{BTK}-EGFP $\Delta F/F_0$ vs. step length for cells co-expressing PH_{BTK}-EGFP and Ci-VSP-G214C (black, n=6) or Ci-VSP-G214C-G365A (red, n=7). Bars represent mean $\pm$ SEM Cells were voltage clamped at -80 mV then subjected to a train of pulses to +80 mV of varying duration. Note that only during shorter depolarizations, Ci-VSP-G214C-G365A has reduced activity compared to Ci-VSP-G214C. Asterisk (*) denotes $p<0.05$.

Our preliminary experiments with Ci-VSP-G214C-G365A suggest that although Ci-VSP and PTEN have high sequence identity in their catalytic domains, these enzymes differ in their substrate specificity. Our results differ with recent reports that suggest G365 is a key residue in regulating Ci-VSP's substrate specificity.[2] Instead, we find that G365 does not play a significant role in determining Ci-VSP's substrate specificity, but it may be important for proper D5 phosphoinositide hydrolysis, as G365A slows the kinetics and steady state levels of PI(4,5)P_2 hydrolysis at all step durations tested. G365A also reduces steady state levels of Ci-VSP mediated PI(3,4,5)P_3 hydrolysis during short depolarizations, further suggesting a role for G365 in promoting fast substrate turnover. Further mutagenesis studies targeting the role of other Ci-VSP catalytic site residues will give more insight into the role of the catalytic domain in regulating the kinetics and substrate specificity of Ci-VSP activity.

Conclusions

We have developed a robust fluorescence method utilizing FP-PH domains to monitor voltage-dependent Ci-VSP mediated changes in multiple PIP pools in *Xenopus laevis* oocytes. We monitored these fluorescence changes with millisecond temporal precision and can follow multiple PIP pools in a single cell. The FP-PH domain report of Ci-VSP activity matches well

with the voltage-dependency of Ci-VSP VSD movement. We also found that larger membrane depolarizations as well as longer depolarization steps led to greater Ci-VSP phosphatase activity.

We applied our fluorescence method to monitor the substrate specificity and kinetics of Ci-VSP activity. We observed possible Ci-VSP D3 phosphoinositide phosphatase activity using the EGFP-PH_{PLC} probe which suggests that Ci-VSP might serve as both a D3 and D5 phosphoinositide phosphatase in living cells. We also found that G365 in the Ci-VSP active site may play a key role in regulating the kinetics of Ci-VSP mediated PIP hydrolysis, and that G365A slows D5 phosphoinositide activity against $PI(4,5)P_2$.

With this new method for monitoring multiple Ci-VSP mediated reactions, we will further characterize the molecular determinants of Ci-VSP substrate specificity and voltage-dependency. Furthermore, orthologs of Ci-VSP have been discovered in other organisms,[5, 42, 54] but not much is known about this family of voltage-sensitive proteins. In particular, TPTE and TPIP, two proposed human orthologs of Ci-VSP, have been shown to be phosphoinositide phosphatases, but their substrate specificity and regulation are not well-understood.[55] We will use our fluorescence method to assess the voltage sensitivity of these proteins and determine their biologically relevant substrates and products. With this information in hand, we can determine the physiological significance of the voltage-sensitive phosphatase family.

Materials and Methods

Molecular Biology. Ci-VSP in the pSD64TF vector was kindly provided by Dr. Y. Okamura (Osaka University, Osaka, Japan). rIRK1 in pGEM-HE was kindly provided by Dr. E. Reuveny (Weizmann Institute of Science, Rehovot, Israel). The EGFP-PH_{AKT}, EGFP-PH_{PLC}, and EYFP-PH_{PLC} constructs were kindly provided by Dr. T. Meyer (Stanford University, Palo Alto, CA) and subcloned into pGEM-HE. The EGFP-$PH_{OSH2\text{-}2T}$, EGFP-PH_{OSH1}, EGFP-PH_{TAPP1}, and PH_{BTK}-EGFP were kind gifts from Dr. T. Balla (National Institutes of Health, Bethesda MD) and subcloned into pGEM-HE. The tubby-C-R332H-EYFP construct was a kind gift from Dr. A. Tinker (University College, London, UK) and was subcloned into pGEM-HE. EGFP was subcloned into the *BamHI* and *HindIII* sites of the pGEM-HE- tubby-C-R332H-EYFP vector to create the tubby-C-R332H-EGFP construct. The ptagRFP vector was a kind gift from Dr. T. Hughes (Montana State University, Bozemann, MT). The coding sequence for tagRFP was subcloned into the *NheI* and *XhoI* sites of the pGEM-HE-EGFP-PH_{PLC} vector to create the tagRFP-PH_{PLC} construct. The S158T mutation (for increase photostability[50]) was added to tagRFP in the pGEM-HE-tagRFP-PH_{PLC} construct using Quikchange (Stratagene).

All point mutations were made using Quikchange (Stratagene). All DNA was confirmed by DNA sequencing. RNA was transcribed using mMessage mMachine SP6 or T7 transcription kits (Ambion).

Heterologous Protein Expression. Surgically extracted *Xenopus laevis* oocytes were injected with 20-42.5 ng RNA (50 nl). The cells were incubated in ND-96 (96 mM NaCl, 2 mM KCl, 1.8 mM $CaCl_2$, 1 mM $MgCl_2$, 50 mg mL^{-1} gentamicin, 2.5 mM Na pyruvate, and 5 mM HEPES, pH 7.6) at 12-18°C for 12-48 h prior to experiments, unless otherwise noted.

Voltage Clamp Fluorometry. Voltage clamp fluorometry was performed as described previously.[56] Briefly, 50 nl mRNA for Ci-VSP at 0.4–0.8 $\mu g\text{-}\mu l^{-1}$ were injected into *Xenopus laevis* oocytes. One hour after injection, oocytes were treated with a 1 mM solution of glycine maleimide[57] to block native cysteines before protein expression. Cells were then incubated at 18°C for 24-48 prior to experiments

On the day of the experiment, cells were incubated in a high potassium solution (98 mM KCl, 1.0 mM$CaCl_2$, 1.8 mM $MgCl_2$, 10 mM HEPES, pH7.2) and 12.5 μM tetramethylrhodamine-6-maleimide (Invitrogen) for 30 minutes on ice and in the dark. After extensive washing with ND-96, the cells were stored in ND-96, in the dark and at 12°C until the time of the experiment. VCF experiments were conducted in ND-96 recording solution (96 mM NaCl, 2 mM KCl, 1.8 mM $CaCl_2$, 1 mM $MgCl_2$ 10 mM HEPES, pH 7.4).

A Zeiss IM inverted microscope with a 20X 0.75 NA fluorescence objective (Nikon) was used with a Dagan CA-1B amplifier (Dagan Corporation), illuminated with a 150 W xenon-mercury arc lamp (Hamamatsu) and intensity was measured with an HC120-05 photomultiplier tube (Hamamatsu). The amplifier, photomultiplier and Uniblitz shutter (Vincent Associates) were controlled by the Digidata-1440 board and PClamp10 software package (Molecular Devices). Light was filtered through an HQ535/50 excitation filter, an HQ610/75 emission filter and a

Q565LP dichroic (Chroma Technology). Fluorescence signals were low pass filtered at 2 kHz through an eight-pole Bessel filter (Frequency Devices). For fluorescence vs. voltage (FV) curves (Figures 5.3, 5.8, and 5.17), cells were held at -80mV then subjected to 500 ms voltage steps from -150mV to +200mV followed by repolarization to -80mV with an intersweep time of 5s. Steady state fluorescence levels obtained at the end of each voltage step were plotted as a function of step voltage to create FV curves. Data were fit using single Boltzmann then normalized and averaged. Data in FV curves represent mean values $\pm$ standard error of the mean (SEM).

FP-PH domain experiments. 50 nl of mRNA for Ci-VSP and the FP-PH domain were coinjected into *Xenopus laevis* oocytes at a 1:1 or 10:1 Ci-VSP:FP-PH domain ratio with a total RNA concentration of ~0.44-0.8 $\mu g\text{-}\mu l^{-1}$. Oocytes were incubated in ND-96 for 24-48 hours at 18°C in the dark until the time of experiments.

All experiments were conducted at room temperature. Oocytes were placed animal pole side down in a RC26-Z recording chamber (Warner Instruments) constructed with a No.1 thickness coverslip bottom (CS22/50, Warner Instrument) and constantly perfused with ND-96 recording solution using a Valve Bank 8 II perfusion system (Automate Scientific). Oocytes were voltage-clamped using two-electrode voltage clamp (TEVC) methods using a CA-1B amplifier (Dagan Corporation), Digidata-1440A board and pClamp10 software (Molecular Devices).

The electrophysiology set-up was coupled to a Zeiss IM inverted microscope with a 20X 0.75 numerical aperture (NA) fluorescence objective (Nikon). Cells were illuminated with a 150 W xenon-mercury arc lamp (Hamamatsu) and fluorescence intensity was measured with an HC120-05 photomultiplier tube (Hamamatsu). The photomultiplier tube and Uniblitz shutter (Vincent Associates) were controlled by the Digidata-1440 board and PClamp10 software package (Molecular Devices). tagRFP fluorescence was imaged using an HQ535/50 excitation filter, an HQ610/75 emission filter and a Q565LP dichroic (Chroma Technology). EGFP and EYFP fluorescence were imaged using an HQ480/40 excitation filter, an HQ535/50 emission filter and a Q505LP dichroic (Chroma Technology). All fluorescence data was sampled at 2 kHz and filtered at 2 kHz using a Cornerstone series FL 8 pole Bessel filter (Dagan).

For all experiments, cells were voltage clamped at -80mV in the dark for two minutes prior to recording to obtain baseline FP-PH domain fluorescence when Ci-VSP was not active. The PMT gain was adjusted so that the resting fluorescence signal was approximately 3 V. Cells were voltage clamped at -80mV for 5-30s with the shutter open to record baseline fluorescence. The shutter remained open for the remainder of the experiment and data were recorded every 500 μs. Cells were then subjected to depolarizing voltage steps ranging from -40 mV to +200 mV with varying durations of 10 ms up to 2 min. Next, cells were then repolarized to -80mV for 20-120 s.

All data analysis was conducted using Microsoft Excel and Igor Pro software. All fluorescence data were normalized using the following equation:

$$F_{norm}=F/F_0$$

where F_0 represents the mean fluorescence signal measured over the course of 1s prior to a voltage step.

For measuring steady-state changes in FP-PH domain fluorescence, the following equation was used:

$$\Delta F/F_0 = (F_{step}-F_0)/F_0$$

where F_0 represents the mean fluorescence signal measured over the course of 1s prior to a voltage step and F_{step} represents the mean steady-state fluorescence measured during or after a voltage step.

For FP-PH domain activity vs. voltage (AV) curves (Figures 5.8 and 5.9), steady state $\Delta F/F_0$ values were plotted vs. voltage step voltage, then data were fit using a single Boltzmann equation. Data were then normalized and averaged.

For U73122 experiments (Figure 5.15), oocytes expressing EGFP-PH_{PLC} in the absence and presence of Ci-VSP-G214C were incubated in ND-96 recording solution containing 10 μM U73122 (CalBioChem) for 60-120 minutes at 18°C in the dark. Cells were then extensively washed with ND-96 recording solution just prior to experiments.

IRK1Q activity assay (Figures 5.3 and 5.9A). We measured Ci-VSP catalytic activity using an electrophysiological assay. Ci-VSP catalytic activity was measured indirectly by detecting the catalytic product, phosphatidylinositol-4,5-bisphosphate ($PI(4,5)P_2$), via its activation of the inwardly-rectifying IRK1 R228Q K^+ channel (IRK1Q). The R228Q mutation of IRK1 was used to alter the sensitivity of the channel for $PI(4,5)P_2$ into an observable range.[8] Voltage was held at different levels with a test every 30 s consisting of a 10 ms step to –100 mV to measure inward current, followed by a 70 ms ramp to 50 mV, confirming that the current was due to IRK1Q and not leak. To reach steady-state currents at each voltage required multiple iterations of the protocol, reflecting the time it takes to establish a steady-state level of $PI(4,5)P_2$ at each level of Ci-VSP activity.

For these experiments, 50 nl of mRNA for Ci-VSP and IRK1Q were coinjected into *Xenopus laevis* oocytes at a 10:1 ratio with a total RNA concentration of ~0.9 $\mu g\text{-}\mu l^{-1}$. Cells were incubated in ND-96 at 18°C for 16–48 hours. The recording solutions contained 90 mM potassium methanesulfonic acid (KMES), 3 mM $Mg(MES)_2$, 8 mM KOH, 10 mM HEPES, pH 7.4. Experiments were conducted on the VCF set-up described above.

IRK1Q Activity Analysis. Kinetic and steady-state traces were analyzed using Igor Pro and Microsoft Excel software. The activity experiments with IRK1Q were leak subtracted by assuming a voltage-independent linear leak. Current was measured at –100 mV after the test holding potential and leak was measured at +50 mV where the IRK channels should be blocked by Mg^{2+} and polyamines and the following equation applied to calculate the leak subtracted (LS) current: $I_{LS} = I_{-100mV} + 2I_{+50mV}$. Multiple iterations of the protocol were tested per holding potential to reach steady-state levels of current. For voltages where steady-state currents could not be reached, the data were extrapolated using a single exponential. Activity vs. Voltage Curves (AV) curves were constructed by plotting steady-state IRK1Q current vs. voltage step. Data for individual cells were fit to a single Boltzmann curve, then normalized and averaged. Data points represent the mean $\pm$ the standard error of the mean (SEM). Solid lines represent single Boltzmann fit of the averaged data.

Data Analysis and Statistics. All data analysis was conducted using Clampfit (Molecular Devices), Excel (Microsoft) or Igor Pro Software. All data represent the mean ± standard error of the mean (SEM). Statistical significance was assessed using the Student's t-test.

Table 5.3. Activity vs. voltage (AV) and fluorescence vs. voltage (FV) curve fit data.

Protein(s)	$V_{1/2}$ (mV)	slope	n
Ci-VSP-G214C + EGFP-PH_{OSH1}	50.5 ± 0.8	15.7 ± 0.7	7
Ci-VSP-G214C + PH_{BTK}-EGFP	75.3 ± 1.9	19.1 ± 1.7	5
Ci-VSP-G214C + EGFP-PH_{PLC}	90.4 ± 1.6	18.8 ± 1.4	17
Ci-VSP-G214C* (Figure 5.8)	71.2 ± 0.8	30.3 ± 0.7	13
Ci-VSP-G214C +IRK1Q	-2.8 ± 0.9	10.9 ± 0.9	11
Ci-VSP-G214C-R217Q + IRK1Q	-43.8 ± 2.1	21.3 ± 1.9	15
Ci-VSP + EGFP-PH_{PLC}	71.1 ± 0.6	12.9 ± 0.5	4
Ci-VSP-R217Q + EGFP-PH_{PLC}	29.5 ± 2.3	22.5 ± 1.9	10
Ci-VSP-G214C* (Figure 5.17)	62.5 ± 0.9	24.7 ± 0.8	4
Ci-VSP-G214C*-G365A (Figure 5.17)	52.3 ± 0.6	22.0 ± 0.5	3

Acknowledgements

Thanks to Sandra Wiese, Whitney McFadden and Tracey Kim and Dr. Max Ulbrich for assistance with cloning. Thanks to Dr. Susy Kohout for performing preliminary experiments with Ci-VSP and the EGFP-PH_{PLC} probe, providing the data for the EGFP-PH_{PLC} AV curve and G214C* FV curve in Figure 5.8, and helpful discussions. Thanks for the Machen Lab (University of California, Berkeley, CA) for kindly providing U73122. Thanks to Dr. Max Ulbrich for helpful discussions and feedback on this manuscript.

References

1. Murata, Y., et al., Phosphoinositide phosphatase activity coupled to an intrinsic voltage sensor. *Nature* **2005,** 435, (7046), 1239-1243.

2. Iwasaki, H., et al., A voltage-sensing phosphatase, Ci-VSP, which shares sequence identity with PTEN, dephosphorylates phosphatidylinositol 4,5-bisphosphate. *Proc. Natl. Acad. Sci. U. S. A.* **2008,** 105, (23), 7970-7975.

3. Halaszovich, C. R.; Schreiber, D. N.; Oliver, D., Ci-VSP Is a depolarization-activated phosphatidylinositol-4,5-bisphosphate and phosphatidylinositol-3,4,5-trisphosphate 5'-phosphatase. *J. Biol. Chem.* **2009,** 284, (4), 2106-2113.

4. Villalba-Galea, C. A.; Miceli, F.; Taglialatela, M.; Bezanilla, F., Coupling between the voltage-sensing and phosphatase domains of Ci-VSP. *J. Gen. Physiol.* **2009,** 134, (1), 5-14.

5. Hossain, M. I., et al., Enzyme domain affects the movement of the voltage sensor in ascidian and zebrafish voltage-sensing phosphatases. *J. Biol. Chem.* **2008,** 283, (26), 18248-18259.

6. Kohout, S. C., et al., Electrochemical coupling in the voltage-dependent phosphatase Ci-VSP. *Nat. Chem. Biol.* **2010,** 6, (5), 369-375.

7. Suh, B.-C.; Hille, B., PIP_2 is a necessary cofactor for ion channel function: How and why? *Annual Review of Biophysics* **2008,** 37, (1), 175-195.

8. Zhang, H., et al., Activation of inwardly rectifying K^+ channels by distinct PtdIns(4,5)P_2 interactions. *Nat. Cell Biol.* **1999,** 1, (3), 183-8.

9. Kohout, S. C.; Ulbrich, M. H.; Bell, S. C.; Isacoff, E. Y., Subunit organization and functional transitions in Ci-VSP. *Nat. Struct. Mol. Biol.* **2008,** 15, (1), 106-108.

10. Murata, Y.; Okamura, Y., Depolarization activates the phosphoinositide phosphatase Ci-VSP, as detected in Xenopus oocytes coexpressing sensors of PIP_2. *J Physiol* **2007,** 583, (3), 875-889.

11. Di Paolo, G.; De Camilli, P., Phosphoinositides in cell regulation and membrane dynamics. *Nature* **2006,** 443, 651.

12. Lemmon, M. A., Phosphoinositide recognition domains. *Traffic* **2003,** 4, (4), 201-213.

13. McLaughlin, S.; Wang, J.; Gambhir, A.; Murray, D., PIP_2 and proteins: Interactions, organization, and information flow. *Annu. Rev. Biophys. Biomol. Struct.* **2002,** 31, (1), 151-175.

14. Várnai, P.; Balla, T., Visualization and manipulation of phosphoinositide dynamics in live cells using engineered protein domains. *Pflügers Archiv European Journal of Physiology* **2007,** 455, (1), 69-82.

15. Balla, T.; Varnai, P., Visualization of cellular phosphoinositide pools with GFP-fused protein domains. In *Current Protocols in Cell Biology*, John Wiley & Sons, Inc.: 2009; Vol. 42, pp 24.4.1-24.4.27.

16. Shaner, N. C.; Patterson, G. H.; Davidson, M. W., Advances in fluorescent protein technology. *J. Cell Sci.* **2007,** 120, (24), 4247-4260.

17. Lippiat, J. D., Whole-cell recording using the perforated patch clamp technique. In *Potassium Channels*, 2009; pp 141-149.

18. Várnai, P.; Balla, T., Live cell imaging of phosphoinositide dynamics with fluorescent protein domains. *Biochimica et Biophysica Acta (BBA) - Molecular and Cell Biology of Lipids* **2006,** 1761, (8), 957-967.

19. Wagner, C. A., et al., The use of Xenopus laevis oocytes for the functional characterization of heterologously expressed membrane proteins. *Cell. Physiol. Biochem.* **2000,** 10, (1-2), 1-12.

20. James, N. D., Oogenesis in Xenopus laevis (Daudin). I. Stages of oocyte development in laboratory maintained animals. *J. Morphol.* **1972,** 136, (2), 153-179.

21. Zhang, L., et al., Mechanosensitivity of GIRK channels is mediated by protein kinase C-dependent channel-phosphatidylinositol 4,5-bisphosphate interaction. *J. Biol. Chem.* **2004,** 279, (8), 7037-7047.

22. Siegel, M. S.; Isacoff, E. Y., A genetically encoded optical probe of membrane voltage. *Neuron* **1997,** 19, (4), 735-741.

23. Ulbrich, M. H.; Isacoff, E. Y., Subunit counting in membrane-bound proteins. *Nat. Meth.* **2007,** 4, (4), 319-321.

24. Pathak, M. M., et al., Closing in on the resting state of the Shaker K^+ channel. *Neuron* **2007,** 56, (1), 124-140.

25. Mannuzzu, L. M.; Moronne, M. M.; Isacoff, E. Y., Direct physical measure of conformational rearrangement underlying potassium channel gating. *Science* **1996,** 271, (5246), 213-216.

26. Dascal, N., Voltage clamp recordings from Xenopus oocytes. *Curr Protoc Neurosci* **2001,** Chapter 6, Unit 6 12.

27. Levine, T. P.; Munro, S., The pleckstrin homology domain of oxysterol-binding protein recognizes a determinant specific to Golgi membranes. *Curr. Biol.* **1998,** 8, (13), 729-39.

28. Balla, A., et al., A plasma membrane pool of phosphatidylinositol 4-phosphate is generated by phosphatidylinositol 4-kinase type-III alpha: Studies with the PH domains of the oxysterol binding protein and FAPP1. *Mol. Biol. Cell* **2005,** 16, (3), 1282-1295.

29. Levine, T. P.; Munro, S., Targeting of Golgi-specific pleckstrin homology domains involves both PtdIns 4-kinase-dependent and -independent components. *Curr. Biol.* **2002,** 12, (9), 695-704.

30. Roy, A.; Levine, T. P., Multiple pools of phosphatidylinositol 4-phosphate detected using the pleckstrin homology domain of Osh2p. *J. Biol. Chem.* **2004,** 279, (43), 44683-9.

31. Yu, J. W., et al., Genome-wide analysis of membrane targeting by S. cerevisiae pleckstrin homology domains. *Mol. Cell* **2004,** 13, (5), 677-88.

32. Balla, A., et al., Maintenance of hormone-sensitive phosphoinositide pools in the plasma membrane requires phosphatidylinositol 4-kinase IIIalpha. *Mol. Biol. Cell* **2008,** 19, (2), 711-721.

33. Stauffer, T. P.; Ahn, S.; Meyer, T., Receptor-induced transient reduction in plasma membrane PtdIns(4,5)$_{P2}$ concentration monitored in living cells. *Curr. Biol.* **1998,** 8, (6), 343-346.

34. Varnai, P.; Balla, T., Visualization of phosphoinositides that bind pleckstrin homology domains: Calcium- and agonist-induced dynamic changes and relationship to Myo-[^{3}H]inositol-labeled phosphoinositide pools. *The Journal of Cell Biology* **1998,** 143, (2), 501-510.

35. Quinn, K. V.; Behe, P.; Tinker, A., Monitoring changes in membrane phosphatidylinositol 4,5-bisphosphate in living cells using a domain from the transcription factor tubby. *J Physiol* **2008,** 586, (Pt 12), 2855-71.

36. Santagata, S., et al., G-protein signaling through tubby proteins. *Science* **2001,** 292, (5524), 2041-2050.

37. Dowler, S., et al., Identification of pleckstrin-homology-domain-containing proteins with novel phosphoinositide-binding specificities. *Biochem. J.* **2000,** 351, (Pt 1), 19-31.

38. Kimber, W. A.; Deak, M.; Prescott, A. R.; Alessi, D. R., Interaction of the protein tyrosine phosphatase PTPL1 with the PtdIns(3,4)P_2-binding adaptor protein TAPP1. *Biochem. J.* **2003,** 376, (Pt 2), 525-35.

39. Watton, S. J.; Downward, J., Akt/PKB localization and 3' phosphoinositide generation at sites of epithelial cell-matrix and cell-cell interaction. *Curr. Biol.* **1999,** 9, (8), 433-6.

40. Servant, G., et al., Polarization of chemoattractant receptor signaling during neutrophil chemotaxis. *Science* **2000,** 287, (5455), 1037-40.

41. Varnai, P.; Rother, K. I.; Balla, T., Phosphatidylinositol 3-kinase-dependent membrane association of the Bruton's tyrosine kinase pleckstrin homology domain visualized in single living cells. *J. Biol. Chem.* **1999,** 274, (16), 10983-9.

42. Segal-Hayoun, Y.; Cohen, A.; Zilberberg, N., Molecular mechanisms underlying membrane-potential-mediated regulation of neuronal $K_{2P}2.1$ channels. *Mol. Cell. Neurosci.* **2010,** 43, (1), 117-126.

43. Martinez-Pinna, J.; Gurung, I. S.; Mahaut-Smith, M. P.; Morales, A. s., Direct voltage control of endogenous lysophosphatidic acid G-protein-coupled receptors in Xenopus oocytes. *The Journal of Physiology* **2010**, -.

44. Leslie, N. R.; Downes, C. P., PTEN: The down side of PI 3-kinase signaling. *Cell. Signal.* **2002,** 14, (4), 285-295.

45. Salim, K., et al., Distinct specificity in the recognition of phosphoinositides by the pleckstrin homology domains of dynamin and Bruton's tyrosine kinase. *EMBO (Eur. Mol. Biol. Organ.) J.* **1996,** 15, (22), 6241-6250.

46. Rameh, L. E., et al., A comparative analysis of the phosphoinositide binding specificity of pleckstrin homology domains. *J. Biol. Chem.* **1997,** 272, (35), 22059-66.

47. James, S. R., et al., Specific binding of the Akt-1 protein kinase to phosphatidylinositol 3,4,5-trisphosphate without subsequent activation. *Biochem. J.* **1996,** 315 (Pt 3), 709-13.

48. Knight, J. D.; Falke, J. J., Single-molecule fluorescence studies of a PH domain: new insights into the membrane docking reaction. *Biophys. J.* **2009,** 96, (2), 566-82.

49. Villalba-Galea, C. A.; Sandtner, W.; Starace, D. M.; Bezanilla, F., S4-based voltage sensors have three major conformations. *Proc. Natl. Acad. Sci. U. S. A.* **2008,** 105, (46), 17600-17607.

50. Shaner, N. C., et al., Improving the photostability of bright monomeric orange and red fluorescent proteins. *Nat. Methods* **2008,** 5, (6), 545-51.

51. Elsliger, M. A., et al., Structural and spectral response of green fluorescent protein variants to changes in pH. *Biochemistry* **1999,** 38, (17), 5296-301.

52. Suh, B.-C.; Inoue, T.; Meyer, T.; Hille, B., Rapid chemically induced changes of PtdIns(4,5)P_2 gate KCNQ ion channels. *Science* **2006,** 314, (5804), 1454-1457.

53. Bleasdale, J. E., et al., Inhibition of phospholipase C dependent processes by U-73122. *Adv. Prostaglandin Thromboxane Leukot. Res.* **1989,** 19, 590-3.

54. Ratzan, W. J.; Okamura, Y.; Jaffe, L. A., A voltage sensitive phosphatase from Xenopus Laevis testis. *Biophys. J.* **2009,** 96, (3, Supplement 1), 594a-594a.

55. Tapparel, C., et al., The TPTE gene family: cellular expression, subcellular localization and alternative splicing. *Gene* **2003,** 323, 189-199.

56. Mannuzzu, L. M.; Moronne, M. M.; Isacoff, E. Y., Direct physical measure of conformational rearrangement underlying potassium channel gating. *Science* **1996,** 271, (5246), 213-6.

57. Borah, H. N.; Boruah, R. C.; Sandhu, J. S., Microwave-induced one-pot synthesis of N-carboxyalkyl maleimides and phthalimides. *Journal of Chemical Research-S* **1998**, (5), 272-+.

Appendix 1

Electro-chemical coupling in the voltage-dependent phosphatase Ci-VSP[3]

[3] This work has been published and is reprinted in full with permission from *Nature Chemical Biology*:

"Electro-chemical coupling in the voltage-dependent phosphatase Ci-VSP"
Susy C. Kohout, Sarah C. Bell, Lijun Liu, Qiang Xu, Daniel L. Minor Jr., and Ehud Y. Isacoff, *Nature Chemical Biology*, 2010, 6,(5), 369-375.

Abstract

In the voltage sensing phosphatase, Ci-VSP, a voltage sensing domain (VSD) controls a lipid phosphatase domain (PD). The mechanism by which the domains are allosterically coupled is not well understood. Using an *in vivo* assay, we find that the inter-domain linker that connects the VSD to the PD is essential for coupling the full-length protein. Biochemical assays show that the linker is also needed for activity in the isolated PD. We identify a late step of VSD motion in the full-length protein that depends on the linker. Strikingly, this VSD motion is found to require $PI(4,5)P_2$, a substrate of Ci-VSP. These results suggest that the voltage-driven motion of the VSD turns the enzyme on by rearranging the linker into an activated conformation, and that this activated conformation is stabilized by $PI(4,5)P_2$. We propose that Ci-VSP activity is self-limited because its decrease of $PI(4,5)P_2$ levels decouples the VSD from the enzyme.

Introduction

The *Ciona intestinalis* voltage-sensing phosphatase, Ci-VSP, has an N-terminal domain that resembles the voltage sensing domain (VSD) of voltage-gated ion channels and a C-terminal domain that is homologous to the "phosphatase and tensin homologue deleted on chromosome 10" (PTEN) protein, a lipid and protein phosphatase(Figure A1.1a). [1-3] Ci-VSP is the first member of the voltage dependent family of proteins that is not an ion channel. Instead, Ci-VSP takes an electrical signal in the form of membrane potential and converts it to a chemical signal through its phosphatase activity. Its discovery has raised questions about how a membrane-spanning sensor domain can couple to both the gates of ion channel pore domains and to a cytoplasmic enzyme. For voltage-gated potassium channels, the linker between S4 in the VSD and S5 in the pore domain has been shown to be necessary for coupling the voltage sensing to the gating of the pore.[4-6]

The homology between the Ci-VSP phosphatase domain (PD) and PTEN led to the discovery that Ci-VSP is a voltage-dependent lipid phosphatase.[1] Although PTEN dephosphorylates the 3-phosphate of phosphatidylinositol 3,4,5-trisphosphate ($PI(3,4,5)P_3$), Ci-VSP has been shown to remove the 5-phosphate of both $PI(3,4,5)P_3$, dephosphorylating it to phosphatidylinositol 3,4-bisphosphate ($PI(3,4)P_2$), and phosphatidylinositol 4,5-bisphosphate ($PI(4,5)P_2$), dephosphorylating it to phosphatidylinositol 4-phosphate (PI(4)P).[7-9] While there are sequence divergences between Ci-VSP and PTEN, there are a number of notable similarities. The catalytic domains are 44% identical, and the residues that are known to be important for catalysis are highly conserved. They share several basic amino acids just upstream of the catalytic domain, which are known as the "$PI(4,5)P_2$ binding motif" (PBM) in PTEN.[10] In PTEN, the PBM is essential for membrane targeting and this has been attributed to an interaction between $PI(4,5)P_2$ and the basic residues in the PBM.[11-14] The homologous region in Ci-VSP links the VSD to the PD (Figure A1.1a), suggesting that it may couple voltage sensing to enzymatic activity, analogous to the function of the S4-S5 linker in K^+ channels.

A major unresolved question about Ci-VSP, and its homologues from sea squirt to vertebrates, is how do the voltage-driven structural rearrangements of the VSD control the

activity of the enzyme? Mutations in the VSD-PD linker have been shown to eliminate activity,[1, 15] suggesting either that this linker plays a direct role in the function of the PD or that it is important for coupling the VSD to the PD. To gain insight into this issue, we examined the activity of linker mutants in the isolated PD of the protein *in vitro*. We found that point mutations substantially reduce activity and that a linker deletion ablates activity altogether. These observations indicate that the linker has a direct role in enzymatic function. Because mutations in the linker directly affect the activity of the enzyme domain, activity cannot be used to determine if the mutants also affect coupling. We therefore developed an alternative coupling assay using Voltage Clamp Fluorometry (VCF).[16, 17] The assay is based on recent evidence that manipulation of the phosphatase by mutation of the catalytic cysteine 363 to a serine or by an active site blocker alters the gating current (also known as "sensing current").[18] This alteration demonstrates that inter-domain coupling between the PD and the VSD of the protein can be detected optically as an influence of PD mutants on VSD motion as measured by VCF.[15, 18, 19] Because the effect of the C363S mutation is modest, we searched for another phosphatase mutation that has a bigger impact on the VSD.

Using VCF to measure the voltage-driven motion of the VSD, we identified a new a catalytic site mutation, D331A, which strongly alters the voltage dependence and kinetics of VSD motion and, thus, provides a high accuracy gauge of inter-domain coupling. With this measure of coupling, we find that mutations in the VSD-PD linker compromise coupling. These linker mutants are also found to alter a late step of VSD motion. Strikingly, we find that $PI(4,5)P_2$ modulates both coupling and the late VSD motion. We propose a model where $PI(4,5)P_2$ interacts with the linker to stabilize an enzyme-activating conformation induced by the depolarization-driven motion of the VSD. The modulation by the substrate could provide a mechanism for enhancing enzymatic activity when $PI(4,5)P_2$ is high and reducing activity when it is low to limit the degree of $PI(4,5)P_2$ depletion.

Results

Effect of mutations in VSD-PD linker on activity

Ci-VSP has an N-terminal VSD and a C-terminal PD that are connected by a 16 amino acid linker (Figure A1.1a). To understand how the voltage-driven motions of the VSD are coupled to the activity of the PD, we examined the linker, which shares 50% identity with the PTEN N-terminal (PBM) (Figure A1.1b, top). The PTEN PBM contains several basic amino acids, including K13 and R15, which have been found to be mutated in cancer cells.[20-22] K13E disrupts the membrane targeting of PTEN, even though the active site is still capable of catalysis.[14] These functionally important PTEN residues lie in the second half of the PBM and are conserved in Ci-VSP's VSD-PD linker as K252 (PTEN K13) and R254 (PTEN R15) (Figure A1.1b, top). A recent study showed that the double mutation of R254A with its neighbor R253A eliminates voltage-dependent changes in activity, leading to the proposal that they serve as a part of a PBM and an inter-domain coupler for Ci-VSP.[15]

We focused on three consecutive residues, K252, R253 and R254 in Ci-VSP (A1.1b, top), and made individual glutamine mutations to neutralize the charge carried by each position. These mutations were made in the background of G214C, which served as a fluorophore labeling site. Because the level of activity will depend on both the rate of catalysis by each molecule of Ci-VSP and on the number of Ci-VSP molecules in the plasma membrane, it was important to determine if the mutations affect expression level. We assessed the expression level of the three mutants following labeling of the G214C position with the fluorescent probe, tetramethylrhodamine maleimide (TMRM). We found that the resting G214C-TMRM (G214C*) oocyte fluorescence at the holding potential of -80 mV (an index of the number of labeled Ci-VSP proteins on the cell surface) was as high in the three mutants (*i.e.* they expressed as well) as in wild type (Figure A1.7), enabling a straightforward comparison of their activity. To measure catalytic activity, we employed a previously established assay that uses an IRK1 channel that is mutated (R228Q) to reduce $PI(4,5)P_2$ affinity.[1, 16] (see Materials and Methods & Figure A1.8). We found that K252Q and R254Q reduce voltage-dependent changes in activity to undetectable levels, and that R253Q reduces this activity by 80 ± 6% (n=8) relative to G214C* alone (Figure A1.1c).

The loss of activity in the linker neutralization mutations could be due to a loss of coupling. Alternatively, it could reflect a direct effect of the mutations on the PD. To distinguish between these possibilities, we examined the effect of the K252Q, R253Q and R254Q mutations on the activity of the isolated PD construct (amino acids 240-576) *in vitro*. Circular dichroism (CD) measurements showed that the three mutant proteins were all well folded (Figure A1.9). Using the malachite green activity assay to monitor phosphatase activity of the purified proteins, [1, 8] we found that R253Q retained wild type levels of activity, but that K252Q and R254Q had reduced activity (Figure A1.1d, Methods). These *in vitro* experiments indicate that two of the three conserved basic residues have a direct influence on PD activity.

To examine the function of the Ci-VSP linker further, we carried out the malachite green *in vitro* activity assay on a PD construct from which the linker was deleted (*i.e.* where the construct begins at amino acid 256, but is otherwise wild type in sequence). This construct was well folded (Figure A1.9) but completely lacked activity towards either a membrane bound $PI(3,4,5)P_3$ substrate or a water soluble inositol-(1,3,4,5)-tetraphosphate (IP_4) substrate (Figure A1.1d, Figure A1.10). An equivalent deletion in PTEN lost activity with the membrane bound $PI(3,4,5)P_2$ but retained activity against the soluble IP_4,[11] distinguishing Ci-VSP from PTEN. Thus, the Ci-VSP linker is necessary for the catalytic function of the PD. These results suggest that in the full-length construct negative voltages may disable the linker, and that depolarization may allow it to assume the activating conformation that it has in the VSD-less construct in solution.

Catalytic domain influence over the VSD

The direct effects of the linker on enzyme activity, which we observed above, mean that in order to gauge VSD-PD coupling in the full-length protein, one needs an assay that does not depend on phosphatase activity. Recently in the zebrafish VSP,[19] the serine mutant at the

catalytic cysteine (analogous to Ci-VSP C363S) and an active site blocker, orthovanadate, were both shown to alter the "sensing" current—the analog of the gating current of voltage-gated channels. Those results imply that changes in the catalytic site influence VSD motion and that they could provide a readout of inter-domain coupling. We therefore turned next to examining the impact of catalytic site mutations on VSD motion, as measured using VCF.

We made mutations in the PD of Ci-VSP at residues that are conserved in PTEN and required for catalysis (Figure A1.1b, bottom). In addition to the C363S mutation of the catalytic cysteine, which was already described,[1, 9] we tested D331A, whose homologous mutation in PTEN (D92A) also ablates activity.[13, 23, 24] The mutations were made in the G214C fluorophore labeling site background, as was done above with the linker mutations. These catalytic mutants were fluorescently labeled to the same degree as wild type, indicating equivalent expression (Figure A1.7). Although they expressed as well as wild type, C363S and D331A had no detectable voltage-dependent changes in enzymatic activity (Figure A1.1c).

To probe the activity of these mutants further, we purified the isolated linker-PD construct for each mutant and tested for activity *in vitro*. CD measurements indicated that the C363S and D331A were well folded and similar to wild type (Figure A1.9). The enzymatic activity was abolished in C363S and reduced by 73 ± 8% in D331A (Figure A1.1d). The *in vivo* and *in vitro* data agree with earlier observations on C363S in the wild type background[1, 9] and show that D331A also interferes with activity.

We used VCF to measure the kinetics and voltage dependence of the structural rearrangements of the VSD by monitoring the fluorescence of the TMRM attached to position G214 (G214C*) at the outer end of S4. We found that both C363S and D331A slowed the repolarization-driven motion of S4 (ΔF_{OFF}) (Figure A1.2a). The mutants also increased the steepness of the fluorescence-voltage (F-V) relation and shifted its midpoint in the negative direction (Figure A1.2b, Table A1.1). D331A had the stronger effects, negatively shifting the midpoint of the F-V by 47 ± 1 mV and slowing the first component of the ΔF_{OFF} by 13 ± 1 fold. The homologous mutation in PTEN to Ci-VSP's D331A (PTEN D92A) can trap the substrate,[25] consistent with what appears to be stabilization by D331A of the activated state in Ci-VSP. This large influence of the catalytic site D331A mutation on VSD motion provided us with a clear report of VSD-PD coupling *in vivo* (A1. 2c).

Role of the VSD-PD linker in coupling

We tested the notion that the linker plays a role in coupling VSD motion to the function of the phosphatase by asking if the linker mutations weaken the influence of the catalytic site D331A mutation on the motion of the VSD. We first examined the effect on S4 motion of each of the three linker neutralizations on its own. We found that the G214C* ΔF_{OFF} and F-V of K252Q and R253Q were similar to those of wild type and that the ΔF_{OFF} and F-V of R254Q were mildly perturbed (Figure A1.11, Table A1.1).

We next examined the effect of the linker mutants on the VSD perturbations caused by the catalytic site mutations. We found that K252Q eliminated the influence of the D331A catalytic site mutation on the VSD, ablating both the slowing of the ΔF_{OFF} (Figure A1.3a) and the negative shift of the F-V (Figure A1.3b, Table A1.1). The R253Q mutant had similar but less complete effects, reducing but not eliminating the slowing of the ΔF_{OFF} (Figure A1.12a) and negative shift of the F-V (Figure A1.12b, Table A1.1) caused by the D331A mutation. The incomplete uncoupling by R253Q is consistent with its incomplete reduction of voltage dependent enzyme activity (Figure A1.1c). These results show that the linker couples the voltage-dependent structural state of the VSD to the functional state of the catalytic site in the PD.

Role of VSD-PD linker in late step VSD motion

Having found that the conserved basic residues in the C-terminal end of the VSD-PD linker are important for coupling, we next endeavored to identify the VSD motion(s) in which the linker participates. To do this, we turned to another TMRM labeling site, Q208C, in the middle of the S3-S4 loop, where we had shown earlier that fluorescence reports on a series of voltage-driven rearrangements[16] (Figure A1.4a). Steps from the holding potential of -80 mV to voltages of between -150 and zero mV evoked fast and monotonic ΔFs, while more positive voltages of up to +100 mV evoked an additional slower component that decreased fluorescence. Even more positive steps, from +100 up to +200 mV, evoked yet an additional component of slow fluorescence increase (Figure A1.4a).

Linker neutralization mutations K252Q, R253Q and R254Q were introduced individually into the Q208C background and their effect on the fluorescence report of TMRM (Q208C*) was tested. While the ΔF_{ON} and ΔF_{OFF} of Q208C* were unaffected by the mutations over the negative voltage range and in the lower end of the positive voltage range, all three of the mutations attenuated the amplitude of the late upward ΔF_{ON} component evoked by the largest depolarizations (Figure A1.4b-d, Figure A1.13a) and shifted its voltage dependence in the positive direction (Figure A1.4e-h, Figure A1.13b, Table A1.1). Thus, the linker specifically plays a role in the late step of VSD motion.

Regulation of VSD motion by PI(4,5)P_2

Considering that the Ci-VSP VSD-PD linker is homologous to the N-terminal PI(4,5)P_2 binding domain (PBM) of PTEN, we wondered if PI(4,5)P_2 might modulate the function of the VSD-PD linker. To test this possibility, we set out to manipulate the concentration of PI(4,5)P_2 in the membrane and determine the effect on the VSD rearrangements which involve the linker according to our above results. We co-expressed Ci-VSP with the serotonin 2C receptor (5HT2C), a G-protein coupled receptor which activates phospholipase C (PLC), leading to the cleavage of a phosphodiester bond of PI(4,5)P_2 into diacyl glycerol (DAG) and inositol-(1,4,5)-trisphosphate (IP_3).[26] We first tested the ability of serotonin to activate the 5HT2C receptor and deplete PI(4,5)P_2 in oocyte membranes by using IRK1Q as a PI(4,5)P_2 sensor, as shown above

(Figure A1.1c). We found that 10 μM serotonin evoked a reliable reduction of IRK1Q current over a time-course of 5 min (Figure A1.14a). We therefore chose this time-point for our analysis.

The 5HT2C receptor was co-expressed with either the catalytically active G214C*, or the catalytically compromised G214C*/D331A. F-Vs were obtained before and 5 minutes after exposure to 10 μM serotonin. Successful activation of PLC was monitored by measuring current through the oocyte's endogenous Ca^{2+} dependent Cl^- channels (Figure A1.15a), which are activated by the IP_3-induced release of Ca^{2+} from internal stores. Both in the catalytically active and catalytically compromised versions of Ci-VSP, the F-V relations were shifted in the positive direction and became shallower following the addition of serotonin (Figure A1.5a, Figure A1.15b, Table A1.2). This shift could also be monitored as a decrease in fluorescence amplitude in response to a step to 0 mV following the addition of the serotonin (Figure A1.15c). Another metabotropic receptor known to activate the PLC pathway, mGluR1, had the same effect (Figure A1.12d, e). The similar effects of activation of the PLC-coupled 5HT2C and mGluR1 receptors indicates that Ci-VSP is modulated either by the depletion of $PI(4,5)P_2$ or by the production of IP_3 or DAG by PLC.

To distinguish between the possibilities that Ci-VSP is modulated either by the depletion of $PI(4,5)P_2$ or by the production of IP_3 or DAG, we chose an alternative method for reducing $PI(4,5)P_2$ in the membrane, which would not produce IP_3 or DAG. For these experiments, we employed an inducible phosphatase that hydrolyzes $PI(4,5)P_2$ into PI(4)P, thus avoiding the IP_3 and DAG signaling cascades.[27, 28] The phosphatase, Inp54p, is a truncated version of a yeast inositol polyphosphate 5-phosphatase that specifically cleaves $PI(4,5)P_2$ at the 5-phosphate.[27] The activity of Inp54p can be triggered by the application of the small, membrane permeable organic molecule rapamycin, thereby permitting VCF measurements of VSD motion to be made before and after $PI(4,5)P_2$ depletion. To make the Inp54p inducible by rapamycin, it was fused with one of two protein domains which heterodimerize upon addition of rapamycin: FKBP (FK506 binding protein) fused to CFP, which enables the membrane localization of the phosphatase to be visualized, and which is referred to as CFInp.[27] The partner protein domain, FRB (the rapamycin binding fragment of mTOR), was fused to the plasma membrane targeted Lyn N-terminal sequence (LDR).[27] Previous studies have shown that rapamycin brings CFInp to the plasma membrane and reduces $PI(4,5)P_2$ concentrations in oocytes.[29] We confirmed that the rapamycin system was functional, finding it to efficiently shuttle the CFInp to the plasma membrane (Figure A1.16a, b) and to decrease IRK1Q current (Figure A1.14b).

Activation of the rapamycin system shifted the F-V to the right and decreased the slope of the F-V both in the catalytically active G214C* and in the catalytically compromised G214C*/D331A (Figure A1.5b, Figure A1.17a, Table A1.3). An enzyme-dead version of the CFInp (CFInp D281A) was mobilized to the plasma membrane by rapamycin just as well as was the wild type CFInp (Figure A1.16a, b), but did not affect the F-V (Figure A1.16c), indicating that the shift in the F-V is specific to $PI(4,5)P_2$ depletion.

Taken together, the similar shifts in the F-V induced by activation of the two PLC coupled GPCRs, 5HT2C and mGluR1, and the rapamycin system that dephosphorylates

$PI(4,5)P_2$ to another product, demonstrate that $PI(4,5)P_2$ depletion alters the voltage-driven rearrangement of the VSD.

$PI(4,5)P_2$ and linker mutants alter late VSD motion

The above results showed that membrane $PI(4,5)P_2$ regulates VSD motion. We next tried to identify the step of VSD motion that is affected by $PI(4,5)P_2$. For this purpose we turned once again to the TMRM labeling site Q208C, whose fluorescence reports on several distinct phases of VSD motion. We found that, in wild type Q208C*, the rapamycin depletion of $PI(4,5)P_2$ decreases the amplitude of the late step of VSD motion that is activated by depolarization to > +100 mV and shifts the voltage dependence of this component to the right (Figure A1.5c, Figure A1.17, Table A1.3).

The effect of $PI(4,5)P_2$ depletion on the late phase of VSD motion was remarkably similar to the effect of the mutation of the basic residues in the VSD-PD linker (compare Figure A1.4e-h to Figure A1.5c, and Figure A1.4a-d to Figure A1.17b). This similarity led us to ask if $PI(4,5)P_2$ modulation actually depends on the basic residues in the linker. To test this, we co-expressed the 5HT2C receptor with the catalytically active G214C*/K252Q or the catalytically compromised G214C*/D331A/K252Q. We found that, in contrast to the wild type linker (Figure A1.5a, Figure A1.15b), the serotonin induced $PI(4,5)P_2$ depletion effect was absent in the K252Q linker mutant (Figure A1.5d, Figure A1.18a, Table A1.3). We also tested the rapamycin system in the catalytically compromised G214C*/D331A protein and obtained a similar result: the $PI(4,5)P_2$ depletion effect, present in the wild type linker (Figure A1.5b), was absent in the K252Q linker mutant (Figure A1.5e, Table A1.3).

Because G214C* does not clearly resolve the various components of VSD motion, we also tested the effect of $PI(4,5)P_2$ on the multiple VSD rearrangements that could be resolved from the fluorescent report of Q208C*. We found that, in contrast to the large effect seen in wild type (Figure A1.5c), the rapamycin induced depletion of $PI(4,5)P_2$ had almost no effect on constructs containing any of the individual linker mutations (Figure A1.5f, Figure A1.18b, c, Table A1.3).

Thus, $PI(4,5)P_2$ and the basic residues in the VSD-PD linker appear to regulate the same late step of VSD motion and single linker neutralization mutations are sufficient to greatly blunt the modulation by $PI(4,5)P_2$. Together, these findings suggest that $PI(4,5)P_2$ acts through the linker.

Discussion

We have probed the interplay between the voltage-driven conformational changes in the VSD of Ci-VSP and the functional state of its PD. We assessed combined catalytic site and inter-domain linker mutations to examine enzyme activity of the full-length protein in live cell membranes and of the isolated PD *in vitro*. We also investigated the structural rearrangements of the VSD of the intact protein measured by Voltage Clamp Fluorometry. The results identify a

rearrangement that depends on both the $PI(4,5)P_2$ substrate and on conserved basic residues in the inter-domain linker.

Previous studies showed that the inter-domain linker is critical for the voltage dependent activity of the full-length protein, with a particular importance of several basic residues at the phosphatase (C-terminal) end of the linker.[1, 15] We found that three basic residues examined individually, K252, R253 and R254 are essential for catalysis in the living cell, with neutralization mutations leaving no detectable voltage dependent activity in K252Q and R254Q and drastically reducing activity in R253Q. We asked whether this loss of activity is due to an effect on inter-domain coupling or to a direct effect on the enzyme. We found K252Q and R254Q have reduced activity in the isolated linker-PD fragment *in vitro*. While the reduction in activity of the linker-PD construct *in vitro* was less extreme than what was seen for the full-length protein in live cells, the direct effect of K252Q and R254Q on the function of the phosphatase prevent a clear cut conclusion about their possible role in coupling. In contrast, R253Q had normal activity in the linker-PD construct *in vitro*, but ~80% reduced activity in the full-length protein in cells, consistent with an effect on coupling.

To clarify the role of the linker in inter-domain coupling, we developed a second assay that measures the coupling in the opposite direction. Rather than measuring the effect of voltage-driven VSD rearrangements on phosphatase activity, we measured the effect of mutations in the phosphatase catalytic site on VSD motion. This approach had the added advantage of a direct, high signal to noise and time-resolved measure of VSD conformation using VCF. We found that linker neutralizations reduced or eliminated the influence of catalytic site mutations on VSD motion. K252Q ablated the PD to VSD influence and completely eliminated voltage dependent activity. R253Q, on the other hand, caused a substantial but incomplete reduction in the influence of the PD mutants on the VSD and largely, but incompletely, reduced voltage dependent activity. Together, the findings show that the conserved basic residues in the VSD-PD linker play a central role in inter-domain coupling.

We wondered how the linker could alter the functional state of the enzyme in response to voltage sensing motions of the VSD. We obtained an insight into this when we found that deletion of the linker from the isolated PD abolishes activity *in vitro*. This suggests that the linker acts as a positive regulator of the enzyme. Moreover, it suggests that the mechanism of coupling is that the voltage-driven rearrangement of the VSD changes the conformation of the linker from an inactive form at negative voltage into an active form, which turns the enzyme on at positive voltage (Figure A1.6).

The homologue of the Ci-VSP linker is the N-terminus of PTEN, which has been shown to bind to $PI(4,5)P_2$ through the same basic residues that we examined here in Ci-VSP.[11-14, 30, 31] A recent study on Ci-VSP proposed that $PI(4,5)P_2$ also binds to the Ci-VSP linker.[15] If this were the case then, given the role we documented for the linker in inter-domain coupling, we would expect that $PI(4,5)P_2$ might have an effect on Ci-VSP gating. Indeed, we found that $PI(4,5)P_2$ modulates a specific step of VSD motion: a late step that takes place at positive voltage. The same late VSD rearrangement was selectively affected by mutation of the linker's basic residues. Our findings suggest that $PI(4,5)P_2$ binding stabilizes the linker in its activating state. This effect

may be explained by $PI(4,5)P_2$ binding to the basic residues, however direct evidence will be required to prove such an interaction.

The finding that the substrate of the enzyme is also a modulator implies that Ci-VSP could function as a feedback system. We propose a model in which the linker is primed and that the VSD and phosphatase are coupled when $PI(4,5)P_2$ levels are high, thus enabling membrane depolarization to turn on phosphatase activity (Figure A1.6). As the enzymatic activity of Ci-VSP progresses and $PI(4,5)P_2$ levels decrease, we propose that the linker loses its $PI(4,5)P_2$ and that the enzyme is consequently uncoupled from the VSD, thereby terminating activity. Such modulation by substrate could enhance catalysis when $PI(4,5)P_2$ is high and lower activity when $PI(4,5)P_2$ is low to prevent excessive depletion.

Author Contributions

S.C.K. designed, conducted and analyzed the VCF experiments and the confocal experiment, as well as conducted and analyzed the malachite green assay and the CD spectroscopy and wrote the paper. S.C.B. designed, conducted and analyzed the *in vivo* activity assay and edited the paper. L.L. expressed and purified the cytosolic domain proteins and edited the paper. Q.X. helped design the malachite green assay as well as expressed and purified the cytosolic domain proteins. D.L.M. designed and initiated the CD spectroscopy as well as edited the paper. E.Y.I. designed the VCF experiments as well as the *in vivo* activity assay and wrote the paper.

Materials and Methods

Molecular Biology. The Ci-VSP in the pSD64TF vector was kindly provided by Dr. Y. Okamura (Osaka University, Osaka, Japan). The cytosolic phosphatase Ci-VSP DNA (encoding amino acids 240-576 or 256-576) was sub-cloned into the *NdeI* and *Hin*dIII sites of the pET-28b vector for bacterial expression. The LDR and CFInp constructs were kindly provided by Dr. T. Meyer (Stanford University, Palo Alto, CA) and subcloned into pGEMHE vectors. The IRK1 construct was kindly provided by Dr. E. Reuveny (Weizmann Institute of Science, Rehovot, Israel). The mGluR1α construct was kindly provided by S. Nakanishi (Osaka Bioscience Institute, Osaka, Japan). All point mutations were made using QuikChange (Stratagene). All DNA was confirmed by DNA sequencing. RNA was transcribed using either T7, T3 or SP6 mMessage mMachine (Ambion) kits.

Protein Purification. The plasmid DNA encoding the cytosolic fragment of Ci-VSP was transformed into *Escherichia coli* Rosetta (DE3) pLysS strains. The bacterial cultures were grown at 37ºC to an OD600 of 0.8 and induced for 30 hours at 18°C with 0.5 mM isopropyl-b-D-thiogalactopyranoside (IPTG) (EMD Chemicals). The cells were harvested by centrifugation (5000xg) and the pellets were frozen by liquid nitrogen and stored at -80ºC. For a typical 2L culture, the cells were disrupted by sonication in 50 ml of lysis buffer (10 mM HEPES pH 7.4, 50 mM NaCl, 1 mM DTT, 10% glycerol, 1 mM PMSF, 25 mg/ml DNAse, 20 mg/ml lysozyme and 0.1% Triton X-100). After centrifugation at 40,000xg, the supernatant was incubated with 4 ml of Talon Co^{2+} resin (Clontech) for 1 hour on a rotary shaker at 4°C. The resin was then bedded in column and washed with 30 ml of buffer A (500 mM NaCl, 10 mM HEPES, pH 7.4), followed by 30 ml of buffer A containing 20 mM imidazole. The bound fractions were then eluted with buffer A containing a stepwise gradient of 50, 100 and 300 mM imidazole, 25 ml each. The Ci-VSP containing elution (with 300 mM imidazole), with 1 ml of 500 mM EDTA (pH 8.0) added, was dialyzed overnight against 4 liters of the final buffer (50 mM Tris pH 8.0, 50 mM NaCl, 3 mM DTT). Protein purity was verified by SDS-PAGE gels. All proteins gave single bands on SDS-PAGE. Protein concentrations were determined by tryptophan absorbance at 280 nm[1]. For circular dichroism (CD) spectra, protein was transferred into CD buffer (10 mM Na phosphate, pH 7.3, 50 mM NaCl, 3 mM DTT) by running over a Superdex 200 gel filtration column (GE Healthcare). All proteins ran as single, monodisperse peaks upon gel filtration.

Circular dichroism (CD). CD measurements were carried out using an Aviv model 215 spectrometer (Aviv Biomedical). The wavelength scans from 300 nm to 200 nm were carried out at 4°C using a 0.1 cm path length cuvette. Five scans of the same sample were averaged. Molar ellipticity was calculated as follows: $\theta = 100(\Delta m)/Cnl$, where Δm is the CD signal in millidegrees, C is the protein concentration in millimolar, n is the number of residues in the peptide, and l is the cuvette path length in centimeters.

***In vitro* phosphatase assay.** Stock solutions of lipid vesicles were prepared by extrusion. First chloroform:methanol:water (1:2:0.8) solutions of 1,2-dioleoyl-sn-glycero-3-phospho-L-serine (PS) and 1,2-dioleoyl-sn-glycero-3-phospho-(1-myo-inositol-3,4,5-trisphosphate), ($PI(3,4,5)P_3$) (Avanti Polar Lipids) lipids were dried in a rotovap and left over a stream of nitrogen for 20 minutes. The lipids were suspended in reaction buffer (50 mM Tris, pH 8.0, 50 mM NaCl, 3

mM DTT) to final concentrations of 75 μM for $PI(3,4,5)P_3$ and 375 μM for PS. Lipids were passed through three rounds of freeze/thaw cycles then extruded through a Northern Lipids, Inc. 1.5 ml capacity extruder using a 100 nm polycarbonate filter. Reactions were initiated by addition of vesicles (40 μM $PI(3,4,5)P_3$) to the purified cytosolic fragment of Ci-VSP (0.5 μM), incubated at 25°C. and stopped by addition of an equal volume of 100 mM NEM. Stopped reactions were spun down and then 30 μl transferred to a 96 well plate followed by 60 μl of malachite green reagent (BioMol Research Laboratories, Inc.). Color was developed for 30 minutes then the absorbance determined on a microplate reader at 650 nm. Phosphate concentrations were determined by comparison to a standard curve of KH_2PO_4 (BioMol Research Laboratories, Inc.) in reaction buffer. C363S mutant proteins gave similar values as no protein controls.

Confocal imaging. Oocytes were injected with RNA as for the voltage clamp fluorometry experiments with co-injections of either G214C/D331A + LDR + CFInp or G214C/D331A + LDR + CFInp D281A. Uninjected cells were also tested as a control. After 48 hours of expression, oocytes were imaged with an Olympus FV1000 inverted confocal microscope in ND-96 buffer using the 405 nm laser and emission range of 430-530 nm with a 20X objective. Oocytes were imaged using Fluoview software (Olympus) at 1 minute intervals for 15 minutes total with rapamycin addition after the first image acquisition.

Voltage Clamp Fluorometry. Voltage clamp fluorometry was performed as described previously[17]. Briefly, *Xenopus laevis* oocytes were injected with 50 nl mRNA at 0.02–1.2 μg/μl depending on the experiment. Different RNA ratios were used for different co-injection experiments: a 40:1 ratio for experiments co-expressing Ci-VSP and 5HT2C receptors (total RNA ~0.8 μg/μl), a 3:1 ratio for experiments co-expressing Ci-VSP and mGluR1α receptors (total RNA ~0.7 μg/μl), and either a 4:1:1 or a 2:1:1 ratio for experiments co-expressing Ci-VSP, LDR, and CFInp (either wild type or D281A, total RNA ~0.8-1.2 μg-μl). Cells were then incubated in ND-96 (96 mM NaCl, 2 mM KCl, 1.8 mM $CaCl_2$, 1 mM $MgCl_2$, 50 mg/ml gentamicin, 2.5 mM Na pyruvate and 5 mM HEPES, pH 7.6) at 18°C for 24–48 hours. Injected oocytes were treated with a 1 mM solution of glycine maleimide[32] to block native cysteines before protein expression. A Nikon Diaphot inverted microscope with a 20X 0.75 NA fluorescence objective (Nikon) was used with a Dagan CA-1 amplifier (Dagan Corporation), illuminated with a 150 W xenon lamp and intensity was measured with a Hamamatsu HC120-05 photomultiplier tube. The amplifier, photomultiplier and Uniblitz shutter (Vincent Associates) were controlled by the Digidata-1440 board and pClamp10 software package (Axon Instruments). Light was filtered through an HQ535/50 excitation filter, an HQ610/75 emission filter and a Q565LP dichroic (Chroma Technology). Fluorescence signals were low pass filtered at 2 kHz through an eight-pole Bessel filter (Frequency Devices).

On the day of the experiment, cells were incubated in a high potassium solution (92 mM KCl, 0.75 mM $CaCl_2$, 1 mM $MgCl_2$, 10 mM HEPES, pH7.5) with 12 μM tetramethylrhodamine-6-maleimide (Invitrogen) for one hour on ice and in the dark. After extensive washing with ND-96, the cells were stored in ND-96, in the dark and at 12°C until the time of the experiment.

Recording solutions were either ND-96' (without the gentamicin or pyruvate) or NMG buffer (110 mM N-methyl-D-glucamine (NMG) methanesulfonic acid (MS), 2 mM KMS, 2 mM $Ca(MS)_2$, 10 mM HEPES, pH 7.5) to limit leak currents. In all experiments only cells with a good control of voltage were analyzed and reported voltages and voltage steps were actual measurements.

Cells were constantly perfused with ND-96' for co-injection experiments. For experiments with 5HT2C, an initial F-V protocol (t=0, voltage jumps from -150 mV to 200 mV in 10 mV increments) was followed by perfusion of 5-10 μM serotonin (Sigma) for 10-40 s. The resulting Ca^{2+} activated Cl^- currents were monitored to confirm expression of the 5HT2C receptor. Then at t=5 minutes, a final F-V protocol was recorded. A similar protocol was used for experiments with mGluR1α, adding 100 μM glutamate. For experiments with LDR and CFInp, the initial F-V protocol (t=0) was followed by perfusion of 0.5-1 μM rapamycin (Sigma) for 3-5 minutes then by ND-96' until the final F-V protocol at t=10 minutes.

Electrophysiological measure of activity. Ci-VSP catalytic activity was measured indirectly by detecting $PI(4,5)P_2$ via its activation of the inwardly-rectifying IRK1 R228Q K^+ channel (IRK1Q) as described previously[17]. The R228Q mutation of IRK1 was used to alter the sensitivity of the channel for $PI(4,5)P_2$ into an observable range. A brief description of the protocol is as follows: the cell was depolarized to 60 mV to turn Ci-VSP on until a steady state current was established (~100 s). Then the cell was hyperpolarized to -100 mV to turn Ci-VSP off until a steady state was re-established (~400 s) (Figure A1.8). The resulting change in current between the on and off states of Ci-VSP was measured and expressed as percent activity. Currents were leak subtracted by assuming a voltage-independent linear leak. Current was measured at –100 mV after the test holding potential and leak was measured at +50 mV where the IRK channels should be blocked by Mg^{2+} and polyamines and the following equation applied to calculate the leak subtracted (LS) current: $I_{ls} = I_{-100mV} + 2I_{+50mV}$. The percent activity was calculated as: $\Delta I/I_{max} = (I_{-100mV\ last} - I_{+60mV\ last})/ I_{-100mV\ last}$. A similar protocol was used to test for $PI(4,5)P_2$ depletion via activation of the 5HT2C receptor, with IRK1Q serving as the $PI(4,5)P_2$ reporter.

For these experiments, 50 nl of mRNA was injected into *Xenopus laevis* oocytes. Different RNA ratios were used for the different experiments: a 10:1 ratio for experiments co-expressing Ci-VSP and IRK1Q (total RNA ~0.9 μg̃/μl), a 4:1 ratio for experiments co-expressing IRK1Q and 5HT2C receptor (total RNA ~0.1 μg̃/μl) and a 2:2:1 ratio for experiments co-expressing LDR, CFInp and IRK1Q (total RNA ~0.5 μg̃/μl). Cells were incubated in ND-96 at 18°C for 16–48 hours. The recording solutions contained 90 mM KMS, 3 mM $Mg(MS)_2$, 8 mM KOH, 10 mM HEPES, pH 7.4. Other conditions were the same as for voltage clamp fluorometry.

Data Analysis. Kinetic and steady-state traces were analyzed using Igor Pro and Microsoft Excel software. Kinetic traces were fit with double exponential equations. Steady-state voltage dependent traces were fit with Boltzmann equations. Data were normalized to the amplitude of the Boltzmann fits and the error bars indicate the standard error of the mean. Statistical significance was determined using the student's t test. Confocal images were analyzed using MatLab software.

Acknowledgments

This work was supported by grants R01NS035549 (E.Y.I.), U24NS57631 (E.Y.I), and R01DC007664 (D.L.M.) from the US National Institutes of Health and an American Heart Association Established Investigator Award (D.L.M). We thank Y. Okamura (Japanese National Institute for Physiological Sciences) for kindly providing the Ci-VSP cDNA, T. Meyer (Stanford University) for kindly providing the LDR and CFInp cDNA, E. Reuveny (Weizmann Institute of Science, Rehovot, Israel) for providing the IRK1 construct, S. Nakanishi (Osaka Bioscience Institute, Osaka, Japan) for providing the mGluR1α receptor, J. Groves and P. Nair (University of California, Berkeley) for access to and instructions on use of the lipid extruder and H. Janovjak, K. Nakajo, E. Peled and F. Tombola for helpful discussion.

References

1. Murata, Y., et al., Phosphoinositide phosphatase activity coupled to an intrinsic voltage sensor. *Nature* **2005,** 435, (7046), 1239-43.

2. Okamura, Y.; Murata, Y.; Iwasaki, H., Voltage-sensing phosphatase: actions and potentials. *J Physiol* **2009,** 587, (Pt 3), 513-20.

3. Worby, C.; Dixon, J., Phosphoinositide phosphatases: emerging roles as voltage sensors? *Mol Interv* **2005,** 5, (5), 274-7.

4. Long, S. B.; Campbell, E. B.; Mackinnon, R., Crystal structure of a mammalian voltage-dependent Shaker family K+ channel. *Science* **2005,** 309, (5736), 897-903.

5. Lu, Z.; Klem, A.; Ramu, Y., Ion conduction pore is conserved among potassium channels. *Nature* **2001,** 413, (6858), 809-13.

6. Lu, Z.; Klem, A.; Ramu, Y., Coupling between voltage sensors and activation gate in voltage-gated K+ channels. *J Gen Physiol* **2002,** 120, (5), 663-76.

7. Halaszovich, C.; Schreiber, D.; Oliver, D., Ci-VSP is a depolarization-activated phosphatidylinositol-4,5-bisphosphate and phosphatidylinositol-3,4,5-trisphosphate 5'-phosphatase. *J Biol Chem* **2009,** 284, (4), 2106-13.

8. Iwasaki, H., et al., A voltage-sensing phosphatase, Ci-VSP, which shares sequence identity with PTEN, dephosphorylates phosphatidylinositol 4,5-bisphosphate. *Proc Natl Acad Sci U S A* **2008,** 105, (23), 7970-5.

9. Murata, Y.; Okamura, Y., Depolarization activates the phosphoinositide phosphatase Ci-VSP, as detected in Xenopus oocytes coexpressing sensors of PIP2. *J Physiol* **2007,** 583, (Pt 3), 875-89.

10. Maehama, T.; Taylor, G. S.; Dixon, J. E., PTEN and myotubularin: novel phosphoinositide phosphatases. *Annu Rev Biochem* **2001,** 70, 247-79.

11. Iijima, M., et al., Novel mechanism of PTEN regulation by its phosphatidylinositol 4,5-bisphosphate binding motif is critical for chemotaxis. *J Biol Chem* **2004,** 279, (16), 16606-13.

12. Rahdar, M., et al., A phosphorylation-dependent intramolecular interaction regulates the membrane association and activity of the tumor suppressor PTEN. *Proc Natl Acad Sci U S A* **2009,** 106, (2), 480-5.

13. Vazquez, F., et al., Tumor suppressor PTEN acts through dynamic interaction with the plasma membrane. *Proc Natl Acad Sci U S A* **2006,** 103, (10), 3633-8.

14. Walker, S. M., et al., The tumour-suppressor function of PTEN requires an N-terminal lipid-binding motif. *Biochem J* **2004,** 379, (Pt 2), 301-7.

15. Villalba-Galea, C.; Miceli, F.; Taglialatela, M.; Bezanilla, F., Coupling between the voltage-sensing and phosphatase domains of Ci-VSP. *J Gen Physiol* **2009,** 134, (1), 5-14.

16. Kohout, S.; Ulbrich, M.; Bell, S.; Isacoff, E., Subunit organization and functional transitions in Ci-VSP. *Nat Struct Mol Biol* **2008,** 15, (1), 106-8.

17. Mannuzzu, L. M.; Moronne, M. M.; Isacoff, E. Y., Direct physical measure of conformational rearrangement underlying potassium channel gating. *Science* **1996,** 271, (5246), 213-6.

18. Villalba-Galea, C.; Sandtner, W.; Starace, D.; Bezanilla, F., S4-based voltage sensors have three major conformations. *Proc Natl Acad Sci U S A* **2008,** 105, (46), 17600-7.

19. Hossain, M., et al., Enzyme domain affects the movement of the voltage sensor in ascidian and zebrafish voltage-sensing phosphatases. *J Biol Chem* **2008,** 283, (26), 18248-59.

20. Duerr, E., et al., PTEN mutations in gliomas and glioneuronal tumors. *Oncogene* **1998,** 16, (17), 2259-64.

21. Gronbaek, K., et al., Alterations of the MMAC1/PTEN gene in lymphoid malignancies. *Blood* **1998,** 91, (11), 4388-90.

22. Steck, P., et al., Identification of a candidate tumour suppressor gene, MMAC1, at chromosome 10q23.3 that is mutated in multiple advanced cancers. *Nat Genet* **1997,** 15, (4), 356-62.

23. Downes, C., et al., Acute regulation of the tumour suppressor phosphatase, PTEN, by anionic lipids and reactive oxygen species. *Biochem Soc Trans* **2004,** 32, (Pt 2), 338-42.

24. Xiao, Y., et al., PTEN catalysis of phospholipid dephosphorylation reaction follows a two-step mechanism in which the conserved aspartate-92 does not function as the general acid--mechanistic analysis of a familial Cowden disease-associated PTEN mutation. *Cell Signal* **2007,** 19, (7), 1434-45.

25. Flint, A.; Tiganis, T.; Barford, D.; Tonks, N., Development of "substrate-trapping" mutants to identify physiological substrates of protein tyrosine phosphatases. *Proc Natl Acad Sci U S A* **1997,** 94, (5), 1680-5.

26. Julius, D.; MacDermott, A.; Axel, R.; Jessell, T., Molecular characterization of a functional cDNA encoding the serotonin 1c receptor. *Science* **1988,** 241, (4865), 558-64.

27. Suh, B.; Inoue, T.; Meyer, T.; Hille, B., Rapid chemically induced changes of PtdIns(4,5)P2 gate KCNQ ion channels. *Science* **2006,** 314, (5804), 1454-7.

28. Varnai, P.; Thyagarajan, B.; Rohacs, T.; Balla, T., Rapidly inducible changes in phosphatidylinositol 4,5-bisphosphate levels influence multiple regulatory functions of the lipid in intact living cells. *J Cell Biol* **2006,** 175, (3), 377-82.

29. Lukacs, V., et al., Dual regulation of TRPV1 by phosphoinositides. *J Neurosci* **2007,** 27, (26), 7070-80.

30. Campbell, R.; Liu, F.; Ross, A., Allosteric activation of PTEN phosphatase by phosphatidylinositol 4,5-bisphosphate. *J Biol Chem* **2003,** 278, (36), 33617-20.

31. Redfern, R., et al., PTEN phosphatase selectively binds phosphoinositides and undergoes structural changes. *Biochemistry* **2008,** 47, (7), 2162-71.

32. Borah, H. N.; Boruah, R. C.; Sandhu, J. S., Microwave-induced one-pot synthesis of N-carboxyalkyl maleimides and phthalimides. *Journal of Chemical Research-S* **1998**, (5), 272-+.

Figures Tables and Legends

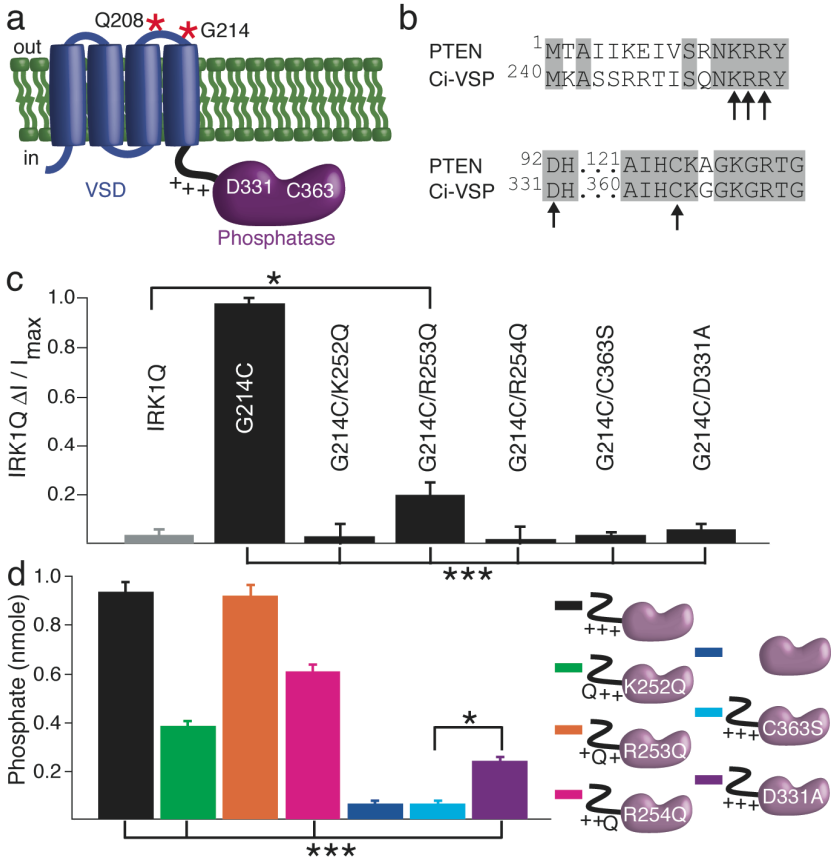

Figure A1.1. Linker and catalytic site mutants reduce or abolish activity. a) Cartoon of Ci-VSP domains. The VSD consists of 4 helices, S1-S4. Q208 and G214 in the S3-S4 external loop are sites of cysteine substitution and attachment of the environmentally sensitive fluorophore TMRM (red asterisks). The sixteen amino acid linker (black) connects S4 of the VSD to the PD (purple). It contains 3 conserved basic residues (+): K252, R253, R254. Two conserved catalytic site residues, D331 and C363, shown in the PD. **b)** Alignment of human PTEN with Ci-VSP: (Top) PTEN N-terminus and VSD-PD linker of Ci-VSP; (Bottom) Active site residues. Identical residues highlighted (gray), arrows mark Ci-VSP residues mutated in this study. **c)** Activity of full-length Ci-VSP in oocytes measured from voltage dependence of IRK1Q current in cells also expressing Ci-VSP. Average data for IRK1Q alone (n=26) or IRK1Q coexpressed with G214C (n=9); G214C/K252Q (n=10); G214C/R253Q (n=8); G214C/R254Q (n=6); G214C/C363S (n=6); G214C/D331A (n=6). $\Delta I/I_{max}$ was calculated from steady-state current of active Ci-VSP (+60 mV) versus inactive Ci-VSP (-100 mV) (Materials and Methods & Supp. Figure. 2). **d)** *In vitro* malachite green activity assay with PS/PI(3,4,5)P_3 vesicles and the cytosolic fragment of Ci-VSP, containing amino acids 240-576, 256-576 or mutations (in linker or PD). Constructs identified in cartoons on right as in (a) with PD in light purple. All error bars are ± SEM. Asterisks indicate statistically significant differences using the student's t test,* = $p<0.05$; *** = $p<0.001$.

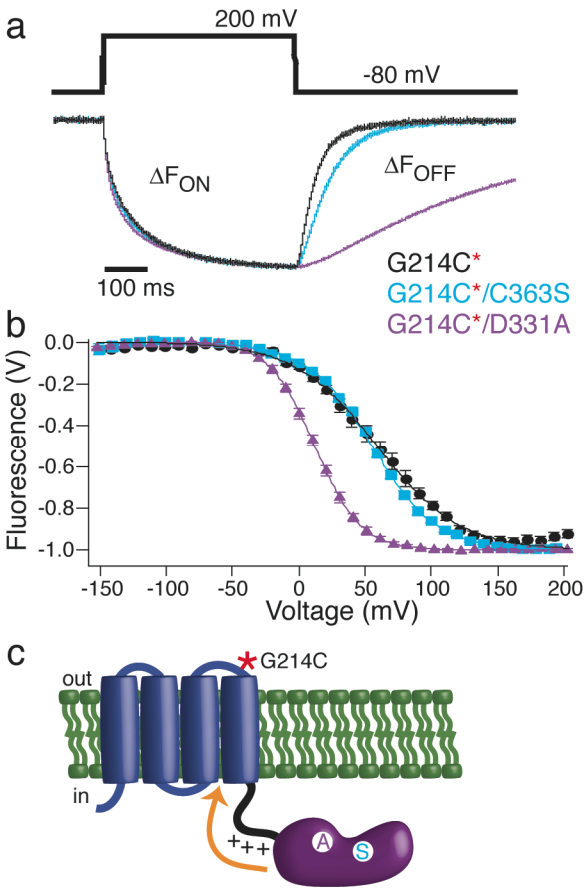

Figure A1.2. Mutations of PD catalytic site alter VSD motion. **a)** Representative fluorescence traces during a step from hp = -80 mV to +200 mV in G214C* (black), G214C*/C363S (blue) and G214C*/D331A (purple). The catalytic site mutations alter S4 ΔF_{ON} and ΔF_{OFF} motions, with more dramatic slowing of the ΔF_{OFF} motion. Traces normalized to the maximal fluorescence change. Voltage trace reports actual voltage recorded during acquisition. **b)** Normalized F-Vs. Same colors and hp as in a). Data fit to single Boltzmann equations (see Materials and Methods, Table A1.1). Catalytic site mutants negatively shift F-V. Error bars (mostly smaller than symbols) are $\pm$ SEM, n $\geq$ 9. **c)** Cartoon depicting influence of mutations at catalytic site of PD on VSD motion detected by TMRM (asterisk) attached to G214C, at the outer end of S4.

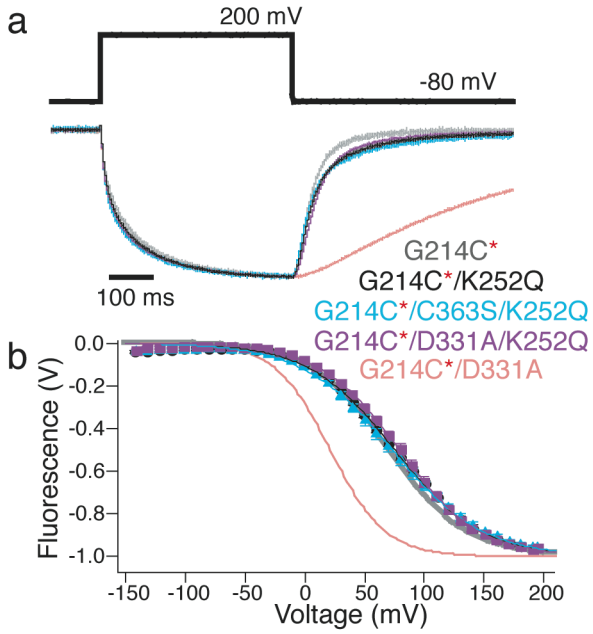

Figure A1.3. Linker charge neutralization eliminates effect of catalytic site mutations on VSD motion. a) Representative normalized fluorescence traces evoked by step from hp = -80 mV to +200 mV. G214C*/K252Q (black, same as in Supp. Figure 5.), G214C*/C363S/K252Q (blue), G214C*/D331A/K252Q (purple), G214C* (gray, from Figure. 2) and G214C*/D331A (pale red, from Figure. 2). **b**) F-Vs fit to single Boltzmann equation, with symbol size indicating ± SEM, n ≥10. Same colors and hp as in (a). K252Q eliminates both the slowing of ΔF_{OFF} (a) and the shift of F-V (b) caused by C363S and D331A catalytic site mutations. Data fit to single Boltzmann equations (see Supp. Table A1.1).

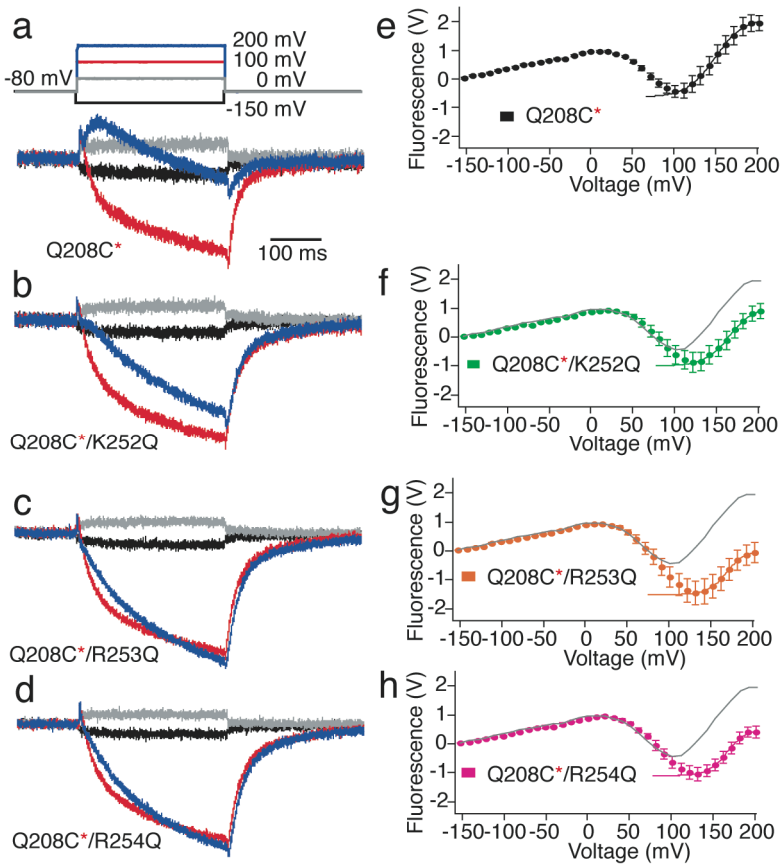

Figure A1.4. Linker mutations alter late component of VSD motion. a-d) Representative Q208C* fluorescence traces evoked by steps from hp= -80 mV to -150 mV (black), 0 mV (gray), +100 mV (red) and +200 mV (blue) in wild type, Q208C* (**a**) and the three linker mutations: Q208C*/K252Q (**b**), Q208C*/R253Q (**c**) and Q208C*/R254Q (**d**) **e-h**) F-V relationships measured at the peak of the second upper component for wild type (Q208C*) and the linker mutants normalized by component from -150 mV to 0 mV. Wild type (Q208C*) from (e) superimposed for comparison in (f-h) as gray line. Linker mutants diminish amplitude of late fluorescence increase component and shift its voltage dependence to the right. Data fit to single Boltzmann equations (Table A1.1), error bars are ± SEM, n ≥8.

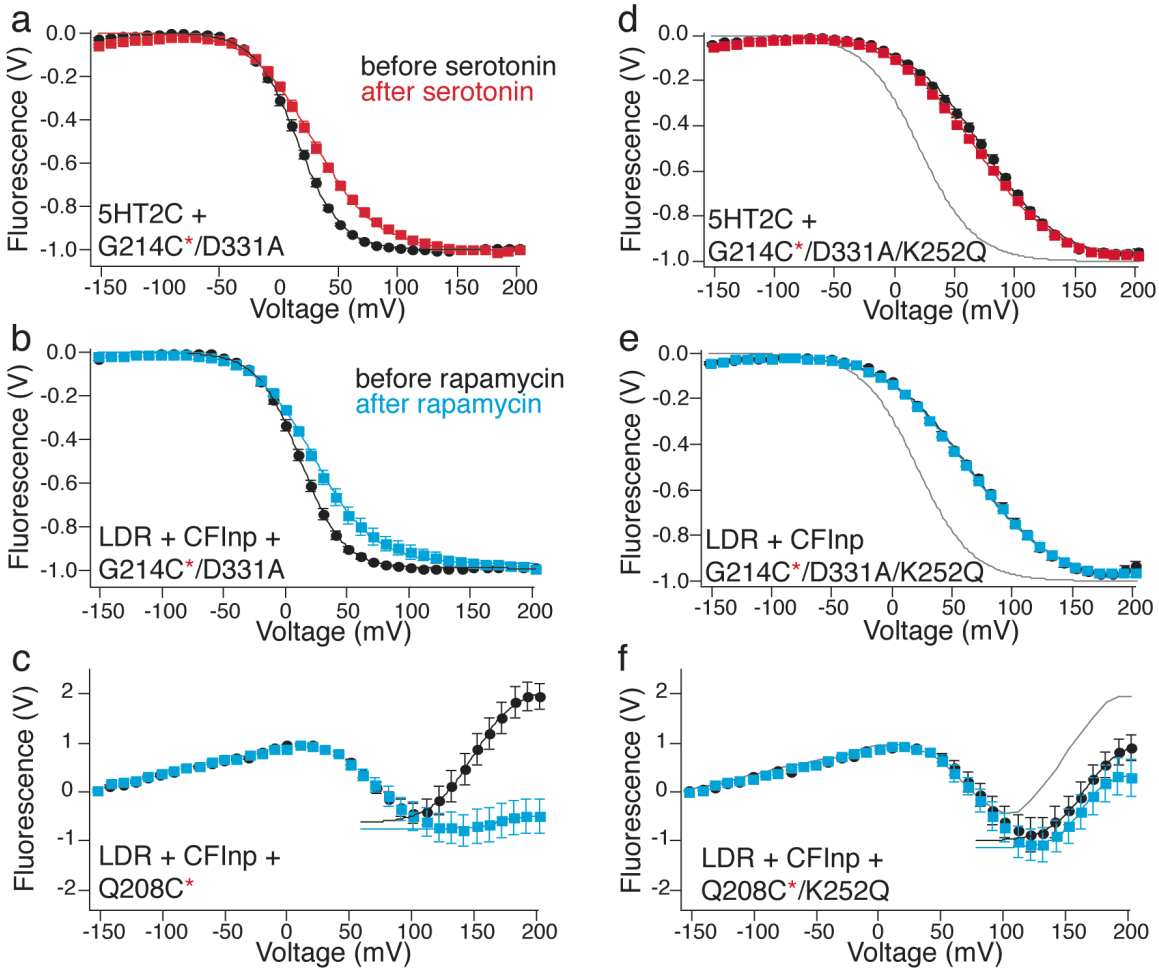

Figure A1.5. PI(4,5)P_2 depletion alters VSD motion in manner dependent on the VSD-PD linker. a) 5HT2C receptor activation by serotonin (activates conversion of PI(4,5)P_2 into IP_3 and DAG by phospholipase C) shifts the F-V of the catalytic site mutation G214C*/D331A to the right and decreases the steepness. F-Vs before (black) and 5 min after addition of 10 μM serotonin (red). **b, c**) Rapamycin-induced membrane localization of the lipid phosphatase CFInp (converts PI(4,5)P_2 into PI(4)P) shifts the F-V of the catalytic site mutation G214C*/D331A to the right and decreases the steepness (**b**), and decreases the amplitude and shifts to the right the late component of fluorescence increase of wild type Q208C* (**c**). F-Vs before (black) and 5-10 min after (blue) addition of 1 μM rapamycin. **d)** Catalytic site mutation, G214C*/D331A, was not affected by 5HT2C receptor activation in presence of K252Q linker mutation. F-Vs before (black) and 5 min after (red) addition of serotonin. F-V of G214C*/D331A with a wild type linker and no 5HT2C activation shown for comparison in gray. **e, f)** Rapamycin-induced PI(4,5)P_2 depletion by activation of CFInp has no detectable effect in G214C*/D331A/K252Q (**e**), and a small effect in the linker mutants Q208C*/K252Q (**f**) compared to wild type Q208C* (**c**). F-Vs before (black) and 5-10 min after rapamycin (blue). (F-V of G214C*/D331A in gray for comparison in **e** and F-V of Q208C* in gray for comparison in **f**). Error bars are ± SEM, n ≥9. Data fit to single Boltzmann equations (see Tables A1.2 & A1.3).

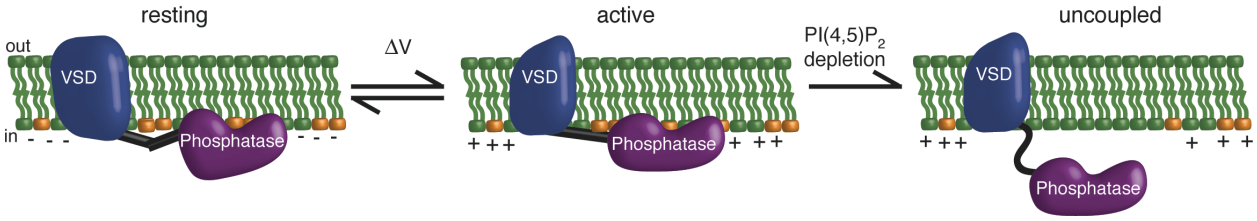

Figure A1.6. Model of linker regulation and coupling in Ci-VSP. Left) At negative voltage the VSD is in a resting state and the linker is distorted into a non-functional state. Middle) At positive voltage the VSD is in an activated conformation and the linker relaxes into the positive regulatory state that is necessary for activity of the isolated PD *in vitro*. $PI(4,5)P_2$ stabilizes the activated state, possibly by interacting with the linker. Right) The depletion of $PI(4,5)P_2$ by Ci-VSP activity leads to a destabilization of the activated state and uncoupling of the VSD from the phosphatase, thus turning the enzyme off even though the membrane is still depolarized.

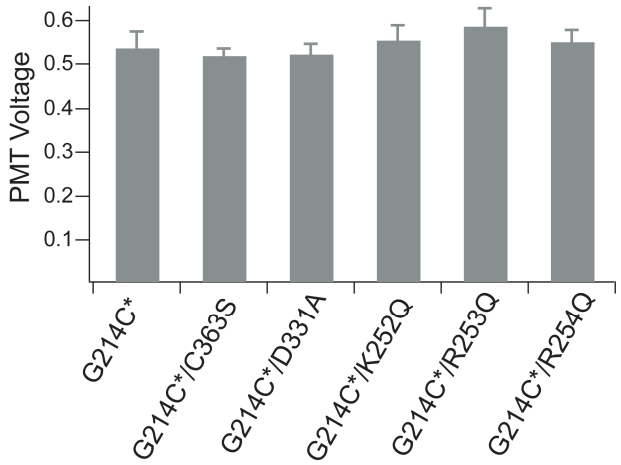

Figure A1.7. Resting level fluorescence indication of protein expression. Protein surface expression levels assessed from cell membrane fluorescence at the holding potential of -80 mV due to TMRM attached to G214C (G214C*) in wild type, linker mutants and catalytic site mutants. Y-axis is PMT voltage needed to bring fluorescence baseline at the holding potential to the same output level for cells expressing G214C* (n=20), G214C*/C363S (n=11), G214C*/D331A (n=16), G214C*/K252Q (n=8), G214C*/R253Q (n=11) and G214C*/R254Q (n=11). Equal PMT voltages (i.e. equal fluorescence intensities) indicate similar surface expression levels of the mutants and wild type proteins.

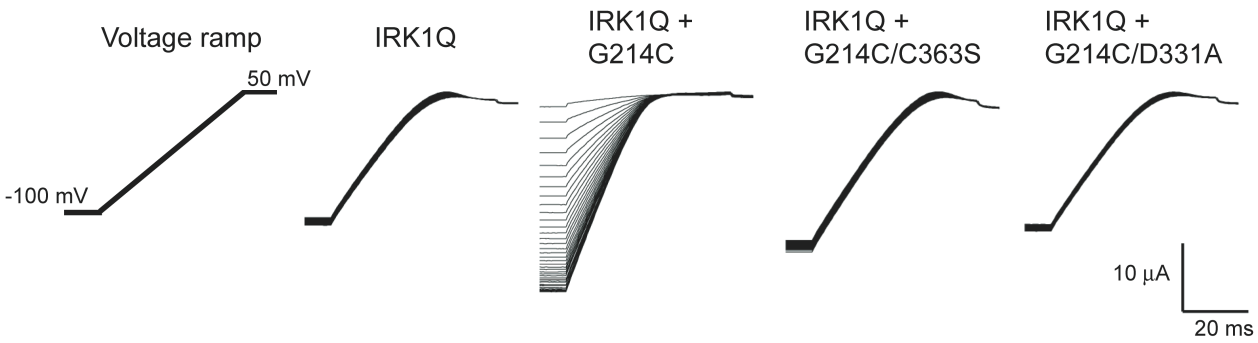

Figure A1.8. Catalytic mutants eliminate voltage dependent changes in IRK1Q current. Single cells expressing either IRK1Q alone, IRK1Q with G214C, G214C/C363S or G214C/D331A were tested for Ci-VSP activity. After reaching a steady IRK1Q current while holding at +60 mV (to activate Ci-VSP, not shown), the holding potential was switched to -100 mV (to deactivate Ci-VSP) and brief (50 ms) voltage ramps were given once every 10s (left) to test for the inwardly rectifying IRK1Q current. The protocol was repeated 40 times to reach a steady state IRK1Q current. Shown are the currents evoked by the 40 voltage ramps as the channel recovers from the $PI(4,5)P_2$ depletion due to the Ci-VSP activity induced by the original depolarization. IRK1Q alone and the two catalytic mutations did not show any change in the magnitude of the IRK1Q current, consistent with a lack of Ci-VSP activity, whereas IRK1Q + wild type Ci-VSP with the G214C mutation for TMRM attachment (but not labeled) showed a marked increase in the IRK1Q current over time.

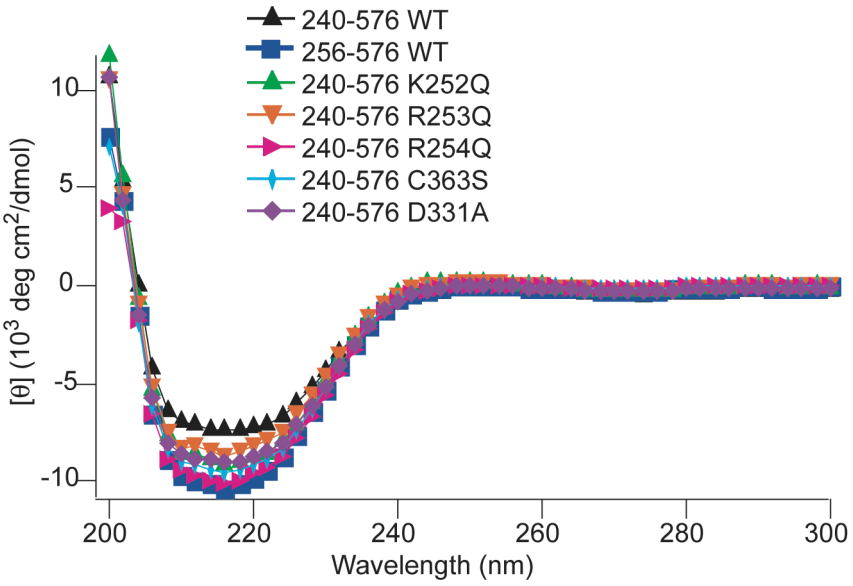

Figure A1.9. Circular dichroism (CD) spectra of the recombinant, purified C-terminal cytosolic fragment of Ci-VSP. CDs on proteins consisting of only the phosphatase (starting at amino acid 256) or the linker + phosphatase (starting at amino acid 240) with a wild type (WT) sequence, or with mutations in the linker or phosphatase catalytic site (see Figure. 1d for cartoon representations of constructs). The spectra indicate that the mutants Ci-VSP proteins are well folded.

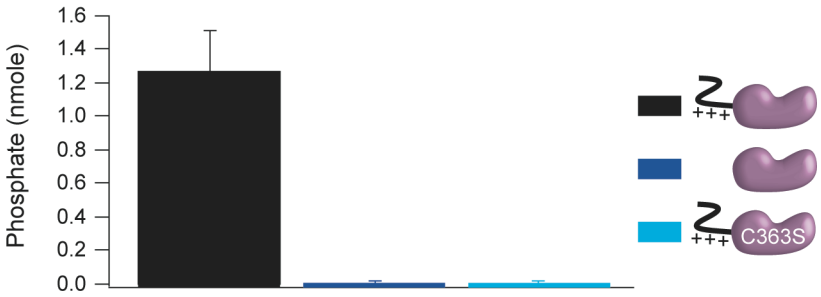

Figure A1.10. ***In vitro*** **malachite green activity assay with soluble substrate.** Assay using IP_4 as a soluble substrate shows that linker-less phosphatase domain has no activity (i.e. is indistinguishable from the catalytically dead reactive cysteine mutant control). Result shows that lack of activity of linker-less phosphatase domain in extruded 100 nm vesicles of PS + $PI(3,4,5)P_3$ (Figure. 1d) is not due to a loss of targeting to the vesicles, but to a loss of ability to catalyze. This result distinguishes Ci-VSP from PTEN, whose PBM Ci-VSP (linker homolog) mutants retain activity in IP_4, but lose activity in $PI(3,4,5)P_3$ vesicles due to loss of lipid association[2].

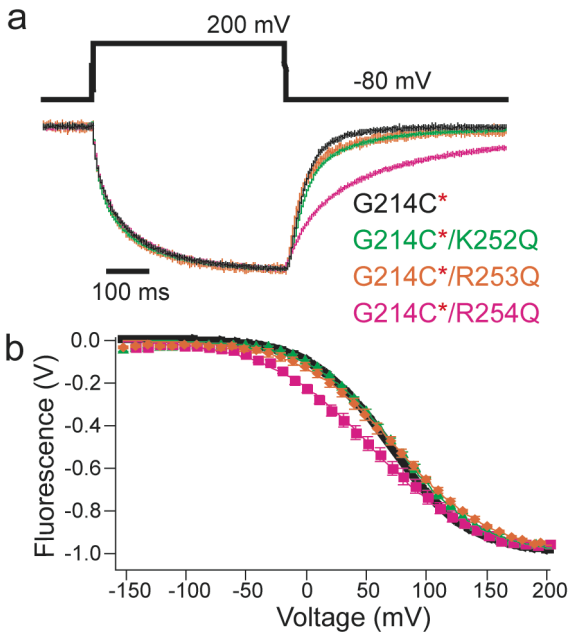

Figure A1.11. Neutralization mutations of conserved basic residues in VSD-phosphatase linker alter VSD motion. a) Representative normalized fluorescence traces evoked by step from hp = -80 mV to +200 mV. G214C* (black, from Figure. 2); G214C*/K252Q (green); G214C*/R253Q (orange); G214C*/R254Q (magenta). **b**) F-Vs fit to single Boltzmann equation (Table A1.1), with symbol size indicating $\pm$ SEM, n $\geq$10. Same colors and hp as in a). Of the three neutralization mutations, R254Q has the most obvious effect on S4 motion, slowing the S4 ΔF_{OFF} (a) and shifting the F-V (b).

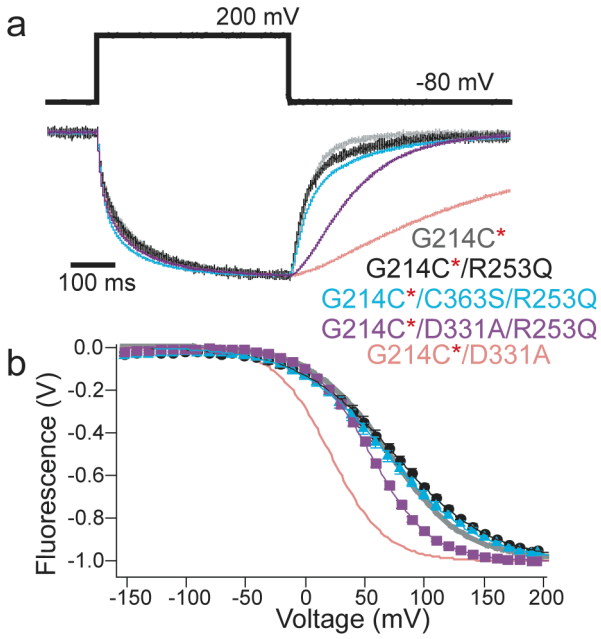

Figure A1.12. Linker charge neutralization diminishes effect of catalytic site mutations on VSD motion. a) Representative normalized fluorescence traces evoked by step from hp = -80 mV to +200 mV. G214C*/R253Q (black, same as Supp. Figure. 5), G214C*/C363S/R253Q (blue), G214C*/D331A/R253Q (purple), G214C* (gray, from Figure. 2) and G214C*/D331A (pale red, from Figure. 2). **b**) F-Vs fit to single Boltzmann equation (Table A1.1), with symbol size indicating $\pm$ SEM, n $\geq$10. Same colors and hp as in a). R253Q diminishes, but does not completely reverse the effects of the C363S and D331A mutants on the ΔF_{OFF} (a) and F-V (b).

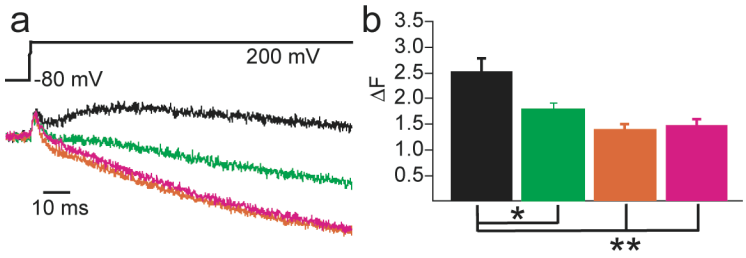

Figure A1.13. Charge neutralizations alter late stage rearrangement of VSD motions. a) Superimposed Q208C* fluorescence traces (from Figure. 4) in response to step from -80 to +200 mV for wild type (black), K252Q (green), R253Q (orange), R254Q (magenta). Expanded time axis shows that the early fluorescence components, an increase and a decrease, are the same for wild type and the mutants, and that only a later component of fluorescence increase is affected, with its amplitude attenuated by the mutants. **b)** Linker neutralization mutations decrease the late component as measured for steps to +200 mV. Data quantified from +200 mV points from F-V plots in Figure. 4. Error bars are $\pm$ SEM, $n \geq 8$. * = $p < 0.05$; ** = $p < 0.005$.

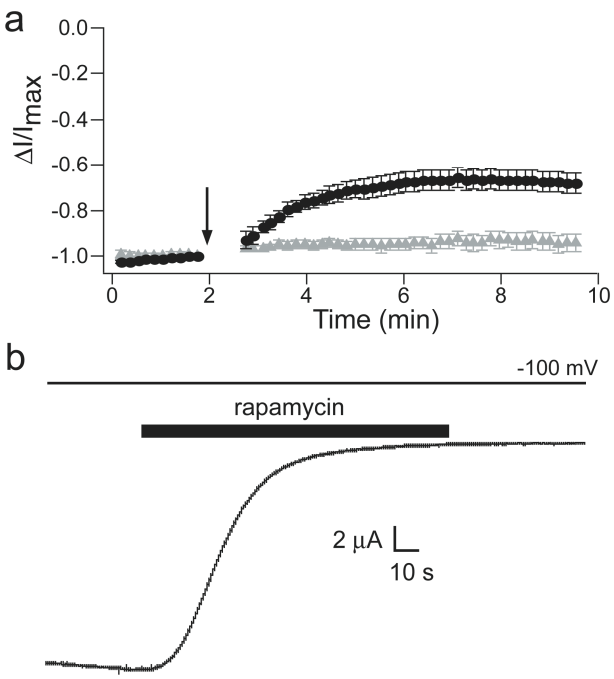

Figure A1.14. PI(4,5)P_2 depletion induced by activation of the 5HT2C receptor and the rapamycin system, as measured by IRK1Q. a) PI(4,5)P_2 depletion in oocytes co-expressing IRK1Q and 5HT2C is elicited by addition of 10 μM serotonin (black, n=9), but not control buffer (gray, n=11), at the time marked by the arrow. IRK1Q current was evoked by a short (50 ms) voltage ramp from -100 mV to +50 mV, once every 10s. The $\Delta I/I_{max}$ was calculated from the leak subtracted steady-state current at -100 mV in cells that retained stable rectification throughout the protocol. Error bars are ± SEM. **b**) PI(4,5)P_2 depletion elicited by 1 μM rapamycin (black bar) in a representative oocyte co-expressing IRK1Q with LDR and CFInp (the rapamycin system) held at a constant voltage of -100 mV. IRK1Q current decreased by >90%.

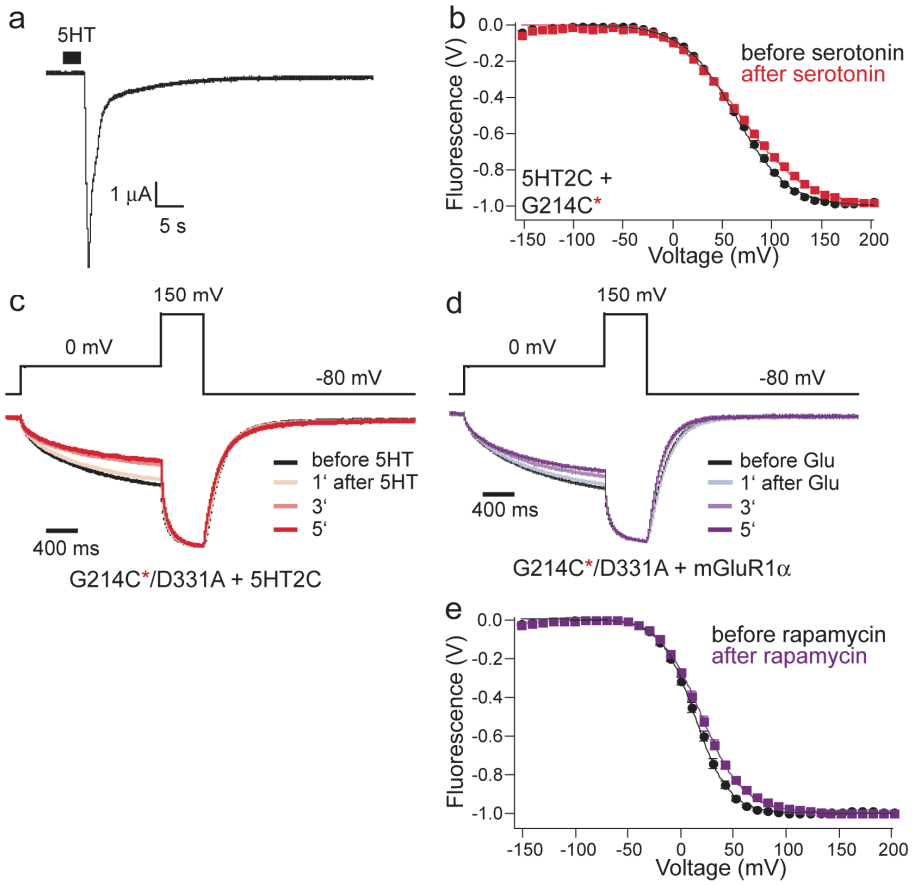

Figure A1.15. PI(4,5)P_2 depletion triggered by two receptors that activate PLC. a) Monitoring successful activation of PLC. Current trace at holding potential = -80 mV shows activation of endogenous calcium-activated chloride channel following addition of serotonin to a cell expressing 5HT2C. 5HT2C activation of the PLC pathways results in an increase in intracellular calcium leading to the activation of the chloride channel. Chloride channel activation served in 5HT2C and mGluR1α experiments to ensure that PLC was activated. **b**) 5HT2C receptor activation by serotonin (to activate conversion of PI(4,5)P_2 into IP_3 and DAG by phospholipase C) shifts to right and decreases the steepness of the F-Vs of wild type G214C*, with normal phosphatase activity. F-Vs before (black) and 5 min after addition of 10 µM serotonin (red). **c, d**) Representative fluorescence traces evoked by steps from hp = -80 mV to 0 mV then to +150 mV before returning to hp for oocytes co-expressing G214C*/D331A with 5HT2C (c) or G214C*/D331A with mGluR1α (d). Shown are traces before and after addition of 10 µM serotonin or 100 µM glutamate, respectively, at indicated times. The +150 mV step was used to normalize the total ΔF because it is at the top of the F-V (see panel d). The fluorescence at 0 mV (in the steep part of the F-V before activation of the receptors) is seen to decrease after serotonin or glutamate induced PI(4,5)P_2 depletion. **e**) The F-V of G214C*/D331A is shifted after addition of glutamate in cells co-expressing mGluR1α, which activates the PLC pathway. F-Vs before (black) and 5 min after (lavender) addition of glutamate. Data fit to single Boltzmann equations. G214C*/D331A before Glu: $V_{1/2}$= 13.4 ± 0.3, slope= 16.1 ± 0.2, n=8; G214C*/D331A after Glu: $V_{1/2}$= 19.3 ± 0.4, slope= 19.8 ± 0.3, n=8).

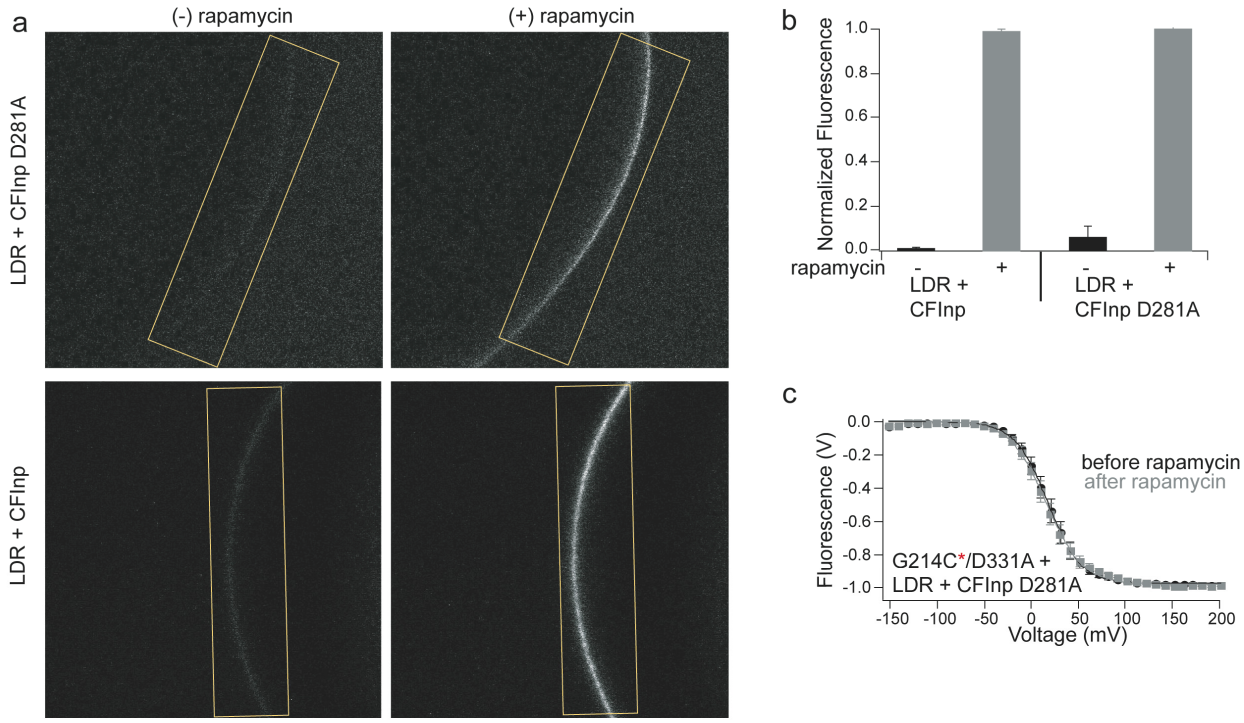

Figure A1.16. Chemically inducible translocation of CF-Inp constructs. **a**) Confocal images of oocytes co-expressing G214C/D331A, LDR and either the active CFInp (bottom) or the catalytically dead CFInp D281A mutant, before (left) and after (right) addition of rapamycin. Rapamycin induces localization to the plasma membrane of both the active CFInp and the catalytically dead CFInp D281A mutant. Yellow boxes mark regions of interest containing the plasma membrane. **b**) Quantification of membrane fluorescence for cells co-expressing G214C/D331A, LDR and either active CFInp (n=5) or CFInp D281A (n=5), before and after addition of rapamycin. **c**) F-V relations of G214C*/D331A for cells co-expressing the rapamycin system proteins, LDR and the catalytically dead CFInp D281A. F-Vs before (black) and 10 min after (gray) addition of rapamycin. Data fit to Boltzmann equations. No change in the F-V was observed when the catalytically inactive CFInp D281A was used instead of catalytically active CFInp (see Figure. 5). (G214C*/D331A before rapamycin: $V_{1/2}$= 17.8 $\pm$ 0.3, slope= 17.6 $\pm$ 0.3, n=8; G214C*/D331A after rapamycin: $V_{1/2}$= 16.0 $\pm$ 0.5, slope= 19.3 $\pm$ 0.4, n=8). Error bars are $\pm$ SEM.

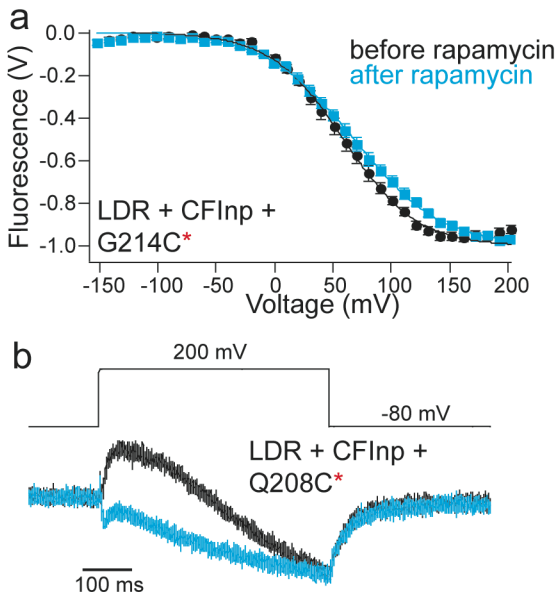

Figure A1.17. PI(4,5)P_2 depletion alters the VSD motions of active Ci-VSP. a) Rapamycin-induced membrane localization of the lipid phosphatase CFInp (to convert PI(4,5)P_2 into PI(4)P) shifts to right and decreases the steepness of the F-Vs of wild type G214C*. F-Vs before (black) and 5-10 min after (blue) addition of 1 μM rapamycin. Data fit to single Boltzmann equations (see Tables A1.2 & A1.3). Error bars are $\pm$ SEM, n $\geq$9. **b**) Representative fluorescence response of wild type Q208C* in response to a single depolarizing step to +200 mV before (black) and 10 min after (blue) addition of 1 μM rapamycin.

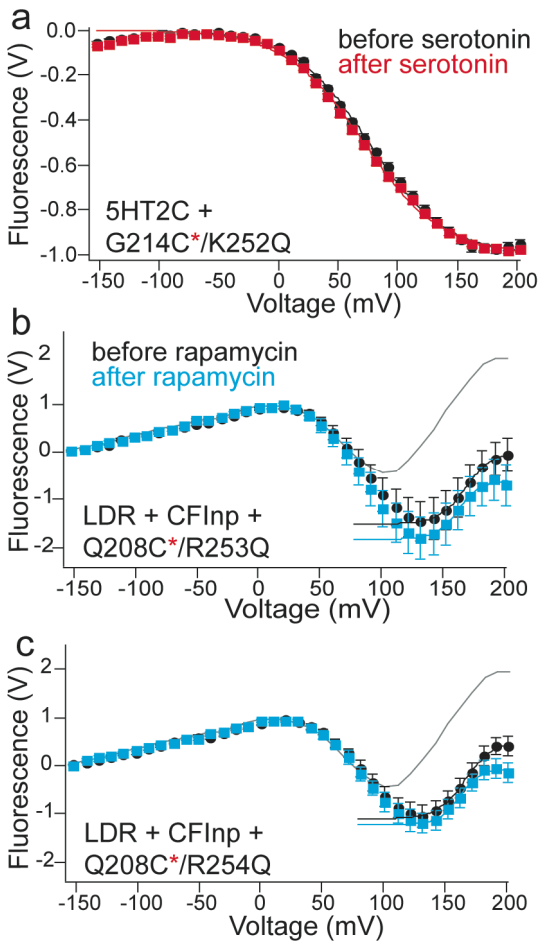

Figure A1.18. PI(4,5)P_2 regulation in VSP with no catalytic mutation is still mediated by the VSD-phosphatase linker. a) K252Q linker mutant in the active G214C* Ci-VSP was not affected by 5HT2C receptor activation to induce PI(4,5)P_2 depletion. F-Vs before (black) and 5 min after (red) addition of serotonin. F-V of G214C* with a wild type linker and no 5HT2C activation shown for comparison in gray. (G214C* and G214C*/K252Q F-Vs overlap). **b, c)** Rapamycin-induced PI(4,5)P_2 depletion by activation of CFInp has a blunted effect compared to wild type Q208C* (gray) in the linker mutants, Q208C*/R253Q (**b**) and Q208C*/R254Q (**c**). F-Vs before (black) and 5-10 min after rapamycin (blue). Error bars are $\pm$ SEM with n $\geq$9. Data fit to single Boltzmann equations (see Tables A1.2 & A1.3).

Table A1.1. Effect of catalytic and linker mutations on VSD motion, as gauged by F-Vs measured from TMRM attached to two cysteine substitution sites outside S4. Values of parameters from single Boltzmann fits to the entire fluorescence vs. voltage (F-V) relation of G214C* and to only the late increasing ΔF component evoked at the most positive voltages (> +100 mV) in Q208C*.

Protein	$V_{1/2}$ (mV)	slope	n
G214C*	59.3 ± 1.1	31.2 ± 1.0	9
G214C*/C363S	55.5 ± 0.4	24.5 ± 0.4	13
G214C*/D331A	12.4 ± 0.2	17.1 ± 0.2	10
G214C*/K252Q	75.0 ± 0.6	35.6 ± 0.6	12
G214C*/R253Q	74.7 ± 0.5	39.8 ± 0.6	11
G214C*/R254Q	54.2 ± 1.1	46.2 ± 1.1	11
G214C*/C363S/K252Q	72.9 ± 0.7	37.6 ± 0.7	12
G214C*/D331A/K252Q	78.7 ± 0.4	33.3 ± 0.4	13
G214C*/C363S/R253Q	69.1 ± 0.5	38.2 ± 0.6	12
G214C*/D331A/R253Q	55.0 ± 0.2	25.1 ± 0.1	12
Q208C*	149.9 ± 1.2	17.3 ± 1.4	10
Q208C*/K252Q	165.9 ± 1.2	15.0 ± 1.5	12
Q208C*/R253Q	169.0 ± 0.4	10.9 ± 0.4	8
Q208C*/R254Q	166.8 ± 1.5	11.6 ± 1.7	8

Table A1.2. $PI(4,5)P_2$ depletion by PLC (activated via the 5HT2C receptor) alters the F-V of G214C*, and the effect is blunted by linker mutation K252Q. Midpoints and slopes of F-V relations in cells expressing wild type (G214C*) and mutant versions of Ci-VSP along with the 5HT2C receptor, before (-) and after (+) addition of serotonin to deplete $PI(4,5)P_2$.

Protein	(-) serotonin		(+) serotonin		
	$V_{1/2}$ (mV)	slope	$V_{1/2}$ (mV)	slope	n
G214C*	63.3 ± 0.5	26.4 ± 0.5	68.2 ± 0.8	32.9 ± 0.8	15
G214C*/D331A	5.9 ± 0.3	18.2 ± 0.2	29.6 ± 0.6	26.3 ± 0.6	10
G214C*/K252Q	76.0 ± 1.1	32.1 ± 1.0	71.3 ± 0.9	32.9 ± 0.9	12
G214C*/D331A/K252Q	74.0 ± 0.8	31.9 ± 0.8	68.3 ± 0.7	32.8 ± 0.7	11

Table A1.3. PI(4,5)P_2 depletion by the rapamycin system alters the F-Vs of G214C* and Q208C*, and the effect is blunted by linker mutations. Midpoints and slopes of F-V relations in cells expressing wild type (G214C* or Q208C*) and mutant versions of Ci-VSP before (-) and after (+) rapamycin induced recruitment to the membrane of the CFInp phosphatase.

Protein	(-) rapamycin		(+) rapamycin		
	$V_{1/2}$ (mV)	slope	$V_{1/2}$ (mV)	slope	n
G214C*	59.3 ± 1.1	31.2 ± 1.0	68.1 ± 0.7	37.3 ± 0.7	9
G214C*/D331A	12.4 ± 0.2	17.1 ± 0.2	23.1 ± 0.6	24.1 ± 0.6	10
G214C*/D331A/K252Q	64.2 ± 1.0	34.5 ± 1.0	63.0 ± 0.7	34.9 ± 0.7	8
Q208C*	149.9 ± 1.2	17.3 ± 1.4	168.9 ± 3.1	9.2 ± 2.9	10
Q208C*/K252Q	165.9 ± 1.2	15.0 ± 1.5	162.7 ± 1.1	10.9 ± 1.2	12
Q208C*/R253Q	169.0 ± 0.4	10.9 ± 0.4	162.7 ± 1.8	9.1 ± 1.8	8
Q208C*/R254Q	166.8 ± 1.5	11.6 ± 1.7	162.2 ± 2.0	8.2 ± 2.0	8